

## University of Southampton Research Repository

Copyright © and Moral Rights for this thesis and, where applicable, any accompanying data are retained by the author and/or other copyright owners. A copy can be downloaded for personal non-commercial research or study, without prior permission or charge. This thesis and the accompanying data cannot be reproduced or quoted extensively from without first obtaining permission in writing from the copyright holder/s. The content of the thesis and accompanying research data (where applicable) must not be changed in any way or sold commercially in any format or medium without the formal permission of the copyright holder/s.

When referring to this thesis and any accompanying data, full bibliographic details must be given, e.g.

Thesis: Author (Year of Submission) "Full thesis title", University of Southampton, name of the University Faculty or School or Department, PhD Thesis, pagination.

Data: Author (Year) Title. URI [dataset]



**University of Southampton**

Faculty of Engineering and Physical Sciences

School of Electronics and Computer Science

**Textile-based triboelectric energy harvester with alternating positive  
and negative freestanding structure**

by

**Watcharapong Paosangthong**

Thesis for the degree of Doctor of Philosophy

December 2021





# University of Southampton

## Abstract

Faculty of Engineering and Physical Sciences

School of Electronics and Computer Science

Doctor of Philosophy

Textile-based triboelectric energy harvester with alternating positive and negative  
freestanding structure

by

Watcharapong Paosangthong

Although wearable and portable electronics have been substantially developed over the past decades, most of these devices still rely on batteries, which require persistent recharging and replacement. An effective way to solve this problem is to introduce a wearable self-charging power system using an energy harvester to scavenge energy from the surrounding environment. Triboelectric energy harvesters, well-known as triboelectric nanogenerators (TENGs), are one of the most promising candidates for powering these systems. They can efficiently convert kinetic energy occurring during or after frictional contact between two dissimilar materials into electricity based on contact electrification and the electrostatic induction effect. Various examples of TENGs have demonstrated flexibility, low weight, biocompatibility and good performance that are essential for wearable devices. According to these properties, textile-based TENGs are proposed to be highly suitable for powering wearable devices and electronic textiles (e-textiles).

This thesis focuses on the methods of implementing TENG into textiles to harvest energy from human motion to create a textile-based TENG (T-TENG). Two novel designs of T-TENGs have been reported. The first design is a T-TENG with alternating positive and negative freestanding grating structure, defined as pnG-TENG. The second design is a T-TENG with an alternating positive and negative freestanding woven structure for harvesting kinetic energy in all sliding directions, defined herein as woven-TENG. In each case, the definition of 'freestanding' in the context of TENG designs is that the triboelectric material can move freely without physical connection to the other electrode. The key novelty of these designs is the introduction of the positive and negative triboelectric materials used as the freestanding triboelectric layer in TENGs operating in the sliding freestanding triboelectric-layer mode (FT-mode). This implementation has significantly improved the electrical output performance of the devices compared to conventional TENGs with a single triboelectric material. The devices have demonstrated successful practical applications as both energy harvesters and sensors. The fabrication processes of the devices are common, low-cost and

compatible with standard textile manufacturing (e.g. weaving, heat-transfer printing and screen printing).

The pnG-TENG is composed of alternate grated strips of positive (nylon fabric) and negative triboelectric material (PVC heat transfer vinyl) and is operating in the sliding FT-mode. Its Ag interdigitated electrodes with matching periodicity have been fabricated using a self-developed screen-printing technique. Whereas most grating-structured TENGs operating in this mode comprise gratings of one type of triboelectric material separated by air gaps, this novel design presents a replacement of the air gaps by another triboelectric material with the opposite polarity to the existing triboelectric material. This method increases performance by increasing the percentage contact area and the amount of transferred charge of the generator.

The pnG-TENG with 10 gratings of nylon fabric and PVC heat transfer vinyl delivers a root mean square (RMS) open-circuit voltage of 136 V and an RMS short-circuit current of 2.68  $\mu\text{A}$ . The average power transfer reaches a maximum value of 125  $\mu\text{W}$  at a load resistance of 50  $\text{M}\Omega$ , a mechanical oscillation of 2 Hz, a contact force of 5 N, a humidity of 25%RH and a temperature of 25 °C. This corresponds to an average power density of 38.8  $\text{mW}/\text{m}^2$ , which is 1.94 and 6.43 times greater than the power generated by the TENG with a single triboelectric material and the TENG with no gratings, respectively.

The woven-TENG operating in the sliding FT-mode has been successfully developed using a standard fabric weaving and doctor blade printing technique. Whereas most woven-structured TENGs operate in contact-separation mode or contact-separation FT-mode and consist of one type of triboelectric material, this novel woven-TENG comprises woven electrodes and woven strips of positive and negative triboelectric material, which form a checker-like pattern over the electrodes with matching periodicity. The idea of implementing an alternating positive and negative freestanding structure matches perfectly with the introduced woven electrode structure. Because of the nature of the woven structure, a symmetric and periodic arrangement of the electrodes and alternating triboelectric materials are self-formed. This implementation has also shown an improvement in the power output of the TENG by a factor of 2.2 compared to the TENG with a single triboelectric material. Furthermore, in contrast to the conventional grating-structured and woven-structured TENGs, which are designed to operate only in one moving direction, this new design also allows the woven-TENG to harvest energy from any arbitrary sliding direction.

The woven-TENG with woven strips of nylon fabric and polytetrafluoroethylenevinyl (PTFE) fabric can generate an RMS open-circuit voltage of 62.9 V and an RMS short-circuit current of 1.77  $\mu\text{A}$ . The average power transfer reaches a maximum value of 34.8  $\mu\text{W}$  at a load resistance of 50  $\text{M}\Omega$ , a mechanical oscillation of 2 Hz, a contact force of 5 N, a humidity of 25%RH and a temperature of 25 °C. This corresponds to an average power density of 5.43  $\text{mW}/\text{m}^2$ .

# Table of Contents

<b>Table of Contents .....</b>	<b>i</b>
<b>List of Tables.....</b>	<b>v</b>
<b>List of Figures .....</b>	<b>vii</b>
<b>Research Thesis: Declaration of Authorship .....</b>	<b>xix</b>
<b>Acknowledgements .....</b>	<b>xxi</b>
<b>Nomenclature .....</b>	<b>xxiii</b>
<b>Abbreviations .....</b>	<b>xxvii</b>
<b>Chapter 1 Introduction.....</b>	<b>1</b>
1.1 Research motivation .....	1
1.2 Aims and objectives.....	3
1.3 Thesis structure .....	4
1.4 Statement of novelty.....	5
1.5 List of publications and conferences.....	6
<b>Chapter 2 Background theory and literature review .....</b>	<b>9</b>
2.1 Introduction.....	9
2.2 Triboelectric effect .....	9
2.2.1 Electronic band structure model.....	10
2.2.2 Interatomic interaction model .....	11
2.3 Triboelectric series .....	13
2.4 Fundamental operation mode and working principle of TENGs .....	15
2.4.1 Vertical contact-separation mode (CS-mode).....	16
2.4.2 Lateral sliding mode (LS-mode).....	17
2.4.3 Single-electrode mode (SE-mode) .....	18
2.4.4 Freestanding triboelectric-layer mode (FT-mode).....	19
2.5 Theory of sliding freestanding triboelectric-layer mode TENG .....	22
2.6 Textile manufacturing .....	25
2.7 Materials.....	29
2.7.1 Triboelectric materials .....	29
2.7.2 Electrode materials .....	30

## Table of Contents

2.7.2.1	Metal-based electrode.....	30
2.7.2.2	Carbon-based electrode.....	31
2.7.2.3	Polymer-based electrode.....	31
2.8	Surface modification.....	32
2.8.1	Topographic modification.....	32
2.8.2	Chemical modification.....	33
2.9	Material and structural design.....	34
2.9.1	Fabric-based TENG.....	34
2.9.1.1	Fabric-based TENG using the fabric as triboelectric layer.....	34
2.9.1.2	Fabric-based TENG using fabric as substrate.....	36
2.9.2	Fibre-based TENG.....	37
2.9.2.1	Single-thread semi-integrated TENG.....	38
2.9.2.2	Single-thread fully-integrated TENG.....	40
2.9.2.3	Multiple-thread fully-integrated TENG.....	42
2.10	Discussion.....	45
2.11	Conclusion.....	49
<b>Chapter 3</b>	<b>Fundamental Experiments .....</b>	<b>55</b>
3.1	Introduction.....	55
3.2	Investigation of triboelectric materials.....	55
3.2.1	Design and methodology.....	56
3.2.1.1	Fabrication.....	56
3.2.1.2	Measurement system.....	57
3.2.1.3	$V_{OC}$ and $I_{SC}$ measurements.....	58
3.2.1.4	Surface charge density ( $\rho_q$ ) measurement.....	59
3.2.2	Results and discussion.....	60
3.2.2.1	$V_{OC}$ and $I_{SC}$ measurements.....	60
3.2.2.2	Surface charge density ( $\rho_q$ ) measurement.....	62
3.2.3	Conclusion.....	63
3.3	Factors influencing power output of TENGs.....	64

3.3.1	Frequency dependence measurement .....	64
3.3.2	Contact force dependence measurement .....	65
3.3.3	Humidity dependence measurement .....	67
3.3.4	Temperature dependence measurement.....	68
3.3.5	Conclusion .....	69
3.4	Rectifier circuit investigation.....	70
3.4.1	Design and methodology .....	70
3.4.1.1	Simulations .....	70
3.4.1.2	Experiments.....	71
3.4.2	Results and discussion.....	71
3.4.2.1	Simulations .....	71
3.4.2.2	Experiments.....	74
3.4.3	Conclusion .....	75
<b>Chapter 4</b>	<b>Textile-based triboelectric energy harvester with alternating positive and negative freestanding grating structure (pnG-TENG).....</b>	<b>77</b>
4.1	Introduction.....	77
4.2	Design and methodology .....	79
4.2.1	Fabrication.....	79
4.2.2	Working principle .....	86
4.2.3	Characterisation and measurement .....	89
4.3	Results and discussion.....	89
4.3.1	Grating number dependence .....	89
4.3.1.1	Simulation and theoretical calculation .....	89
4.3.1.2	Experiment .....	94
4.3.2	Oscillation frequency dependence .....	100
4.3.3	Contact force dependence .....	102
4.3.4	Durability and washability.....	104
4.3.5	Energy harvesting from human motion and applications .....	107
4.4	Conclusion .....	111

<b>Chapter 5 Textile-based triboelectric energy harvester with alternating positive and negative freestanding woven structure for harvesting kinetic energy in all sliding directions (woven-TENG).....</b>	<b>113</b>
5.1 Introduction .....	113
5.2 Design and methodology .....	115
5.2.1 Fabrication .....	115
5.2.2 Working principle.....	119
5.2.3 Characterisation and measurement .....	121
5.3 Result and discussion.....	122
5.3.1 Effect of the number of elements per each side of the upper substrate (N) .....	122
5.3.1.1 Simulation and theoretical calculation .....	122
5.3.1.2 Experiment.....	124
5.3.2 Effect of the positive and negative triboelectric material.....	127
5.3.3 Direction dependence .....	130
5.3.4 Oscillation frequency dependence .....	134
5.3.5 Contact force dependence .....	136
5.3.6 Durability and washability .....	137
5.3.7 Applications in wearable electronics .....	140
5.4 Conclusion.....	144
<b>Chapter 6 Conclusions and future work.....</b>	<b>145</b>
6.1 Conclusions .....	145
6.2 Future work.....	147
<b>Appendix A Arduino codes for the <math>\mu</math>-stepper motor and pedometer .....</b>	<b>149</b>
<b>Appendix B Simple pnG-TENG.....</b>	<b>153</b>
<b>Appendix C Alternative fabrication methods for the pnG-TENGs.....</b>	<b>159</b>
<b>Appendix D Direction dependence calculation for the woven-TENG .....</b>	<b>165</b>
<b>List of References .....</b>	<b>169</b>

## List of Tables

<b>Table 2.1</b>	Triboelectric series proposed by Diaz et al. Reproduced with permission from Ref [61]. Copyright 2017, American Institute of Physics. ....	14
<b>Table 2.2</b>	Triboelectric series and their triboelectric charge density (TECD) proposed by Zou et al. Reproduced with permission from Ref [62]. Copyright 2019, Nature Research. ....	15
<b>Table 2.3</b>	Parameter applied in the calculation of the outputs of sliding FT-mode TENGs. Reprinted with permission from Ref. [96]. Copyright 2015, Elsevier. ....	24
<b>Table 2.4</b>	Summary of important parameters of fabric-based TENGs.....	51
<b>Table 2.5</b>	Summary of important parameters of fibre-based TENGs .....	52
<b>Table 3.1</b>	Details of the triboelectric materials used in this thesis. ....	56
<b>Table 4.1</b>	Summary of the electrical outputs of the different TENGs .....	99





## List of Figures

<b>Figure 1.1</b>	Available power sources of human body from different daily activities. Reproduced with permission from Ref. [1]. Copyright 2014, John Wiley & Sons, Inc. ....2
<b>Figure 2.1</b>	(a) Schematic energy band model for metal-dielectric contact in the situations of (i) before contact, (ii) in contact. (b) Schematic energy band model for dielectric-dielectric contact in the situations of (i) before contact, (ii) in contact, and (iii) after contact. Reproduced with permission from Ref [54]. Copyright 2019, Elsevier.11
<b>Figure 2.2</b>	Interatomic interaction model for explaining triboelectric charge transfer between two materials based on electron cloud interaction. Schematic illustration of the electron cloud and potential energy profile (3D and 2D) of two atoms belonging to material A and B, respectively, (a) before contact, (b) in contact, (c) after contact and (d) at elevated temperature. The right inset shows detailed illustration of (b) that the increasing electron cloud overlapping leads to a lower potential barrier and thus to interatomic electron transition and possible photon emission. Reproduced with permission from Ref [54]. Copyright 2019, Elsevier. ....12
<b>Figure 2.3</b>	Four fundamental operation modes of TENGs: (a) Vertical contact-separation mode (CS-mode), (b) lateral sliding mode (LS-mode), (c) single-electrode mode (SE-mode) and (d) freestanding triboelectric-layer mode (FT-mode).....16
<b>Figure 2.4</b>	(a) Schematic diagram of cloth-based TENG with a linear-grating structure, (b) SEM image of the microstructure of nylon cloth's surface, (c) photograph of one part of the TENG and (d) fabrication process of the TENG. Reproduced from Ref. [83]. Copyright 2015 American Chemical Society. ....18
<b>Figure 2.5</b>	(a) Schematic diagram for fabrication process of single-thread based wearable TENG in serpentine shape sewed on a textile and its applications, including (b) smartwatch, (c) motion sensor system and (d) wireless wearable keyboard. Reproduced with permission from Ref. [89]. Copyright 2016, John Wiley & Sons, Inc. ....19
<b>Figure 2.6</b>	T-TENG operating in freestanding triboelectric-layer contact-separation mode (FCS-mode): (a) schematic illustration and (b) power generation mechanism of the T-TENG contacted with palm skin. Photographs and the corresponding $I_{SC}$ of the

	T-TENG using different materials, including (c) terylene, (d) cotton, (e) rubber, (f) fur, (g) silk and (h) nylon as the freestanding triboelectric-layer. Reproduced with permission from Ref. [37]. Copyright 2017, Elsevier.....	21
<b>Figure 2.7</b>	(a) Dependence of the peak power of the double-layer TENG on load resistances and (b) time-dependent capacitor voltage of the different capacitors charged by the double-layer TENG. Reprinted with permission from Ref. [37]. Copyright 2017, Elsevier. ....	21
<b>Figure 2.8</b>	(a) Theoretical model of sliding FT-mode TENGs and (b) the corresponding equivalent circuit model. Reprinted with permission from Ref. [96]. Copyright 2015, Elsevier. ....	22
<b>Figure 2.9</b>	Output properties of sliding FT-mode TENGs under single frequency harmonic vibration. (a) Transferred charge–time relationship at different load resistances. (b) Current–time relationship at different load resistances. (c) Voltage–time relationship at different load resistances. (d) The dependence of the total energy harvested in a single period on the load resistance. Reprinted with permission from Ref. [96]. Copyright 2015, Elsevier. ....	24
<b>Figure 2.10</b>	Influence of the freestanding height $h$ on (a) short-circuit transferred charge $Q_{SC}$ , (b) total capacitance $C$ , (c) open-circuit voltage $V_{OC}$ and (d) the harvested energy in one cycle under different load resistance of sliding FT-mode TENGs. Reprinted with permission from Ref. [96]. Copyright 2015, Elsevier. ....	25
<b>Figure 2.11</b>	Three basic weaves: (a) plain weave (b) twill weave and (c) satin weave. Reprinted with permission from Ref. [20]. Copyright 2019, Elsevier. ....	27
<b>Figure 2.12</b>	Two basic knitted structures (a) weft knitting and (b) warp knitting. Reprinted with permission from Ref. [4]. Copyright 2017, MDPI. ....	27
<b>Figure 2.13</b>	T-TENG with three different knitted structures: (a) Schematic illustration of the T-TENG, (b) plain-knitted structure, (c) double-knitted structure, and (d) rib-knitted structure with insets of the magnified photos. Reproduced with permission from Ref. [105]. Copyright 2017, American Chemical Society.....	28
<b>Figure 2.14</b>	(a) Schematic illustration of T-TENG with plain weaving structure, (b) photograph of the textile weaving process and (c) dependence of the electrical output on the different woven structures. Reproduced with permission from Ref. [106]. Copyright 2016, Springer Nature. ....	29

<b>Figure 2.15</b>	(a) Schematic illustration of conformal ultrathin T-TENG and (b) $I_{SC}$ and $V_{OC}$ of the conformal T-TENGs for different types of fabric tested as triboelectric materials. Reproduced with permission from Ref. [119]. Copyright 2016, Elsevier. ....34
<b>Figure 2.16</b>	(a) Schematic illustration of T-TENG with a corrugated structure and (b) power generation mechanism via stretching and releasing. Reproduced with permission from Ref. [137]. Copyright 2017, Nature.....35
<b>Figure 2.17</b>	(a) Schematic illustration of T-TENG fabricated by plain-weaving stripes of Ni-cloth and P-Ni-cloth, and (b) power generation mechanism via a repeated compressive force. Reproduced with permission from Ref. [92]. Copyright 2015, John Wiley & Sons, Inc.....36
<b>Figure 2.18</b>	(a) Schematic diagram of the fabrication process of the fabric-based TENG proposed by Guo et al. Load resistance dependence of (b) peak output voltage and current, and (c) corresponding instantaneous power of the TENG. Reproduced with permission from Ref. [68]. Copyright 2016, American Chemical Society.....37
<b>Figure 2.19</b>	(a) Schematic illustration of core-shell yarns, (b) industrialised stainless-steel/PU core-shell yarns with different colours and (c) three possible operation modes of the T-TENGs: i. SE-mode, ii. CS-mode and iii. FT-mode. Reproduced with permission from Ref. [91]. Copyright 2017, American Chemical Society.....39
<b>Figure 2.20</b>	Schematic illustration of fibre-based hybrid nanogenerator combining a semi-integrated TENG (Output 1) and PENG (Output 2). The power is generated via a contact with an external material (Nylon fibre). Reproduced with permission from Ref. [40]. Copyright 2014, American Chemical Society. ....39
<b>Figure 2.21</b>	(a) Schematic illustration of single-thread fully-integrated TENG and (b) its operation principle in CS-mode [116]. ....40
<b>Figure 2.22</b>	Schematic diagrams of the fabrication process for the fibre-based TENG revealed by Kim et al. Reproduced with permission from Ref. [75]. Copyright 2015, American Chemical Society. ....41
<b>Figure 2.23</b>	(a) Power generation mechanism via contact-separation of multiple-thread fully-integrated TENG and (b) schematic illustration of the fabrication process. Reproduced with permission from Ref. [76]. Copyright 2014, American Chemical Society.....42

<b>Figure 2.24</b>	(a) Schematic illustration of the fabrication process and structure of the T-TENG proposed by Zhao et al. and (b) the working principle of the T-TENG. Reprinted from Ref. [74]. Copyright 2016, with permission from John Wiley & Sons, Inc.43
<b>Figure 2.25</b>	(a) Schematic illustration of the structure of 3D orthogonal woven TENG. Frequency dependence of (b) $V_{OC}$ and (c) $I_{SC}$ of the TENG. Reprinted from Ref. [39]. Copyright 2017, with permission from John Wiley & Sons, Inc. .... 44
<b>Figure 2.26</b>	(a) Power generation mechanism of the T-TENG proposed by Chen et al., (b) Schematic illustration of the woven structure (left side) and photograph (right side) of the T-TENG (scale bar: 2.5 cm), (c) dependence of the $V_{OC}$ and the transferred charges on the PTFE diameter and (d) dependence of the $V_{OC}$ and the transferred charges on the interval distance of the carbon wires. The insets show the photographs of the corresponding T-TENGs. Reprinted from Ref. [140]. Copyright 2018, with permission from Elsevier. .... 45
<b>Figure 2.27</b>	Contact force dependence of the output voltage and current of the T-TENG operating in CS-mode proposed by Seung et al. [15]..... 46
<b>Figure 3.1</b>	Schematic illustration of (a) upper and (b) lower substrate of simple FT-mode TENG..... 57
<b>Figure 3.2</b>	Photograph of belt-driven linear actuator consisting of a v-slot linear rail, a stepper motor, a v-slot gantry plate with 4 wheels, a 3D-printed lower stage, 4 pillars and a $\mu$ -stepper controller board. .... 57
<b>Figure 3.3</b>	Photograph of (a) lower substrate with two metal electrodes fixed on the lower stage and (b) upper substrate with a triboelectric material fixed under the upper stage and acrylic stage holder..... 58
<b>Figure 3.4</b>	Cross-section view of measurement system for simple sliding FT-mode TENG. Lower substrate is driven by a stepper motor and moves horizontally relative to upper substrate, which is fixed by four pillars. .... 58
<b>Figure 3.5</b>	Equivalent circuit for measuring (a) $V_{OC}$ and (b) $I_{SC}$ of TENGs. .... 59
<b>Figure 3.6</b>	Surface charge density measurement system. (a) Photograph of Faraday's cup connected to an electrometer and (b) schematic illustration of Faraday's cup.60
<b>Figure 3.7</b>	(a) Peak and (b) RMS values of $V_{OC}$ and $I_{SC}$ of simple FT-mode TENGs for different triboelectric materials rubbed against Al..... 61

<b>Figure 3.8</b>	(a) Peak and (b) RMS values of $V_{OC}$ and $I_{SC}$ of simple FT-mode TENGs for different triboelectric materials rubbed against Ag. ....	61
<b>Figure 3.9</b>	Absolute values of $\rho_q$ and RMS $I_{SC}$ for different triboelectric materials rubbed against (a) Al and (b) Ag.....	62
<b>Figure 3.10</b>	Dependence of transient (a) $V_{OC}$ and (b) $I_{SC}$ on oscillation frequency of simple FT-mode TENG with PTFE and Ag electrodes. Corresponding (c) peak values and (d) RMS values of the $V_{OC}$ and $I_{SC}$ as a function of the oscillation frequency.....	65
<b>Figure 3.11</b>	Dependence of transient (a) $V_{OC}$ and (b) $I_{SC}$ on contact force of simple FT-mode TENG with PTFE and Ag electrodes. Corresponding (c) peak values and (d) RMS values of the $V_{OC}$ and $I_{SC}$ as a function of the contact force. ....	66
<b>Figure 3.12</b>	Dependence of transient (a) $V_{OC}$ and (b) $I_{SC}$ on relative humidity of simple FT-mode TENG with PTFE and Ag electrodes. Corresponding (c) peak values and (d) RMS values of the $V_{OC}$ and $I_{SC}$ as a function of the relative humidity. ....	67
<b>Figure 3.13</b>	Dependence of transient (a) $V_{OC}$ and (b) $I_{SC}$ on temperature of simple FT-mode TENG with PTFE and Ag electrodes. Corresponding (c) peak values and (d) RMS values of the $V_{OC}$ and $I_{SC}$ as a function of the temperature. ....	68
<b>Figure 3.14</b>	Electronic band structure model showing electron transfer back to metal and shifting of Fermi–Dirac distribution when temperature increases. Reproduced with permission from Ref. [53]. Copyright 2014, John Wiley & Sons, Inc.....	69
<b>Figure 3.15</b>	COMSOL simulation of simple FT-mode TENG at a stationary state when the PTFE is located exactly between the electrodes. When a DC voltage of 1 V is applied between the electrodes, electric charges of 2.43 pC are transferred to the left electrode.....	72
<b>Figure 3.16</b>	Equivalent circuit of FT-mode TENG connected to (a) Bennet’s doubler circuit, (b) half-wave bridge and (c) full-wave bridge. ....	72
<b>Figure 3.17</b>	(a) The maximum simulated $V_C$ after a charging time of 600 s as a function of $C_{store}$ and (b) simulated transient $V_C$ of Bennet’s doubler circuit for the different $C_{store}$ . The inset shows the magnified transient $V_C$ for $C_{store} = 1, 10$ and $100$ nF at the time between 590 and 600 s. ....	73
<b>Figure 3.18</b>	Simulated transient $V_C$ of FT-mode TENG connected to different rectifier circuits. ....	73

<b>Figure 3.19</b>	Experimental transient $V_C$ of FT-mode TENG (a) for Bennet's doubler circuit with various $C_{store}$ and (b) for the different rectifier circuits.....	74
<b>Figure 4.1</b>	Schematic illustration of (a) sliding nG-TENG proposed by Xie et al. (Reproduced with permission from Ref. [150]. Copyright 2014, John Wiley & Sons, Inc), (b) rotational nG-TENG proposed by Bi et. al (Reprinted with permission from Ref. [156]. Copyright 2017, Elsevier), (c) sliding pG-TENG proposed by Pu et. al (Reproduced with permission from Ref. [90]. Copyright 2016, John Wiley & Sons, Inc) and (d) sliding nG-TENG proposed by Chen et. al (Reprinted with permission from Ref. [140]. Copyright 2018, Elsevier). .....	78
<b>Figure 4.2</b>	Schematic illustration of (a) rolling pnG-TENG published by Gue et al. and (b) its operation mechanism. Reproduced with permission from Ref. [157]. Copyright 2015, American Chemical Society. ....	79
<b>Figure 4.3</b>	Schematic illustration of (a) upper substrate of pnG-TENG for $N = 10$ with PVC HTV as negative material and nylon fabric as positive material and (b) lower substrate of the pnG-TENG with interdigitated Ag electrodes .....	80
<b>Figure 4.4</b>	Flowchart showing the fabrication steps of upper substate of pnG-TENG.....	81
<b>Figure 4.5</b>	Photograph of (a) PVC HTV heat pressed on a piece of nylon fabric and (b) finished upper substrate of a pnG-TENG with nylon fabric and PVC HTV as positive and negative triboelectric material, respectively.....	81
<b>Figure 4.6</b>	Photograph of the upper substrates of pnG-TENG with nylon and PVC HTV for the different grating numbers ( $N = 2, 4, 6, 8$ and $10$ ). The PVC HTV is blue and the nylon is black. ....	81
<b>Figure 4.7</b>	Flowchart showing the fabrication steps of lower substate of pnG-TENG.....	82
<b>Figure 4.8</b>	Schematic illustration of IDEs fabrication steps using adhesive vinyl stencil and screen-printing. ....	82
<b>Figure 4.9</b>	Photograph of (a) transferred adhesive vinyl stencil on PVC fabric (step ii) and (b) IDEs after curing and removing the vinyl stencil (step iv) for $N = 10$ . ....	83
<b>Figure 4.10</b>	Microscope image of a short position between two IDEs for the IDEs with a final gap of $282 \pm 13 \mu\text{m}$ . ....	84

<b>Figure 4.11</b>	Photograph of (a) the upper substrate and (b) the lower substrate of the pnG-TENG without the acrylic sheet for $N = 10$ . ....85
<b>Figure 4.12</b>	Scanning electron microscope (SEM) images of (a) the upper substrate and (b) the lower substrate.....85
<b>Figure 4.13</b>	Schematic illustration of (a) TENGs with no grating and (b) G-TENGs with single triboelectric material. ....86
<b>Figure 4.14</b>	Schematic illustration of the operating mechanism of pnG-TENG for $N = 2$ with finite load resistance. ....87
<b>Figure 4.15</b>	Schematic illustration of the operating mechanism of pnG-TENG for $N = 2$ in open-circuit condition.....88
<b>Figure 4.16</b>	Simulated electric potential distribution of pnG-TENG with nylon and PVC for $N = 2$ using Comsol.....90
<b>Figure 4.17</b>	Peak $V_{OC}$ as a function of grating number for different types of TENGs (a) for $N = 1 - 10$ and (b) zoom-in illustration for $N = 2 - 10$ . ....91
<b>Figure 4.18</b>	Schematic illustration applied for theoretical calculation of average $I_{SC}$ . ....92
<b>Figure 4.19</b>	Calculated average $I_{SC}$ as a function of grating number for different types of TENGs.....93
<b>Figure 4.20</b>	Schematic illustration of the electrical outputs of pnG-TENG compared to pG-TENG and nG-TENG. The outputs of pnG-TENG are equal to the sum of the outputs of pG-TENG and nG-TENG. ....94
<b>Figure 4.21</b>	(a) Transient $V_{OC}$ and (b) $I_{SC}$ of different types of TENGs. The insets show the magnified illustration of the $V_{OC}$ and $I_{SC}$ of the pnG-TENG with $N = 10$ for one moving cycle ( $\Delta t = 0.5$ s). ....95
<b>Figure 4.22</b>	(a) Capacitor voltage, (b) calculated capacitor charging current and (c) calculated capacitor charging power as a function of time for different types of TENGs.96
<b>Figure 4.23</b>	(a) Peak $V_{OC}$ , (b) Peak $I_{SC}$ , (c) RMS $V_{OC}$ , (d) RMS $I_{SC}$ and (f) $V_C$ at a charging time of 600 s as a function of grating number for the different types of TENGs. ....97

## List of Figures

<b>Figure 4.24</b>	(a) The dependence of the peak voltage $V_{pk}$ , peak current $I_{pk}$ and peak power $P_{pk}$ on the external load resistance for the pnG-TENG (Nylon/PVC, $N = 10$ ) and (b) the corresponding RMS and average values. ....	98
<b>Figure 4.25</b>	(a) Load-dependent peak power $P_{pk}$ and (b) load-dependent average power $P_{avg}$ for different types of TENGs.....	99
<b>Figure 4.26</b>	(a) $V_{OC}$ , (b) $I_{SC}$ and (c) $V_C$ of pnG-TENGs ( $N = 10$ ) as a function of time for different triboelectric materials. ....	100
<b>Figure 4.27</b>	Transient (a) $V_{OC}$ and (b) $I_{SC}$ of pnG-TENG (Nylon/PVC HTV, $N = 10$ ) for the different frequencies.....	101
<b>Figure 4.28</b>	Corresponding (a) peak values and (b) RMS values of $V_{OC}$ and $I_{SC}$ as a function of oscillation frequency. ....	101
<b>Figure 4.29</b>	(a) Transient $V_C$ of pnG-TENG for different oscillation frequencies, (b) corresponding maximum $V_C$ , $I_C$ and $P_C$ as a function of oscillation frequency.....	102
<b>Figure 4.30</b>	Transient (a) $V_{OC}$ and (b) $I_{SC}$ of the pnG-TENG (Nylon/PVC HTV, $N = 10$ ) for the different contact forces.....	103
<b>Figure 4.31</b>	Corresponding (a) peak values and (b) RMS values of $V_{OC}$ and $I_{SC}$ as a function of contact force. ....	103
<b>Figure 4.32</b>	(a) Transient $V_C$ of pnG-TENG for different contact forces, (b) corresponding maximum $V_C$ , $I_C$ and $P_C$ as a function of contact force. ....	104
<b>Figure 4.33</b>	Transient (a) $V_{OC}$ and (b) $I_{SC}$ of pnG-TENG for the different operating cycles and after cleaning.....	105
<b>Figure 4.34</b>	SEM images of Ag IDE (a) before and (b) after stability test (30000 cycles). ....	105
<b>Figure 4.35</b>	Photograph of an adhesive tape test during which the tape does not pick up any material. ....	106
<b>Figure 4.36</b>	Transient (a) $V_{OC}$ and (b) $I_{SC}$ of pnG-TENG for the different washing cycles. .	106
<b>Figure 4.37</b>	Photographs of pnG-TENG embedded into a lab coat for harvesting energy from (a) walking and (b) running. ....	107
<b>Figure 4.38</b>	Transient $V_{OC}$ of the pnG-TENG produced during (a) walking and (b) running.....	107



<b>Figure 4.39</b>	$V_C$ of the pnG-TENGs as a function of time for different capacitors charged during (a) walking and (b) running.....108
<b>Figure 4.40</b>	Circuit diagrams of using pnG-TENG for powering (a) a digital watch, (b) night-time warning indicator, (c) wireless transmitter and (d) pedometer. ....108
<b>Figure 4.41</b>	Photographs of (a) digital watch and (b) wearable night-time warning indicator for pedestrians driven by the output of pnG-TENG ( $N = 10$ ) during running. ....109
<b>Figure 4.42</b>	(a) Transient RSSI at the receiver, and transient $V_C$ and $I_T$ at the wireless transmitter powered by the pnG-TENG during walking. (b) The zoom-in image showing the first transmission and the transmitter active period. ....110
<b>Figure 4.43</b>	Photograph showing the utilisation of the pnG-TENG as a sensor for step counting via arm motion (pedometer). ....110
<b>Figure 5.1</b>	(a) Schematic illustration of the triboelectric nanogenerator based on checker-like electrodes proposed by Guo et al. (b) Enlarged illustration of the red dotted box in (a) showing the electrode alignment. (c) Photograph of the sliding panel and electrodes. Reproduced with permission from Ref. [161]. Copyright 2015, John Wiley & Sons, Inc. ....113
<b>Figure 5.2</b>	(a) Schematic illustration of the triboelectric nanogenerator based on honeycomb-like electrodes proposed by Xia et al. (b) Enlarged illustration of the red dotted box in (a) showing the electrode alignment. (c) Photograph of sliding panel and electrodes. Reproduced with permission from Ref. [162]. Copyright 2018, Elsevier.....114
<b>Figure 5.3</b>	Schematic illustration of woven-TENG for $N = 4$ with nylon fabric as positive material and PTFE fabric as negative material. ....115
<b>Figure 5.4</b>	Photograph of the upper substrates woven-TENG with nylon fabric (black) and PTFE fabric (brown) for the different element numbers ( $N = 2, 4, 6$ and $8$ ). 115
<b>Figure 5.5</b>	Flowchart showing the fabrication steps of upper substate of woven-TENG.116
<b>Figure 5.6</b>	Flowchart showing the fabrication steps of lower substate of woven-TENG.116
<b>Figure 5.7</b>	Photograph of doctor blade coating of Ag ink on PVC fabric. ....117
<b>Figure 5.8</b>	Photograph of (a) warp Ag electrode, (b) weft Ag electrode before weaving and (c) Ag electrodes of woven-TENG for $N = 8$ after weaving. ....117

## List of Figures

<b>Figure 5.9</b>	Photograph of lower electrodes of woven TENG for $N = 4$ fabricated using adhesive vinyl stencil and doctor blading. ....	117
<b>Figure 5.10</b>	Photograph of (a) the upper substrate and (b) the lower substrate of woven-TENG for $N = 8$ showing their flexibility. ....	118
<b>Figure 5.11</b>	Scanning electron microscope (SEM) images of (a) the upper substrate and (b) the lower substrate of woven-TENG. ....	119
<b>Figure 5.12</b>	Schematic illustration of the operating mechanism of woven-TENG for $N = 2$ connected to a finite load resistance. ....	120
<b>Figure 5.13</b>	Schematic illustration of the operating mechanism of woven-TENG for $N = 2$ in open-circuit condition. ....	121
<b>Figure 5.14</b>	Simulated electric potential distribution of woven-TENG for $N = 2$ using COMSOL. ....	122
<b>Figure 5.15</b>	Simulated peak $V_{OC}$ and calculated average $I_{SC}$ for different $N$ . ....	124
<b>Figure 5.16</b>	Experimental results of transient (a) $V_{OC}$ and (b) $I_{SC}$ of woven-TENGs for different $N$ . ....	124
<b>Figure 5.17</b>	(a) Corresponding experimental peak values of $V_{OC}$ and $I_{SC}$ for different $N$ . (b) Corresponding experimental RMS values of $V_{OC}$ and $I_{SC}$ for different $N$ . ....	125
<b>Figure 5.18</b>	(a) Transient capacitor voltage $V_C$ and (b) corresponding maximum capacitor voltage at a charging time of 600 s, maximum capacitor charging current $I_C$ and maximum capacitor charging power $P_C$ for different $N$ . ....	126
<b>Figure 5.19</b>	Dependence of (a) peak values and (b) RMS values of voltage, current and power on the external load resistance for the woven-TENG with $N = 8$ . ....	127
<b>Figure 5.20</b>	(a) Peak power and (b) average power as a function of load resistance for the woven-TENG with different $N$ . ....	127
<b>Figure 5.21</b>	Photograph of (a) bottom substrate before attachment of fabrics, (b) after attached to nylon fabric and (c) after attached to PTFE fabric of checker-like patterned TENG with single triboelectric material. ....	128

<b>Figure 5.22</b>	Transient (a) $V_{OC}$ and (b) $I_{SC}$ for the woven-TENG with PTFE/nylon ( $N = 4$ ), a checker-like patterned TENG with one negative material (PTFE) and a checker-like patterned TENG with one positive material (nylon).....	129
<b>Figure 5.23</b>	(a) Transient $V_C$ and (b) corresponding transient $I_C$ and (c) corresponding transient $P_C$ for different types of TENGs. ....	129
<b>Figure 5.24</b>	(a) Peak power and (b) average power as a function of load resistance for different types of TENGs.....	130
<b>Figure 5.25</b>	Schematic illustration applied for theoretical calculation of woven-TENG for $N = 2$ . ....	131
<b>Figure 5.26</b>	Schematic illustration applied for theoretical calculation of transferred charges in (a) $0^\circ$ , (b) $45^\circ$ , and (c) $90^\circ$ direction with respect to the x-axis.....	132
<b>Figure 5.27</b>	(a) Calculated percentage of maximum output compared with experimental RMS $V_{OC}$ and RMS $I_{SC}$ as a function of sliding direction with respect to the x-axis. (b) Transient $V_C$ for different sliding directions. ....	134
<b>Figure 5.28</b>	Transient (a) $V_{OC}$ and (b) $I_{SC}$ of the woven-TENG with $N = 4$ for the different frequencies. ....	135
<b>Figure 5.29</b>	Corresponding (a) peak values and (b) RMS values of $V_{OC}$ and $I_{SC}$ as a function of oscillation frequency. ....	135
<b>Figure 5.30</b>	(a) Transient $V_C$ of the woven-TENG with $N = 4$ for different oscillation frequencies. (b) Corresponding maximum $V_C$ , $I_C$ and $P_C$ as a function of oscillation frequency. ....	135
<b>Figure 5.31</b>	Transient (a) $V_{OC}$ and (b) $I_{SC}$ of the woven-TENG with $N = 4$ for different contact forces. ....	136
<b>Figure 5.32</b>	Corresponding (a) peak values and (b) RMS values of $V_{OC}$ and $I_{SC}$ as a function of contact force.....	136
<b>Figure 5.33</b>	(a) Transient $V_C$ of the woven-TENG with $N = 4$ for different contact forces. (b) Corresponding maximum $V_C$ , $I_C$ and $P_C$ as a function of contact force.....	137
<b>Figure 5.34</b>	Transient (a) $V_{OC}$ and (b) $I_{SC}$ of the woven-TENG with $N = 4$ for various operating cycles and after hand-washing. ....	138

## List of Figures

<b>Figure 5.35</b>	Photograph of (a) top triboelectric materials and (b) bottom electrodes after 40000 operating cycles before washing. Photograph of (c) top triboelectric materials and (d) bottom electrodes during hand-washing using a brush... 138
<b>Figure 5.36</b>	SEM image of (a) Ag electrode (b) PTFE fabric and (c) nylon fabric before operation. SEM image of (d) Ag electrode (e) PTFE fabric and (f) nylon fabric after 40000 operating cycles followed by a hand wash and 4 machine washes... 139
<b>Figure 5.37</b>	Transient (a) $V_{OC}$ and (b) $I_{SC}$ of the woven-TENG with $N = 4$ after different washing times..... 140
<b>Figure 5.38</b>	Photographs of the woven-TENG with $N = 8$ embedded into a lab coat for harvesting energy from (a) walking and (b) running..... 141
<b>Figure 5.39</b>	Transient $V_{OC}$ of the woven-TENG with $N = 8$ produced during (a) walking and (b) running. .... 141
<b>Figure 5.40</b>	$V_C$ of the woven-TENG with $N = 8$ as a function of time for different capacitors charged by (a) walking and (b) running..... 141
<b>Figure 5.41</b>	Circuit diagrams of using woven-TENG for powering (a) a night-time warning indicator, (b) digital watch, (c) Bluetooth transceiver and (d) pedometer... 142
<b>Figure 5.42</b>	Photograph of (a) wearable night-time warning indicator for pedestrians and (b) digital watch powered by the output of the woven-TENG with $N = 8$ during running. .... 142
<b>Figure 5.43</b>	(a) Transient $V_C$ and $I_T$ of a Bluetooth transceiver and microcontroller SoC driven by the woven-TENG with $N = 8$ during running. (b) Zoom-in transient $V_C$ and $I_T$ of the area marked in yellow in (a). (c) Photograph of a Bluetooth advertisement received by a smartphone using BLE scanner application. .... 143
<b>Figure 5.44</b>	Photograph presenting the use of the woven-TENG as a sensor for step counting via arm motion (pedometer)..... 144

## Research Thesis: Declaration of Authorship

Print name: Watcharapong Paosangthong

Title of thesis: Textile-based triboelectric energy harvester with alternating positive and negative freestanding structure

I declare that this thesis and the work presented in it are my own and has been generated by me as the result of my own original research.

I confirm that:

1. This work was done wholly or mainly while in candidature for a research degree at this University;
2. Where any part of this thesis has previously been submitted for a degree or any other qualification at this University or any other institution, this has been clearly stated;
3. Where I have consulted the published work of others, this is always clearly attributed;
4. Where I have quoted from the work of others, the source is always given. With the exception of such quotations, this thesis is entirely my own work;
5. I have acknowledged all main sources of help;
6. Where the thesis is based on work done by myself jointly with others, I have made clear exactly what was done by others and what I have contributed myself;
7. Parts of this work have been published as listed in Section 1.5.

Signature: ..... Date: .....



## Acknowledgements

This dissertation would not have been possible and successful without encouragement and support from many people despite the Covid-19 pandemic and my personal health issue. I owe my deepest gratitude to everyone. Especially, I would like to thank:

Professor Steve Beeby, my supervisor, for offering me an opportunity to write my thesis in his workgroup, supervising me and sharing his profound knowledge in numerous discussions throughout my entire PhD. I am particularly grateful for his trust in my ability, encouraging me and giving me opportunity to attend numerous conferences and workshops.

Dr Russel Torah, my 2<sup>nd</sup> supervisor, for his invaluable advice, his continuous support during my PhD study, providing me with laboratory resources and solving technical issues with equipment.

Dr Mahmoud Wagih for supporting me in programming and realising applications, including pedometers and wireless transceivers.

All members of the SEMS group, especially, Dr Abiodun Komolafe, Dr Sheng Yong and Dr Junjie Shi for their support, insights and general discussions.

The Engineering and Physical Sciences Research Council, for supporting this research with grant reference EP/P010164/1.

My parents and friends for their tremendous understanding, mental and physical supports and encouragements.

Finally, I am deeply grateful to Pailin Kladpetch, my wife, for her love, kindness and support that made my study and life in the UK a wonderful time.





## Nomenclature

$A_M$ .....	Area of triboelectric materials
$C$ .....	Capacitance
$C_{res}$ .....	Reservoir capacitor
$C_{store}$ .....	Capacitance of store capacitor
$d$ .....	Thickness
$d_m$ .....	Thickness of metal electrode
$E_A$ .....	Occupied energy level of atom of the material A
$E_B$ .....	Occupied energy level of atom of the material B
$E_1$ .....	Potential energy for electrons to escape the potential well of material A
$E_2$ .....	Potential energy for electrons to escape the potential well of material B
$E_F$ .....	Energy of the Fermi level
$E_g$ .....	Band gap energy
$f$ .....	probability to find electron
$g$ .....	Electrode gap
$h$ .....	Freestanding height
$h$ .....	The Planck constant ( $6.62607015 \times 10^{-34}$ J·Hz)
$\theta$ .....	Angle
$I_C$ .....	Capacitor charging current
$I_{C,max}$ .....	Maximum capacitor charging current
$I_{pk}$ .....	Peak current
$I_{RMS}$ .....	RMS current
$I_{SC}$ .....	Short-circuit current
$I_{SC,RMS}$ .....	RMS value of short-circuit current
$l$ .....	Length

## Nomenclature

$k$ .....	The Boltzmann constant ( $1.380649 \times 10^{-23}$ J·K)
$k$ .....	Distance from the left edge of the dielectric to the area.
$N$ .....	Number of grating (pnG-TENG)
$N$ .....	Number of elements per each side of the upper substrate (woven-TENG)
$p$ .....	percentage of the transferred electrons
$P_C$ .....	Capacitor charging power
$P_{C,max}$ .....	Maximum capacitor charging power
$P_{pk}$ .....	Peak power
$P_{avg}$ .....	Average power
$Q$ .....	Electric charge
$Q_{SC}$ .....	Short-circuit transferred charges
$R$ .....	Resistance
$r$ .....	Distance from the point charge
$T$ .....	Temperature
$v$ .....	Motion average velocity
$V$ .....	Electric potential different
$V_C$ .....	Reservoir capacitor voltages
$V_{OC}$ .....	Open-circuit voltage
$V_{pk}$ .....	Peak voltage
$V_{RMS}$ .....	RMS voltage
$s$ .....	Travel distance
$S$ .....	Total area of one electrode
$t$ .....	time
$w$ .....	Width
$W$ .....	Width of upper substrate
$x$ .....	Moving distance
$\alpha$ .....	Normalized triboelectric series

$\Delta E$ .....	Change in capacitor energy
$\Delta Q_{SC}$ .....	Short-circuit transferred charge
$\Delta \sigma_{SC}$ .....	Short-circuit transferred charge density
$\epsilon_r$ .....	Relative permittivity
$\epsilon_0$ .....	Relative permittivity of vacuum ( $8.8541878128 \times 10^{-12} \text{ F} \cdot \text{m}^{-1}$ )
$\rho$ .....	Surface charge density
$\rho_q$ .....	Surface charge density
$\sigma$ .....	Triboelectric charge density
$\nu$ .....	Photon frequency



## Abbreviations

2D .....	Two-dimension
3D .....	Three-dimension
ABS .....	Acrylonitrile butadiene styrene
AC .....	Alternate current
ACMO .....	4-acryloylmorpholine
Ag .....	Silver
AgNPs .....	Silver nanoparticles
AgNWs.....	Silver nanowires
Al .....	Aluminium
AlNPs .....	Aluminium nanoparticles
APTES .....	Aminopropyltriethoxysilane
Au .....	Gold
BLE.....	Bluetooth low energy
CB .....	Conduction band
CBY .....	Conductive bundle yarn
CCT .....	Cotton thread
CE .....	Contact electrification
CF .....	Conductive fabric
CNT.....	Carbon nanotube
CS-mode .....	Vertical contact-separation mode
CVD.....	Chemical vapor deposition
Cu .....	Copper
DC.....	Direct current
DIW .....	Direct-Ink-Writing
FAS .....	Fluoroalkyl silane
FEM .....	Finite element method

## Abbreviations

FEP .....	Fluorinated ethylene propylene
FOTS.....	1H, 1H, 2H, 2H-perfluorooctyltrichlorosilane
FCS-mode.....	Freestanding triboelectric-layer contact-separation mode
FT-mode.....	Freestanding triboelectric-layer mode
G-TENG .....	Grating-structured triboelectric nanogenerator
HDPE .....	High-density polyethylene
HTV .....	Heat transfer vinyl
HTP.....	Heat transfer paper
IDEs .....	Interdigitated electrodes
ITO .....	Indium tin oxide
Kapton .....	Polyimide
LDPE.....	Low-density polyethylene
LED .....	Light-emitting diode
LS-mode.....	Lateral sliding mode
MWCNT .....	Multi-wall carbon nanotube
nG-TENG .....	Grating-structured triboelectric nanogenerator with single negative triboelectric material
Ni.....	Nickel
NiSO <sub>4</sub> .....	Nickel(II) sulfate
NPs.....	Nanoparticles
NWs .....	Nanowires
O <sub>2</sub> .....	Oxygen
PA.....	Polyacetylene
PA-66 .....	Polyamide 66
PC.....	Clear polycarbonate
PCCT.....	PTFE and carbon nanotube coated cotton thread
PDMS .....	Polydimethylsiloxane
PE .....	Polyester

PEEK .....	Polyetheretherketone
PEI .....	Ultem polyetherimide
PET .....	Polyethylene terephthalate
PEDOT .....	Poly-(3,4-ethylene dioxythiophene)
pG-TENG.....	Grating-structured triboelectric nanogenerator with single positive triboelectric material
PI .....	Polyimide
PMMA .....	Polymethyl methacrylate (Clear cast acrylic)
pnG-TENG.....	Grating-structured triboelectric nanogenerator with alternate strips of positive and negative triboelectric material
P-Ni-cloth .....	Parylene-coated Ni-fabric
PP .....	Polypropylene
PPS .....	Poly(phenylene Sulfide)
PPy.....	Polypyrrole
PS .....	Polystyrene
PSS .....	Polystyrene sulfonate
PTFE.....	Polytetrafluoroethylene (Teflon)
PU .....	Polyurethane
PVC.....	Polyvinyl chloride
PVDF.....	Polyvinylidene fluoride
PVDF-TrFE.....	Poly (vinylidene fluoride-co-trifluoroethylene)
RIE .....	Reactive ion etcher
RMS.....	Root mean square
SAM.....	Self- assembled monolayer
SE-mode .....	Single-electrode mode
Sn.....	Tin
SoC .....	System on chip
SR .....	Silicone rubber

## Abbreviations

SS ..... Stainless-steel

STDEV..... Standard deviation

TECD..... Triboelectric charge density

TENG ..... Triboelectric nanogenerator

T-TENG ..... Textile-based triboelectric nanogenerator

VB..... Valence band

W..... Work function

ZnO ..... Zinc oxide



# Chapter 1 Introduction

## 1.1 Research motivation

Wearable and portable electronics are becoming more ubiquitous in our daily life. They are continually developing into more sophisticated and multifunctional devices. Thanks to the substantial progress in e-textile development, electronic components, such as power storage systems, power management systems, wireless communication systems and transducers, can be embedded in textiles in the form of fibres, yarns and/or fabrics using cost-effective and well-established textile fabrication processes such as weaving and printing. The rapid growth in the wearable and portable devices market in the past decades has attracted a substantial amount of interest in micro- and nano-energy research to solve the problem of powering these systems. Since such devices are typically battery powered, they normally operate on an economical energy budget and the recharging and replacement of the batteries are inevitable over time. The reliance on a battery power supply hinders the widespread adoption of wearable electronic systems.

An effective solution investigated by many researchers is the implementation of a self-powered system utilising energy harvesting to convert energy from the surrounding environment such as light, thermal and kinetic energy into electrical energy. The human body is also an effective power source for wearable electronics. Activities of daily living, such as footstep or arm movement of a typical 68-kg adult can deliver a peak power of approximately 67 W and 60 W, respectively, as shown in Figure 1.1 [1]. A small portion of this power will be sufficient to drive many kinds of portable devices. Other energy harvester techniques, for examples, photovoltaic textiles [2]–[4], textile-based thermoelectric [5]–[7] and piezoelectric generators [8]–[10] have also been proposed as wearable harvesters. However, they are not yet sufficiently robust and are often impractical in real world applications. For instance, photovoltaics require direct sunlight to operate at their maximum energy production. Thermoelectric harvesters have relatively low energy output, especially at a low temperature gradient of the human body. Moreover, their fabrication processes are complicated and expensive and the materials required to make them are often toxic or not bio-compatible. Piezoelectric generators rely on strain, whereas textiles are conformal materials, therefore strain transferred to the load is minimal and thus their power outputs are low.

A prospective transduction technique for converting kinetic energy into electrical energy was proposed by Z. L. Wang's research group in 2012. They demonstrated a flexible triboelectric energy harvester based on contact electrification and electrostatic induction effect and named it a "Triboelectric nanogenerator (TENG)" [11]. Subsequently, significant advances have been made

both in their performance [12]–[16] and versatility [17]–[19]. Due to their properties, including low weight, flexibility, washability, high efficiency and biocompatibility, they are highly suitable for wearable applications. As a result, textile-based TENGs have attracted particular interest and numerous examples have been demonstrated [20]–[24]. A TENG can be used to harvest energy in the large-scale, such as harvesting energy from wind [25]–[27] or water waves [28], [29] or in the small-scale, such as from human motion [30]–[32]. This approach is well suited to textiles and provides a potentially more efficient way to scavenge this biomechanical energy from human motion because it relies on relative motion or compressive forces rather than strain (as in the case of piezoelectrics). Textile-based TENGs (T-TENGs) have been produced in various forms, including fibres, yarns and fabrics, which provide a convenient approach for their integration with wearable e-textile electronics [33]–[35]. Applications of T-TENGs have been extensively demonstrated either as a power source or as a sensor. For instance, they have been used to power various portable and wearable electronics, such as a night-time warning indicator for pedestrians [36], a pedometer [36], a digital watch [36], a calculator [37] and wireless sensor systems [38]. The sensing applications typically involve force and strain monitoring to detect motion [39], pressure [40] and physiological signals, such as breathing and pulse, as indicators of personal health [41]. In addition to harvesting energy from the human body via clothing, there is a possibility to utilise T-TENGs in many other applications. Textiles are found in many areas, including home interiors (carpeting, bedding, furnishing), leisure (backpacks, tents, nets, flags), transportation (vehicle interiors) and engineering (ground reinforcement, building structures and marine textiles). As examples, bedding and flag-type T-TENG were demonstrated by Lin et al. and Zhao et al., respectively [42], [43].

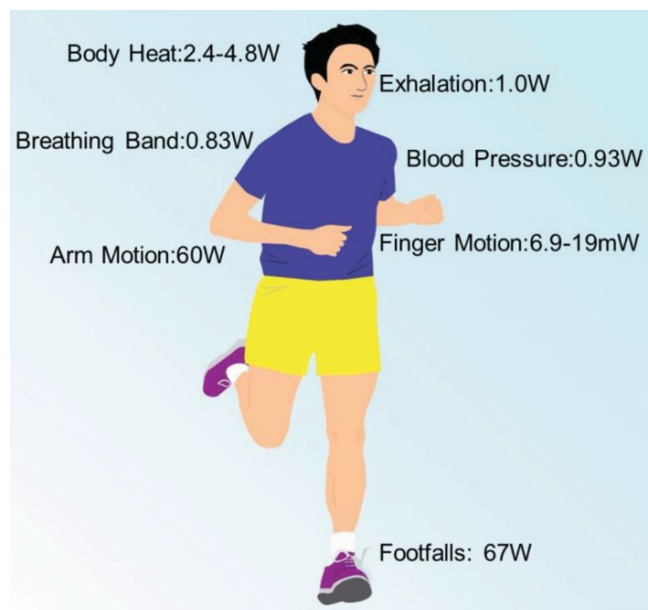


**Figure 1.1** Available power sources of human body from different daily activities. Reproduced with permission from Ref. [1]. Copyright 2014, John Wiley & Sons, Inc.

## 1.2 Aims and objectives

The aim of this thesis is to fabricate novel T-TENGs, which can harvest energy from body motion by embedding the T-TENGs in clothes, such as shirts, trousers and/or shoes. The fabrication process should be compatible with standard textile manufacturing processes, such as weaving and printing. With the aid of a power management circuit and an energy storage system, it should deliver sufficient power to drive small electronic devices either continuously or intermittently. Their applications include driving LEDs for lighting and signalling, powering wearable devices and wireless systems.

The objectives of this research are as follows:

1. Reviewing recent progress and development in T-TENGs to understand the principles and the background theories behind TENGs, to determine problems and limitations of state of the art T-TENGs, to obtain perspective of future T-TENG and to find research gaps.
2. Evaluating different triboelectric materials, including flexible materials and textile-based materials to find appropriate materials for T-TENGs. To realise this, a simple TENG will be built and electrical outputs of the TENG with different triboelectric materials, such as open-circuit voltage ( $V_{oc}$ ), short-circuit current ( $I_{sc}$ ) and surface charge density ( $\rho_q$ ) will be compared.
3. Identifying, testing and understanding factors that can affect the power output of T-TENGs. The dependence of the performance of T-TENGs on contact force, operating frequency, load resistance, humidity and temperature will be studied.
4. Designing, fabricating and characterising novel T-TENGs, which demonstrate an improvement in the performance compared to conventional T-TENGs by using fabrication processes which are compatible with the standard textile manufacturing.
5. Demonstrating the feasibility of using the T-TENGs as wearable energy harvesters to harvest energy from human motion, such as arm movement during walking and running. The applications of the T-TENGs as both energy harvesters and sensors will be identified.

### 1.3 Thesis structure

This thesis is divided into six chapters as follows:

Chapter 1 provides the overall introduction to Triboelectric Nanogenerators (TENGs), the research objectives and identifies the key novelties of this work.

Chapter 2 presents the physics behind TENGs and reviews the recent development and novel techniques applied in T-TENGs. Firstly, the background theory, the operating modes and the working principles of TENGs are described. Next, the basic textile manufacturing methods are introduced. The surface modification and other methods used to enhance the performance of T-TENG is described. Furthermore, examples of various types of T-TENGs categorised according to their structural and material design are covered in detail. Finally, the performance measurement and the practicalities in real applications scenarios of T-TENGs are summarised.

Chapter 3 focuses on fundamental experiments which need to be performed to gather essential information before starting to design new T-TENGs presented in Chapter 4 and 5. Firstly, various triboelectric materials are evaluated to identify potential materials for fabricating the T-TENGs. Next, experimental results on factors that affect the performance of TENGs, such as contact force, operating frequency, load resistance, humidity and temperature are investigated. Lastly, different rectifier circuits, including Bennet's doubler, half-wave and full-wave bridge rectifier, are investigated.

Chapter 4 reports a novel design of grating-structured T-TENG (G-TENG) with alternate strips of positive and negative triboelectric material (pnG-TENG) operating in freestanding triboelectric-layer mode (FT-mode). Different fabrication methods are demonstrated and discussed. The electrical outputs of the pnG-TENGs with nylon and PVC, G-TENGs with single positive triboelectric material, G-TENGs with single negative triboelectric material and T-TENGs with no grating are simulated, theoretically calculated and experimentally investigated. The effects of grating number, operation frequency and contact force on their performance are evaluated. Additionally, durability, washability and possible applications of the pnG-TENG are demonstrated.

In chapter 5, a novel T-TENG with woven strips of positive and negative triboelectric material (woven-TENG) designed to operate at all angles of relative sliding displacement has been fabricated and characterised. The dependence of the electrical outputs of the woven-TENG on the moving angle, element number, operation frequency and contact force are simulated, theoretically calculated and experimentally investigated. The results of durability tests, washability tests and practical applications of the woven-TENG are revealed.

Chapter 6 summarises the key research findings and contributions beyond the state of the art. Proposals of future work directions for this research project are also highlighted in this chapter.

## 1.4 Statement of novelty

The main novelties of this research are presented in Chapter 4 and 5. The author has proposed novel designs of T-TENGs operating in sliding FT-mode, defined as pnG-TENG and woven-TENG by employing both positive and negative triboelectric material as the freestanding triboelectric layer. The implementation of the positive and negative triboelectric materials significantly improves the performance of the TENGs. Furthermore, the fabrication processes are common, low-cost and compatible with standard textile manufacturing (e.g. weaving, heat-transfer printing and screen printing).

### Regarding the pnG-TENG:

- While most grating-structured TENGs operating in the FT-mode comprise gratings of one type of triboelectric material separated by air gaps, the new design presented in this thesis replaces the air gaps with another triboelectric material with the opposite polarity to the existing triboelectric material. This design increases the effective contact area and thus the triboelectric charge transfer.
- The average power generated by the pnG-TENG with 10 gratings is 1.94 and 6.43 times greater than the power generated by the TENG with single triboelectric material and the TENG with no grating.

### Regarding the woven-TENG:

- It is the first fully textile-based TENG for harvesting energy from all-planar directions, while the other conventional TENGs with this ability are made of rigid materials, which are inappropriate for wearable devices.
- The idea of implementing alternating positive and negative freestanding structure matches perfectly with the introduced woven structure. Because of the nature of the woven structure, a symmetric and periodic arrangement of the electrodes and alternating triboelectric materials are inherent in the fabrication process. This implementation has also shown an improvement in the power output of TENG by a factor of 2.2 compared to the TENG with single triboelectric material.
- This is the first TENG with woven structure operating in sliding FT-mode, while most of the woven-structured TENGs operate in contact-separation mode or contact-separation FT-

mode. Therefore, this novel development allows this form of energy harvesting to be integrated in to more flexible wearable applications; contributing to the solution of the battery replacement goal of the e-textile community.

## 1.5 List of publications and conferences

### Journal papers

1. **W. Paosangthong**, R. Torah, and S. Beeby, "Recent progress on textile-based triboelectric nanogenerators," *Nano Energy*, vol. 55, pp. 401–423, Jan. 2019. [20]
2. **W. Paosangthong**, M. Wagih, R. Torah, and S. Beeby, "Textile-based triboelectric nanogenerator with alternating positive and negative freestanding grating structure," *Nano Energy*, vol. 66, p. 104148, Dec. 2019. [44]
3. **W. Paosangthong**, M. Wagih, R. Torah, and S. Beeby, "Textile-based triboelectric nanogenerator with alternating positive and negative freestanding woven structure for harvesting sliding energy in all directions," *Nano Energy*, vol. 92, p. 106739, Feb. 2022 [45].

### Conference papers

1. **W. Paosangthong**, R. Torah, and S. Beeby, "Textile-based freestanding triboelectric-layer nanogenerator with alternate positive and negative grating structure," *J. Phys. Conf. Ser.*, vol. 1407, no. 1, pp. 0–5, 2019. [46]
2. **W. Paosangthong**, M. Wagih, R. Torah, and S. Beeby, "Textile Manufacturing Compatible Triboelectric Nanogenerator with Alternating Positive and Negative Freestanding Grating Structure," *Proceedings*, vol. 32, no. 1, p. 23, Jan. 2020. [47]
3. **W. Paosangthong**, M. Wagih, R. Torah, and S. Beeby, "Textile Manufacturing Compatible Triboelectric Nanogenerator with Alternating Positive and Negative Woven Structure," *Proceedings*, vol. XX, no. X, p. XX, XXX. 2022. (Publishing).

### Conferences and awards

1. Energy Harvesting 2018, 9<sup>th</sup> May 2018, Bristol UK (**Best demonstrator award**)
2. EnerHarv 2018, 29<sup>th</sup>-31<sup>st</sup> May 2018, Cork, Ireland (Poster session)
3. PowerMEMS 2018, 4<sup>th</sup>-7<sup>th</sup> Dec 2018, Daytona Beach, USA (Demonstration and poster session)
4. NiPS Lab Summer School 2019, 3<sup>rd</sup>-6<sup>th</sup> Sep 2019, Perugia, Italy (Poster session)
5. International Conference on the Challenges, Opportunities, Innovations and Applications in Electronic Textiles (E-Textiles 2019), 12<sup>nd</sup> Nov 2019, London, UK (**Best poster award**)
6. PowerMEMS 2019, 2<sup>nd</sup>-6<sup>th</sup> Dec 2019, Krakow, Poland (Poster session)

7. International Conference on the Challenges, Opportunities, Innovations and Applications in Electronic Textiles (E-Textiles 2021), 3<sup>rd</sup>-4<sup>th</sup> Nov 2021, Manchester, UK (Oral presentation)





## Chapter 2 Background theory and literature review

### 2.1 Introduction

To be able to identify research gaps and design novel T-TENGs, which are the main aim of this thesis, it is importance to fully understand the physics behind TENGs and to research the recent development and progress on T-TENGs. Therefore, this chapter starts with the physics of the triboelectric effect. Then, the working principles of each fundamental operating mode, especially the theory of the sliding FT-mode used in Chapter 3, 4 and 5 are explained. Next, recent development and novel technique applied in T-TENGs are reviewed. The literature review will mainly focus on textile applications only. Subsequently, the basic textile manufacturing methods are introduced since this influences the choice of materials and assembly methods for T-TENGs. The surface modification and techniques used to enhance the performance of T-TENG are described and examples of various types of T-TENG categorised according to their structural and material design are covered in detail. Additionally, their performance, measurement of performance and the practicalities in real applications scenarios of T-TENGs are summarised. Issues, such as standardised measurement parameters, the challenges and limitations of T-TENG are also discussed in this chapter.

### 2.2 Triboelectric effect

The triboelectric effect is also known as triboelectricity or triboelectric charging. It is a type of contact electrification (CE), in which electrical charges are separated and transferred from one material to the other material after they are brought into physical contact. The surface of one material will become negatively charged, while the surface of the other material will become positively charged. The contact between the surfaces does not have to be a translational or frictional motion. However, the motion, such as rubbing, will significantly enhance the effect due to multiple microscopic contact-separation between the materials [48].

History of triboelectricity began more than 2600 years ago, when Thales of Miletus, a pre-Socratic Greek philosopher discovered that after amber was rubbed against another material, such as wool, cat's fur or silk etc., it could attract other light objects, like hay, straw, threads or feathers etc. The word "triboelectric" is derived from a combination of two Greek words: "Tribo" (τριβος) means "rub" or "friction" and "electric" (ήλεκτρον) stems from the word "amber" [49]. Another well-known and recorded triboelectric effect is lightning during thunderstorms occurring when the local electric field of the water droplets exceeds the breakdown electric field of air. This local

electric field of the water droplets is caused by contact electrification between the water droplets and air under strong wind, where the water droplets become negatively charged.

The fundamental mechanism of triboelectricity is very complex and has not been well clarified. It is believed that the effect involves electron transfer, ion transfer and/or mass transfer [50]–[52]. It involves many local physical and chemical processes, such as elastic/plastic deformations, fracturing, and generation of heat. The triboelectricity can occur at interface of materials with different state of matters, such as solid-solid, solid-liquid, liquid-gas interface etc. Due to the nature of textile, this thesis will only focus on triboelectricity at solid-solid interface. For semiconductors and metals, the effect is well explained by electron transfer due to a difference in work function. For example, when two metals with different work functions are brought into contact, electrons will flow from the metal with a lower work function to the metal with a higher work function to equalize the Fermi levels [52]. For metal-dielectric and dielectric-dielectric interface, Z. L. Wang's research group has proposed that it is an electron-dominated transition process [53], [54]. They have explained the origin of the effect based on the electronic band structure model and the interatomic interaction model as follows.

### 2.2.1 Electronic band structure model

The triboelectric charge transfer can be well explained using energy band diagrams shown in Figure 2.1. Figure 2.1a reveals the energy band diagrams in case of metal-dielectric contact. In metal at absolute zero temperature, all energy states below the Fermi level ( $E_F$ ) are fully occupied by electrons. The work function ( $W$ ) is defined as the minimum energy needed to remove an electron to the vacuum energy level. In dielectric material or insulator, the Fermi level lies between the valence band (VB) and the conduction band (CB), which are separated by a band gap ( $E_g$ ), where no energy states can exist due to the quantization of energy. However, some quantized energy states can exist inside the band gap due to defects in the structure, such as surface defects, point defects or impurities etc. (Figure 2.1a(i)). When the metal and the dielectric are brought into contact, some of the energy states in the band gap below  $E_F$  will be filled by electrons transferred from the metal to the dielectric leading to excess negative charges on the dielectric surface and net positive charge on the metal surface (Figure 2.1a(ii)). Inversely, if the energy level of the occupied electron states inside the band gap of the dielectric is higher than  $E_F$  of the metal, some electrons in these states will be transferred to the metal until the equilibrium is reached resulting in net negative charges on the metal surface and net positive charges on the dielectric surface.

Figure 2.1(b) illustrates the energy band diagrams for the dielectric-dielectric contact. Due to the defects mentioned above, some surface and defect states presence in the band gap of the

dielectric A and B. Because of the difference in electronic band structure of each material, the energy level of some occupied electron states of the dielectric A could be higher than that of some unoccupied electron states of the dielectric B (Figure 2.1b(i)). Once they are brought into a physical contact, some electrons will be transferred from the dielectric A to the dielectric B resulting in excess negative charges on the dielectric B surface and net positive charges on the dielectric A surface (Figure 2.1b(ii)). Once they are separated, these electrons are in bounded surface states and cannot move freely in case of the materials with low conductivity. Theoretically, these charges will stay eternally on the surface if undisturbed. Nevertheless, these electrons can be removed from the energy states, for example, through thermal energy fluctuations (Figure 2.1b(iii)).

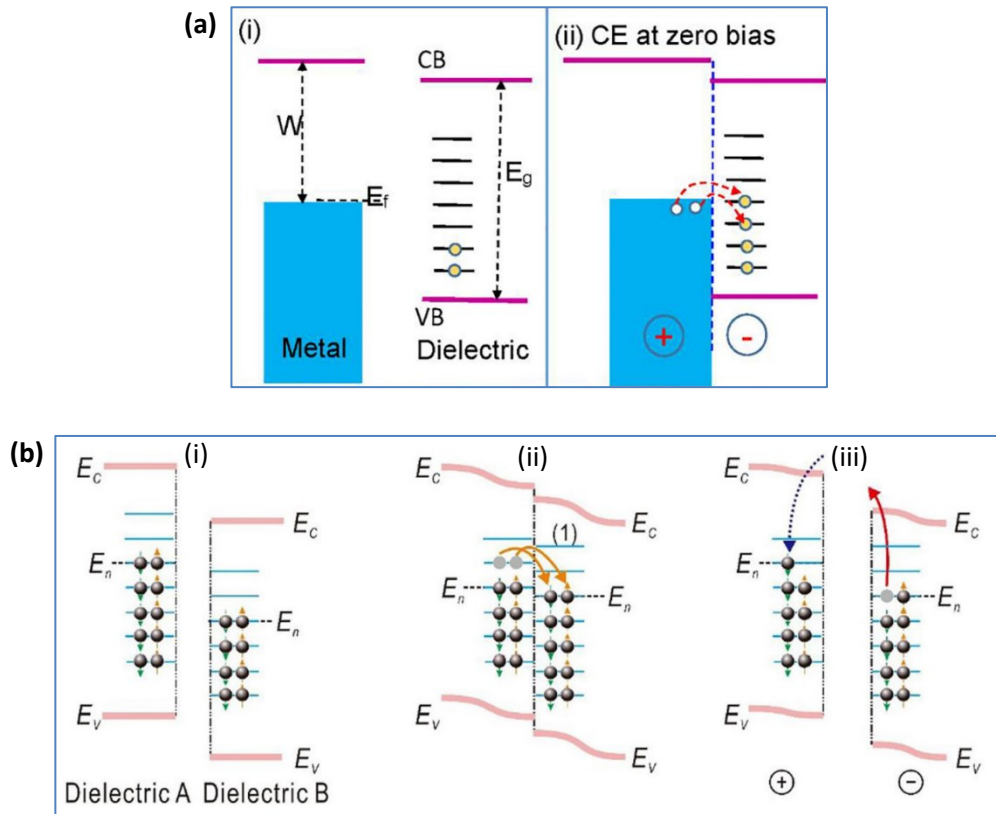


**Figure 2.1** (a) Schematic energy band model for metal-dielectric contact in the situations of (i) before contact, (ii) in contact. (b) Schematic energy band model for dielectric-dielectric contact in the situations of (i) before contact, (ii) in contact, and (iii) after contact. Reproduced with permission from Ref [54]. Copyright 2019, Elsevier.

### 2.2.2 Interatomic interaction model

Although triboelectric effect for solid-solid contact can be well described by the electronic band structure model, not all materials can be well represented by band structure, for example, polymers, rubbers and natural triboelectric materials, such as wool, fur and hair. Therefore, another model is required for explanation of general materials based on fundamental electron cloud interaction, shown in Figure 2.2.

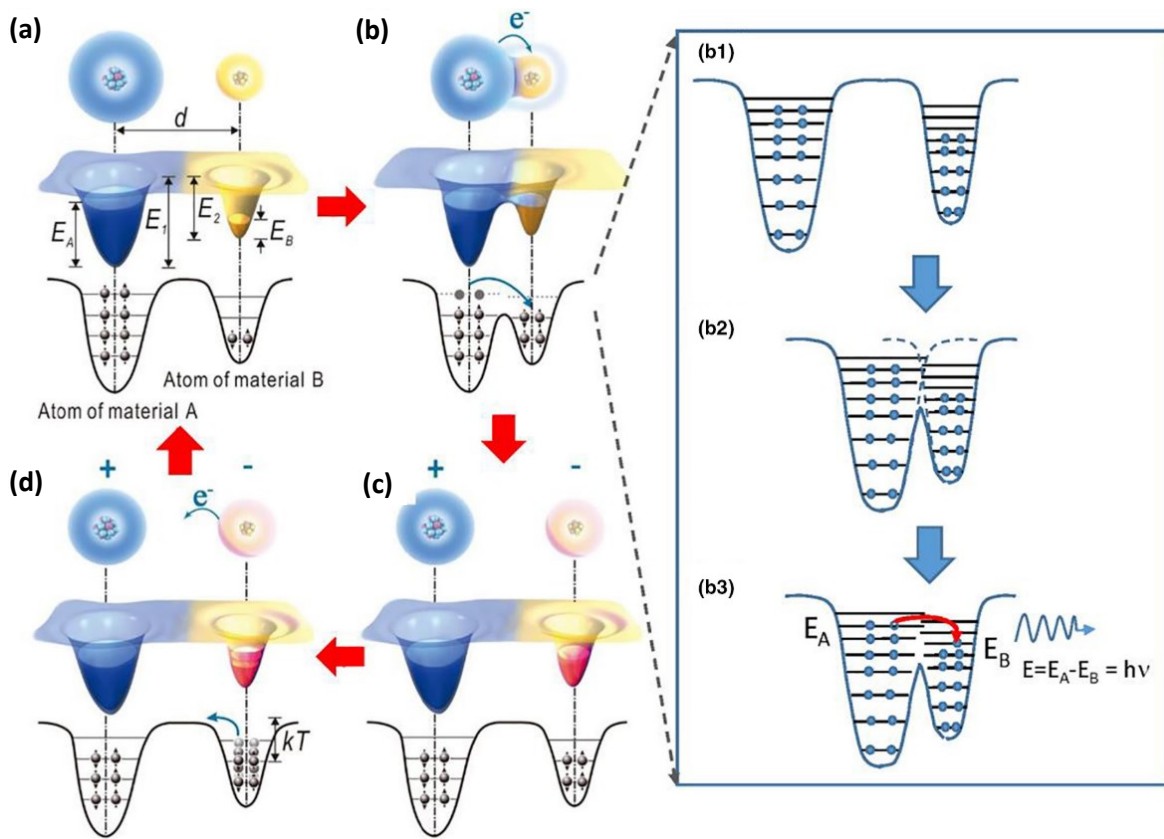


**Figure 2.2** Interatomic interaction model for explaining triboelectric charge transfer between two materials based on electron cloud interaction. Schematic illustration of the electron cloud and potential energy profile (3D and 2D) of two atoms belonging to material A and B, respectively, (a) before contact, (b) in contact, (c) after contact and (d) at elevated temperature. The right inset shows detailed illustration of (b) that the increasing electron cloud overlapping leads to a lower potential barrier and thus to interatomic electron transition and possible photon emission. Reproduced with permission from Ref [54]. Copyright 2019, Elsevier.

When the distance between atom of material A and B is larger than the bond length or the interatomic distance at equilibrium, they are in an attractive force region and the electron clouds are separated without overlap. In this region, the electrons are tightly bound in specific orbitals and cannot escape the potential wells. The occupied energy level of the atom of material A  $E_A$  and material B  $E_B$  are lower than the potential energy of material A  $E_1$  and of material B  $E_2$  for electrons to escape the potential wells, respectively (Figure 2.2a). When material A and B are brought into contact with each other, the electron clouds overlap and the potential wells merge into an asymmetric double-well potential. As a result, the potential barrier between the two wells sinks. The electrons at higher occupied energy levels of the atom of the material A can then transfer to unoccupied energy levels of the atom of the material B, which have lower energy. During the electron transfer, energy in the form of photon emission, plasmon excitation and/or phonon excitation can be released (Figure 2.2b). This effect occurs in a repulsive force region, when the distance between the atom of the material A and B is smaller than the bond length or the interatomic distance at equilibrium due to the compressive force applied during rubbing, sliding or

contacting. After the separation of the atom of material A and B, the transferred electrons are trapped in the potential well of material B due to the increased potential barrier (Figure 2.2c) and remain there. However, these electrons can hop out the potential well and jump back to the higher energy levels, for example, when the temperature increases and the energy fluctuations of the electrons become larger than the potential barrier between the atoms (Figure 2.2d).

### 2.3 Triboelectric series

Triboelectric series is a list of various materials sorted by their tendency to lose or gain electrons. For example, a material at the top of the list will lose electrons and become positively charged when rubbed against a material at the bottom of the list that will receive electrons and become negatively charged. The further apart in the list the two materials are, the greater is the tendency for electron transfer. For this reason, a TENG should consist of at least two materials, which are separated as far as possible on the list.



In 1757, the first triboelectric series was published by Johan Carl Wilcke, a Swedish physicist, in his doctoral thesis using Leyden jar. He listed about ten kinds of common materials in the order of their polarity [55]. Afterwards, various triboelectric series were proposed by different research groups and their results were fairly consistent [48], [56]–[60]. The most popular experimental method to establish triboelectric series is to measure the surface charge of each triboelectric materials after contacting with different metals with known work function. By interpolating the graph between the surface charge and the work function of the different metals, the work function of each triboelectric material is obtained. One of the most widely used triboelectric series today is published by Diaz et al. in 2014, where different qualitative and quantitative triboelectric series are compared and combined [48]. Common triboelectric materials sorted according to the triboelectric series proposed by Diaz et al. is illustrated in Table 2.1 [61].

Recently, Zou et al. have proposed a universal standard method to quantify the triboelectric series for a wide range of polymers, establishing quantitative triboelectrification as a fundamental materials property [62]. They measured triboelectric performance of different tested materials by firstly depositing copper (Cu) to their back surfaces and dipping their front surfaces into liquid metals of mercury at a temperature of 20 °C and a humidity of 0.43% RH. The use of the liquid mercury helps maximise the contact area between the tested materials and the liquid metal, since the liquid metal is shape-adaptive to their solid surfaces. In contact-separation mode, electrical outputs were recorded and their triboelectric charge density (TECD)  $\sigma$  were determined. The normalized triboelectric series  $\alpha$  is defined as  $\alpha = \frac{\sigma}{|\sigma_{PTFE}|}$ . The Triboelectric series, their triboelectric charge density (TECD) and the normalized triboelectric series proposed by Zou et al. is

shown in Table 2.2. It is to note that the position of the Hg in the Triboelectric series has not been widely studied and published due to its state of matter. However, according to Table. 2, Hg tends to be a very triboelectric positive material.

**Table 2.1** Triboelectric series proposed by Diaz et al. Reproduced with permission from Ref [61].

Copyright 2017, American Institute of Physics.

<b>Positive</b> 	Polyurethane foam	(continued)	 <b>Negative</b>
	Etylcellulose	Polyester (Dacron)	
	Sorbothane	Polyisobutylene	
	Polyamide 6-6	Polyurethane flexible sponge	
	Hair, oily skin	Polyethylene Terephthalate (PET)	
	Wool, Knitted	Polyvinyl butyral	
	Silk, woven	Polychlorobutadiene	
	Aluminum	Natural rubber	
	Paper	Polyacrilonitrile	
	Cotton, woven	Polystyrene	
	Steel	Polyimide	
	Wood	Neoprene	
	Hard rubber	Polyehylene	
	Nickel, copper	Polypropylene	
	Sulfur	Polyimide (Kapton)	
	Brass, silver	Polyvinyl chloride (PVC)	
	Acetate, Rayon	Latex (natural) rubber	
	Polymethyl methacrylate (Lucite)	Santoprene rubber	
	Polyvinyl alcohol	Polydimethylsiloxane (PDMS)	
	(continued)	Polytetrafluoroethylene (Teflon)	

**Table 2.2** Triboelectric series and their triboelectric charge density (TECD) proposed by Zou et al. Reproduced with permission from Ref [62]. Copyright 2019, Nature Research.

Materials	Abbr.	Average TECD ( $\mu\text{C m}^{-2}$ )	STDEV	$\alpha$
Chemical-Resistant Viton® Fluoroelastomer Rubber		-148.20	2.63	-1.31
Acetal		-143.33	2.48	-1.27
Flame-retardant garolite		-142.76	1.49	-1.26
Garolite G-10		-139.89	1.31	-1.24
Clear cellulose		-133.30	2.28	-1.18
Clear polyvinyl chloride	PVC	-117.53	1.31	-1.04
Polytetrafluoroethylene	PTFE	-113.06	1.14	-1.00
Abrasion-resistant polyurethane rubber		-109.22	0.86	-0.97
Acrylonitrile butadiene styrene	ABS	-108.07	0.50	-0.96
Clear polycarbonate (Glossy)	PC	-104.63	1.79	-0.93
Polystyrene	PS	-103.48	2.48	-0.92
Ultem polyetherimide	PEI	-102.91	2.16	-0.91
Polydimethylsiloxane*	PDMS	-102.05	2.16	-0.90
Polyester fabric (Plain)		-101.48	1.49	-0.90
Easy-to-machine electrical-insulating garolite		-100.33	1.79	-0.89
Food-grade high-temperature silicone rubber		-94.03	0.99	-0.83
Polyimide film	Kapton	-92.88	2.58	-0.82
DuraLar polyester film	PET	-89.44	0.86	-0.79
Polyvinylidene fluoride	PVDF	-87.35	2.06	-0.77
Polyetheretherketone	PEEK	-76.25	1.99	-0.67
Polyethylene	PE	-71.20	1.71	-0.63
High-temperature silicone rubber		-69.95	0.50	-0.62
Wear-resistant garolite		-68.51	1.99	-0.61
Low-density polyethylene	LDPE	-67.94	1.49	-0.60
High impact polystyrene		-67.37	1.79	-0.60
High-density polyethylene	HDPE	-59.91	1.79	-0.53
Weather-resistant EPDM rubber		-53.61	0.99	-0.47
Leather strip (Smooth)		-52.75	1.31	-0.47
Oil-filled cast nylon 6		-49.59	0.99	-0.44
Clear cast acrylic	PMMA	-48.73	1.31	-0.43
Silicone		-47.30	1.49	-0.42
Abrasion-resistant SBR rubber		-40.13	1.31	-0.35
Flexible leather strip (Smooth)		-34.40	0.86	-0.30
Noryl polyphenyl ether		-31.82	0.86	-0.28
Poly(phenylene Sulfide)	PPS	-31.82	0.86	-0.28
Pigskin (Smooth)		-30.10	0.86	-0.27
Polypropylene	PP	-27.23	1.31	-0.24
Slippery nylon 66		-26.09	0.50	-0.23
Weather- and chemical-resistant santoprene rubber		-25.23	0.50	-0.22
Chemical- and steam-resistant aflas rubber		-22.65	1.31	-0.20
Polysulfone		-18.92	0.86	-0.17
Cast nylon 6		-18.35	0.99	-0.16
Copy paper		-18.35	0.50	-0.16
Chemical-resistant and low-temperature fluorosilicone rubber		-18.06	0.86	-0.16
Delrin® Acetal Resin		-14.91	0.50	-0.13
Wood (marine-grade plywood)		-14.05	0.99	-0.12
Wear-resistant slippery garolite		-11.47	0.50	-0.10
Super-stretchable and abrasion-resistant natural rubber		-10.61	0.50	-0.09
Oil-resistant buna-N rubber		2.49	0.23	0.02
Food-grade oil-resistant buna-N/vinyl rubber		2.95	0.13	0.03

Note: STDEV refers to the standard deviation. The  $\alpha$  refers to the measured triboelectric charge density of tested materials over the absolute value of the measured triboelectric charge density of the reference material. The material marked with an asterisk "\*" means it has strong adhesion with mercury, a small drop of mercury is observed when it is separated with mercury. The measured TECD value may be a bit lower than its real value. Source data are provided as a Source Data file.

## 2.4 Fundamental operation mode and working principle of TENGs

TENGs are devices, which can be used to transform kinetic energy occurring during relative motion and frictional contact between two materials with different electron affinities into electricity based on the triboelectric effect and electrostatic induction [63]. The external kinetic energy will periodically drive the charged surfaces resulting in a relative displacement between the surfaces and electrodes and thus leading to a periodic change in an induced potential difference between the electrodes. When the electrodes are connected through an electrical load, free electrons will continuously flow back and forth between the electrodes to reduce the induced potential difference and to maintain the electrostatic equilibrium between them. With this

principle, an alternate power output is extracted at the load. Depending on different configurations of the triboelectric materials and the electrodes, and their relative movement, the fundamental operation modes of TENG can be categorised into the four following modes [64], [65].

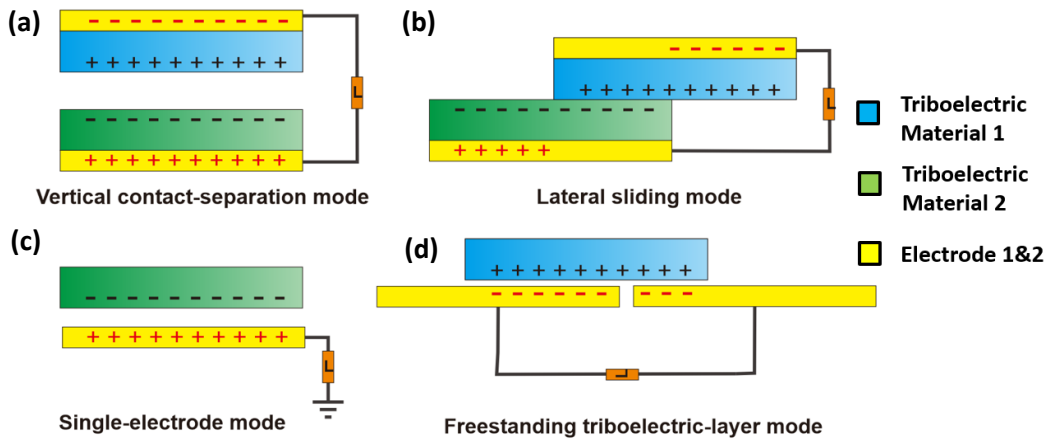


**Figure 2.3** Four fundamental operation modes of TENGs: (a) Vertical contact-separation mode (CS-mode), (b) lateral sliding mode (LS-mode), (c) single-electrode mode (SE-mode) and (d) freestanding triboelectric-layer mode (FT-mode).

#### 2.4.1 Vertical contact-separation mode (CS-mode)

As shown in Figure 2.3a, TENG operating in the CS-mode consists normally of two dissimilar triboelectric materials facing to each other with an electrode deposited on the reverse side forming a stacked configuration. To be able to contain the charge on the surface, at least one of the triboelectric materials has to be a dielectric. A frictional contact between the triboelectric materials will lead to a charge transfer and thus two oppositely charged surfaces. As the two materials are separated, the potential difference between the two electrodes increases. The electric potential of the electrode deposited close to the positive surface is higher than that of the electrode deposited close to the negative surface. To balance the potential, the electrons flow from the electrode with lower potential to the one with higher potential until the potential difference disappears. When the gap is reduced, the potential difference is built up again because the number of the electrons in the electrode exceeds the surface charges and thus these excess electrons have to flow back.

Most examples of TENGs are operated in this mode because of the manner of human movements and the simplicity of the fabrication. For example, they can be built inside shoe insoles to harvest energy from human walking [66] or embedded inside a fabric to generate power from pressing or stretching the fabric. Such motions lead to a contact-separation movement between the triboelectric materials. The structure of this type of TENG has been designed in various forms, such as multi-stacked fabrics [15], [67]–[71] or yarns [39], [41], [72]–[77]. The first TENG is also operated in this mode. It was invented in early 2012 by Fan et al. [11]. The TENG comprised



polyethylene terephthalate (PET) and polyimide (Kapton) film with sputtered gold (Au) electrode on its backside. Through a periodic deformation force, a peak voltage of 3.3 V, a current of 0.6  $\mu\text{A}$  and a peak power density of 0.37  $\mu\text{W}/\text{cm}^2$  were generated.

#### 2.4.2 Lateral sliding mode (LS-mode)

The operation of the LS-mode is shown in Figure 2.3b. Similar to the contact mode, it comprises two triboelectric materials with two back electrodes. When the top and the bottom triboelectric materials are fully aligned, the positive and negative surface charges are compensated, thus there is no potential difference between the electrodes. In contrast, when the materials are misaligned, there is a potential building up in the non-overlapping parts of the electrodes and a resultant potential difference occurs. As a result, electrons flow between the electrodes. Once the substrates move back to the initial aligned position, the electrons have to flow back to balance the potential. The AC output is obtained from the periodic sliding between the materials [63]. Compared to the CS-mode, the in-plane movements enable a TENG to harvest energy from planar motion [78], disc rotations [79] or cylindrical rotations [80]. Additionally, a larger frictional contact occurring during sliding enhances the charge separation and thus improves the performance of TENG. However, the higher friction can lead to greater material abrasion and, due to the lateral movement of the assembly, at least twice as much area is required as the CS-mode equivalent. To improve the performance of this mode, most TENGs are fabricated with a linear-grating structure, since this reduces the required sliding distance to operate the device with the same surface area and such a design dramatically increases the frequency and the amplitude of the output current and thus the power proportional to the size and the number of grating strips [81].

An early example of the LS-mode T-TENGs was demonstrated by Jung et al. in 2014 [82]. They fabricated a grating TENG comprising alternating strips of polyimide (PI) and polyurethane (PU) mounted on a sleeve and alternating strips of polydimethylsiloxane (PDMS) and aluminium (Al) attached to the torso. Carbon fabrics were used as both electrodes. The friction generated between the sleeve and the torso produced a power density of 1.8  $\text{mW}/\text{m}^2$  at a frequency of 1.5 Hz. Another example, Cui et al. developed a wearable TENG with grating-structured nylon and Dacron cloth, illustrated in Figure 2.4a [83]. The SEM image of the textile surface is shown in Figure 2.4b. A photograph of one part of the TENG is shown in Figure 2.4c illustrating the grating structure comprising the nylon and Dacron (PET) materials. A second identical grating is arranged on top of this to form the overall T-TENG as shown in Figure 2.4d. The gratings were fabricated on top of cotton fabric substrates with the nylon and Dacron strips being attached to the substrates with an intermediate copper (Cu) electrode. Relative sliding between the substrates, for example, when attached to the arm and body, causes that an alternating current flows between the nylon and

Dacron back electrodes. With this arrangement, the  $I_{sc}$  and the  $V_{oc}$  reached a value of 0.2 mA and 2 kV, respectively.

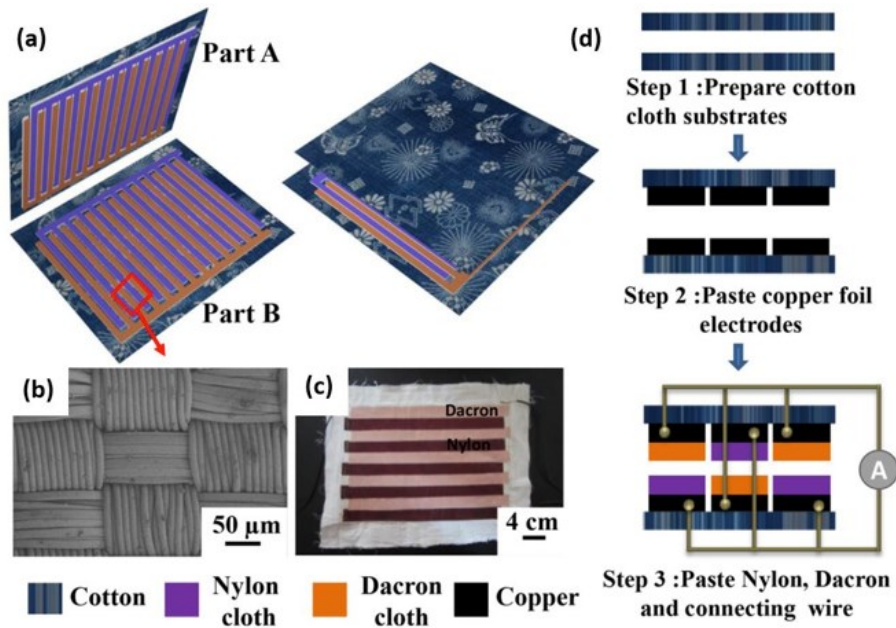


**Figure 2.4** (a) Schematic diagram of cloth-based TENG with a linear-grating structure, (b) SEM image of the microstructure of nylon cloth's surface, (c) photograph of one part of the TENG and (d) fabrication process of the TENG. Reproduced from Ref. [83]. Copyright 2015 American Chemical Society.

### 2.4.3 Single-electrode mode (SE-mode)

The SE-mode TENG overcomes a limitation of the CT and LS-modes that requires the moving triboelectric materials to be attached to electrodes which need to be connected to an external electrical load. The SE-mode offers the advantage of requiring only one electrode and therefore one electrical connect. The operation of the SE-mode is shown in Figure 2.3c, in which the TENG comprises only one dielectric material and one electrode. However, it should be noted that in practical applications, a reference electrode is often connected to the primary electrode to serve as a source of electrons. The periodic vertical contact-separation movement of the dielectric causes electrons to flow between the primary electrode and the ground (or reference electrode) due to a change in the induced potential at the primary electrode. Because the potential change takes place mainly at one electrode, the output performance of this mode is lower compared to the other modes. Moreover, the reference electrode can shield the electric field when the electrodes are too close to each other, which results in a further decrease in the output [84].

This mode is one of the most common operating modes for T-TENGs since the freely moving dielectric does not require an electrical connection or electrode. Consequently, it enables alternative materials to be used as a dielectric, such as conventional fabrics [38], [85]–[87] or human skin [88], [89]. An example of this mode was published by Lai et al. who fabricated a single-

thread based wearable TENG sewn in serpentine shape on a textile as shown in Figure 2.5a [89]. The thread was made of a stainless-steel (SS) conductive core coated with a silicone rubber (SR) shell. Via contact to and separation from the skin, the device delivered an  $I_{sc}$  of 200  $\mu\text{A}$ , a  $V_{oc}$  of 200 V and a power density of 953  $\text{mW/m}^2$  at  $1\text{M}\Omega$  load resistance. This power was shown to be sufficient to drive different applications, including a smartwatch, motion sensor system and wireless wearable keyboard, shown in Figure 2.5b - d, respectively.

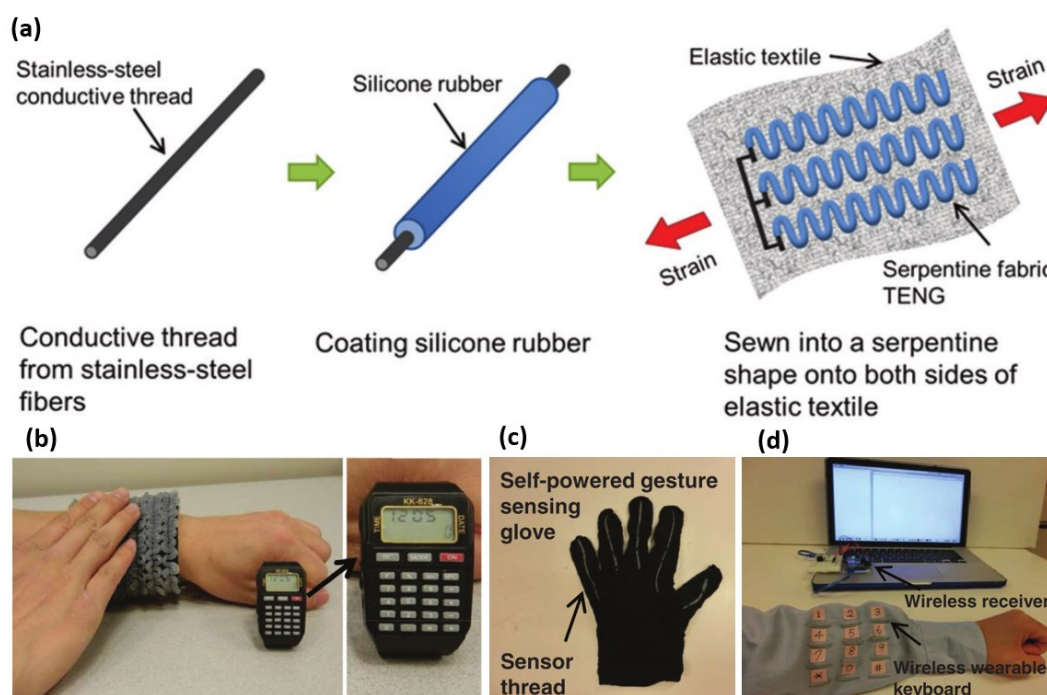


**Figure 2.5** (a) Schematic diagram for fabrication process of single-thread based wearable TENG in serpentine shape sewed on a textile and its applications, including (b) smartwatch, (c) motion sensor system and (d) wireless wearable keyboard. Reproduced with permission from Ref. [89]. Copyright 2016, John Wiley & Sons, Inc.

#### 2.4.4 Freestanding triboelectric-layer mode (FT-mode)

The operation of the FT-mode is illustrated in Figure 2.3d, which consists of two electrodes, aligned vertically or horizontally, and a triboelectric material. Similar to the SE-mode, the triboelectric material can move freely without electrode or electrical connection. When the triboelectric material (e.g. positive charged) is closer to one electrode, electrons will be attracted to that electrode due to a rise in the electric potential. When the triboelectric material is moved closer to the second electrode, the electrons will flow from the first electrode to the second. Relative movement backwards and forwards between the electrodes results in an AC output through the external load. Compared to the SE-mode, this mode benefits from the potential change at both electrodes and there is no shielding effect [84], and therefore the performance is better. The triboelectric material can either be in contact or not with the electrodes during the operation

due to the fact that the surface charge on some materials can remain for hours. For this reason, this operation mode suffers less from material abrasion and heat generation [63]. For example, Pu et al. proposed a T-TENG consisting of a stator and a slider fabric [90]. Two interdigitated electrodes were fabricated on the stator fabric by electroless plating of nickel (Ni) and then fully covered by a parylene layer serving as a triboelectric material. The slider fabric has grating-structured segments of Ni serving as the freestanding-layer. The T-TENG with 1 mm wide segment can generate a maximum power density of  $3.2 \text{ W/m}^2$  at a speed of  $0.75 \text{ m/s}$ . Another example of T-TENG operating in this mode was demonstrated by Yu et al. [91]. Here, a polyester (PE) textile was used as the freestanding-layer and PU/SS textiles were used as the electrodes. The T-TENG operating in this mode exhibits an  $I_{SC}$  and a  $V_{OC}$  of  $1 \mu\text{A}$  and  $56 \text{ V}$ , respectively.

Most of the TENGs operating in this mode are fabricated with a linear-grating structure [43] or operated in combination with the CS-mode, this being known as the contact-separation FT-mode or the freestanding triboelectric-layer CS-mode (FCS-mode) [37], [92]–[95]. The device structures comprise three triboelectric materials with the first two materials being arranged in strips with electrodes on the back or in the core. The strips (which can be fabric) are woven together forming a textile substrate. The third material, which acts as a freestanding triboelectric-layer and typically has an electron affinity between the first two materials, moves vertically in contact to and separation from the woven substrate. Based on contact electrification, positive and negative charges are generated at the surface of the first and the second materials. The periodic movement of the third material results in a potential difference between the electrodes and thus an electric power is produced. Tian et al. proposed this type of TENG using Ni-coated PE (conductive textile) and the SR-coated conductive textile as the woven substrate (shown in Figure 2.6a) [37]. The power generation mechanism, as described previously, is represented in Figure 2.6b. In this example, palm skin was used as the freestanding triboelectric-layer and the  $I_{SC}$  and  $V_{OC}$  of the single-layer and double-layer TENG were  $60 \mu\text{A}$  and  $140 \mu\text{A}$ , and  $500 \text{ V}$  and  $540 \text{ V}$ , respectively. In addition to skin, the energy harvested using terylene, cotton, rubber, fur, silk and nylon as the freestanding triboelectric-layer is shown in Figure 2.6c - h, respectively. The  $I_{SC}$  for all materials exceeded  $100 \mu\text{A}$  and cotton and fur achieved over  $150 \mu\text{A}$ . In Figure 2.7a, the maximum peak power of the double-layer TENG reaches  $22.3 \text{ mW}$  at a load resistance of  $10 \text{ M}\Omega$ , corresponding to a power density of  $8,920 \text{ mW/m}^2$ . Figure 2.7b shows that the output of the double-layer TENG at a frequency of  $3 \text{ Hz}$  and a contact force of  $300 \text{ N}$  can charge up a  $22\text{-}\mu\text{F}$ ,  $10\text{-}\mu\text{F}$ ,  $4.7\text{-}\mu\text{F}$  and  $1\text{-}\mu\text{F}$  capacitor to a voltage of  $10 \text{ V}$  in 8, 28, 54 and 120 seconds respectively.

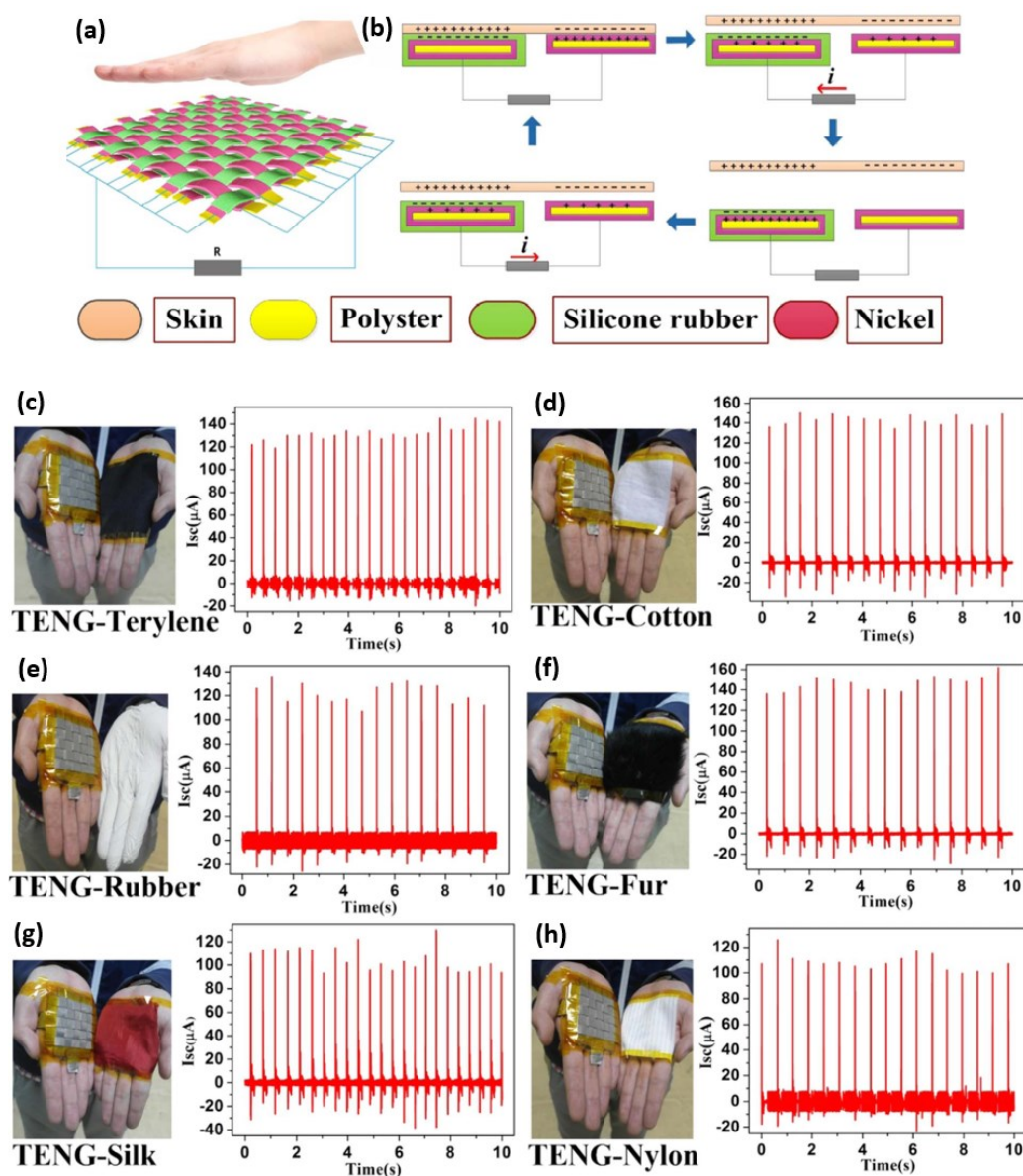


**Figure 2.6** T-TENG operating in freestanding triboelectric-layer contact-separation mode (FCS-mode): (a) schematic illustration and (b) power generation mechanism of the T-TENG contacted with palm skin. Photographs and the corresponding  $I_{sc}$  of the T-TENG using different materials, including (c) terylene, (d) cotton, (e) rubber, (f) fur, (g) silk and (h) nylon as the freestanding triboelectric-layer. Reproduced with permission from Ref. [37]. Copyright 2017, Elsevier.

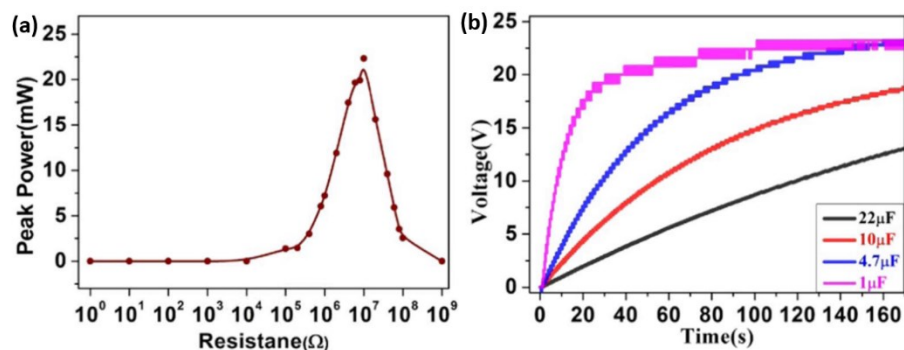


**Figure 2.7** (a) Dependence of the peak power of the double-layer TENG on load resistances and (b) time-dependent capacitor voltage of the different capacitors charged by the double-layer TENG. Reprinted with permission from Ref. [37]. Copyright 2017, Elsevier.

## 2.5 Theory of sliding freestanding triboelectric-layer mode TENG

Since this thesis will mainly focus on sliding FT-mode TENGs, it is necessary to understand the theory behind this mode in more detail. Niu et al. have proposed the first theoretical model of sliding FT-mode TENG as shown in Figure 2.8.

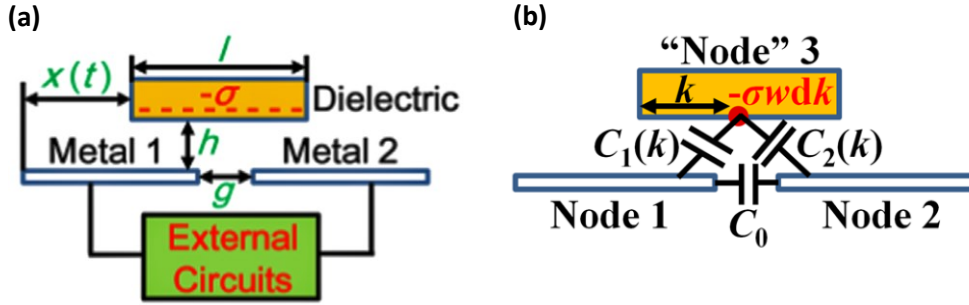


**Figure 2.8** (a) Theoretical model of sliding FT-mode TENGs and (b) the corresponding equivalent circuit model. Reprinted with permission from Ref. [96]. Copyright 2015, Elsevier.

In Figure 2.8a, the model comprises a freestanding dielectric layer with a length  $l$  and two metal electrodes with the same length. The dielectric can freely slide in one direction between the electrodes with a velocity  $v$ . The distance between the dielectric and the electrodes is defined as the freestanding height  $h$ . The electrodes are located in the same plan with a gap  $g$  between them. The width of this structure is defined as  $w$ . The dielectric start moving from the left edge of the metal 1. The moving distance between the left edge of the metal 1 to the left edge of the dielectric is defined as  $x(t)$ , which is in a function of time  $t$ . The dielectric movement can be described by a harmonic vibration expressed as Equation 2.1 below:

$$x(t) = \frac{l+g}{2} \left( 1 - \cos\left(\frac{\pi vt}{l+g}\right) \right) \quad (2.1)$$

The electric potential superposition principle, the node concept and the equivalent circuit model showed in Figure 2.8b are applied to analyse the working principle of FT-mode TENGs. Initially, It is assumed that only a small area of  $w dk$  on the bottom of dielectric surface has the triboelectric charges with a charge density  $-\sigma$ , where  $k$  is the distance from the left edge of the dielectric to this area. The capacitance between this area and the node 1 and node 2 are defined as  $C_1(k)$  and  $C_2(k)$ , respectively. The capacitance between the electrodes and the total capacitance are defined as  $C_0$  and  $C$ , respectively. Under short-circuit condition, the potential difference over  $C_1$  and  $C_2$  are equal and we obtain Equation 2.2 below:

$$\frac{dQ_1}{C_1(k)} = \frac{dQ_2}{C_2(k)} \quad (2.2)$$



Where  $Q_1$  and  $Q_2$  are the amount of charge on node 1 and 2, respectively. Because of charge conservation and electrostatic induction, the total charge on node 1 and 2 can be given by Equation 2.3 below:

$$dQ_1 + dQ_2 = \sigma w dk \quad (2.3)$$

Combining the Equation 2.2 and 2.3,  $dQ_1$  and  $dQ_2$  can be expressed as Equation 2.4 and 2.5 below:

$$dQ_1 = \frac{\sigma w dk}{1 + \frac{C_2(k)}{C_1(k)}} \quad (2.4)$$

$$dQ_2 = \frac{\sigma w dk}{1 + \frac{C_1(k)}{C_2(k)}} \quad (2.5)$$

According to the superposition principle of the electrostatic field, the total charges on metal 1 and metal 2 considering the whole charges on the dielectric surface is the integration of each small triboelectric charged area, which can be expressed as Equation 2.6 and 2.7 below:

$$Q_1 = \sigma w \int_0^l \frac{dk}{1 + \frac{C_2(k)}{C_1(k)}} \quad (2.6)$$

$$Q_2 = \sigma w \int_0^l \frac{dk}{1 + \frac{C_1(k)}{C_2(k)}} \quad (2.7)$$

The short-circuit transferred charge amount when the dielectric fully moved from metal 1 to metal 2 is defined as  $Q_{SC,final}$ . It can be calculated from the difference between the total charge on metal 1 in the final state ( $x = g+l$ ) and in the initial state ( $x = 0$ ) given as Equation 2.8 and 2.9 below:

$$Q_{SC,final} = Q_{1,final} - Q_{1,initial} = \sigma w \int_0^l \frac{dk}{1 + \left(\frac{C_2(k)}{C_1(k)}\right)_{x=g+l}} - \sigma w \int_0^l \frac{dk}{1 + \left(\frac{C_2(k)}{C_1(k)}\right)_{x=0}} \quad (2.8)$$

$$Q_{SC,final} = Q_{1,final} - Q_{1,initial} = 0 - \sigma w l = -\sigma w l \quad (2.9)$$

When  $x = 0$  the dielectric is much closer to metal 1 than metal 2, therefore  $C_1$  is much larger than  $C_2$ , so  $C_2/C_1$  is close to 0 for all values of  $k$ . As a result,  $Q_{1,initial}$  is equal to  $\sigma w l$ . By contrast, when  $x = g+l$  the dielectric is much closer to metal 2 than metal 1, therefore  $C_1$  is much smaller than  $C_2$ , so  $C_2/C_1$  is close to infinity for all values of  $k$ . As a result,  $Q_{1,final}$  is equal to zero. For this reason  $Q_{SC,final}$  can reach  $\sigma w l$ , as shown in Equation 2.9.

By applying V-Q-x relationship and Ohm's law [97], we obtain the equation for the external load resistance  $R$ , the amount of transferred charges  $Q$  and the potential difference between the electrodes  $V$  as described in Equation 2.10 below:

$$R \frac{dQ}{dt} = V = V_{OC} - \frac{Q}{C} \quad (2.10)$$

Using the above equations and the parameters listed in Table 2.3 numerical calculation can be performed and the results are plotted in Figure 2.9 and Figure 2.10.

**Table 2.3** Parameter applied in the calculation of the outputs of sliding FT-mode TENGs. Reprinted with permission from Ref. [96]. Copyright 2015, Elsevier.

Structure component	Parameter utilized
Dielectric	$d=500\text{ }\mu\text{m}$ , $\varepsilon_r=2$
Width of the structure $w$	0.1 m
Length of electrode $l$	0.05 m
Thickness of metal electrode and freestanding layer	$d_m=10\text{ }\mu\text{m}$
Tribo-charge surface density $\sigma$	$20\text{ }\mu\text{C m}^{-2}$
Electrode gap $g$	1 cm
Freestanding height $h$	0 mm
Motion average velocity $v$	$1\text{ m s}^{-1}$

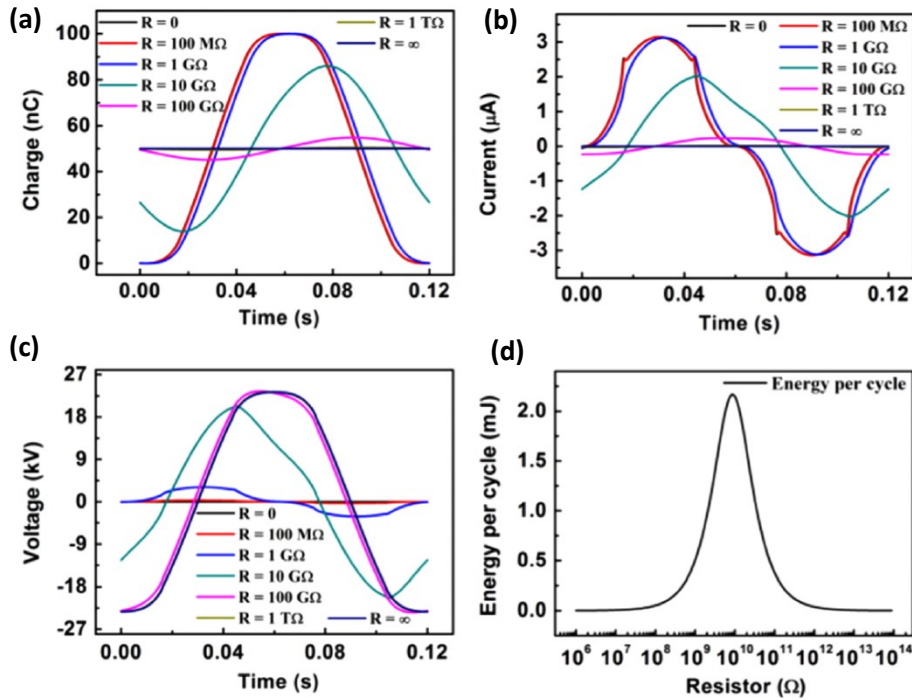


**Figure 2.9** Output properties of sliding FT-mode TENGs under single frequency harmonic vibration. (a) Transferred charge–time relationship at different load resistances. (b) Current–time relationship at different load resistances. (c) Voltage–time relationship at different load resistances. (d) The dependence of the total energy harvested in a single period on the load resistance. Reprinted with permission from Ref. [96]. Copyright 2015, Elsevier.

In Figure 2.9a, the oscillation amplitude of transferred charge curve approaches  $Q_{sc,final}$  when the load resistance is small. With increasing  $R$ , the oscillation magnitude reduces to approximately 0 and the base of the charge transfer curve converge to half of the maximum. The



same tendency is observed for the current. However, current reaches the maximum when the dielectric passes the centre of the gap between the electrodes ( $x = 3$  cm), as the gradient of the  $Q$ - $t$  graph is maximum. The current are the lowest when  $x = 0$  and  $x = g+l$  (Figure 2.9b). When  $R$  is infinite, the current reduces to zero. In Figure 2.9c, the oscillation amplitude of the voltage increases with increasing  $R$  and reach  $V_{OC}$  when  $R$  is infinite. In Figure 2.9d, the maximum energy per cycle is reached, when the load resistance matches the impedance of  $C$ . Figure 2.10a - d shows the Influence of the freestanding height  $h$  on  $Q_{SC}$ ,  $C$ ,  $V_{OC}$  and the energy per cycle, respectively.  $Q_{SC}$ ,  $V_{OC}$  and the energy per cycle increases with decreasing  $h$  caused by a change in  $C_2/C_1$ . They reach a maximum when the dielectric contacts the electrodes ( $h = 0$ ). By contrast, the total capacitance only slightly increases with increasing  $h$ , since the capacitance between the electrodes  $C_0$  is dominant and mainly responsible for the total capacitance.

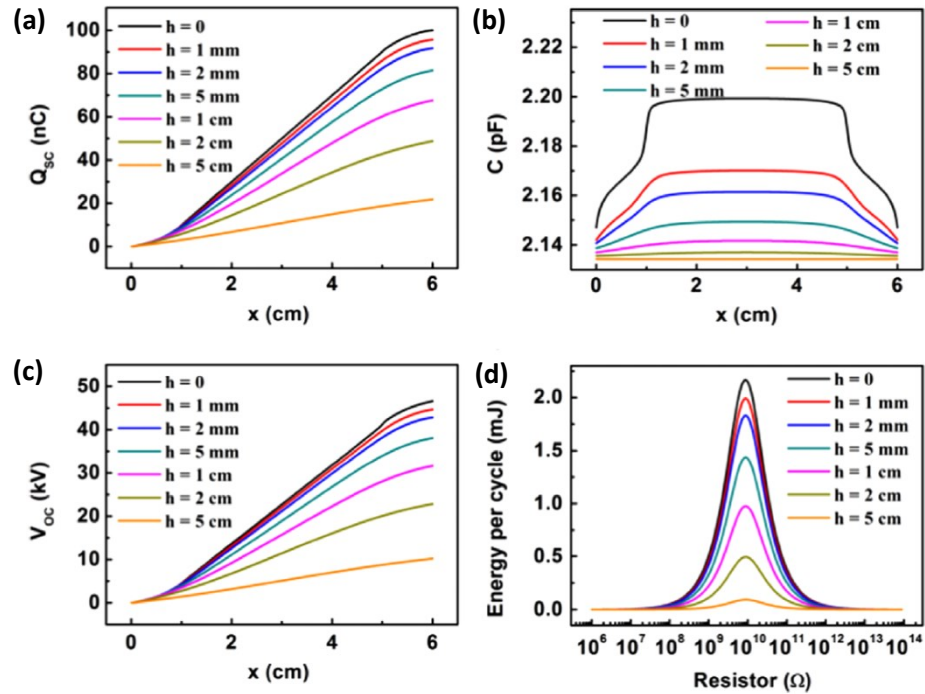


**Figure 2.10** Influence of the freestanding height  $h$  on (a) short-circuit transferred charge  $Q_{SC}$ , (b) total capacitance  $C$ , (c) open-circuit voltage  $V_{OC}$  and (d) the harvested energy in one cycle under different load resistance of sliding FT-mode TENGs. Reprinted with permission from Ref. [96]. Copyright 2015, Elsevier.

## 2.6 Textile manufacturing

Textiles are basic materials that are essential for human protection and comfort. Evidence has been found indicating the existence of textiles goes back more than 20,000 years [98]. Since the Industrial Revolution, textile manufacturing has developed in all aspects including technique, cost, quality and throughput. With regard to T-TENGs, textile production techniques and its

structure can have a considerable impact on its performance. Therefore, it is important to pay attention to the basic fundamental of fabric manufacturing.

Fabrics are made from yarns that are typically composed of spun fibres. Two essential dimensional features of fibres are their fineness and length. Flexibility stems from fineness and length provides coherence. Fineness is often expressed by linear density using an SI unit called tex (g/km). The linear density of fibres typically varies between 0.1 and 2 tex [99]. The length of fibres can be only a few centimetres (staple fibres) or several kilometres (filament fibres) and it is typically several hundred times the diameter. The diameter of fibres typically ranges from ten to several hundred micrometres. Fibres can be classified into two main categories: natural and man-made. Natural fibres stem from animals (wool, silk, hair), plants (cotton, linen, hemp) and minerals (asbestos, glass fibre). Animal and plant fibres are typically soft, breathable, absorbent and biodegradable, however, they can shrink in hot water, wrinkle easily and some of them can irritate the skin. Man-made fibres can be divided into two groups, namely cellulosic and noncellulosic. Cellulosic fibres are regenerated fibres made from natural materials, which are chemically processed, for instance, rayon and acetate. Noncellulosic fibres are synthetic polymer fibres made by refining crude oil or coal e.g. nylon, polyester (PE) and acrylic. Man-made fibres are typically durable, lightweight, inexpensive and quick drying but can have reduced breathability and biodegradability. Yarns are long continuous strands produced by spinning the fibres together. When two or more yarns are twisted together, they are known as ply yarns. Different fibres require different preparation processes before they can be spun into yarns. In the case of cotton, the world's most important natural fibre, its standard processes are opening, cleaning, blending, carding, combing, drafting, twisting and winding [100].

Textiles are formed by interlocking yarns together by, most commonly, weaving using a hand or power loom and knitting using a knitting needle, crochet hook or knitting machine. Woven fabrics are made by interlacing warp yarns (vertical yarns) and weft yarns (horizontal yarns). Different weaving techniques can achieve a diverse range of fabric structures. Three basic weaves are used for the majority of two-dimensional (2D) fabrics, these being plain, satin and twill as shown in Figure 2.11a - c. Other weaving structures include basket, pile, crepe jacquard, ribbed, braided and triaxial woven [100], [101].

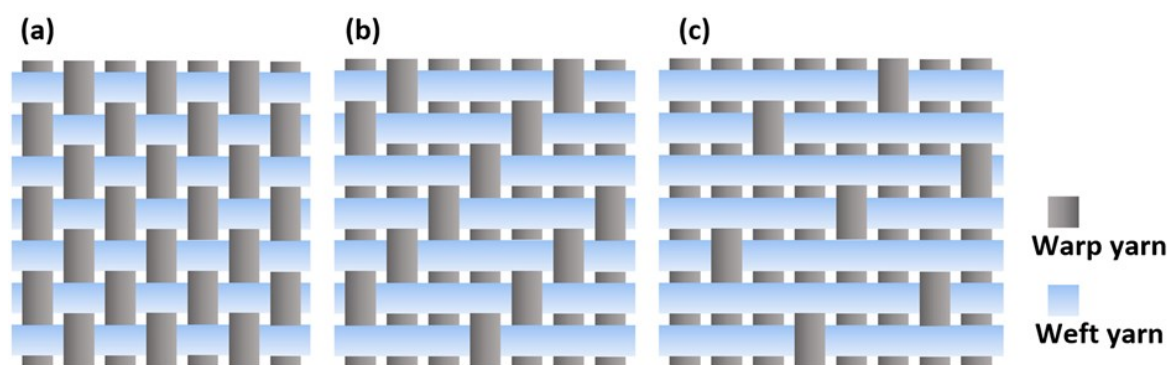


**Figure 2.11** Three basic weaves: (a) plain weave (b) twill weave and (c) satin weave. Reprinted with permission from Ref. [20]. Copyright 2019, Elsevier.

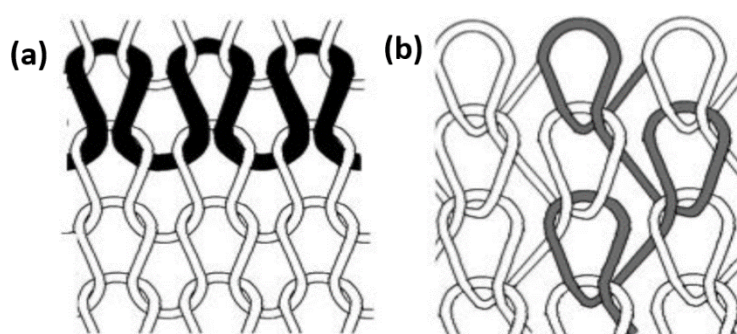


**Figure 2.12** Two basic knitted structures (a) weft knitting and (b) warp knitting. Reprinted with permission from Ref. [4]. Copyright 2017, MDPI.

Knitted fabrics are produced by forming interlocking loops of yarn. The horizontal row and each vertical row of loops is known as the course and wale, respectively. There are various ways of looping, which generate two main types of knitted fabric known as weft and warp knitting. Figure 2.12a represents weft knitting with one continuous yarn forming courses across the fabric and Figure 2.12b shows warp knitting with a series of yarns forming wales in the vertical direction [102]. Other knitting processes include Raschel, crochet, Milanese, fleece, and terry knit [100]. There is also a class of fabrics known as non-woven that have a web-like structure made up of short fibres that are held together by various techniques, including needling, knitting, stitching, thermal and chemical bonding. Examples of the common non-woven fabrics are felted fabrics that are produced by pressing wool or fur under a certain pressure, moisture and heat and bonded fabrics that are produced by bonding fibres together using methods such as stitching or adhesion. The electrospinning method can also be utilized to make nanofibre-based non-woven fabrics. An electric field is used to draw charged threads towards a grounded collector from polymer solutions or melts thereby forming fine fibres with diameters ranging from 2 nm to several micrometres. The properties of non-woven fabrics produced by this technique can be adjusted (e.g. porosity) and can achieve a much denser structure with a higher surface-to-volume ratio compared to conventional techniques [103], [104].

Three-dimensional (3D) fabrics can also be manufactured by weaving, knitting, braiding, stitching and non-woven methods. The simplest form of 3D fabric is made up of 2D fabrics that are stacked on top of each other and bound together in the thickness direction using the techniques, such as stitching, needle-punching, chemical bonding or lamination. 3D woven structures can be realised using multiple yarns sets including a z-yarn aligned through the thickness of the fabric. The weaving process is performed both in-plane and out-of-plane directions. Although through-the-thickness fibre reinforcement improves out-of-plane properties of 3D woven composites, in-plane mechanical properties are generally low. 3D knitted fabrics are produced by the 3D spatial formation of 2D warp or weft knitted fabrics. Due to their characteristic looped architecture and low fibre volume fraction, the mechanical properties are reduced. The 3D fabrics are often utilised as reinforcement materials in various fields, such as civil engineering and military industry [101].

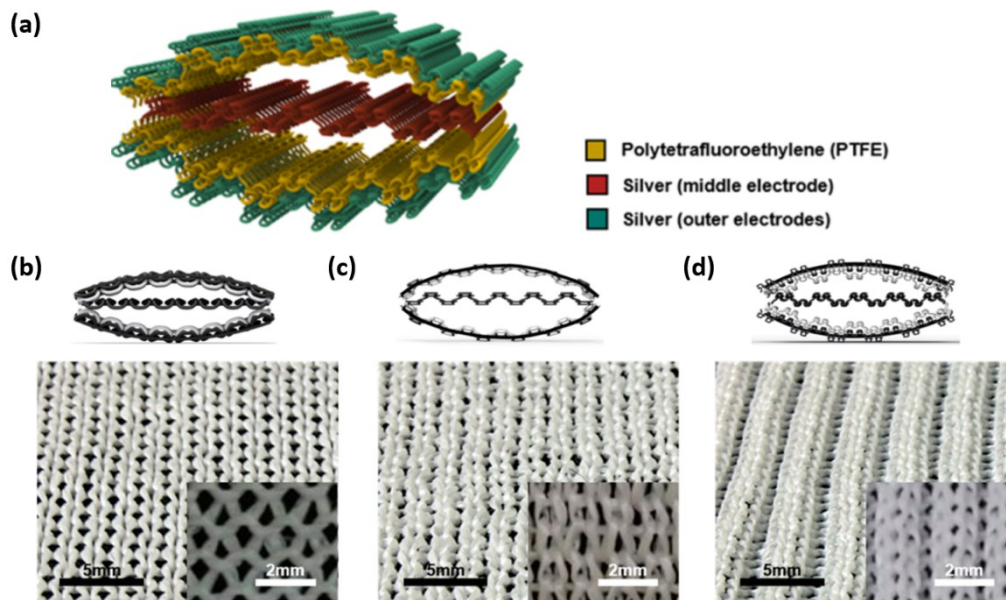


**Figure 2.13** T-ENG with three different knitted structures: (a) Schematic illustration of the T-ENG, (b) plain-knitted structure, (c) double-knitted structure, and (d) rib-knitted structure with insets of the magnified photos. Reproduced with permission from Ref. [105]. Copyright 2017, American Chemical Society.

The effect of fabric structure on the performance of T-ENG was demonstrated by Kwak et al. [105]. As shown in Figure 2.13a, PTFE yarns and silver (Ag) yarns were knitted together forming stacks of two PTFE triboelectric layers, one Ag inner electrode and two Ag outer electrodes. This work investigated the performance of plain-, double-, and rib-structure weft-knitted fabrics (illustrated in Figure 2.13b - d). Under a cyclical compressive force, an alternating current between the Ag inner electrode and outer electrodes was obtained. The study showed that the TENG with rib-knitted structure exhibited the maximum effective contact area and stretchability. As a consequence, it produced a  $V_{oc}$  of 23.50 V, which is more than ten times and almost two times greater than the plain- and double-structures, respectively.

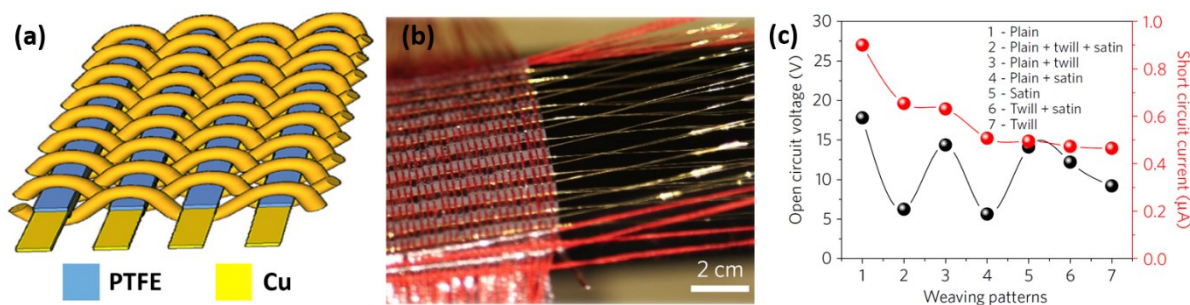


**Figure 2.14** (a) Schematic illustration of T-TENG with plain weaving structure, (b) photograph of the textile weaving process and (c) dependence of the electrical output on the different woven structures. Reproduced with permission from Ref. [106]. Copyright 2016, Springer Nature.

Chen et al. have confirmed the importance of the textile structure [106]. They demonstrated a hybrid harvester comprising photovoltaic textile and T-TENG. The electrical output of the T-TENG woven from PTFE strips and Cu fibres varies depending upon the variation in the effective contact area relating to the string-packing density in the different woven structures. Figure 2.14a shows a schematic illustration of the T-TENG with a plain weaving structure. The photograph in Figure 2.14b reveals the textile weaving process and Figure 2.14c shows the dependence of the electrical output generated via hand clapping on the different woven structures. From the three basic woven structures, the T-TENG with plain weave produces the highest power, followed by satin and twill weave, while the output of the TENGs with mixed woven structures lies between the corresponding basic structures.

## 2.7 Materials

There is a limited range of materials that possess the mechanical and electrical properties necessary to be used in a T-TENG. The desirable properties are, for example, flexible, stretchable, biocompatible, light, durable, washable and breathable. The materials can be sorted into two following major groups.

### 2.7.1 Triboelectric materials

Triboelectric materials are the materials on whose surface the triboelectric effect takes place when they are brought into contact with each other. The choice of triboelectric material plays a fundamental role in the output performance of the T-TENG. The individual properties of materials, such as the electron affinity and the work function, can determine the polarity and the charge density of materials. A guideline for material selection is the triboelectric series [61], which is a list of various materials sorted by their tendency to lose or gain electrons. The further apart in the list the two materials are, the greater the tendency for electron transfer. For this reason, a TENG should

consist of at least two materials, which are separated as far as possible on the list. Theoretically, each material can become either positively or negatively charged depending on the triboelectric property of the material it makes contact with. However, there are certain choices of materials for T-TENG, which are typically selected as the positive or negative triboelectric materials. Metal, including Al, Cu, Ni, and Ag, are often used as the positive triboelectric materials because they are at the top of the triboelectric series and can also be used as an electrode at the same time. Most textiles, such as nylon, cotton and silk also tend to become positively charged and polyurethane (PU) is the most positive material in the triboelectric series. Typical negative materials are PDMS, parylene, polyvinylidene fluoride (PVDF), silicone rubber, PTFE and FEP. These materials are often coated on fibres or textiles to improve the triboelectric properties of T-TENGs [107]–[109].

### **2.7.2 Electrode materials**

Electrodes are essential parts of T-TENG. They are electrical conductors where the electrostatic induction takes place. Poor electrical properties, such as low carrier mobility, and low free carrier density can lead to a considerable energy loss in the materials and thus a reduction in the efficiency of the TENG. In this section, different techniques to achieve conductive and flexible electrodes suitable for T-TENGs will be discussed.

#### **2.7.2.1 Metal-based electrode**

The simplest metal-based electrode is made of metal foil [68], [83]. It can be attached to the triboelectric textile materials with adhesive or double-sided adhesive tape. This type of electrode benefits from high electrical conductivity but the assembly is prone to failure after cyclical bending and they are not stretchable or breathable. Furthermore, the additional thickness arising from the adhesive layer causes a drop in the potential difference and a corresponding reduction in performance of the TENG [97], [110]. The more popular approach is to utilise metal-based conductive fabrics (CF). A metallic thin film can be deposited on fabric using standard microfabrication processes, such as sputtering [85] or evaporation [87]. The disadvantages of these methods include incompatibility with large-scale textile manufacturing processes, high cost of production, unsuitability for complex surface topologies and porous fibres and lack of mechanical durability [111]. Alternatively, the metal layer can be deposited using electroless plating. For instance, a Ni-coated PE fabric has been prepared by immersing PE cloth into Nickel(II) sulfate ( $\text{NiSO}_4$ ) aqueous solution [94]. Another technique is to introduce metallic nanoparticles (NPs) or nanowires (NWs) on textiles. For example, Lee et al. demonstrated polymer/Kevlar coated with silver nanoparticles (AgNPs). It exhibited a good mechanical stability after 3000 bending and a low resistivity of  $0.15 \, \Omega/\text{cm}$  [112]. Besides, Guo et al. successfully fabricated conductive fabric by dip-



coating nylon cloth with a solution of silver nanowires (AgNWs). Their T-TENG with AgNWs electrode was used as a personal energy management device for wearable applications [68]. Nevertheless, the resistance of these examples is likely to increase with stretching and conductive particles can be removed during washing reducing conductivity and potentially polluting the environment [113]. Resistance to the effects of stretching can be improved by, for instance, covering a stretched substrate surface with NWs to create buckled conductive layer after release [41], [114], [115] or adding a supplemental material such as graphene [71] or 3-aminopropyltriethoxysilane (APTES) [116] to the NWs layer. Most recently, Yang et al. have demonstrated a liquid-metal-based TENG by injecting Galinstan into silicone rubber fibres, which enables Galinstan electrodes to remain conductive even when stretched. The TENG successfully demonstrated its suitability for powering wearable devices, such as pedometer, minicalculator and electronic watch [117]. For fibre-based TENGs, metal fibres are often used as electrodes. They can simply be spun into yarns and/or woven with other commercial yarns using standard industrial processes. This technique provides the opportunity for the mass production and commercialisation of T-TENGs [91], [106].

#### **2.7.2.2 Carbon-based electrode**

Carbonaceous materials such as carbon nanotubes (CNTs), carbon nanoparticles, carbon fibres and graphene are promising for the use as electrodes in T-TENG. According to Zeng et al., they possess high intrinsic carrier mobility ( $10^6 \text{ cm}^2 \text{ V}^{-1} \text{ S}^{-1}$ ), high electrical conductivities ( $10^4 \text{ S/cm}$ ), excellent mechanical properties (elastic modulus in the order of 1 TPa) and environmental stability [1]. CNTs are the most widely used carbon-based materials for T-TENG due to the simple fabrication process and low fabrication cost [111]. The common technique used is called “dipping and drying” by which fabric [38] or yarn [118] is immersed in a conductive ink solution containing single-wall or multi-wall CNTs (MWCNTs). Graphene is a form of carbon comprising a single layer of carbon atoms arranged in a hexagonal lattice. Recently, Chu et al. published research on a graphene-based TENG where the electrode was formed from ultrathin double-layer graphene with a thickness less than 1 nm grown by thermal chemical vapour deposition (CVD). Its potential application as a self-powered conformal touch sensor was also illustrated [119]. Another graphene-based T-TENG was demonstrated by Zhu et al. with one of the electrodes fabricated from nylon fabric coated with graphene ink [120]. Despite the advantages, carbon-based T-TENGs still have not been commercialised yet because of difficulties in scale-up and the high cost of the materials [92].

#### **2.7.2.3 Polymer-based electrode**

Conductive polymers are a promising material for wearable electronics due to their inherent flexibility and environmental stability. However, the major drawback is the low conductivity.

Shirakawa et al [121] introduced the first conductive polymer by exposing polyacetylene (PA) polymer to iodine vapour and achieved a conductivity of 30 S/cm. Nowadays, the most intensively explored conductive polymers are polypyrrole (PPy) and poly-(3,4-ethylene dioxythiophene) (PEDOT). PPy is commonly synthesized by electrochemical polymerisation [122], [123]. However, due to its poor insolubility, large-scale fabrication is limited [124]. PEDOT is a conductive polymer with high conductivity resulting from its unique structure, which comprises dioxyalkylene bridging groups at positions 3 and 4 of its heterocycle ring [111]. Conductivity can be regulated from  $10^{-4}$  to  $10^3$  S/cm [125]. Sutka et al. demonstrated that PEDOT can be used as both a triboelectric and an electrode material for TENG, which produced ~3 times more power density than TENG with indium tin oxide (ITO) electrodes [126]. Similar to PPy, PEDOT is insoluble but when doped with polystyrene sulfonate (PSS), PEDOT:PSS becomes highly soluble in water. This opens up new processing possibilities such as dipping and drying [127], and vacuum filtration [70]. The latter is exemplified in the work of membrane-based flexible T-TENG undertaken by Das et al [70]. Recently, Jing et al. has introduced a core-shell T-TENG with organogel electrode as the core layer. This organogel was synthesized by the photo-crosslinking of 4-acryloylmorpholine (ACMO) in propylene carbonate solution. The proposed electrode exhibits a resistivity of 1.83 k $\Omega$ -cm under unstretched condition [128].

## 2.8 Surface modification

### 2.8.1 Topographic modification

The performance of TENGs is strongly determined by its nano/microscopic surface roughness. Various methods have been applied to form different micro or nanostructures on the surface, for example, pyramids [12], [67], NWs [15], [75] and NPs [13], [14], [129], [130]. These structures can be formed by standard microfabrication processes such as etching or thermal deposition. In the case of standard TENGs, several investigations have been reported. For example, Fan et al. investigated the effect of different surface patterns on the performance of a TENG by introducing arrays of lines, cubes and pyramids on PDMS films using a silicon mould [131]. The PDMS film was attached to a PET/ITO substrate to form a CS-mode TENG. They found that the maximum output performance was obtained from the TENG with the array of pyramids, followed by cubes, lines and no array, respectively. The results revealed an almost four times improvement in the performance of the pyramids-structured TENG compared to the TENG with no arrays. Similarly, Jeong et al. studied the effect of nanodots, nanogrates and nanomeshes patterned silica surfaces on the performance of a PTFE/Silica TENG [132]. The results showed that the power output of the nanomesh patterned TENG was 6.3 times higher than that of the plain TENG. Zhang et al.



reported that the combination of micro/nano dual scale patterns on the PDMS film enhanced the current and voltage output of the TENG by 157% and 100%, respectively [133]. Focusing on T-TENGs, Lee et al. used textiles as the top and the bottom substrate with the top textile coated with aluminium nanoparticles (AlNPs) using thermal evaporation, and the bottom textile with spin-coated PDMS [14]. The PDMS was then etched using reactive ion etcher (RIE) to form NWs on the surface. With this approach, a very high instantaneous power density of  $336 \text{ W/m}^2$  was obtained at an external load of  $20 \text{ } \Omega$ . Ko et al. investigated the effect of different nanostructures on the performance of T-TENG [134]. The device comprised nano-structured conductive bundle yarns (CBYs) serving as positive triboelectric material and PDMS serving as the negative triboelectric material. They found out that the growth of zinc oxide (ZnO) NWs coated with ZnO NPs on the CBY surface increased the power density of the T-TENG by approximately 45 times and 8 times compared to plain CBYs and CBYs with only ZnO NWs, respectively.

### 2.8.2 Chemical modification

In contrast to the topographic modification, which usually involves additional physical fabrication processes, the chemical modification process is simpler and can be performed without new substrate design. In this case, the substrate will be commonly covered with an ultrathin layer of molecules containing fluorine. The fluorine atom has very high ionisation energy, and therefore the electron binding energy of the substrate increases and the treated surface will tend to gain electrons rather than to lose them [16], [135], [136]. Zhang et al. demonstrated that the fluorocarbon plasma treatment of the surface of PDMS enhanced the output power of a TENG by 278% [16]. Song et al. engineered molecularly surface of PDMS in TENG by self-assembled monolayers (SAMs) [87]. First, the PDMS surface was exposed to an oxygen plasma to form hydroxyl groups. Subsequently, SAMs containing different end-functional atoms were deposited on the PDMS surface by either liquid-phase or a vapour-phase deposition method. The results showed that the TENG with SAM containing end-fluorine atoms exhibited the best output performance with an  $I_{SC}$  of  $27 \text{ } \mu\text{A}$ , a  $V_{OC}$  of  $105 \text{ V}$  and a power density of  $1.8 \text{ W/m}^2$ , which is more than 60 times higher than that of an unmodified TENG. T-TENGs fabricated from fabrics such as silk, cotton, and PET (Dacron) with surface modification by SAMs were also represented in their research. The modified fabrics were brought into contact with a PET/ITO film. While the  $V_{OC}$  of the T-TENG with Dacron increased from  $25.7 \text{ V}$  to  $42 \text{ V}$ , the values for the silk and the cotton decreased from  $54.7 \text{ V}$  and  $35.7 \text{ V}$  to  $23.1 \text{ V}$  and  $20.6 \text{ V}$ , respectively, due to a decline in the triboelectric charge gap between the fabrics and the PET/ITO film in the triboelectric series.

## 2.9 Material and structural design

There are numerous example T-TENGs in the literature and the following review has been categorised into two main groups, fabric-based TENG and fibre-based TENG.

### 2.9.1 Fabric-based TENG

Fabric-based TENGs are the most common type of T-TENG due to its relatively straightforward fabrication process and high electrical output. It is composed of conventional fabric, which can either be directly used as a triboelectric material and/or just serves as a substrate.

#### 2.9.1.1 Fabric-based TENG using the fabric as triboelectric layer

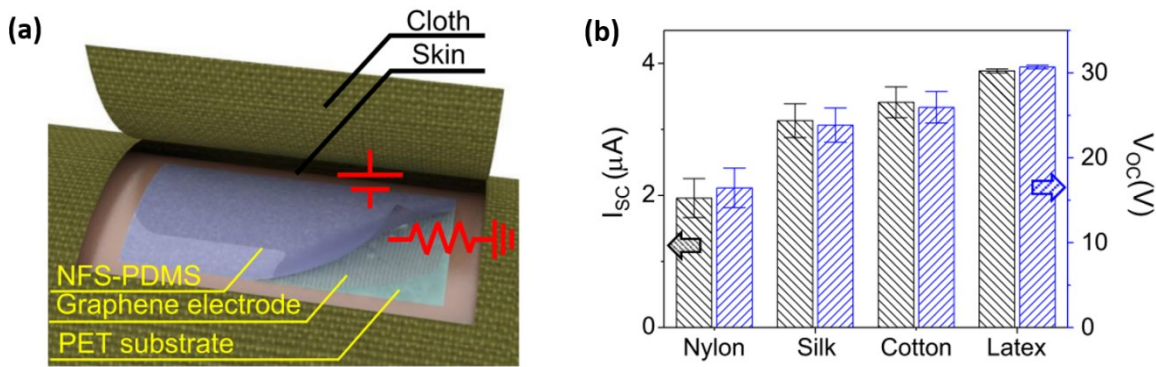


**Figure 2.15** (a) Schematic illustration of conformal ultrathin T-TENG and (b)  $I_{sc}$  and  $V_{oc}$  of the conformal T-TENGs for different types of fabric tested as triboelectric materials. Reproduced with permission from Ref. [119]. Copyright 2016, Elsevier.

In this case, fabric is used as one or both of the triboelectric materials. It can be a fixed part of T-TENG or can only serve as the freestanding-layer in FT-mode, FCS-mode and SE-mode. For example, Chu et al. demonstrated a conformal ultrathin T-TENG operating in the SE-mode [119]. Figure 2.15a illustrates its structure, which is composed of a thin PET layer ( $<0.9 \mu m$ ), graphene ( $<1 \text{ nm}$ ) and PDMS ( $<1.5 \mu m$ ) serving as the substrate, the electrode and a triboelectric material, respectively. The PDMS surface was nanostructured by  $O_2$  plasma etching and chemically modified by  $SF_6$  plasma and these treatments increased the output current and voltage by a factor of more than 10. Due to its thickness and flexibility, the device could be applied to human skin and used to generate power when the PDMS comes into contact with the cloth. Different types of fabric, including nylon, silk, cotton and latex were tested as triboelectric materials. It was found out that the effective contact area, which varied from 21% to 98% of the total contact area, was related to the woven structure of the fabrics and the  $V_{oc}$  and  $I_{sc}$  ranged from 16.3 V to 30.9 V and 1.9  $\mu A$  to 3.9  $\mu A$  respectively, as illustrated in Figure 2.15b. By dint of a hand tapping with a nitrile glove, the device generated a maximum  $V_{oc}$ ,  $I_{sc}$  and power density of 47.1 V, 7  $\mu A$  and 144  $mW/m^2$ , respectively.

One simple way to fabricate this type of T-TENG is to use the fabric as a triboelectric layer and coat one surface of the fabric with a conductive material to collect the induced charges. With this concept, Zhu et al. designed a 3D spacer fabric-based TENG consisting of three layers: two outer nylon weft-knitted fabric layers and a PE spacer layer [120]. The upper surface of the nylon layer was coated with a graphene ink to form the electrode and the lower nylon fabric layer was coated with PTFE. When the TENG was periodically pressed and released, charge separation occurred at the surface of the nylon fabric and PTFE coated nylon fabric leading to charge induction at the electrodes. A power density of  $53.3 \text{ mW/m}^2$  was obtained at a frequency of 1 Hz and an external load of  $0.6 \text{ M}\Omega$ .

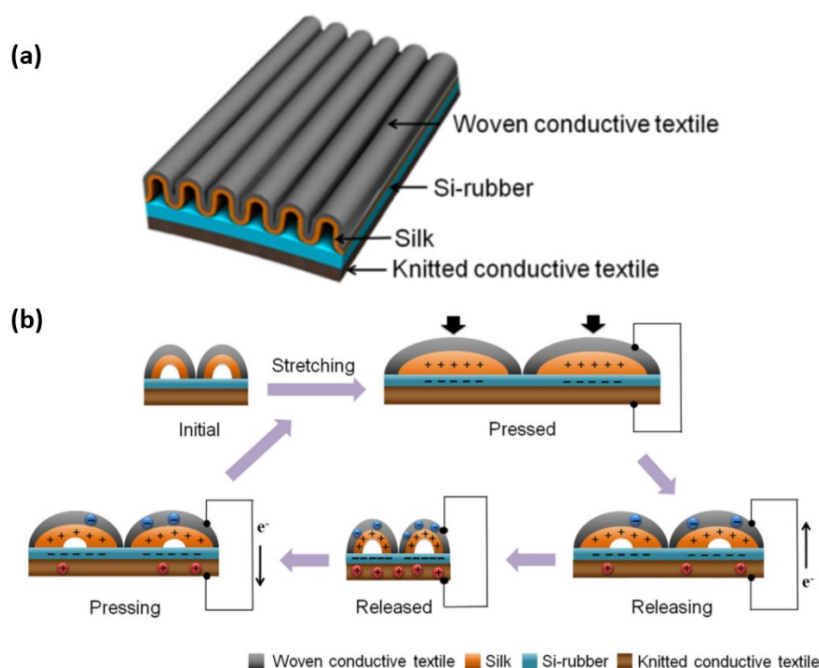


**Figure 2.16** (a) Schematic illustration of T-TENG with a corrugated structure and (b) power generation mechanism via stretching and releasing. Reproduced with permission from Ref. [137]. Copyright 2017, Nature.

A good example of T-TENG, which can operate in a lateral stretching and release mode was reported by Choi et al. They designed a T-TENG with a corrugated structure, shown in Figure 2.16a [137]. The top layer was produced by backstitching silk with a woven conductive fabric (Sn/Cu/Ag-plated nylon). The bottom layer was made of a knitted conductive fabric (Ag-plated nylon) coated with silicone rubber. Then, the corrugated top layer was sewn on the bottom layer. As shown in Figure 2.16b, the triboelectric effect arose from the contact-separation between the silk and the silicon rubber during stretching and release. A maximum  $V_{OC}$ ,  $I_{SC}$  and power density of 28.13 V, 2.71  $\mu\text{A}$  and  $166 \text{ mW/m}^2$  could be reached, respectively.

### 2.9.1.2 Fabric-based TENG using fabric as substrate

In many example T-TENGs, the fabric only serves as one or both substrates i.e. they provide mechanical support and another material with better triboelectric properties is attached to the textile. Because of this, the material choice and the performance of the T-TENG can be significantly increased. A simple method to fabricate this type of T-TENG was demonstrated by Pu et al. [92]. The T-TENG was fabricated by plain-weaving stripes of Ni-coated PE fabric (Ni-cloth) and parylene-coated Ni-fabric (P-Ni-cloth) as shown in Figure 2.17a. The conductive Ni-cloths, which serve as both electrodes, were produced by electroless plating of Ni on the PE cloths, whereas the P-Ni-cloths were coated by CVD deposited parylene. The power generation mechanism is demonstrated in Figure 2.17b. The contact-separation between two TENG cloths under repeated force lead to a charge separation between the Ni-cloths and the P-Ni-cloths and an alternating current flow between their electrodes. The resultant T-TENG fabric largely maintained the flexibility, the washability and comfort of the PE cloth. In CS-mode, the power cloth could produce a power density of up to  $393.7 \text{ mW/m}^2$  at a frequency of  $0.7 \text{ Hz}$  and a load resistance of  $70 \text{ M}\Omega$ .

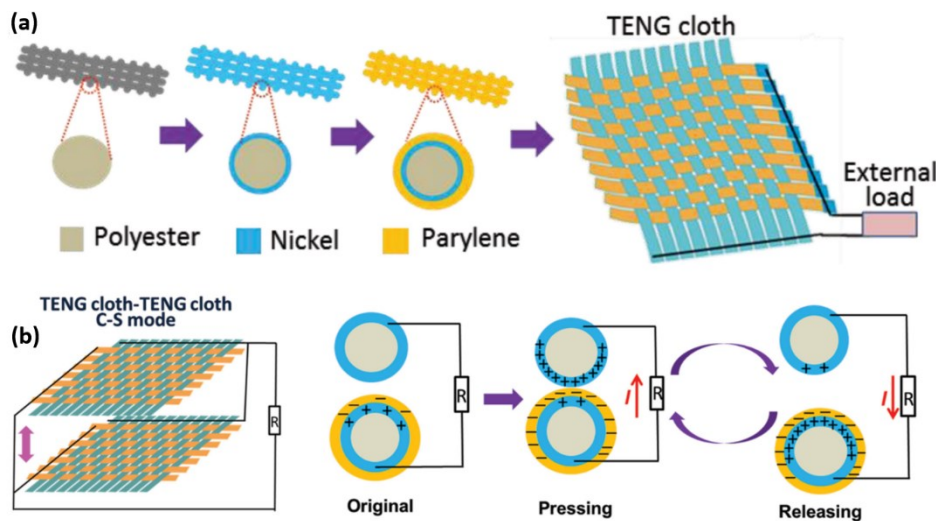


**Figure 2.17** (a) Schematic illustration of T-TENG fabricated by plain-weaving stripes of Ni-cloth and P-Ni-cloth, and (b) power generation mechanism via a repeated compressive force. Reproduced with permission from Ref. [92]. Copyright 2015, John Wiley & Sons, Inc.

A more complex T-TENG structure was proposed by Liu et al. [67] who used a 3D spacer PET fabric with a three-dimensional structure. One surface of the fabric was coated with PDMS forming a pyramid-structured surface combined with a CNT sheet electrode and the other surface was coated with Ag to act as an electrode. By mean of a contact-separation movement through a repeated compressive force, opposite charges were generated on PET and PDMS surfaces causing a current flow between the Ag and CNT electrode. This T-TENG produced  $V_{OC}$ ,  $I_{SC}$  and power density of  $500 \text{ V}$ ,  $20 \mu\text{A}$  and  $153.8 \text{ mW/m}^2$ , respectively. It was also shown that there is no significant change in the performance after 3000 cycles of pressing and releasing.

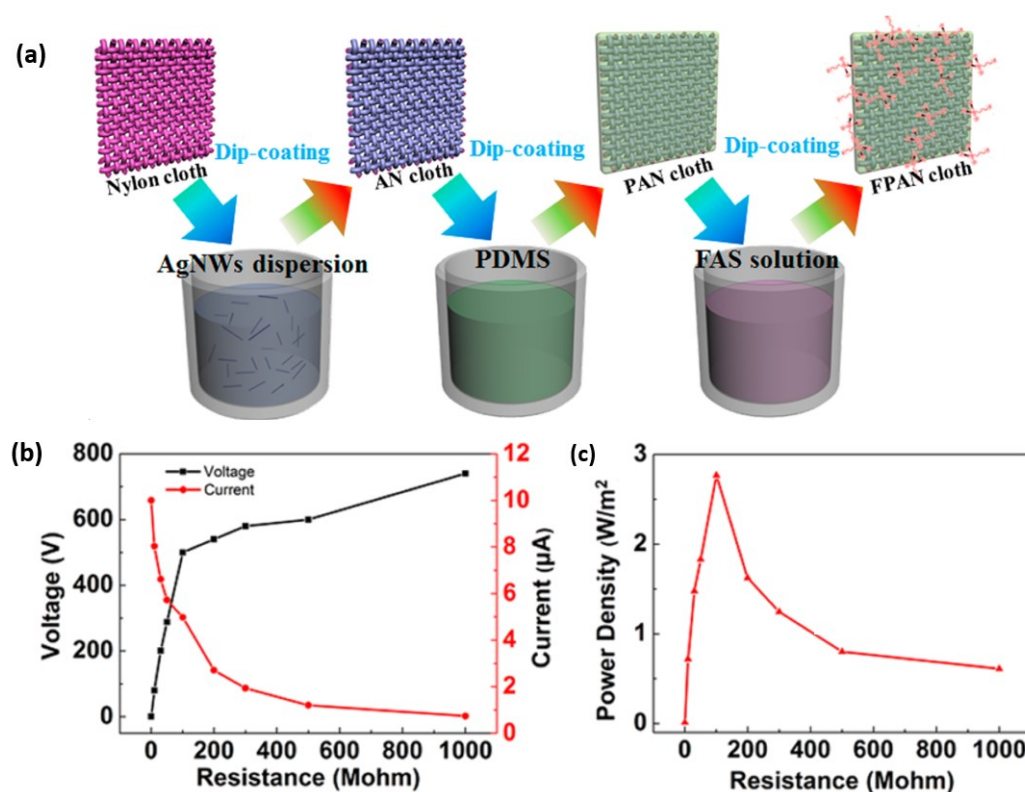


**Figure 2.18** (a) Schematic diagram of the fabrication process of the fabric-based TENG proposed by Guo et al. Load resistance dependence of (b) peak output voltage and current, and (c) corresponding instantaneous power of the TENG. Reproduced with permission from Ref. [68]. Copyright 2016, American Chemical Society.

A high-performance T-TENG was demonstrated by Guo et al. in 2016 [68] who used a nylon cloth as the substrate dip-coated with AgNWs, PDMS, and fluoroalkyl silane (FAS) in sequence. The fabrication process is presented in Figure 2.18a. The AgNWs, PDMS, and FAS layer functioned as an electrode, a triboelectric material and the chemically modified surface, respectively. The other electrode was composed of a commercial PET cloth, double sided tape and Al foil electrode. The addition of the FAS layer resulted in increased  $V_{OC}$  and  $I_{SC}$  from 53.2 V to 575 V and 1.1  $\mu\text{A}$  to 12.1  $\mu\text{A}$  compared to the device without the FAS layer. The load resistance dependence of the electrical outputs is shown in Figure 2.18b and the electrical power output is given in Figure 2.18c, which shows a clear peak of 2.77  $\text{W/m}^2$  at a load resistance of 100 M $\Omega$ . Furthermore, this T-TENG showed an increase in thermal insulation by 8% and good durability after 12000 test cycles.

## 2.9.2 Fibre-based TENG

Fibre-based TENG consist of one single or multiple fibres, which can partly or fully function as TENG and can be later woven or knitted into fabric. Based on its structure and energy harvesting capability, fibre-based TENGs can be divided into three groups, namely single-thread semi-integrated TENG, single-thread fully-integrated TENG and multiple-thread fully-integrated TENG.

### 2.9.2.1 Single-thread semi-integrated TENG

Single-thread semi-integrated TENG is a TENG which is in the form of a thread. It is typically composed of a conductive core and a dielectric shell. The stand-alone thread cannot produce electricity by itself but requires contact with an external triboelectric material. To increase the electrical output from a textile, several threads can be interlocked and their electrodes can be connected together. Dong et al. published their work about all-yarn-based TENG [138]. They fabricated a fabric from threads made of semi-integrated TENG using the weft-knitting technique. Each thread comprised a three-ply spun stainless-steel/PE fibre blended yarn in the core and silicone rubber in the shell. By contacting with an acrylic plate in the SE-mode at a frequency of 3 Hz, a load resistance of 100 M $\Omega$  and a contact force of 11 N, the T-TENG generated a power density of 85 mW/m<sup>2</sup>. Furthermore, it showed no considerable degradation in the performance after 50,000 contact-separation cycles and 15 washing cycles.

Yu et al. developed a T-TENG fabrication process, which is compatible with the standard industrial processes for mass production of textiles [91]. As shown in Figure 2.19a and b, a commercial machine was used to twist natural or man-made fibres around conductive fibres resulting in core-shell yarns. Afterwards, the yarns could be woven or knitted into fabric by ordinary textile manufacturing. The resultant fabric exhibited very similar physical properties to conventional fabric being flexible, comfortable, washable and durable. The operations of the T-TENG in the SE-mode, CS-mode, and FT-mode are illustrated in Figure 2.19c. The maximum power of 60 mW/m<sup>2</sup> was achieved in the SE-mode when stainless-steel, PU and PE were used as the core fibres, the spun man-made fibres and the external triboelectric material, respectively. Note, only the T-TENG operating in SE-mode belongs to single-thread semi-integrated TENG, whilst the T-TENG operating in CS- and FT-mode are classified into multiple-thread fully-integrated TENG, which will be discussed in detail later.



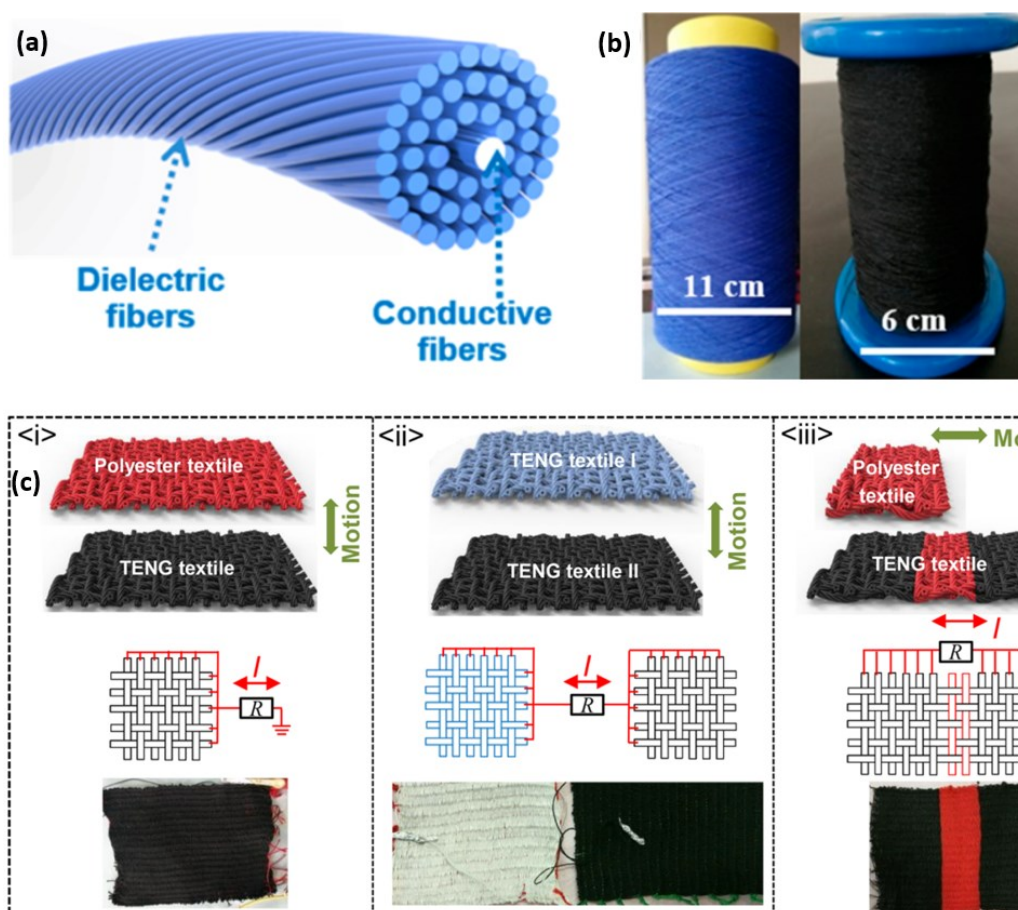


**Figure 2.19** (a) Schematic illustration of core-shell yarns, (b) industrialised stainless-steel/PU core-shell yarns with different colours and (c) three possible operation modes of the T-TENGs: i. SE-mode, ii. CS-mode and iii. FT-mode. Reproduced with permission from Ref. [91]. Copyright 2017, American Chemical Society.

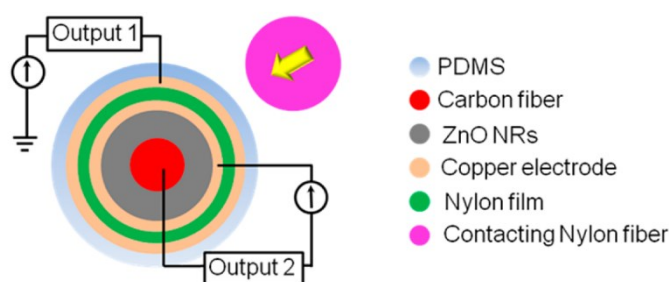


**Figure 2.20** Schematic illustration of fibre-based hybrid nanogenerator combining a semi-integrated TENG (Output 1) and PENG (Output 2). The power is generated via a contact with an external material (Nylon fibre). Reproduced with permission from Ref. [40]. Copyright 2014, American Chemical Society.

As shown in Figure 2.20, a fibre-based hybrid nanogenerator combining a SE-mode semi-integrated TENG and piezoelectric nanogenerator (PENG) was realised by Li et al [40]. The PENG in the core was made from carbon fibre and ZnO NWs wrapped by a nylon film, which was coated with Ti/Cu on both sides. The inner Ti/Cu layer acted as an electrode for the PENG. The fibre was finally dip-coated with PDMS. The PDMS and the outer Ti/Cu layer served as the triboelectric layer

and the electrode. A nylon fibre was chosen as the external material for contacting the T-TENG and pressing the PENG at the same time. The power density of the T-TENG and the PENG reached 42.6 and 10.2 mW/m<sup>2</sup>, respectively. In addition, five fibres of the generator were woven with cotton thread to form a power suit to harvest energy under arm motion. However, they generated very low current output of only 70 nA and 4 nA for the T-TENG and the PENG, respectively.

Recently, Chen et al. have demonstrated a fibre-based TENG fabricated using Direct-Ink-Writing (DIW) 3D printing method [139]. It has a core-sheath structure. The conductive ink for core layer is composed of graphene/PDMS solution and the ink for sheath is obtained by mixing PTFE particles and PDMS. A bespoke 3D printer was used to print the coaxial fibre by filling the both inks in the printing pipe simultaneously. By pressing the fibre with a finger, the T-TENG can generate a  $V_{oc}$  of up to 7 V. This signal is large enough for its use as a tactile sensor.

### 2.9.2.2 Single-thread fully-integrated TENG

Single-thread fully-integrated TENG is a stand-alone thread, which is complete with all necessary components of the TENG and can generate electrical power by itself without interaction with any external material. It is typically fabricated in a core-shell structure with one electrode at the core and the other electrode in the shell. The power is produced by relative movement between the core and the shell based on CS-mode and/or LS-mode.

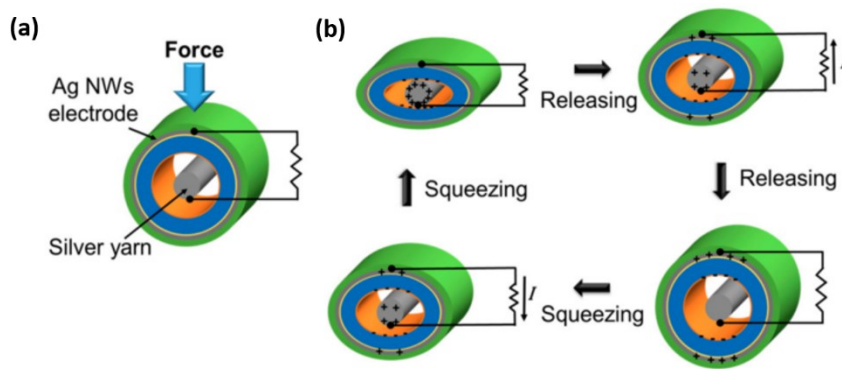


**Figure 2.21** (a) Schematic illustration of single-thread fully-integrated TENG and (b) its operation principle in CS-mode [116].

As an example, Kim et al. developed a T-TENG from woven fibres. Each fibre comprised a Ag-yarn acting as the core electrode and a flexible tube acting as the shell substrate, as shown in Figure 2.21a [116]. The outer surface of the tube was coated with AgNWs and a mixture of PDMS and EcoFlex, which served as the other electrode and the insulating layer respectively. The inner surface of the tube was coated with 1H, 1H, 2H, 2H-perfluorooctyltrichlorosilane (FOTS) to chemically modify the surface by adding fluorine end-functional atoms. This layer increased the output voltage by a factor of 12. The operation principle of the TENG is shown in Figure 2.21b. The contact-separation between the Ag yarn and the FOTS layer under repeated force lead to an alternating



current flow between the AgNWs layer and Ag yarn. A 5x5 array of the threads exhibited a power density of  $480 \text{ mW/m}^2$  under a compressive force of 10 N at 3 Hz. Although the size of the thread is fairly large, which is inappropriate for implementing in textiles, it provides a good concept for fibre-based TENG.

Cheng et al. designed a stretchable fibre-based TENG also with a core-shell structure [41]. The core fibre comprised a pre-stretched PU fibre coated with AgNWs and PTFE layer. The shell was made from a pre-stretched PDMS film coated with AgNWs. The device could harvest energy from various mechanical energy forms, such as stretching, bending, twisting and pressing. The maximum power of  $22.5 \text{ } \mu\text{W/m}^2$  was obtained when the fibre was twisted at a frequency of 1 Hz with a twisting angle of  $135^\circ$  and a load of 50 M $\Omega$ . Moreover, the device was demonstrated as a wearable self-powered healthcare monitoring sensors capable of detecting finger bending, walking, breathing, pulse and phonation.

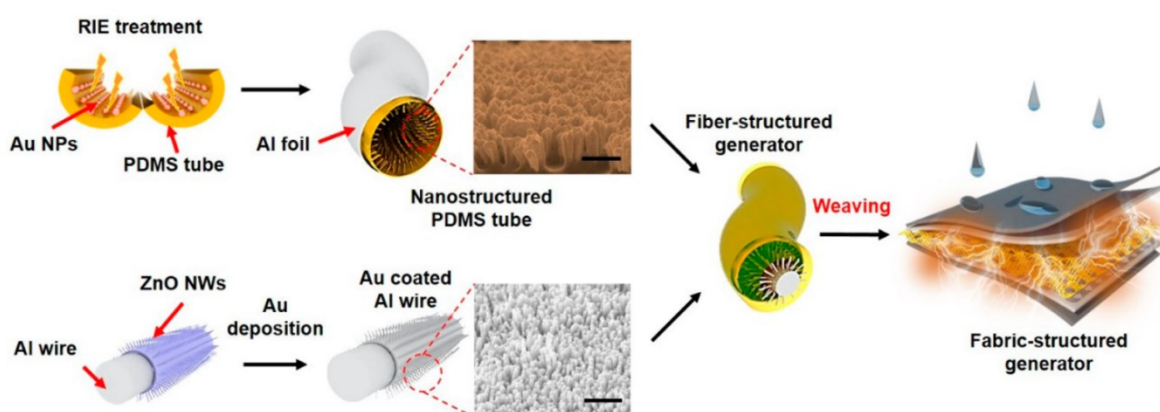


**Figure 2.22** Schematic diagrams of the fabrication process for the fibre-based TENG revealed by Kim et al. Reproduced with permission from Ref. [75]. Copyright 2015, American Chemical Society.

A surface modified fibre-based TENG was revealed by Kim et al. [75] which used nanostructure structures on both the outer surface of the core and the inner surface of the shell (Figure 2.22). First, the ZnO NWs were grown on Al wires by a hydrothermal process. Then, it was deposited with thin gold (Au) film using e-beam evaporation. The shell was made from PDMS tube, whose inner wall was etched using RIE forming NWs on the surface. The core was then manually inserted into the PDMS tube and the whole fibre was wrapped in Al foil. Finally, three fibres were assembled together to form weft and warp yarns, which were later woven together to produce a plain fabric. Under a periodic compressive force of 50 N, the T-TENG obtained an instantaneous power density of  $204 \text{ mW/m}^2$ , even in a high humidity environment of  $\sim 95\% \text{ RH}$ .

### 2.9.2.3 Multiple-thread fully-integrated TENG

Multiple-thread fully-integrated fibre-based TENGs require an interaction between at least two fibres to be able to harvest energy. Generally, each fibre will comprise an electrode and the T-ENG will operate in CS-mode, LS-mode or FT-mode. Because of the relative movement between the fibres, the electric potential is built up between the electrodes, as shown in Figure 2.23a. In 2014, the first fibre-based TENG was explored by Zhong et al [76]. It was composed of two modified cotton yarns twisted together. One was a CNT coated cotton thread (CCT), and the other was a PTFE and CNT coated cotton thread (PCCT). The fabrication process is illustrated in Figure 2.23b. A dipping and drying process was used to produce both the CCTs, where the cotton threads were coated with an MWCNT ink and the PCCTs, where the CCTs were coated with PTFE. Lastly, the CCT and PCCT were entangled together to double-spiral structure and then woven into a fabric. It was employed to harvest energy from finger bending and delivered an average power density of around  $1 \text{ mW/m}^2$ . After 90,000 operation cycles, only a minimal decrease in output current was observed, indicating a highly reliable power generator.

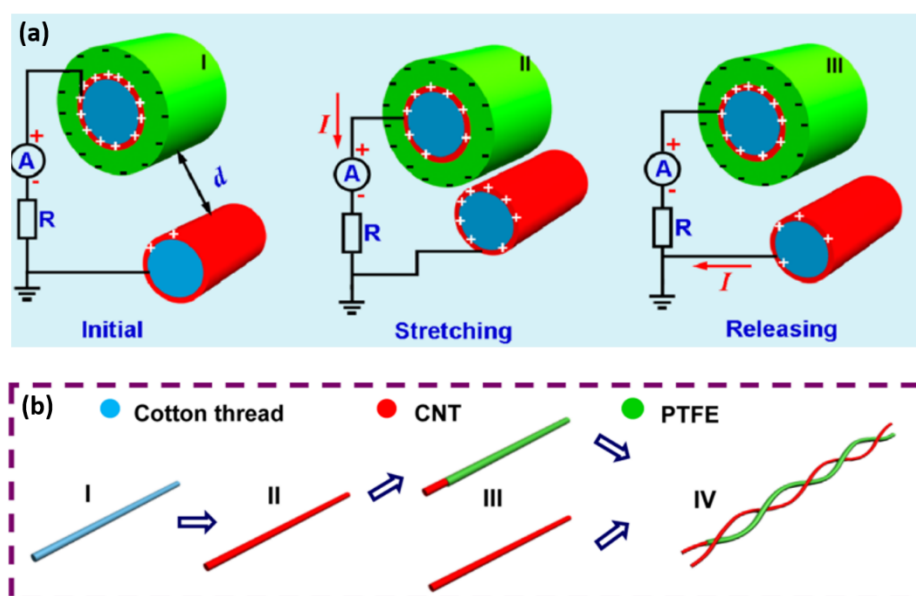


**Figure 2.23** (a) Power generation mechanism via contact-separation of multiple-thread fully-integrated TENG and (b) schematic illustration of the fabrication process. Reproduced with permission from Ref. [76]. Copyright 2014, American Chemical Society.

Another example of a multiple-thread fully-integrated TENG was presented by Zhao et al., in which all fibres interacted with each other [74]. As shown in Figure 2.24a, the TENG was constructed by plain-weaving 2-ply Cu-coated PET (Cu-PET) warp yarns and PI-coated Cu-PET (PI-Cu-PET) weft yarns together using an industrial weaving loom. Firstly, 1-ply Cu-PET yarns were prepared by depositing PET yarns using a polymer-assisted metal deposition method. To decrease the resistance to  $0.17 \text{ } \Omega/\text{cm}$ , the 1-ply Cu-PET yarns were spun into the 2-ply Cu-PET yarns. To produce the PI-Cu-PET yarns, the Cu-PET yarns were coated with PI precursor via the dipping and drying method. The

properties of the resultant yarns are quite similar to conventional industrial yarns and under cycled deformation, the contact area between weft and warp yarns changed leading to a varying charge distribution at yarn crisscross intersections, shown in Figure 2.24b. The maximum power densities of 23.86 under bending and 33.16 mW/m<sup>2</sup> under compression were observed. Furthermore, this design exhibited good durability and output power stability even after 1000 tapping cycles and 20 washing cycles.

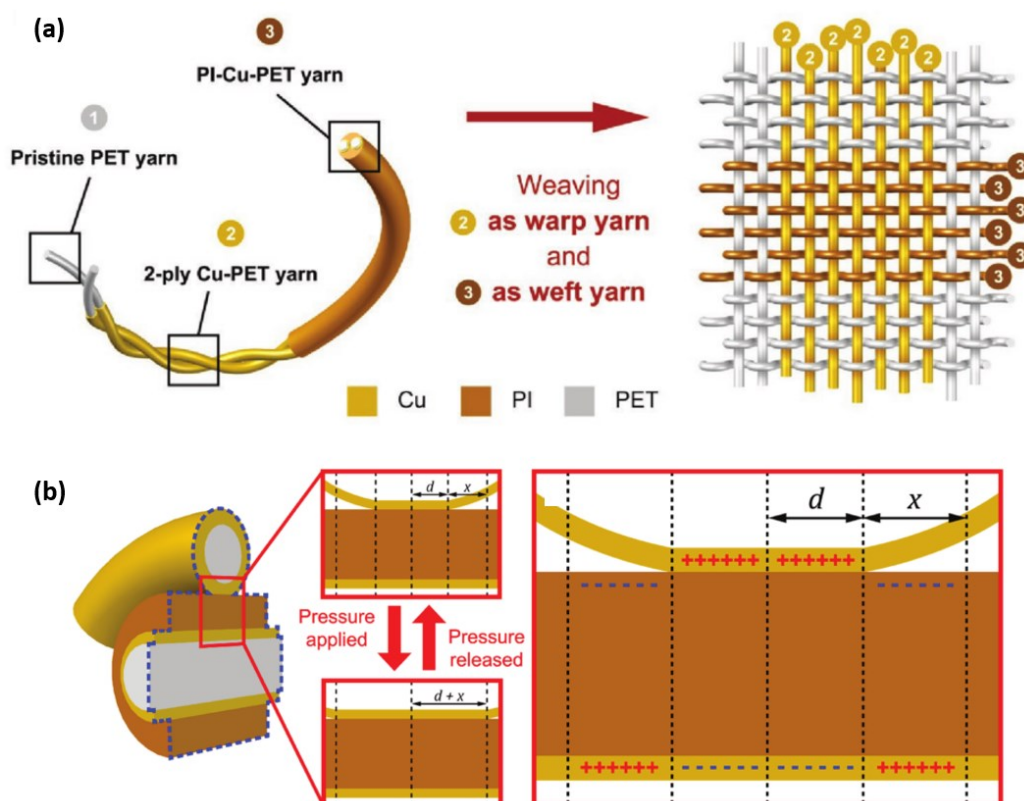


**Figure 2.24** (a) Schematic illustration of the fabrication process and structure of the T-TENG proposed by Zhao et al. and (b) the working principle of the T-TENG. Reprinted from Ref. [74]. Copyright 2016, with permission from John Wiley & Sons, Inc.

To increase the power output of fibre-based TENG, a 3D orthogonal woven TENG was invented by Dong et al [39]. As shown in Figure 2.25a, the generator comprised three stacks of yarns. The middle stack was created from conductive 3-ply-twisted SS/PE fibre blended yarns (weft yarns). The top and the bottom stacks were made from 3-ply-twisted SS/PE fibre blended yarns (warp yarns) coated with PDMS. The weft and warp yarns were not interlaced, but they were arranged perpendicularly to each other and bound by non-conductive Z-yarns. Under periodic tapping, an AC output was generated between the outer electrodes (top and bottom) and the middle electrodes. Figure 2.25b and c illustrate the frequency dependence of the  $V_{OC}$  and  $I_{SC}$ , respectively. The  $V_{OC}$  rises slightly at low frequency, then remains constant as the frequency increases, whereas the  $I_{SC}$  increases considerably with increasing frequency. At a tapping frequency

of 3 Hz, a power of 263.36 mW/m<sup>2</sup> was generated. Moreover, there was no significant decline in the performance after 10 washing cycles and 1500 tapping cycles.

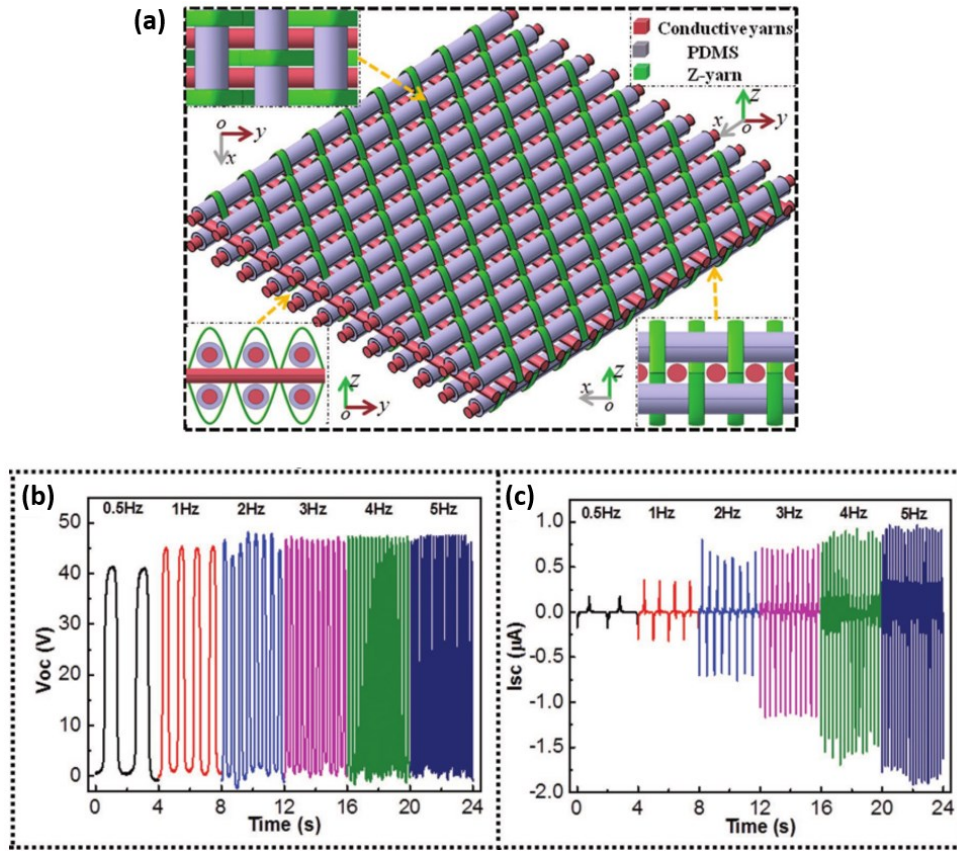


**Figure 2.25** (a) Schematic illustration of the structure of 3D orthogonal woven TENG. Frequency dependence of (b)  $V_{oc}$  and (c)  $I_{sc}$  of the TENG. Reprinted from Ref. [39]. Copyright 2017, with permission from John Wiley & Sons, Inc.

Another T-TENG was demonstrated by Chen et al. who developed a T-TENG by weaving cotton, carbon and PTFE wires on a traditional shuttle-flying weaving machine [140]. In the CS-mode, an alternating current is generated between the carbon wires due to the surface charge caused by the contact between the PTFE wires and the carbon wires, as shown in Figure 2.26a. Furthermore, they have found out that the dimensional features affecting the yarn-packing density, such as the PTFE diameter ( $d$ ) and the interval distance ( $h$ ) of the carbon wires (Figure 2.26b) influence the electrical output of the T-TENG. The results in Figure 2.26c and d reveal that the  $V_{oc}$  and the transferred charge decline with increasing  $d$  and  $h$ , since an increase in the PTFE diameter results in a reduction in the effective contact area and in the induction effect due to a thicker triboelectric layer. An increase in the interval distance of the carbon wires leads to a decrease in the induced charges. At a frequency of 5 Hz, the T-TENG with 3x3 cm<sup>2</sup> area delivers a  $V_{oc}$  of around 175 V and an  $I_{sc}$  of around 8  $\mu$ A.



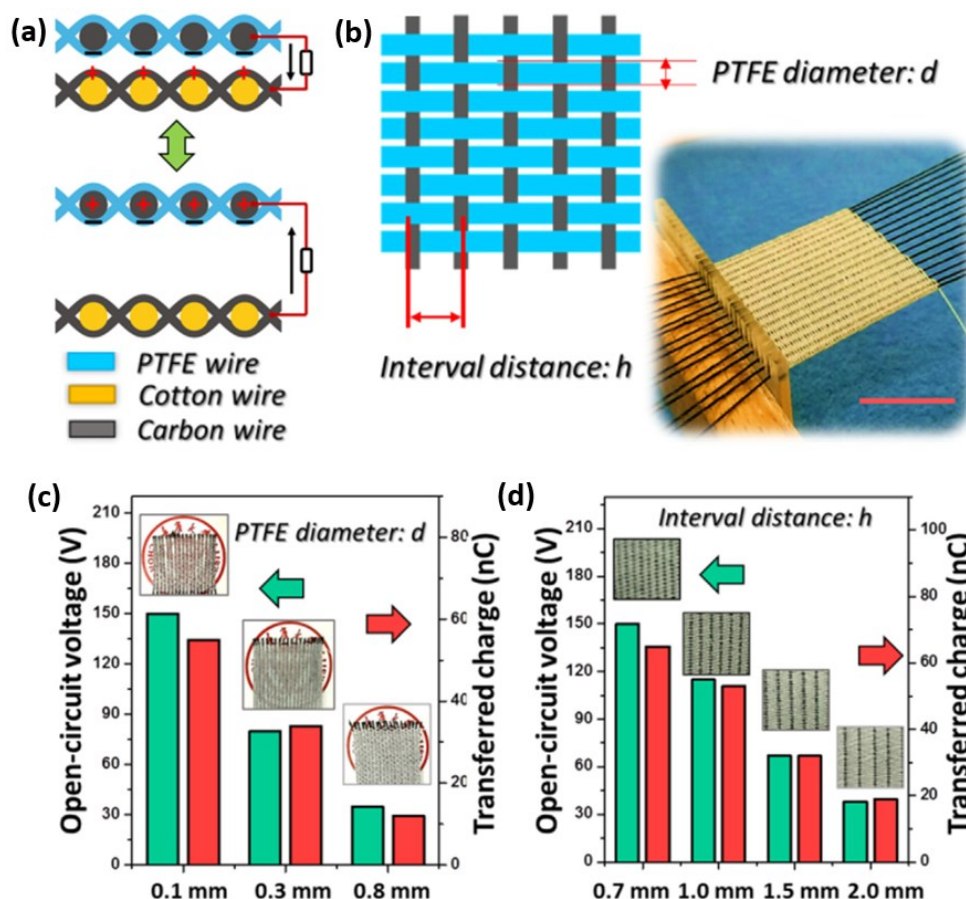


**Figure 2.26** (a) Power generation mechanism of the T-TENG proposed by Chen et al., (b) Schematic illustration of the woven structure (left side) and photograph (right side) of the T-TENG (scale bar: 2.5 cm), (c) dependence of the  $V_{OC}$  and the transferred charges on the PTFE diameter and (d) dependence of the  $V_{OC}$  and the transferred charges on the interval distance of the carbon wires. The insets show the photographs of the corresponding T-TENGs. Reprinted from Ref. [140]. Copyright 2018, with permission from Elsevier.

## 2.10 Discussion

Numerous T-TENGs have been demonstrated and are discussed in this section and it is clear triboelectric energy harvesting is well suited to textile-based energy harvesting applications. The various T-TENGs are summarised in Table 2.4 and Table 2.5, shown at the end of the chapter. However, it is clear there is a lack of standardisation in the methods and presentation of performance data. In 2015, Zi et al. proposed a structural figure-of-merit, which depends on the operation mode, and a material figure-of-merit, which is the square of the surface charge density [141]. This approach is not widely used because it is difficult to precisely measure the surface charge density. Instead of this, most papers give the electrical outputs of TENG, such as  $I_{SC}$ ,  $V_{OC}$  and quote an area power density. Typically, the values quoted are peak instantaneous values and the duration of the energy generating output is not discussed. There are several examples where TENGs have been used to blink light-emitting diodes (LEDs). In this case, peak outputs are of interest. However,

in most cases, the energy harvester output is conditioned and stored for use when the energy is required by the load electronics, which generally require continuous direct current (DC) power.

Furthermore, these parameters are influenced by various factors, including the humidity, the thickness, the operation frequency, and the contact force, and this detail is often not provided in the literature. For example, the output performance of TENGs is significantly degraded under high humidity condition [75], [142], [143]. Secondly, TENGs with a larger thickness (e.g. more stacks) deliver a higher area power density [15], [69]. Thirdly, a higher operation frequency leads to a higher power output since  $I_{SC}$  increased with frequency, whilst  $V_{OC}$  remained constant [39], [118], [120], [138]. Lastly, the output power increases with increasing contact force until it saturates at a certain force, at which point the effective contact area cannot be further increased [15], [89], [119]. Figure 2.27 shows the contact force dependence of the output voltage and current of a T-TENG operating in CS-mode [15]. The output can be divided into three regions: R(i) steep increase region, R(ii) linear increase region and R(iii) saturation region. Another important parameter missing from most papers is the energy conversion efficiency. As mentioned above, it is obvious that with increasing frequency and force, the output power of the TENG rises, since the input power to the system increases. Because of this, it is more expedient to look at the ratio between the input and the output power through the system using Root Mean Square (RMS) values over a given period of time instead of only the instantaneous peak power output.

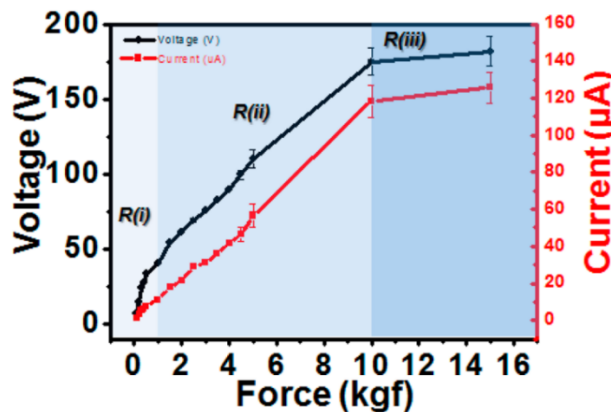


**Figure 2.27** Contact force dependence of the output voltage and current of the T-TENG operating in CS-mode proposed by Seung et al. [15].

When comparing the performance of the various T-TENGs given the data available, the peak power density of the fibre-based and the fabric-based devices range from 22.5 nW/m<sup>2</sup> to 953 mW/m<sup>2</sup> and from 1.25 to 8,920 mW/m<sup>2</sup> respectively. The reason why the most fibre-based TENGs tend to produce lower power density compared to the fabric-based TENG could be due to the complexity of the fabrication process. The fabrication of the fabric-based TENGs is less complex and do not require high precision, thus it is easier to perform additional processes, which help improve their output performance. Compared to bulk TENGs with a record power density of 500 W/m<sup>2</sup> [81],

the outputs of T-TENGs are relatively low. One of the main reasons could be a reduction in effective contact area caused by the uneven surface of the textile related to the manufacturing technique used for interlacing the weft and warp yarns. It should be noted that the previous evaluation excludes a paper that claimed an unusually high power density of  $336 \text{ W/m}^2$  [14] at an external load resistance of  $20 \Omega$ , which is very low compared to other papers with a typical load value in an order of  $\text{M}\Omega$ . Also, the claimed current density used to calculate the power density is not in good agreement with the output currents, which are only about  $78 \mu\text{A}$ .

TENGs typically generate a relatively high voltage, which can reach several hundred volts, but very low current in a level of  $\mu\text{A}$ . Moreover, the claimed maximum power densities were obtained at the external load resistance in an order of  $\text{M}\Omega$ . However, in the real application of TENGs, the load resistance of the circuit is much lower and the desired operating voltage is in the range of a few volts. This disparity requires the use of a power conditioning circuit, typically combined with some form of storage. Recently, Xi et al. has proposed a universal power management strategy and achieved an energy conversion efficiency of 85% using a DC buck converter and a power management module [144]. Another power conditioning circuit demonstrated the use of Bennet's doubler circuit, which claims to exponentially boost the output energy of TENGs compared to standard diode bridge circuits [145]. Another approach to reduce this problem is to integrate many small TENGs together to increase the current instead of using a single large size TENG. Concerning the energy storage for T-TENGs, many research groups have developed textile-based supercapacitor, which can successfully be integrated with the T-TENG [94], [138], [146] and solve the problem of alternate and unstable power output in the real operation [147]. Given the requirements of practical applications, another method for presenting performance data should be the time taken to charge up a suitable capacitor given a specified mechanical input. This would provide a more complete picture of the energy harvesting potential of a given TENG design and factor in losses at the power conditioning stage.

Due to a wide range of material choices, operating modes and structural designs, T-TENGs have been found in many applications. Most power generation applications involve driving LEDs for lighting, decoration or signalling, such as a wearable night-time warning indicator for pedestrians [85]. T-TENGs have been used to charge a battery [83] or capacitor [138] and power various wearable and portable devices, such as a cell phone [106], calculator, digital watch [117] and wireless systems [38]. For sensing applications, several types of self-powered sensors have been demonstrated, typically in force and strain sensing to monitor motion [39], pressure [40] and personal health [41]. In addition to wearable, there is a clear potential to utilise T-TENGs in other applications that use textiles. For example, to harvest energy from foot traffic using a triboelectric carpet or for self-powered sensing of seat occupancy in car interiors.

Towards a practical implementation of T-TENGs, it is important that the properties of textile remain the same after implementing the T-TENG. Since T-TENGs can be realised using functional yarns, these can be woven or knitted into standard textile structures and have minimal impact on fabric properties. In the case of fabric-based TENGs, thin layers of flexible materials can be used to realize the TENG without affecting the mechanical properties of the textile [148]. Thanks to the nature of textile structures, most T-TENGs are therefore inherently flexible and some of them are stretchable [41], [118], [137]. One challenge of T-TENGs is that their appearance is often not aesthetically pleasing since the applied coatings will alter the appearance of the fabric. Coatings could potentially reduce breathability depending upon the coating thickness and area affected. Durability and washability are also crucial for T-TENG, since normal clothes should be able to withstand detergents, washing, drying and ironing. Fibre-based TENGs have been demonstrated that they can withstand 20 standardised washes [74] or even 120 washes if protected by placing in a laundry bag [91]. However, most papers do not consider washability properly. Additional washing issues include untwisting of yarns, materials abrasion and pilling, shrinkage, wrinkling and drying capability. Given that TENGs operate on frictional contact between two materials, the abrasion of the textile cannot be neglected and standard textile abrasion tests should be performed to quantify device lifetimes. Another approach to avoid abrasion is to design the T-TENGs to operate in the FT-mode, which experience less friction compared to other modes. Finally, the ability to tailor a fabric is highly desirable for the end production of garments, since industrial fabrics are produced in a long roll or material. Yu et al. demonstrated a T-TENG that can be cut in half with each piece retaining almost half of the original output. After sewing them together, the T-TENG returns to nearly full output [91]. This demonstrated T-TENG textiles can in principle be tailored but the electrodes will have to be manually reconnected and that will require extra time and work.

The majority of published work focus on enhancing the performance of T-TENGs and complex and sophisticated fabrication techniques have been demonstrated that are often not suitable for scaling-up and mass production. Many examples of surface modification require expensive equipment, the size of samples are limited and process are incompatible with roll-to-roll fabrication processes typically associated with textiles. More recently, research has tended to focus on fibre-based TENGs, which can be fabricated in a manner compatible with standard textile manufacturing processes and maintain the properties of a standard yarn. However, this type of T-TENGs exhibits fairly low power outputs. The next-generation of fibre-based TENGs will be fully-integrated in the textile and exhibit improved electrical and mechanical properties compared with the current state of the art. Furthermore, the nascent work on T-TENGs co-located in a fabric alongside energy storage devices such as supercapacitor yarns shows great promise for realising textile power modules for multiple applications.



## 2.11 Conclusion

This section has provided a background theory of TENGs and a review of textile-based TENGs (T-TENGs). The triboelectric effect is also known as triboelectricity. It is a type of contact electrification, in which electrical charges are separated and transferred from one material to the other material after they are brought into physical contact. It is believed that the effect involves electron transfer, ion transfer and/or mass transfer. However, it has been recently proposed that it is an electron-dominated transition process. The triboelectric materials are sorted in a list by their tendency to lose or gain electrons called triboelectric series. A material at the top of the list will lose electrons and become positively charged when contacts with a material at the bottom of the list that will receive electrons and become negatively charged. The further apart in the list the two materials are, the greater is the electron transfer. Depending on different configurations of the triboelectric materials and the electrodes, and their relative movement, the fundamental operation modes of TENG can be categorised into the four modes, namely, vertical contact-separation mode (CS-mode), lateral sliding mode (LS-mode), single-electrode mode (SE-mode) and freestanding triboelectric-layer mode (FT-mode).

With respect to the structure, T-TENGs can be classified into two main groups, namely fabric-based TENG and fibre-based TENG. Fabrics can be used directly as a triboelectric material but more often they only serve as substrates for other materials that possess better triboelectric properties. The fibre-based TENGs are made of interlacing fibres, which are typically fabricated in a core-shell structure. Most examples of T-TENGs are operated in the CS-mode because of the high power output, the simplicity of the fabrication and the nature of human motion, such as footsteps, hand tapping and joint movements that can be coupled to the T-TENG through compressing, stretching or twisting. Concerning the performance of T-TENGs, their power densities are relatively low compared to bulk TENG because of a decrease in their effective contact area relating to their structure. Due to the complexity of the fabrication process, most fibre-based TENGs tend to exhibit lower power density compared to the fabric-based TENGs. The peak power density of the fibre-based and the fabric-based devices vary from  $22.5 \mu\text{W}/\text{m}^2$  to  $953 \text{ mW}/\text{m}^2$  and from  $1.25 \text{ mW}/\text{m}^2$  to  $8,920 \text{ mW}/\text{m}^2$ , respectively. Apart from performance, the main challenge relating to the implementation of the T-TENG is maintaining the properties of the conventional textile and the use of processes compatible with standard large-scale textile manufacturing. Some processes have been demonstrated that are familiar to the textile industry such as the use of a commercial machine to twist dielectric fibres around conductive fibres resulting in core-shell yarns, which could be afterwards woven or knitted into a fabric. Whilst many novel and interesting textile implementations have been demonstrated with significant peak power outputs, judging the practical power output is not straightforward. This would be aided by the use of RMS values and a

discussion around the practical factors that can affect the power output, such as the humidity. Other important parameters are often missing from the literature such as thickness, test frequency and the contact force. The durability of some devices also appears promising with tens of thousands of operating cycles having been demonstrated. Given suitable rigorous characterisation of performance and lifetime, T-TENGs may well offer a practical approach for energy harvesting for textile-based applications. Additionally, an interesting gap in the literature, which can be focused on, is the fabrication of the FT-mode pnG-TENG using processes that are compatible with the standard textile manufacturing and finding appropriate methods to evaluate its performance.

**Table 2.4** Summary of important parameters of fabric-based TENGs.

Mode	Triboelectric material	Electrode	Substrate	Surface modification	Area (cm <sup>2</sup> )	Frequency (Hz)	Force (N)	Voltage (V)	Current (μA)	Power density (mW/m <sup>2</sup> )	Durability Test (cycles)	Washability Test (times)	Refs
FCS	Nylon, PE and acrylic	Ag	-	-	125.4	-	-	95	2.5	-	-	-	[93]
CS	Nylon and PTFE	MWCNT, PEDOT:PSS And CF	-	-	17.35	-	-	109.6	0.35	8	-	-	[70]
LS	Nylon and Dacron	Cu foil	Cotton	-	588	43(Grating)	30	2000	200	-	5,400	Washable	[83]
SE	Nylon and FEP	Ag	Nylon	-	16	5	-	22	2	46.5	24,000	Washable	[85]
SE	Fabrics and PDMS	CNT	Cotton	-	16	8	-	200	0.6	37.5	170,000	-	[38]
SE	Al, fabrics and PDMS	Al	-	FOTS-SAM	6	1.25	3	105	27	1,800	20,000	-	[87]
SE	PDMS and fabrics	Graphene	PET	NWs and Plasma treatments	9	-	72	47.1	7	144	-	-	[119]
CS	Nylon and PTFE	Graphene	Nylon	-	3	1	-	3.5	0.28	53.3	-	-	[120]
CS	Nylon and elastomer	Ag	PET	Cu NPs	16	-	60	470	26	7500	3000	-	[129]
CS	Silk and SR	Sn/Cu/Ag	Nylon	-	15	4	2	28.13	2.71	166	-	-	[137]
LS, CS	PU/Al and PI/PDMS	Carbon	Fabric	-	45	1.5	2	33	0.25	1.8	-	-	[82]
CS, FCS,LS	Ni and parylene	Ni	PE	-	25	0.7	-	50	4	393.7	-	Washable	[92]
CS	CF and PVDF	CF	Fabric	Nano-structured	30	1.8	-	210	45	700	-	-	[66]

CS	PET and PDMS	Ag and CNT	PET	Pyramids	25	1	400	500	20	153.8	3,000	-	[67]
CS	PET and FAS	Al foil and AgNW	Nylon	-	9	1.8	-	575	12.1	2,770	12,000	-	[68]
CS	Ni and PDMS	Ni	PET	-	6.25	0.5	35-40	23.39	0.39	1.25	-	-	[69]
CS	Ag and PDMS	Ag	Fabric	ZnO NWs	-	-	100	170	120	-	12,000	-	[15]
FT	Ni/Parylene	Ni	PE	-	22	500(Grating)	-	105	55	3200	1200	Washable	[90]
FCS	Ni and SR	Ni	PE	-	25	3	300	540	140	8,920	100,000	-	[37]
CS	Silk and PVDF	CF	Fabric	Nanofibre	8	2	25.7	500	12	3100	10000	-	[104]
CS	PU and PDMS	CF and carbon-based PU	Fabric	-	133	1.6	760	1468 RMS(566)	25.4 RMS(5.9)	356.6 RMS(135.1)	-	-	[108]
SE	Al NPs and PDMS	AlNPs	Fabric	NPs, NWs	49	1.2	-	250	78	336,000	-	-	[14]
SE	PTFE and CNT	CNT	Cotton	-	20	7	-	100	2	121	10,000	5	[146]

**Table 2.5** Summary of important parameters of fibre-based TENGs

Mode	Triboelectric material	Electrode	Substrate	Surface modification	Area (cm <sup>2</sup> )	Frequency (Hz)	Force (N)	Voltage (V)	Current (μA)	Power density (mW/m <sup>2</sup> )	Durability Test (cycles)	Washability Test (times)	Refs
CS	Ag and PVDF-TrFE	Ag	PU	-	-	10	-	0.024	-	-	10,000	-	[72]
SE	Skin and PTFE/PDMS	Graphene /PDMS	-	-	-	1	10	7	-	-	-	-	[139]
SE	SR and Nitrile glove	Organogel	-	-	36	3	50	40	1.98	-	10,000	Washable	[128]
SE	Skin and SR	SS	fabric	-	146.7	-	-	200	200	953	-	-	[89]
SE, CS, FT	PU and PE	SS	-	-	36	-	-	75	1.2	60	5 h, 8 cm/s	120	[91]

CS	ZnO and PDMS	SS	-	NWs and NPs	2.52	-	-	140.4	21.54	1.2	1,000	-	[134]
SE	Acrylic and SR	SS	-	-	16	3	11	150	0.96	85	50,000	15	[138]
SE	Nylon and PDMS	Cu	Carbon fibre	-	1.08	2	-	23	0.3	42.6	-	-	[40]
CS	Au and PDMS	Al wire and Al foil	-	NWs	196	10	50	40	210	204	-	-	[75]
CS	AgNWs and PTFE	Ag NW	PDMS and PU	AgNWs	-	1	0.05	0.66	0.02	0.0225	4,000	-	[41]
CS	Nylon and SR	Metal wire	PDMS	-	-	0.5	-	4	0.08	1.3	1,600	-	[77]
CS	Ni and SR	Ni and CNTs	SR	-	18.85	3	300	380	11	869	21600	-	[107]
CS	Ag and SR	AgNWs and Ag yarn	-	FOTS	36	3	10	37	36	480	8,000	-	[116]
CS	Cu and SR	Cu and CNT	-	-	-	2	-	142.8	7.38	15	10,800	-	[118]
CS	CNT and PTFE	CNT	Cotton	-	-	5	-	-	0.01122	1	90,000	-	[76]
CS	Cu and PI	Cu	PET	-	24	10 cm/s	-	4.98	37.2	33.16	1,000	20	[74]
CS	SS and PDMS	SS	PE	-	18	3	-	45	9.9	263.36	1,500	10	[39]
CS	Ag and PTFE	Ag	-	-	100	3.3	-	RMS(23.5)	RMS(1.05)	RMS(6)	-	-	[105]
CS	Cu and PTFE	Cu	-	-	16	-	-	18	0.9	-	-	-	[106]
CS, FT	Carbon and PTFE	Carbon	Cotton	-	9	5	-	175	8	-	36000	-	[140]
FCS	PVDF-TrFE and PA66	SS	-	-	25	3	200	96	8.5	93	20000	5	[95]



## Chapter 3 Fundamental Experiments

### 3.1 Introduction

To gather essential information before starting to design the T-TENGs shown in Chapter 4 and Chapter 5, many fundamental experiments need to be initially performed. Firstly, simple sliding FT-mode TENGs were built including a bespoke linear actuator for performing electrical measurements. Next, the TENG with different triboelectric materials and electrodes were investigated to find some appropriate triboelectric materials for the fabrication of the T-TENGs. Their triboelectric properties, such as open-circuit voltage ( $V_{OC}$ ), short-circuit current ( $I_{SC}$ ) and surface charge density ( $\rho_q$ ) were measured and compared. After that, factors influencing the output performance of TENGs were studied. These experiments include frequency dependence measurement, contact force dependence measurement, humidity dependence measurement and temperature dependence measurement. Finally, since TENGs usually produce alternating electrical outputs, a rectifier circuit is required. Therefore, different rectifier circuits, including full-wave bridge rectifier, half-wave bridge rectifier and Bennet's doubler rectifier were also investigated with the aid of simulations and experiments.

### 3.2 Investigation of triboelectric materials

To evaluate potential materials for building the T-TENGs, simple sliding FT-mode TENGs with different triboelectric materials were firstly fabricated. The triboelectric materials were rubbed against two types of metal electrodes, aluminium (Al) and silver (Ag), using a self-designed linear actuator and the electrical outputs ( $V_{OC}$ ,  $I_{SC}$  and  $\rho_q$ ) were measured and compared. The names of all materials, the abbreviations, the thicknesses and the suppliers are listed in Table 3.1 following the sequence in the triboelectric series from the most positive material to the most negative material. In this project, flexible polymers, flexible metal electrodes and textile-based materials were focused on because of their flexibility, low weight, cost, biocompatibility and feasibility. Al adhesive tape and PVC coated polyester fabric (PVC fabric) screen-printed with Ag were simultaneously used as both electrodes and triboelectric materials, whereas the other materials serve only as triboelectric materials.

**Table 3.1** Details of the triboelectric materials used in this thesis.

Material	Abbreviation	Thickness ( $\mu\text{m}$ )	Supplier
1. Polyurethane interface	PU interface	159	Smart Fabric Inks Ltd
2. Polyurethane-coated Nylon fabric	PU coated Nylon	76	Emmakites
3. Nylon fabric	Nylon fabric	127	Hemline
4. Nylon sheet	Nylon sheet	254	CS Hyde
5. Silk fabric	Silk	137	Fabric land
6. Aluminium adhesive tape	Al	51	Thermawrap
7. Cotton fabric	Cotton	180	Fabric land
8. Silver polymer ink	Ag	51	Smart Fabric Inks Ltd
9. Polyethylene terephthalate film	PET film	76	Dupont
10. PU heat transfer vinyl	PU HTV	80	HOHO Industry
11. Polyester film	PE film	127	Polybag
12. Polyimide film	Kapton	76	Dupont
13. PVC coated polyester fabric	PVC fabric	450	VALMEX FR 7546
14. PVC heat transfer vinyl	PVC HTV	160	HOHO Industry
15. Polyvinyl chloride film	PVC film	254	HXSS
16. Polytetrafluoroethylene film	PTFE film	76	CS Hyde
17. PTFE coated fibreglass fabric	PTFE fabric	127	Xinghoo

### 3.2.1 Design and methodology

#### 3.2.1.1 Fabrication

For the materials evaluation measurement, simple sliding FT-mode TENGs with freestanding upper substrates comprising the triboelectric materials and lower substrates comprising two electrodes were fabricated. The rectangular upper substrate with a size of  $46 \times 70 \text{ mm}^2$  was made of stacks of a 3-mm-thick acrylic, a double-sided tape, a 1-mm-thick fabric, a double-sided tape and the triboelectric materials, as shown in Figure 3.1a. The rectangular lower substrate with a size of  $100 \times 70 \text{ mm}$  was made of a 3-mm-thick acrylic fully covered by two strips of metal (Al tape or Ag screen-printed PVC fabric) with a gap of 0.5 mm between the strips, as shown in Figure 3.1b). These two strips serve as the two electrodes of the FT-mode TENG. The fabrication of Ag screen-printed PVC fabric will be fully revealed in Section 4.2.1. The Al tape is used here because it is a simple way to fabricate the electrodes and it can provide a very quick overview of results.



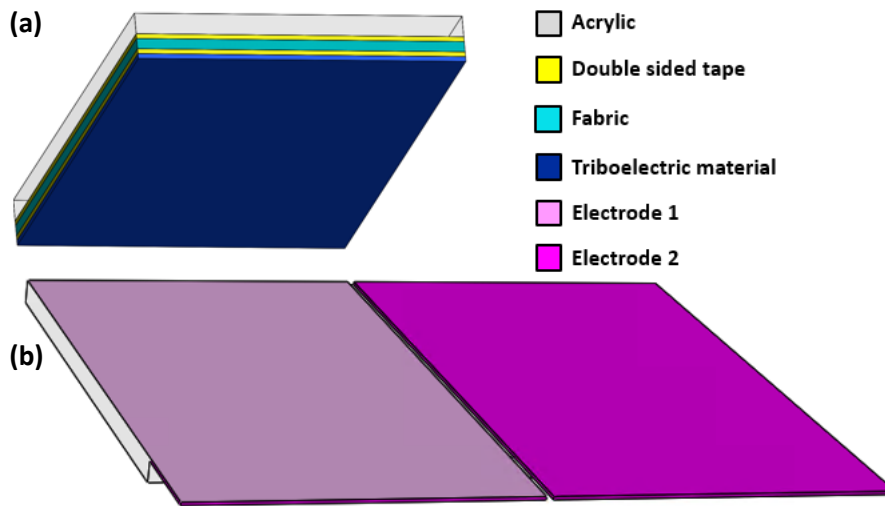


**Figure 3.1** Schematic illustration of (a) upper and (b) lower substrate of simple FT-mode TENG.

### 3.2.1.2 Measurement system

To obtain scientific measurement results and to assure the repeatability of the experiments, measurement systems were designed to eliminate the uncertainty factors and to keep all parameters as constant as possible. The parameters, which can significantly affect the outputs of TENG, are, for example, the contact force, the operating frequency, and the moving direction. A belt-driven linear actuator was built to generate lateral sliding between the upper substrate and the lower substrate. It consists of a v-slot linear rail with a length of 50 cm, a NEMA17 stepper motor, a GT2 timing belt, a v-slot gantry plate with four wheels, a 3D-printed lower stage, four pillars and a  $\mu$ -stepper controller board, as shown in Figure 3.2.

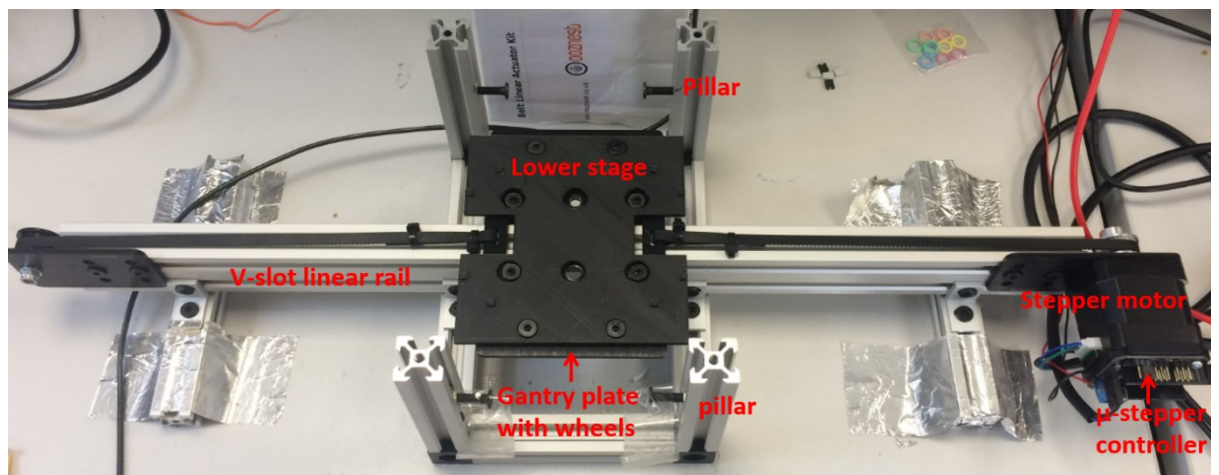


**Figure 3.2** Photograph of belt-driven linear actuator consisting of a v-slot linear rail, a stepper motor, a v-slot gantry plate with 4 wheels, a 3D-printed lower stage, 4 pillars and a  $\mu$ -stepper controller board.

During the measurements, the lower substrate was fixed to the lower stage (Figure 3.3a), which can be horizontally moved by the stepper motor. The upper substrate was fixed to a 3D-

printed upper stage and a stage holder made of an acrylic sheet (Figure 3.3b). The stage holder was placed between the four pillars so that the upper substrate and the lower substrate were faced and contact with each other. With this configuration, the lower substrate can horizontally move along the belt, while the upper substrate is horizontally fixed but can freely move in the vertical direction. This enables the control of the contact force by a weight laid over the stage holder and the lateral sliding between the triboelectric material and the metal electrodes along the belt direction. The schematic illustration of the measurement system is revealed in Figure 3.4. The oscillation frequency, speed and travel distance of the lower stage can be controlled by the Arduino-based  $\mu$ -stepper controller board. The codes and parameters for Arduino can be found in Appendix A.

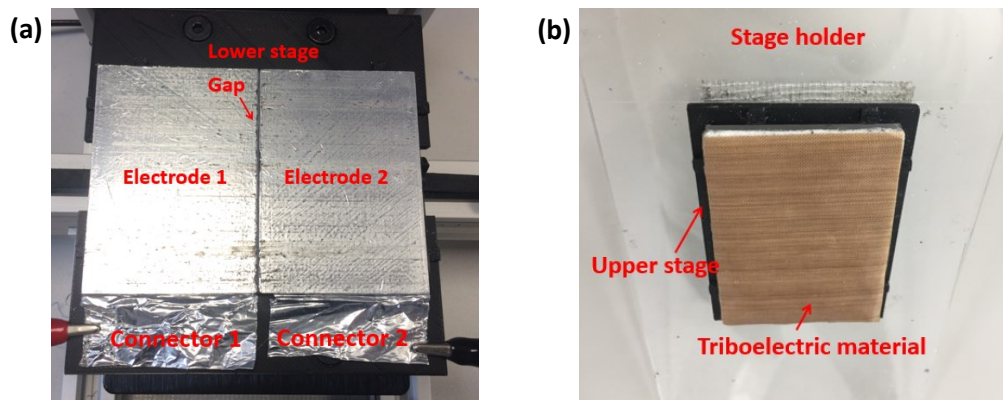


**Figure 3.3** Photograph of (a) lower substrate with two metal electrodes fixed on the lower stage and (b) upper substrate with a triboelectric material fixed under the upper stage and acrylic stage holder.

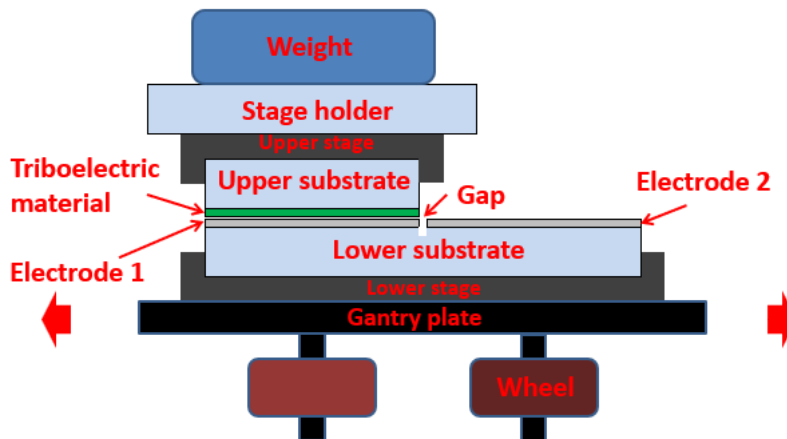


**Figure 3.4** Cross-section view of measurement system for simple sliding FT-mode TENG. Lower substrate is driven by a stepper motor and moves horizontally relative to upper substrate, which is fixed by four pillars.

### 3.2.1.3 $V_{OC}$ and $I_{SC}$ measurements

$V_{OC}$  and  $I_{SC}$  measurements were performed using the linear actuator placed in an environmental chamber (Weiss Technik WKL100) at an oscillation frequency of 2 Hz, a travel

distance of the lower substrate of 48 mm, a contact force of 5 N, a temperature of around 25 °C and a humidity of around 25 %RH. When the electrical outputs of the TENGs between the two electrodes stayed constant, the zero to peak and RMS values of  $V_{OC}$  and  $I_{SC}$  of the TENGs with the different triboelectric materials were recorded and compared. The two types of metal electrodes used in this project are Al adhesive tape and Ag screen-printed PVC fabric. The  $V_{OC}$  measurements were carried out using an oscilloscope (Agilent DSO3062A) with a 10-M $\Omega$  probe. To increase the load of the system, a 1-G $\Omega$  resistor was connected in series with the probe and then across the TENGs. Thus, the recorded output voltages from the oscilloscope were multiplied by a factor of 101 to obtain the true  $V_{OC}$  of the TENGs according to the voltage divider principle. The  $I_{SC}$  measurements were performed using a DC power analyser (Agilent N6705B) by connecting it in series with the TENG, as shown in Figure 3.5. It is to note that 3 TENGs were built and tested, and the best output is presented in the following experimental result section.

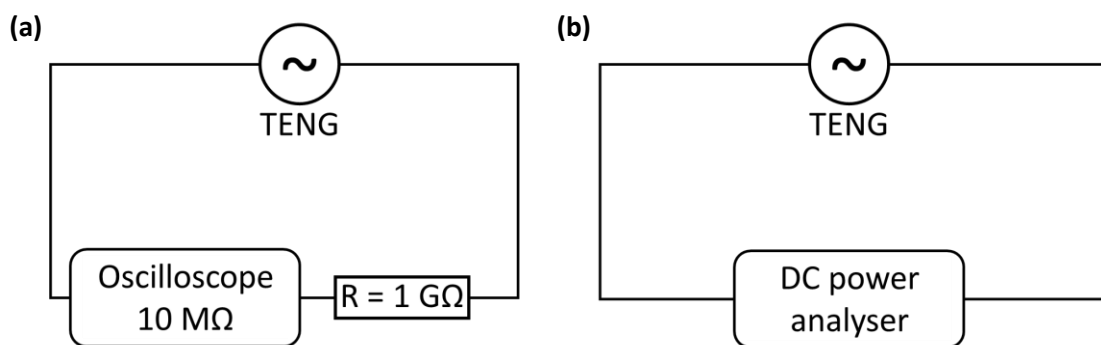


**Figure 3.5** Equivalent circuit for measuring (a)  $V_{OC}$  and (b)  $I_{SC}$  of TENGs.

#### 3.2.1.4 Surface charge density ( $\rho_s$ ) measurement

To measure the surface charge density of the triboelectric materials, the triboelectric materials were rubbed against the electrodes using the linear actuator placed in the environmental chamber at an oscillation frequency of 2 Hz, a travel distance of the lower substrate of 48 mm, a contact force of 5 N, a temperature of around 25 °C and a humidity of around 25 %RH. The  $V_{OC}$  of the TENGs were monitored using the oscilloscope. When the  $V_{OC}$  stayed constant, the triboelectric materials were removed from the upper stage and immediately put in a Faraday's cup which was connected to an electrometer (Keithley 6514), shown in Figure 3.6a. The Faraday's cup is composed of an inner and outer conductive cup, which serves as an inner and outer electrode, shown in Figure 3.6b. The inner and outer cup are connected to the electrometer and is separated from the outer cup by an insulator. When the charged triboelectric material is put into the inner cup, the same quantity of charges with the opposite polarity will be transferred from the outer cup through the electrometer to the inner cup. The amount of transferred charge is equal to the charge on the surface of the triboelectric material and can be measured via the electrometer.

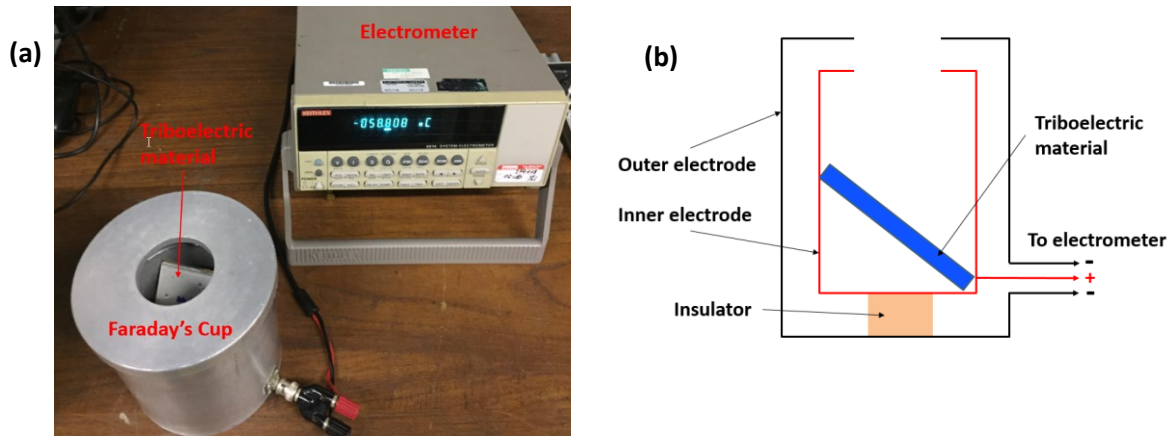


**Figure 3.6** Surface charge density measurement system. (a) Photograph of Faraday's cup connected to an electrometer and (b) schematic illustration of Faraday's cup.

### 3.2.2 Results and discussion

#### 3.2.2.1 $V_{OC}$ and $I_{SC}$ measurements

Figure 3.7a and b show zero to peak values and RMS values of  $V_{OC}$  and  $I_{SC}$  of the simple FT-mode TENGs for the different triboelectric materials rubbed against Al, respectively. According to the triboelectric series shown in Table 2.1, the position of Al is located between silk and cotton. Therefore, the first 6 materials on the left of the bar chart (PUs, nylons and silk) become positively charged when contacting with Al, while the rest of the materials become negatively charged. Similarly, Figure 3.8a and b show zero to peak values and RMS values of  $V_{OC}$  and  $I_{SC}$  of the simple FT-mode TENGs for the different triboelectric materials rubbed against Ag, respectively. The position of Ag lies between cotton and PET, thus the first 7 materials on the left of the bar chart (PUs, nylons, silk and cotton) become positively charged when contacting with Ag, while the rest of the materials become negatively charged. The polarity of the materials can be determined by the direction of the  $V_{OC}$  and  $I_{SC}$  peaks relating to the position of the triboelectric materials and the positive electrode. For example, if the triboelectric material is positively charged and moves over the electrode connected to the positive probe of the oscilloscope, electrons will be attracted to this electrode resulting in a current flowing from the positive probe to the negative probe and thus a positive output peak is generated. The result shows that the triboelectric polarities for all materials are in good agreement with the positions in the triboelectric series.

Regarding the level of the electrical outputs with respect to Al, the TENG with PTFE fabric produces the maximum outputs with a peak  $V_{OC}$ , peak  $I_{SC}$ , RMS  $V_{OC}$  and RMS  $I_{SC}$  of 717 V, 1.61  $\mu$ A, 486 V and 0.93  $\mu$ A, respectively, followed by PVC HTV and PVC film with almost the same peak outputs. Focusing on the positive materials, the TENG with nylon sheet generates the maximum outputs with a peak  $V_{OC}$ , peak  $I_{SC}$ , RMS  $V_{OC}$  and RMS  $I_{SC}$  of 677 V, 1.57  $\mu$ A, 437 V and 0.64  $\mu$ A,

respectively. Regarding the level of the electrical outputs with respect to Ag, the TENG with PTFE fabric still produces the maximum outputs with a peak  $V_{OC}$ , peak  $I_{SC}$ , RMS  $V_{OC}$  and RMS  $I_{SC}$  of 879 V, 1.95  $\mu$ A, 631 V and 1.24  $\mu$ A, respectively, followed by PVC HTV, while the most positive material is nylon sheet with a peak  $V_{OC}$ , peak  $I_{SC}$ , RMS  $V_{OC}$  and RMS  $I_{SC}$  of 929 V, 1.74  $\mu$ A, 629 V and 1.00  $\mu$ A, respectively. However, considering the feasibility of the T-TENG fabrication, the PTFE fabric and nylon fabric are the best candidates for the T-TENGs materials because firstly, they are made of fabric with good textile properties, such as lightweight, flexibility and washability. Secondly, they are quite thin and have the same thickness, which causes no height difference in surface topology when they are integrated, and thirdly they exhibit high outputs. Despite the highest positive outputs, nylon sheet is inappropriate for T-TENG because it is quite thick and not so flexible. Other potential materials are PU HTV and PVC HTV because of their compatibility with textile manufacturing and the high outputs.

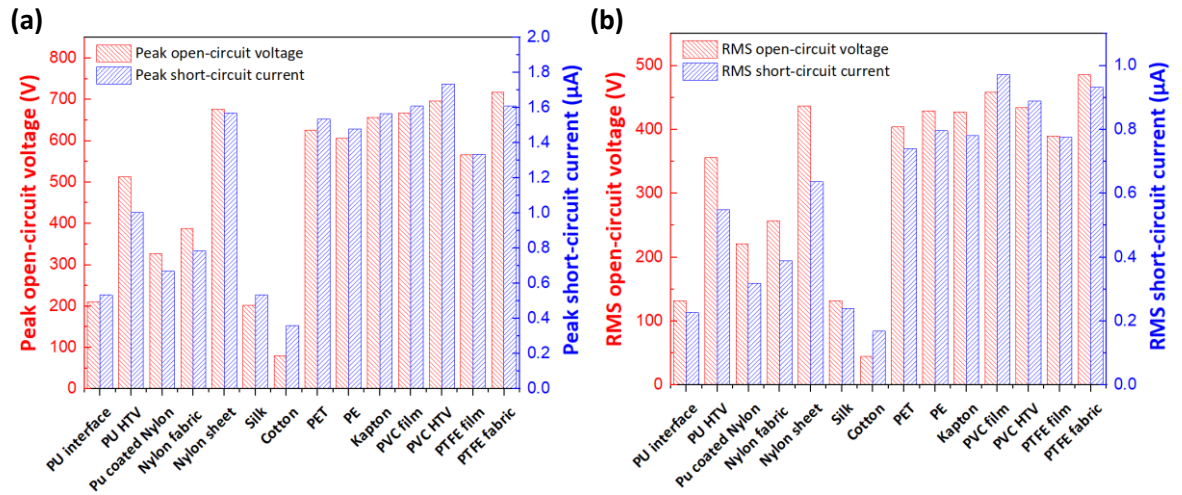


**Figure 3.7** (a) Peak and (b) RMS values of  $V_{OC}$  and  $I_{SC}$  of simple FT-mode TENGs for different triboelectric materials rubbed against Al.

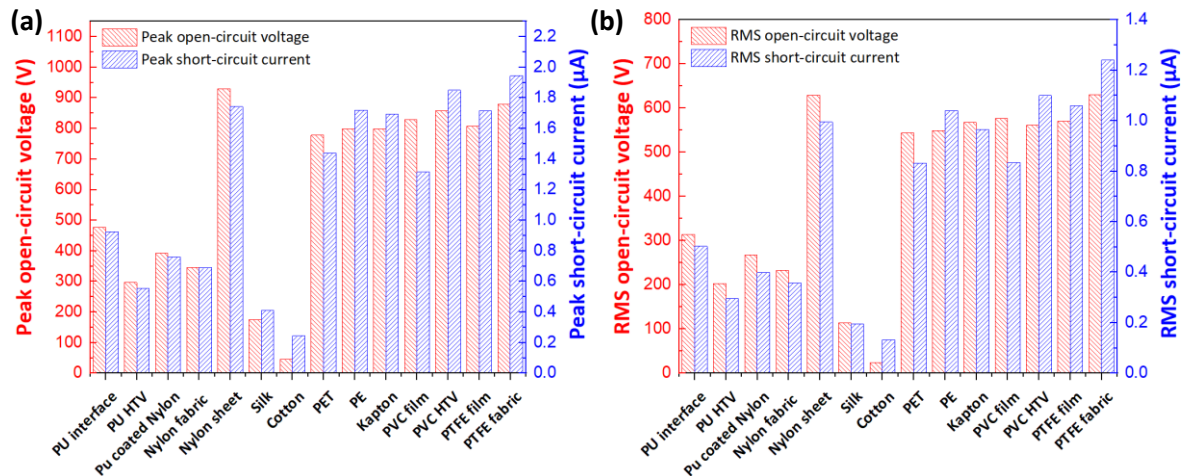


**Figure 3.8** (a) Peak and (b) RMS values of  $V_{OC}$  and  $I_{SC}$  of simple FT-mode TENGs for different triboelectric materials rubbed against Ag.



### 3.2.2.2 Surface charge density ( $\rho_q$ ) measurement

The absolute values of surface charge density ( $\rho_q$ ) for the different triboelectric materials with respect to Al and Ag are plotted in Figure 3.9a and b, respectively. The error bars show the standard deviation of 5 measurements. They are also plotted and compared with the RMS  $I_{SC}$  because theoretically, the  $\rho_q$  will be directly proportional to the RMS  $I_{SC}$  if the charges are uniformly distributed over the whole surface area. Both bar charts show that the level of the  $\rho_q$  and the RMS  $I_{SC}$  are in good agreement for almost all materials except for PU coated nylon and nylon fabric, which have quite high  $\rho_q$ . The reason for this is unclear and still need to be further investigated.

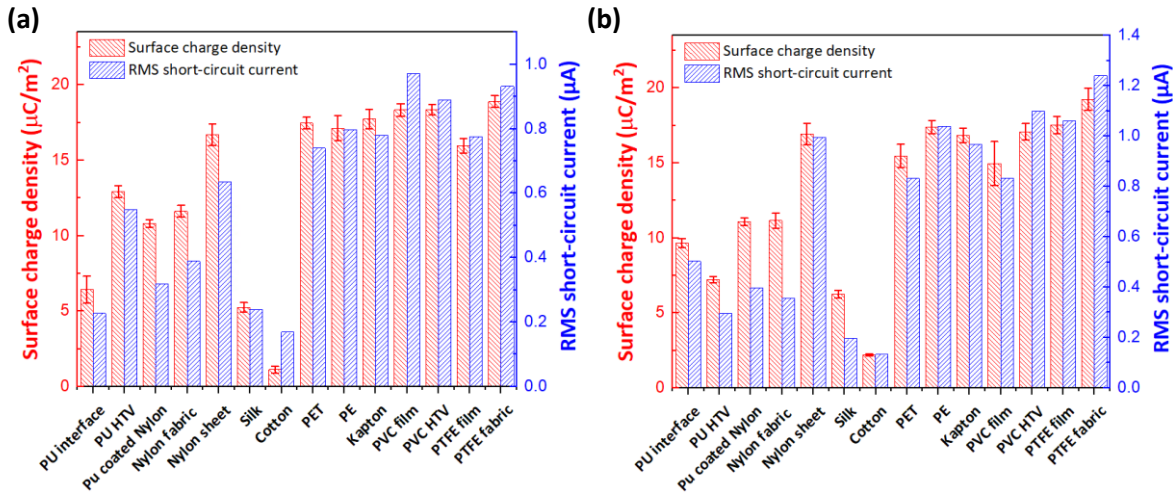


**Figure 3.9** Absolute values of  $\rho_q$  and RMS  $I_{SC}$  for different triboelectric materials rubbed against (a) Al and (b) Ag.

The electric polarity of the materials can be explicitly determined by the sign of the  $\rho_q$ , which can be directly read from the electrometer. The results are in accordance with the  $V_{OC}$  and  $I_{SC}$  measurements and the triboelectric series. With respect to Al, the values of  $\rho_q$  for the 6 materials on the left of the graph (PU interface to silk) are positive and the values for the rest of the materials on the right side are negative. With respect to Ag, the values of  $\rho_q$  for the 7 materials on the left of the graph (PU interface to cotton) are positive and the values for the rest of the materials on the right side are negative. For both Al and Ag, the PTFE fabric exhibits the maximum  $\rho_q$  of  $-18.89 \mu\text{C}/\text{m}^2$  and  $-19.24 \mu\text{C}/\text{m}^2$ , respectively. These are smaller but are in the same order of magnitude compared to values from the literature ( $-27.5 \mu\text{C}/\text{m}^2$  [149]). The deviation could stem from the different contacted materials, preparation methods, measurement methods and environmental conditions. Focusing on fabric, the material with the highest positive value of  $\rho_q$  is the nylon fabric with a  $\rho_q$  of  $11.63 \mu\text{C}/\text{m}^2$  and  $11.15 \mu\text{C}/\text{m}^2$  for Al and Ag, respectively ( $2.83 \mu\text{C}/\text{m}^2$  [149]). It is to note that apart from the material types and the materials they contact with, factors that strongly affect the  $\rho_q$  are the effective contact area during rubbing and the surface topology of the triboelectric materials.

For these reasons, the same materials, for examples, PTFE film and PTFE fabric, or nylon sheet and nylon fabric, do not show exactly the same values.

### 3.2.3 Conclusion

Focusing on the textile-based triboelectric materials, the best negative triboelectric material is PTFE fabric and the best positive triboelectric material is nylon fabric. These are confirmed by the experimental results that the TENGs with these materials exhibit the maximum  $V_{OC}$ ,  $I_{SC}$  and  $\rho_q$ . The surface charge density measurement shows that the  $\rho_q$  of PTFE fabric and nylon fabric with respect to the Al electrodes are  $-18.89 \mu\text{C}/\text{m}^2$  and  $11.63 \mu\text{C}/\text{m}^2$ , respectively and with respect to the Ag electrodes are  $-19.24 \mu\text{C}/\text{m}^2$  and  $11.15 \mu\text{C}/\text{m}^2$ , respectively. Considering the fabrication process and the triboelectric performance, the PU HTV and PVC HTV have also great potential to be used as triboelectric materials.

### 3.3 Factors influencing power output of TENGs

The dependence of output performance of TENGs on factors, such as frequency, contact force, humidity and temperature will be revealed in this section. The  $V_{OC}$  and  $I_{SC}$  of a simple FT-mode TENG with PTFE fabric and Ag electrodes, shown in the previous section, were recorded by varying the factor desired to study and keeping the other factors constant. The experiments were carried out using the linear actuator placed in the environmental chamber at an oscillation frequency of 2 Hz, a travel distance of the lower substrate of 48 mm, a contact force of 5 N, a temperature of 25 °C and a humidity of 25 %RH using the same method as described in Section 3.2.1.

#### 3.3.1 Frequency dependence measurement

The frequency dependence measurement was performed by varying the oscillation frequency of the linear actuator from 1 Hz to 3 Hz in increments of 0.5 Hz and maintaining the other factors. The transient  $V_{OC}$  and  $I_{SC}$  of the TENG for the different frequencies are demonstrated in Figure 3.10a and b, respectively. The corresponding peak and RMS value of the  $V_{OC}$  and the  $I_{SC}$  are plotted as a function of oscillation frequency in Figure 3.10c and d, respectively. In the beginning, the  $V_{OC}$  rises strongly with increasing frequency, then it saturates for the frequency over 2.5 Hz. This can be explained by Equation 3.1 below [150]:

$$V_{OC} = \frac{\sigma_{sc} \cdot S}{C} \quad (3.1)$$

where  $\sigma_{sc}$  is the short-circuit transferred charge density,  $S$  is the area of the first or the second electrode and  $C$  is the capacitance between the first and the second electrode. Because  $S$  and  $C$  are constant, the  $V_{OC}$  is directly proportional to  $\sigma_{sc}$ , which is normally equal to the surface charge density  $\rho_q$  of the PTFE fabric, if the same number of electrons in the electrodes is induced by the triboelectric charges on the triboelectric surface. As a result, the  $\sigma_{sc}$  grows with increasing frequency and saturate after a certain frequency. The  $I_{SC}$  shows approximately a linear relationship with the frequency. This can be explained by Equation 3.2 below:

$$I_{SC} = \frac{\rho_q dA}{dt} \quad (3.2)$$

where  $A$  is the total area of the PTFE fabric, and  $t$  is the time taken of the charges transferred from the first electrode to the second electrode. Assuming that the charge transfer time between electrodes is very short and can be neglected, this time will be equal to the travel time of the upper substrate. Therefore, the  $I_{SC}$  is inversely proportional to time and thus directly proportional to frequency.



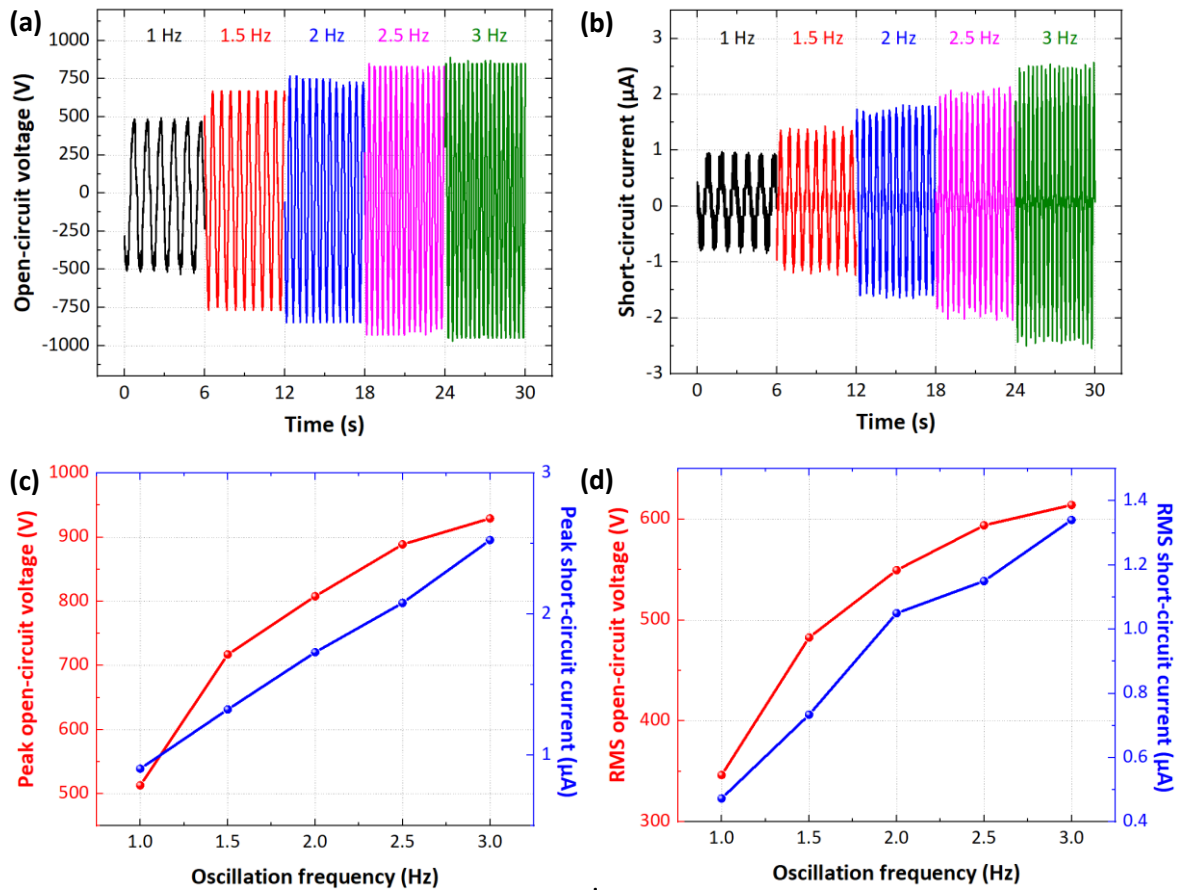


**Figure 3.10** Dependence of transient (a)  $V_{OC}$  and (b)  $I_{SC}$  on oscillation frequency of simple FT-mode TENG with PTFE and Ag electrodes. Corresponding (c) peak values and (d) RMS values of the  $V_{OC}$  and  $I_{SC}$  as a function of the oscillation frequency.

### 3.3.2 Contact force dependence measurement

The contact dependence measurement was performed by varying the contact force of the weight placed over the upper substrate from 1 N to 11 N in increments of 2 N and keeping the other factors constant. The transient  $V_{OC}$  and  $I_{SC}$  of the TENG for the different contact forces are demonstrated in Figure 3.11a and b, respectively. The corresponding peak and RMS value of the  $V_{OC}$  and the  $I_{SC}$  are plotted as a function of contact force in Figure 3.11c and d, respectively. Both  $V_{OC}$  and  $I_{SC}$  shows the same tendency. They rise quickly for the contact force between 1 N and 5 N. After that they gradually increase and seem to reach a saturation point for the contact force above 9 N. These could be explained by Equation 3.1 and 3.2 and the fact that an increase in contact force leads to a higher effective contact area and thus a greater charge transfer. Considering the interatomic interaction model shown in Section 2.2.2, the increase in contact force will cause a further overlapping between electron clouds of atoms, which lowers the potential barrier between the atoms and therefore a greater electron transfer, which again result in a growth in the surface charge density. However, this will be saturated at some point, when the potential barrier is lower

than the occupied energy levels of both atoms (see Figure 2.2b1 - b3) and no further electrons can be transferred.

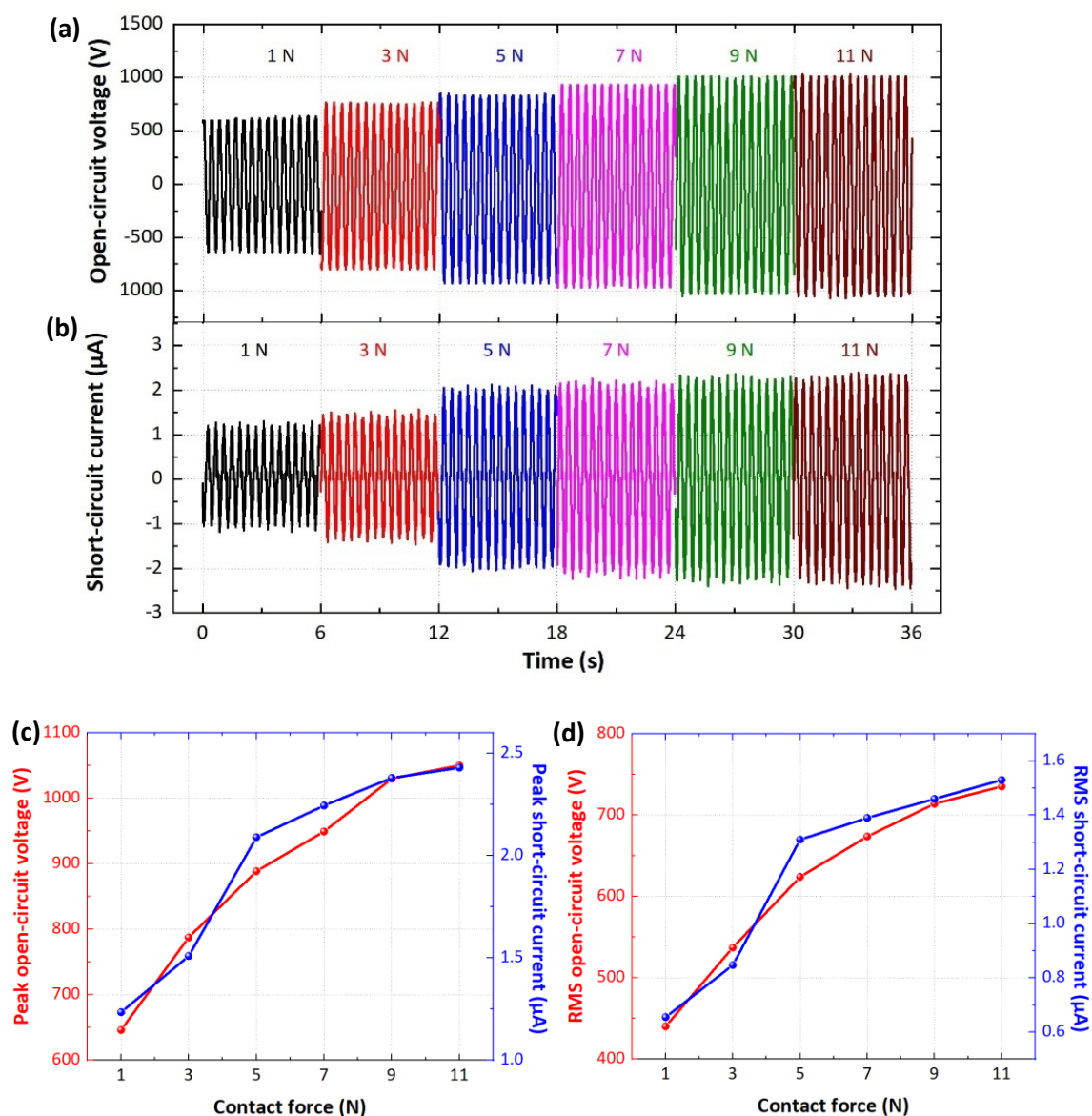


**Figure 3.11** Dependence of transient (a)  $V_{OC}$  and (b)  $I_{SC}$  on contact force of simple FT-mode TENG with PTFE and Ag electrodes. Corresponding (c) peak values and (d) RMS values of the  $V_{OC}$  and  $I_{SC}$  as a function of the contact force.

### 3.3.3 Humidity dependence measurement

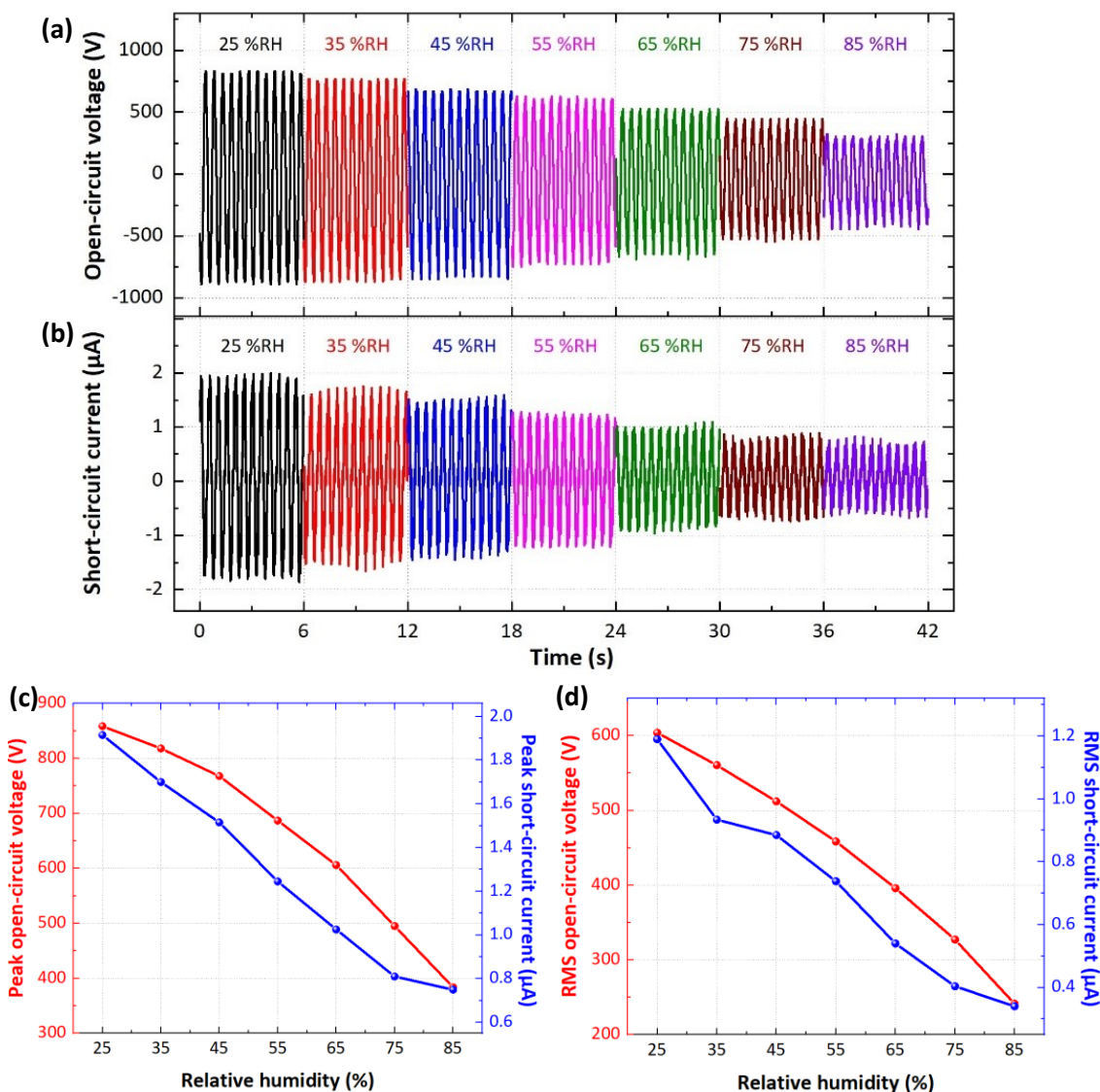


**Figure 3.12** Dependence of transient (a)  $V_{OC}$  and (b)  $I_{SC}$  on relative humidity of simple FT-mode TENG with PTFE and Ag electrodes. Corresponding (c) peak values and (d) RMS values of the  $V_{OC}$  and  $I_{SC}$  as a function of the relative humidity.

The humidity dependence measurement was performed by varying the relative humidity inside the environmental chamber from 25 % to 85 % in increments of 10 % and keeping the other factors constant. This humidity range is limited by the performance of the environmental chamber. However, this is sufficient to cover the normal operating humidity range of wearable devices. The transient  $V_{OC}$  and  $I_{SC}$  of the TENG for the different relative humidities are shown in Figure 3.12a and b, respectively. The corresponding peak and RMS value of the  $V_{OC}$  and the  $I_{SC}$  are plotted as a function of relative humidity in Figure 3.12c and d, respectively. Both  $V_{OC}$  and  $I_{SC}$  decline significantly with increasing relative humidity. The RMS  $V_{OC}$  and  $I_{SC}$  for 85%RH drop by approximately 60% and 71% compared to those for 25 %RH, respectively. This degradation can be explained that with increasing humidity, a thicker layer of water is formed on the surfaces of triboelectric materials.

These water layer increases the surface conductivity of the materials and causes electrostatic discharge between the surfaces [142].

### 3.3.4 Temperature dependence measurement

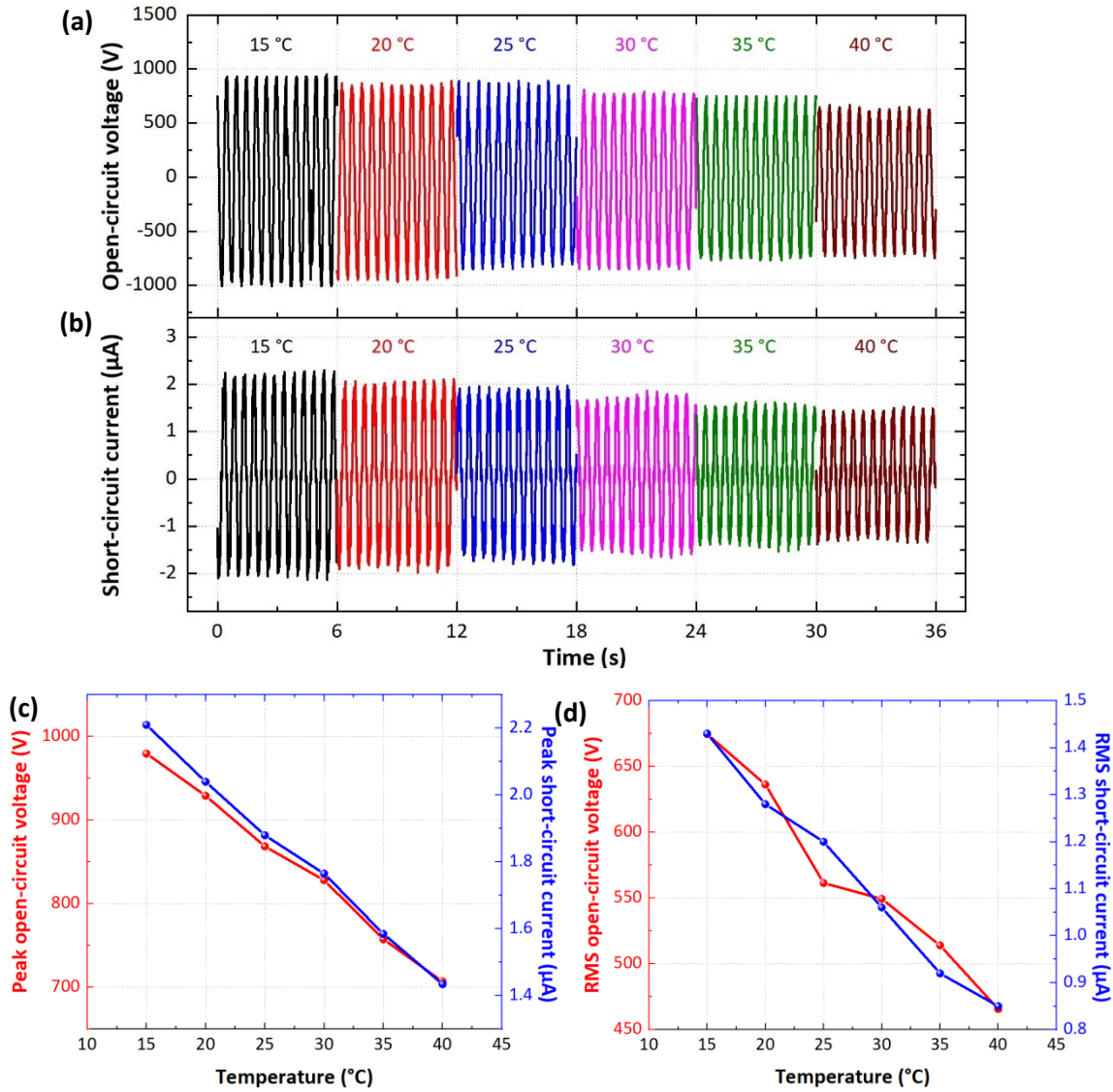


**Figure 3.13** Dependence of transient (a)  $V_{OC}$  and (b)  $I_{SC}$  on temperature of simple FT-mode TENG with PTFE and Ag electrodes. Corresponding (c) peak values and (d) RMS values of the  $V_{OC}$  and  $I_{SC}$  as a function of the temperature.

The temperature dependence measurement was performed by varying the temperature inside the environmental chamber from 15 °C to 40 °C in increments of 5 °C and keeping the other factors constant. This temperature range is limited by the performance of the environmental chamber if the humidity is maintained at 25 %RH. However, this temperature range should reflect the normal operating temperature range of wearable devices. The transient  $V_{OC}$  and  $I_{SC}$  of the TENG for the different temperatures are shown in Figure 3.13a and b, respectively. The corresponding peak and RMS value of the  $V_{OC}$  and the  $I_{SC}$  are plotted as a function of temperature in Figure 3.13c

and  $d$ , respectively. Both  $V_{OC}$  and  $I_{SC}$  decrease with increasing temperature. This can be explained by the electronic band structure model shown in Figure 3.14 and the Fermi–Dirac distribution function below:

$$f = \frac{1}{\exp((E-E_F)/kT)+1} \quad (3.3)$$

where  $f$  is the probability that an electron has energy  $E$ ,  $E_F$  is the energy of the Fermi level,  $k$  is the Boltzmann constant, and  $T$  is the temperature. When the temperature increases, the Fermi–Dirac distribution function shifts upwards. Thus, there is a higher probability to find electrons in higher energy levels. When these occupied energy levels are higher than the potential barrier  $W$ , electrons will hop back from dielectric to metal resulting in a lower surface charge density on the dielectric surface [53]. Moreover, it has also been proposed that higher temperature can lead to surface oxidation which reduces the surface defects, e.g. dangling bonds. Therefore, the ability of the triboelectric material to use such defects to store electrons will become weaker resulting in a lower surface charge density [151].

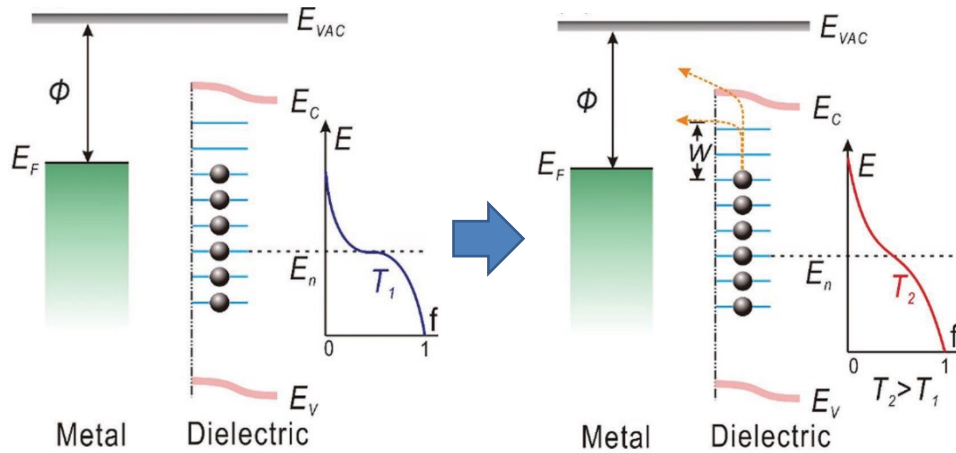


**Figure 3.14** Electronic band structure model showing electron transfer back to metal and shifting of Fermi–Dirac distribution when temperature increases. Reproduced with permission from Ref. [53]. Copyright 2014, John Wiley & Sons, Inc.

### 3.3.5 Conclusion

The output performance of TENGs is affected by many factors. The 4 main factors include the operating frequency, contact force, humidity and temperature. Regarding frequency,  $V_{OC}$  and  $I_{SC}$  increase with increasing frequency but  $V_{OC}$  will saturate at a certain frequency. Regarding contact force,  $V_{OC}$  and  $I_{SC}$  increase with increasing contact force but they will reach a saturation point at a certain contact force. Regarding humidity and temperature in the wearable range, TENGs will deliver the best performance at low humidity and low temperature.

### 3.4 Rectifier circuit investigation

Due to the fact that the electrical outputs of TENGs are alternating and variable, a suitable method to evaluate the performance of TENGs is to monitor the transient capacitor voltage by charging a suitable capacitor. An efficient rectifier circuit is required in order to minimise energy losses between the output of the TENGs and the capacitor. Therefore, this paper also includes an investigation into the design of a passive rectification circuit and its influence on the energy transferred to the storage capacitor. Ghaffarinejad et al. previously identified that the best energy transfer efficiency was achieved with the Bennet's doubler followed by half-wave and full-wave bridge rectifier circuits for TENGs operating in CS-mode with capacitance ratios above 2 [145], [152]. However, for the FT-mode TENGs, the performance of the different rectifier circuits has not previously been fully investigated.

#### 3.4.1 Design and methodology

##### 3.4.1.1 Simulations

According to Niu et al. [96], the equivalent circuit of FT-mode TENGs can be presented as a constant AC source and a fixed capacitor. To confirm that the capacitance of the TENG is constant and to find the value of this capacitance, a simple FT-mode TENG was first simulated using a finite element method (FEM) implemented in the COMSOL Multiphysics software. The structure of the TENG is similar to the TENGs shown in Chapter 3. It is composed of a PTFE upper substrate and two Al electrodes surrounded by air. The Electrostatics and Electrical Circuit Physics, stationary study and normal free triangular mesh were chosen for the simulation model. To determine the capacitance, an electrode is connected to the ground and a constant DC voltage source of 1 V was connected between the electrodes. The capacitance is therefore equal to the transferred charges between the electrodes, which can be extracted from COMSOL. Two stationary states were simulated, namely the state when the PTFE fully covers one of the electrodes and the state when the PTFE is located between the electrodes to observe the capacitance change.

Subsequently, the equivalent circuit of the FT-mode TENG connected to three different rectifier circuits (Bennet's doubler circuit, half-wave and full-wave bridge) and a 10- $\mu$ F-reservoir capacitor were simulated using a SPICE software, Multisim. The 10- $\mu$ F-reservoir capacitor ( $C_{res}$ ) was used here because it is widely used in most literature [37], [137], [153] and the capacitor voltage is at an appropriate level which is suitable for low power electronics. For Bennet's doubler circuit, the capacitance of the store capacitor ( $C_{store}$ ) was varied investigate its effect and to maximise



efficiency. The transient analysis of the reservoir capacitor was performed for a time ranging from 0 to 600 s.

### 3.4.1.2 Experiments

The FT-mode TENG with a PTFE upper substrate and two Al electrodes was used as an energy source. The substrate and the electrodes were rubbed against each other using the linear actuator at an oscillation frequency of 2 Hz, a contact force of 5 N, a temperature of around 23.0 °C and a humidity of around 32 %RH. The humidity and temperature are slightly different from the previous sections since, at the time when the experiments were performed, there was still no environmental chamber available. The experiments were thus performed at standard room temperature and humidity in an air-conditioned room. The TENG was connected to four different rectifier circuits, including Bennet's doubler circuit, half-wave, full-wave bridge and a commercial full-wave rectifier (Diodes Inc DF10M). The Bennet's doubler circuit, half-wave, full-wave bridge were built on a breadboard. 1N4007 diodes were used here because they can withstand the peak repetitive reverse voltage of up to 1000 V. An electrolytic capacitor with a capacitance of 10  $\mu$ F was chosen as the reservoir capacitor and five different store capacitors (100 pF, 1 nF, 10 nF, 100 nF and 1  $\mu$ F) were chosen for the Bennet's doubler circuit. The rectified outputs were used to charge the reservoir capacitor. During charging-up, the reservoir capacitor voltages ( $V_c$ ) were recorded every 30 s for 10 minutes using a digital multimeter (Tenma 72-7780) and then compared. It is to note that 3 TENGs were built and tested, and the best output is presented in the following experimental result section.

## 3.4.2 Results and discussion

### 3.4.2.1 Simulations

To find an equivalent circuit of the FT-mode TENG with the PTFE upper substrate and the Al electrodes, COMSOL was used to determine the capacitance of the TENG. Figure 3.15 demonstrates the electric potential of the TENG. The PTFE upper substrate is here located exactly in the middle between the Al electrodes. An electric potential difference ( $V$ ) of 1 V is applied to the left electrode, while the right electrode is connected to the ground. As a result, electric charges  $Q$  of 2.43 pC are transferred to the left electrode. According to Equation 3.4 below:

$$C = \frac{Q}{V} \quad (3.4)$$

the capacitance  $C$  of the TENG can be calculated to 2.43 pF. The other simulated state is the state when the PTFE fully covers the left electrode. At this state, the charges of 2.37 pC are transferred to the left electrodes, resulting in a capacitance of 2.37 pF. Because both electrodes are fixed, the

only factor that can affect the capacitance of the TENG is the permittivity of the materials surrounding the electrodes. These two states should present the maximum change of the capacitance of the TENG since the permittivity of the TENG changes the maximum due to the position of the PTFE. The capacitance changes by 2.5% and therefore it can be assumed that the capacitance of the TENG is constant at 2.4 pF, which is the average of the capacitances.

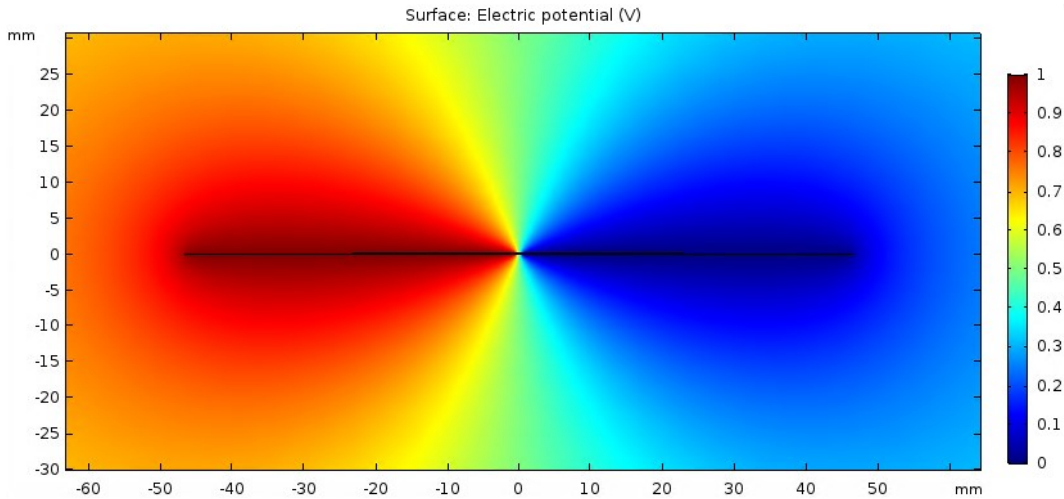


**Figure 3.15** COMSOL simulation of simple FT-mode TENG at a stationary state when the PTFE is located exactly between the electrodes. When a DC voltage of 1 V is applied between the electrodes, electric charges of 2.43 pC are transferred to the left electrode.

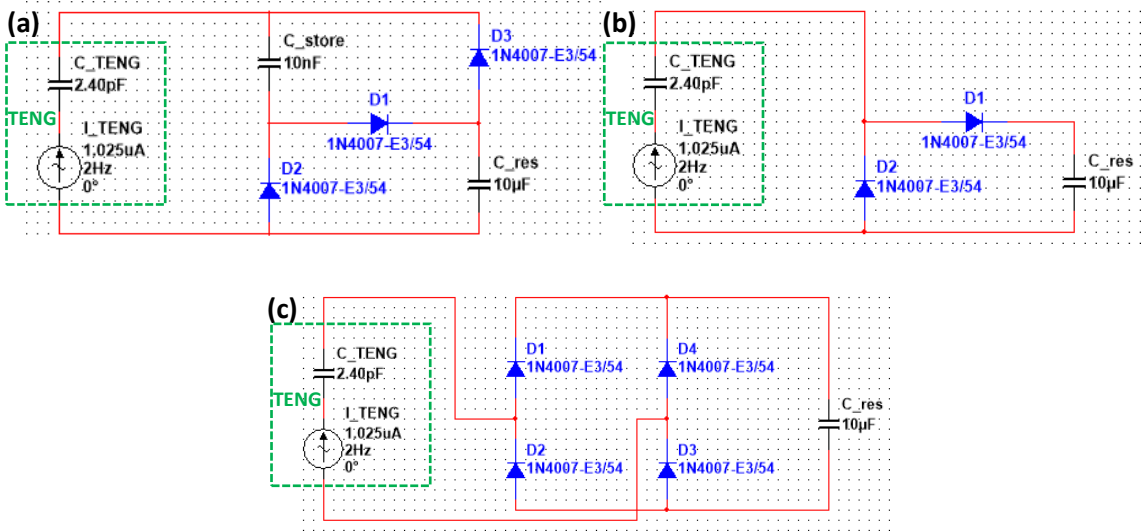


**Figure 3.16** Equivalent circuit of FT-mode TENG connected to (a) Bennet's doubler circuit, (b) half-wave bridge and (c) full-wave bridge.

From the results of the COMSOL simulation and the experimental result of the TENG with PTFE fabric and Al substrate, an equivalent circuit of the TENG can be drawn. It is composed of an AC source with a peak value of 1.025  $\mu$ A operating at 2 Hz and a fixed capacitor of 2.4 pF. With this model, it is possible to simulate the  $V_c$  of the TENG for the different rectifier circuits using Multisim. Figure 3.16a, b and c illustrate the equivalent circuit of the FT-mode TENG connected to the Bennet's doubler circuit, half-wave and full-wave bridge, respectively. The maximum  $V_c$  after a



charging time of 600 s and the transient  $V_C$  of the Bennet's doubler circuit are demonstrated for the different  $C_{store}$  in Figure 3.17a and b, respectively. In Figure 3.17a, the maximum  $V_C$  rises sharply with increasing  $C_{store}$  for the  $C_{store}$  smaller than 1 nF. Next, it stays almost constant for the  $C_{store}$  between 1 nF and 100 nF, then decreases rapidly when the  $C_{store}$  exceeds 100 nF. The maximum  $V_C$  peaks at a value of 18.19 V for  $C_{store} = 10$  nF. Figure 3.17b shows that the  $V_C$  increases with time for all  $C_{store}$  and reaches maximum values of 13.31 V, 18.08 V, 18.19 V, 18.04 V and 16.55 V at  $t = 600$  s for  $C_{store} = 100$  pF, 1 nF, 10 nF, 100 nF and 1  $\mu$ F, respectively.

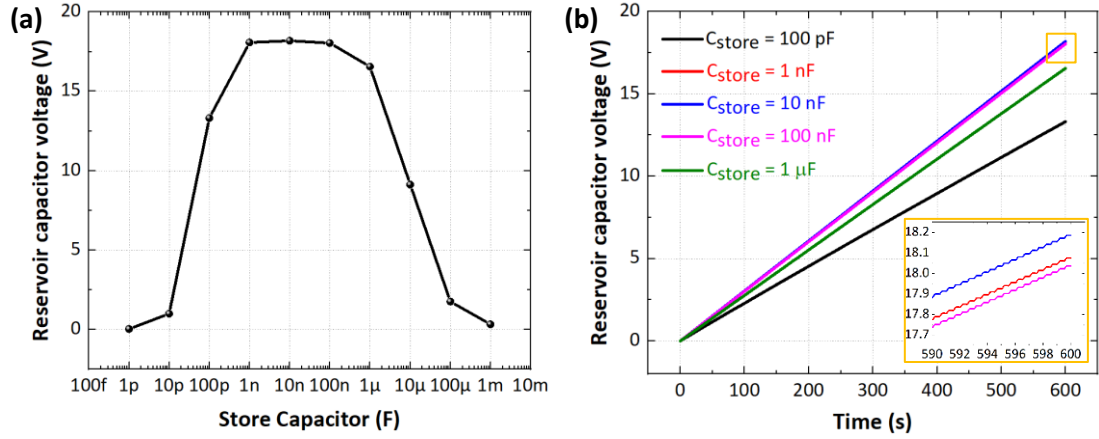


**Figure 3.17** (a) The maximum simulated  $V_C$  after a charging time of 600 s as a function of  $C_{store}$  and (b) simulated transient  $V_C$  of Bennet's doubler circuit for the different  $C_{store}$ . The inset shows the magnified transient  $V_C$  for  $C_{store} = 1, 10$  and 100 nF at the time between 590 and 600 s.

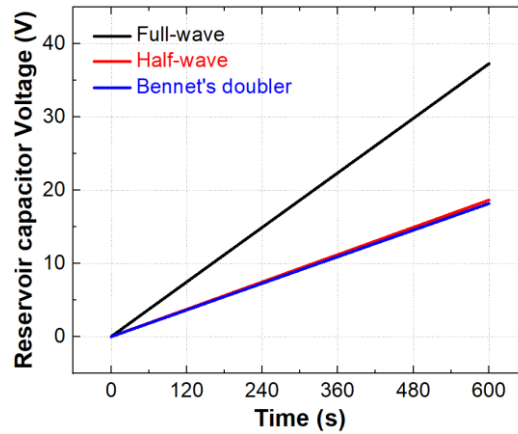


**Figure 3.18** Simulated transient  $V_C$  of FT-mode TENG connected to different rectifier circuits.

In Figure 3.18, the  $V_C$  are plotted as a function of charging time for the different rectifier circuits. The full-wave bridge exhibits the best rectifying performance, followed by the half-wave bridge and the Bennet's doubler ( $C_{store} = 10$  nF). At the charging time of 600 s, the  $V_C$  for the full-wave bridge, the half-wave bridge and the Bennet's doubler are 37.29 V, 18.66 V and 18.19 V, respectively.

### 3.4.2.2 Experiments

The transient  $V_C$  of the TENG connected to the Bennet's doubler circuit for various  $C_{store}$  are presented in Figure 3.19a. The maximum  $V_C$  of 13.75 V is obtained for  $C_{store} = 10$  nF at a charging time of 600 s, followed by those for  $C_{store} = 100$  nF, 1 nF, 1  $\mu$ F and 100 pF. The transient  $V_C$  for the different rectifier circuits are shown in Figure 3.19b. The full-wave bridge rectifier with 1N4007 diodes exhibits the best rectifying performance with a maximum  $V_C$  of 25.70 V. The TENG with commercial rectifier (DF10M) generates a slightly lower maximum  $V_C$  of 24.68 V, whereas the output of the TENG with the half-wave bridge and Bennet's doubler rectifiers are very close and are much lower than output of the full-wave rectifiers. This is due to half of the electric output of the TENG is lost due to the configuration of the diodes and the alternating polarity of the electric potential at the electrodes. By contrast, in the case of the CS-mode TENGs, their equivalent circuit can be represented as a constant DC voltage source and a variable capacitor. Therefore, the potential of one electrode is always higher than the other. Consequently, the CS-mode TENGs can benefit from the half-wave bridge and Bennet's doubler rectifier [145]. Compared to the simulation results in Figure 3.17b and Figure 3.18, the sequence of the maximum  $V_C$  for the different  $C_{store}$  and the different rectifier circuits are in good agreement with the simulation results, except the sequences for  $C_{store} = 10$  nF and 100 nF, which are swapped since their values in the simulation are very close. The experimental values of  $V_C$  are lower than the simulation result due to losses in the circuits, e.g. resistive loss.

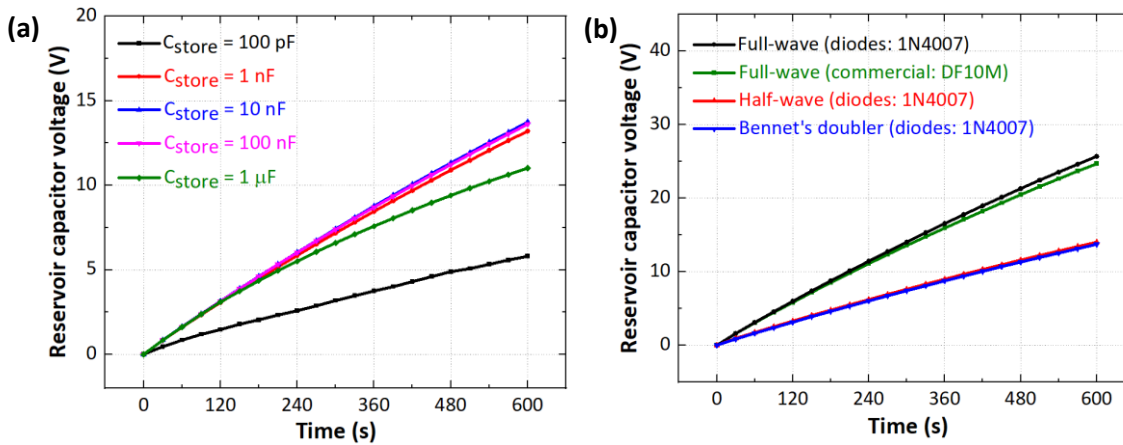


**Figure 3.19** Experimental transient  $V_C$  of FT-mode TENG (a) for Bennet's doubler circuit with various  $C_{store}$  and (b) for the different rectifier circuits.

### 3.4.3 Conclusion

For FT-mode TENGs, the most suitable rectifier circuit is the full-wave bridge rectifier. Both the simulation and experimental results show that the performance of the full-wave bridge rectifier is much better than the half-wave bridge and Bennet's doubler rectifier since, unlike the CS-mode TENG, half of the electric output of the TENGs with the half-wave bridge or Bennet's doubler rectifier is lost due to the configuration of the diodes and the alternate polarity of the electric potential at the electrodes. The simulated capacitor voltage charged by a simple FT-mode TENG after a charging time of 600 s for the full-wave bridge, the half-wave bridge and the Bennet's doubler are 37.29 V, 18.66 V and 18.19 V, respectively.



## Chapter 4 Textile-based triboelectric energy harvester with alternating positive and negative freestanding grating structure (pnG-TENG)

### 4.1 Introduction

As mentioned in Section 2.4, most TENGs operating in the lateral sliding mode (LS-mode) and freestanding triboelectric-layer mode (FT-mode) are fabricated with a grating structure to improve their electrical outputs. For the lateral-sliding mode (LS-mode), the grating-structured TENGs (G-TENGs) can be found with a single positive or single negative triboelectric material (pG-TENGs or nG-TENGs) [79]–[81], [154] or with an alternating positive and negative grating structure (pnG-TENGs) [82], [83], [155]. However, for the FT-mode, most G-TENGs can only be found in a form of either nG-TENGs or pG-TENGs, which comprises gratings of one type of triboelectric material separated by air gaps. Nevertheless, the air gaps between the triboelectric materials cause a reduction in the effective contact area and thus the performance of the devices declines.

The examples of the conventional G-TENGs operating in FT-mode are as follows. Xie et al. demonstrated an nG-TENG comprising segments of fluorinated ethylene propylene (FEP) separated by air gaps on the upper substrate and aluminium (Al) interdigitated electrodes (IDEs) on the lower substrate, shown in Figure 4.1a [150]. The nG-TENG with 16 grating segments produced a maximum power density of  $1.2 \text{ W/m}^2$ . In Figure 4.1b, Bi et al. revealed a rotational nG-TENG with a grated polytetrafluoroethylene (PTFE) rotator acting as triboelectric material and a Cu stator as IDEs [156]. This nG-TENG with 16 grating segments delivered a peak power density of  $1.3 \text{ W/m}^2$  at 750 rpm. In Figure 4.1c, a textile-based pG-TENG proposed by Pu et al. is demonstrated [90]. The T-TENG consists of a stator fabric and a slider fabric. IDEs were fabricated on the stator fabric by electroless plating of nickel (Ni) and then fully covered by a parylene layer serving as a triboelectric material. The slider fabric has grating-structured segments of Ni serving as the freestanding layer. The T-TENG with a 1-mm-wide segment can generate a maximum power density of  $3.2 \text{ W/m}^2$  at a speed of 0.75 m/s. In this structure, the gaps between the segments of Ni were filled by pristine textile instead of air gaps. Since both Ni and pristine (polyester) textile segments on the slider became positively charged after rubbing against the electrodes, the performance of the T-TENG was degraded. Similarly, Chen et al. fabricated a textile-based nG-TENG with gratings of polytetrafluoroethylene (PTFE) wires and cotton wires rubbing against carbon wires [140].

However, cotton is not a good triboelectric material and rarely acquires an electrical charge (Figure 4.1d).

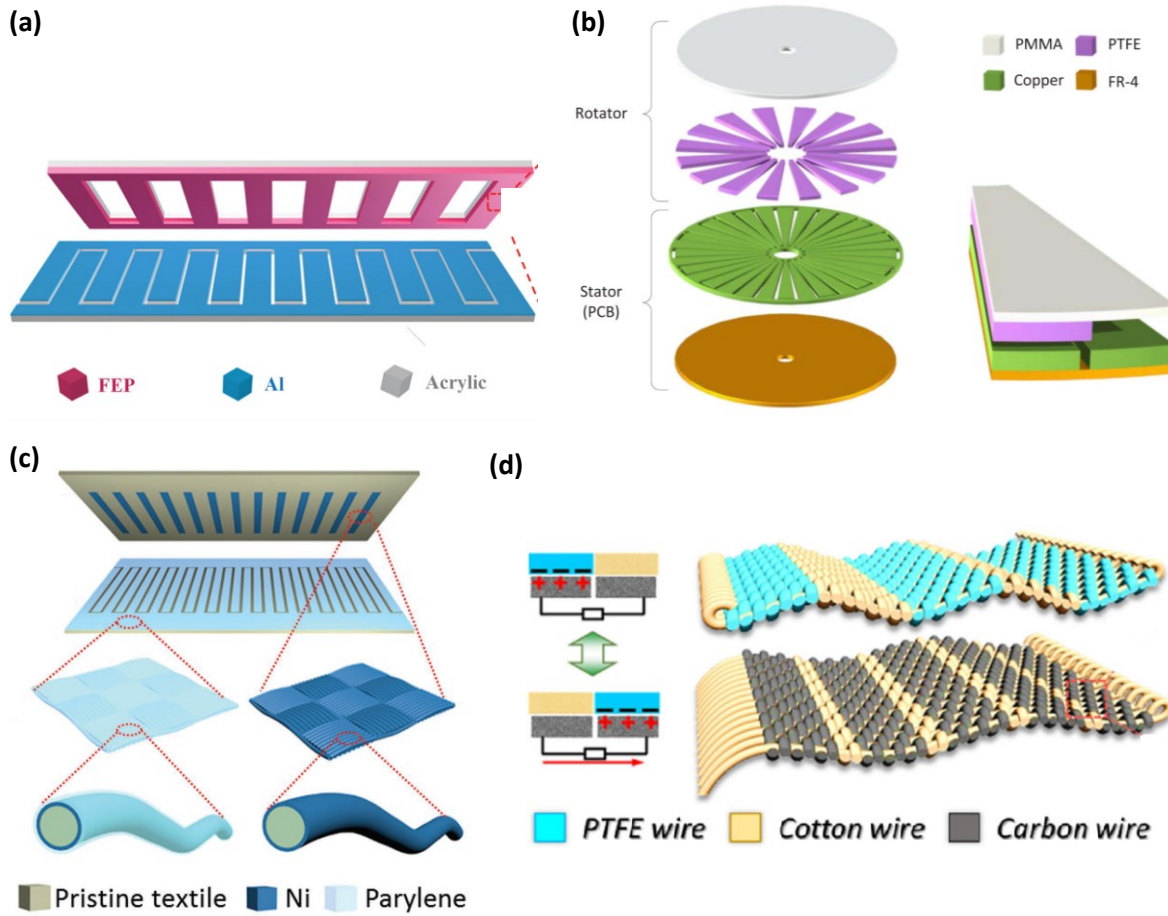


**Figure 4.1** Schematic illustration of (a) sliding nG-TENG proposed by Xie et al. (Reproduced with permission from Ref. [150]. Copyright 2014, John Wiley & Sons, Inc), (b) rotational nG-TENG proposed by Bi et. al (Reprinted with permission from Ref. [156]. Copyright 2017, Elsevier), (c) sliding pG-TENG proposed by Pu et. al (Reproduced with permission from Ref. [90]. Copyright 2016, John Wiley & Sons, Inc) and (d) sliding nG-TENG proposed by Chen et. al (Reprinted with permission from Ref. [140]. Copyright 2018, Elsevier).

A similar idea to the FT-mode pnG-TENGs was published by Gue et al. in 2015, shown in Figure 4.2a [157]. The Device is composed of an Al rod, an outer cylinder stator with Cu IDEs and an inner cylinder rotator. The rotator was fabricated by coating a thin FEP film with paralleled Cu strips with matching periodicity. Due to rolling friction between the Al rod and the rotator, triboelectric charges were replenished into FEP and Cu strips. Figure 4.2b shows the operation mechanism of the TENG. Via the rotation of the rotator, an alternate current is induced between the IDEs. The negative charges on the FEP strips were generated by triboelectric charge separation, while the positive charges on the Cu strips were transferred from the existing triboelectric charges on the Al rod due to the charge distribution between Al and Cu. The amount of charge on the Cu strips is considerably less than the total charge generated by triboelectric charge separation as in the case

of the proposed pnG-TENG because the triboelectric charge is distributed between the two conductive materials (Al and Cu).

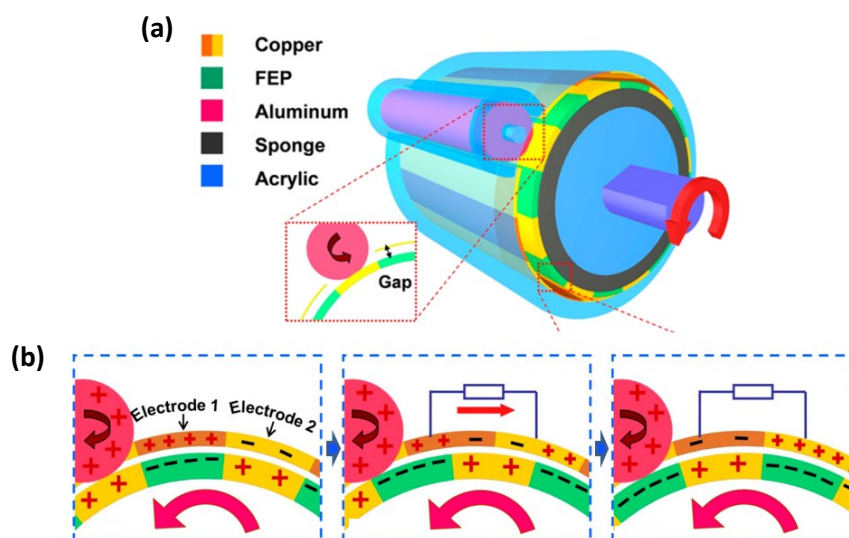


**Figure 4.2** Schematic illustration of (a) rolling pnG-TENG published by Gue et al. and (b) its operation mechanism. Reproduced with permission from Ref. [157]. Copyright 2015, American Chemical Society.

This chapter presents a novel structure of T-TENG with alternate grated strips of positive and negative triboelectric material operating in FT-mode. Whereas most G-TENGs operating in an FT-mode comprise gratings of one type of triboelectric material separated by air gaps, this design presents a replacement of the air gaps by another triboelectric material with the opposite polarity to the existing triboelectric material. This is predicted to increase performance by increasing the contact area of the generator. The main advantage of operation in FT-mode is the absence of an electrical connection between the moving and stationary parts of the TENGs and the reduction in the friction between the triboelectric materials [158]. The proposed pnG-TENG is composed of an upper substrate with gratings of nylon fabric and polyvinyl chloride heat transfer vinyl (PVC HTV) and a lower substrate with screen-printed silver (Ag) IDEs on a PVC coated polyester fabric (PVC fabric). The processes involved in the manufacture of the pnG-TENG, namely screen-printing and heat transfer, are cost-effective, straightforward and compatible with standard textile manufacturing. The objective of this chapter is to explore the degree of improvement offered by the pnG-TENGs compared to the single material G-TENGs and the TENG with no grating.

## 4.2 Design and methodology

### 4.2.1 Fabrication

To prove the ideas of pnG-TENG, a simple pnG-TENG was firstly produced using a simple fabrication method. This helps save time and cost, and enable a quick review of its performance

and electrical outputs. It is composed of an upper substrate with alternate strips of Nylon and PTFE fabric attached to a 1-mm thick fabric using double-sided tape, and a lower substrate with two IDEs with matching periodicity made of Al adhesive tape. Nylon and PTFE fabric are chosen since they exhibit good triboelectric performance according to the experiment shown in Section 3.2. The detailed fabrication method and experimental results on the simple-pnG-TENG were published in the PowerMEMS conference 2018, which can be found in Appendix B.

After the successful pre-test, textile-based pnG-TENGs were fabricated using different alternative processes, which are compatible with standard manufacturing. The attempted fabrication methods for the upper substrate are, for examples, dispenser-printing liquid PTFE on PVC fabric, spray-coated PTFE on PVC fabric, dispenser-printing PU interface on PVC fabric and heat-pressed PVC-HTV on different fabrics. Regarding the electrodes, the attempted methods include dispenser-printing Ag ink on PVC fabric, screen-printing Ag ink on a heat transfer paper and screen-printing Ag ink on PVC fabric. However, some methods do not work well or are too sophisticated. Further details on unselected methods can be found in Appendix C. The most appropriate methods selected for fabrication of the upper and the lower substrate of the pnG-TENG are heat-pressed PVC-HTV on different fabrics and screen-printing Ag ink on PVC fabric, respectively, because they are simple, low cost, provide high power output and are compatible with standard textile manufacturing. Nylon fabric was selected as the positive triboelectric material as it is one of the most positive fabrics in the triboelectric series [16], [17]. Other fabrics, such as silk and cotton, were also investigated. PVC HTV is chosen as the negative triboelectric material due to its stretchability, washability and durability. It is also widely used in the textile industry as it can last the lifetime of the fabric with no fading or cracking. Moreover, nylon fabric and PVC HTV exhibit a good triboelectric performance as shown in Section 3.2.

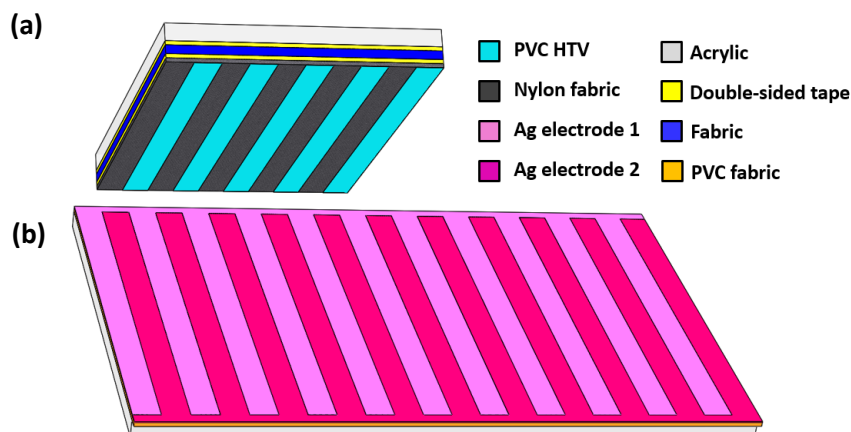


**Figure 4.3** Schematic illustration of (a) upper substrate of pnG-TENG for  $N = 10$  with PVC HTV as negative material and nylon fabric as positive material and (b) lower substrate of the pnG-TENG with interdigitated Ag electrodes



A schematic illustration of the proposed pnG-TENG is revealed in Figure 4.3a and b. It is composed of an upper substrate with  $N$  alternate strips of adhesive nylon fabric (Hemline) and PVC HTV (HOHO Industry) acting as a freestanding part ( $N = 10$  for Figure 4.3a) and a lower acrylic substrate with two Ag IDEs with matching periodicity ( $N = 10$  for Figure 4.3b).

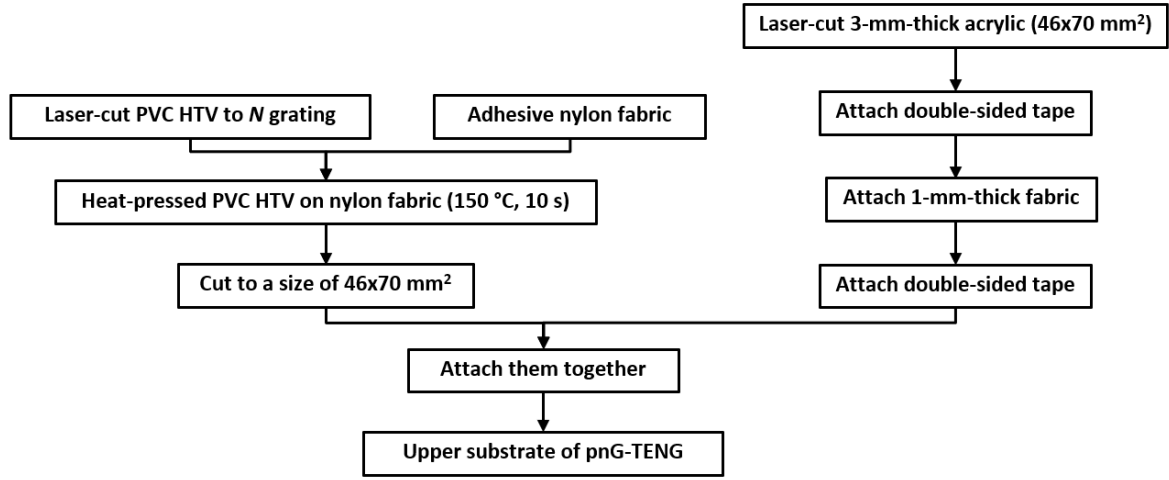


**Figure 4.4** Flowchart showing the fabrication steps of upper substrate of pnG-TENG.

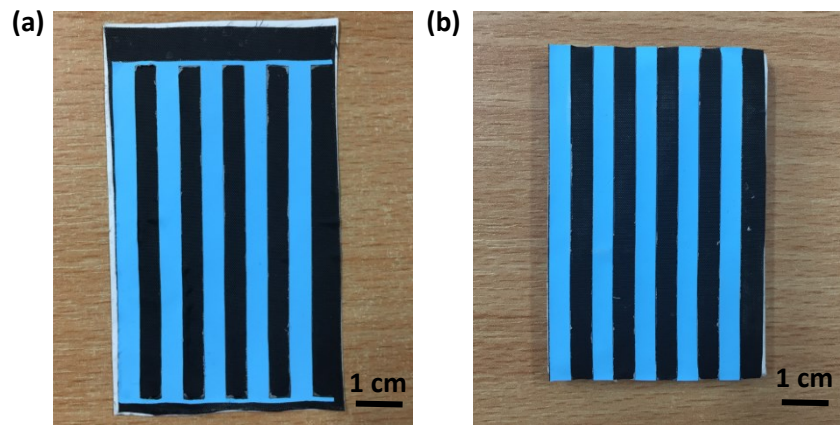


**Figure 4.5** Photograph of (a) PVC HTV heat pressed on a piece of nylon fabric and (b) finished upper substrate of a pnG-TENG with nylon fabric and PVC HTV as positive and negative triboelectric material, respectively.

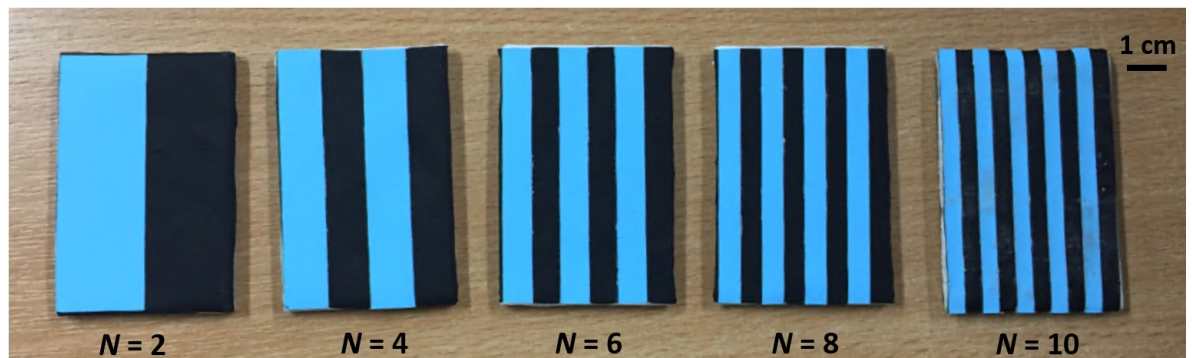


**Figure 4.6** Photograph of the upper substrates of pnG-TENG with nylon and PVC HTV for the different grating numbers ( $N = 2, 4, 6, 8$  and  $10$ ). The PVC HTV is blue and the nylon is black.

The flowchart of the fabrication steps of the upper substate of pnG-TENG is shown in Figure 4.4. Firstly, the 160- $\mu\text{m}$ -thick PVC HTV with its carrier sheet was cut to  $N/2$  strips separated by air gaps with a width of  $46/N$  mm using a laser cutter (Epilog Mini 24 Laser). A low power setting was used to completely cut through the PVC HTV but not through the underlying carrier sheet. Unwanted PVC HTV parts were then removed from the carrier sheet. Subsequently, the PVC HTV and carrier sheet were positioned on top of a piece of nylon fabric and heat pressed together using a heat-press machine (Digital Knight DK20S) at 150 °C for 10 s, as shown in Figure 4.5a. The carrier sheet was then peeled away and the nylon fabric with the grated PVC HTV was cut to a  $46 \times 70$  mm<sup>2</sup> rectangle and bonded to the 1-mm-thick fabric carrier and attached to a 3-mm-thick acrylic sheet for testing purposes, as shown in Figure 4.5b. The acrylic sheet enables consistent and repeatable testing and would not be required in an actual e-textile application. The 1-mm-thick fabric is very flexible which allows it to conform to the surface below and thus increases the effective contact area of the triboelectric materials. The upper substrate was fabricated with  $N = 2, 4, 6, 8$  and 10, as shown in Figure 4.6.

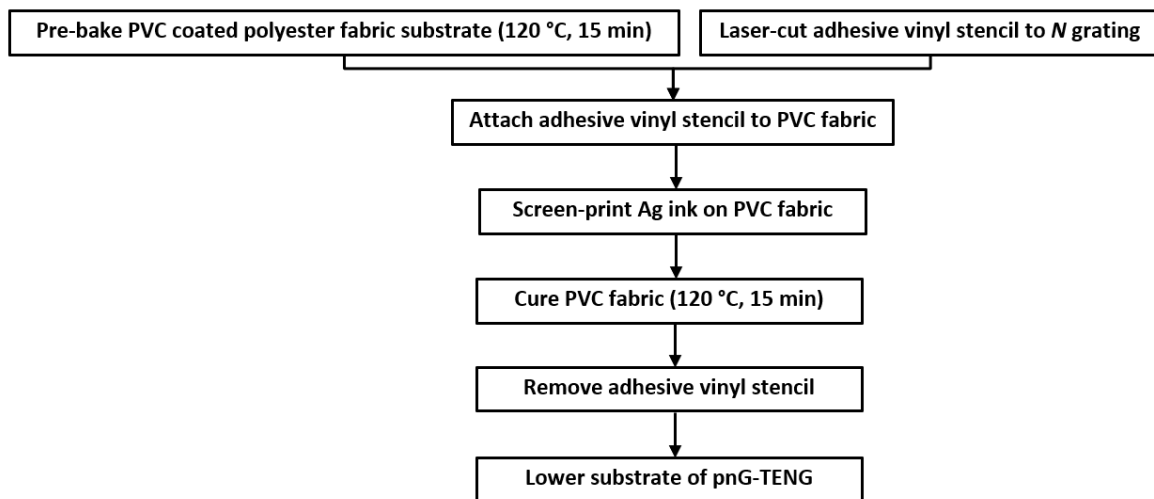


**Figure 4.7** Flowchart showing the fabrication steps of lower substate of pnG-TENG.

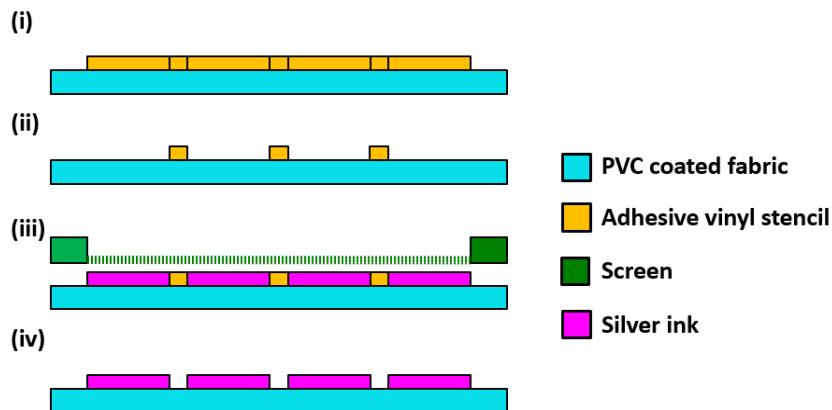


**Figure 4.8** Schematic illustration of IDEs fabrication steps using adhesive vinyl stencil and screen-printing.

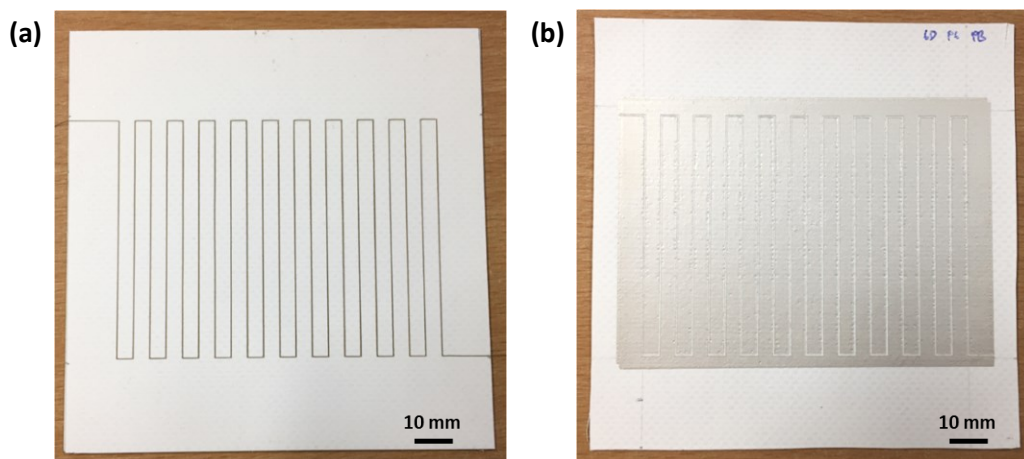


**Figure 4.9** Photograph of (a) transferred adhesive vinyl stencil on PVC fabric (step ii) and (b) IDEs after curing and removing the vinyl stencil (step iv) for  $N = 10$ .

The flowchart and fabrication steps of the IDEs are shown in Figure 4.7 and Figure 4.8, respectively. Firstly, a piece of 450- $\mu\text{m}$ -thick PVC coated polyester fabric substrate (VALMEX FR 7546) was pre-baked (120 °C for 15 minutes) to eliminate outgassing from the PVC layer which could delaminate the subsequent printed layers. Next, a piece of adhesive vinyl was laser-cut to form a stencil which will produce a gap of around 0.6 mm between the tines and then transferred to the PVC fabric using a transfer tape (Figure 4.8(i)). The unwanted parts of the adhesive vinyl stencil were peeled off (Figure 4.8(ii) and Figure 4.9a) and the Ag ink (Fabinks TC-C4001) was screen-printed with 6 deposits on the PVC fabric using a DEK 248 screen printer at a printing speed of 70 mm/s, a printing gap of 1 mm and printing pressure set to 5 kg (Figure 4.8(iii)). The screen has a pattern of a 75 x 105 mm<sup>2</sup> rectangle, which is larger than the lower acrylic substrate (70x100 mm<sup>2</sup>) enabling the excess area to serve as the connections to the external circuit. The PVC fabric with the printed Ag ink was then cured in a Carbolite box oven at a temperature of 120 °C for 15 min and the vinyl stencil was removed forming the gap between the IDEs (Figure 4.8(iv) and Figure 4.9b). A photograph of the transferred adhesive vinyl stencil on PVC fabric at the fabrication step ii is shown in Figure 4.9a for  $N = 10$ . In Figure 4.9b, a photograph of IDEs after curing and removing the vinyl stencil at the fabrication step iv is illustrated for  $N = 10$ . The widths of the gap were measured at 10 different points over the whole substrate using an optical microscope and the average width was calculated. Finally, the height profile of the Ag ink along the width was investigated using the Alphastep profiler. Ten measurements were performed over the whole substrate and an average of the Ag thickness was calculated.

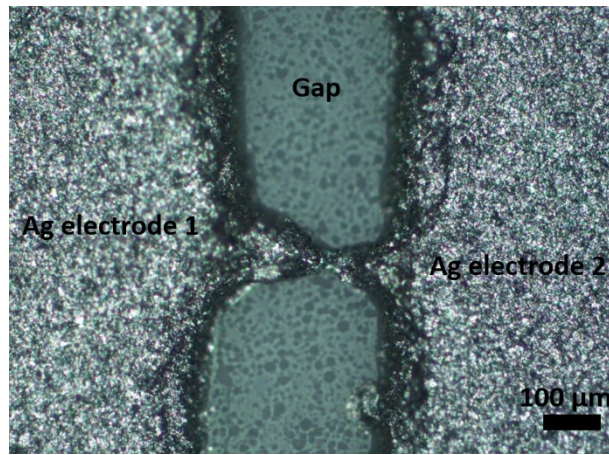


**Figure 4.10** Microscope image of a short position between two IDEs for the IDEs with a final gap of  $282 \pm 13 \mu\text{m}$ .

The size of the gap and IDE tines are defined by the vinyl stencil and the overall size of the IDEs is defined by the screen. The IDEs were fabricated for the designed vinyl stencil width of  $400 \mu\text{m}$  and  $600 \mu\text{m}$ . After the laser-cutting, the real vinyl stencil widths were measured using an optical microscope. They reduced to  $265 \pm 20 \mu\text{m}$  and  $425 \pm 12 \mu\text{m}$ , respectively, due to the finite size of the laser spot. After screen-printing and removing the stencil, the final widths of the gap between the IDEs became  $282 \pm 13 \mu\text{m}$  and  $508 \pm 34 \mu\text{m}$ , respectively. The smaller the gap, the larger is the effective contact area between the upper substrate and the IDEs, especially for the pnG-TENG with large grating numbers, since the total area of the gaps between the IDEs fingers increases with the grating number. However, the smaller the gap, the higher is the possibility that the IDEs electrically short, especially in the real operation. For this reason, the IDEs with a final width of  $508 \pm 34 \mu\text{m}$  was chosen for the pnG-TENGs. The average thickness of the Ag IDEs is  $51 \pm 11 \mu\text{m}$ . Figure 4.10 shows an example of a short position between 2 electrode fingers of the IDEs with the final gap of  $282 \pm 13 \mu\text{m}$ . Finally, the PVC fabric with the Ag IDEs was cut and attached to the acrylic lower substrate. The size of the IDE tines was fabricated to match the size of the strips of the triboelectric materials on the upper substrate for  $N = 2, 4, 6, 8$  and  $10$ . Once the optimum IDE structure and the corresponding value for  $N$  is defined, it is possible to directly print the required IDEs design using a patterned screen which is better suited for high-volume production. However, for this work, it is more flexible and cost-effective to use the vinyl stencil since alternative IDEs structures can be promptly designed, fabricated and investigated.



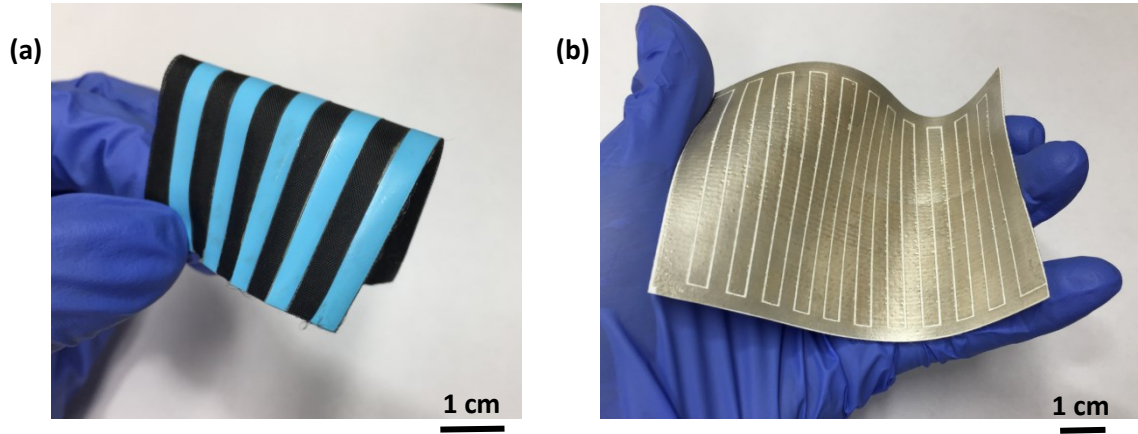


**Figure 4.11** Photograph of (a) the upper substrate and (b) the lower substrate of the pnG-TENG without the acrylic sheet for  $N = 10$ .

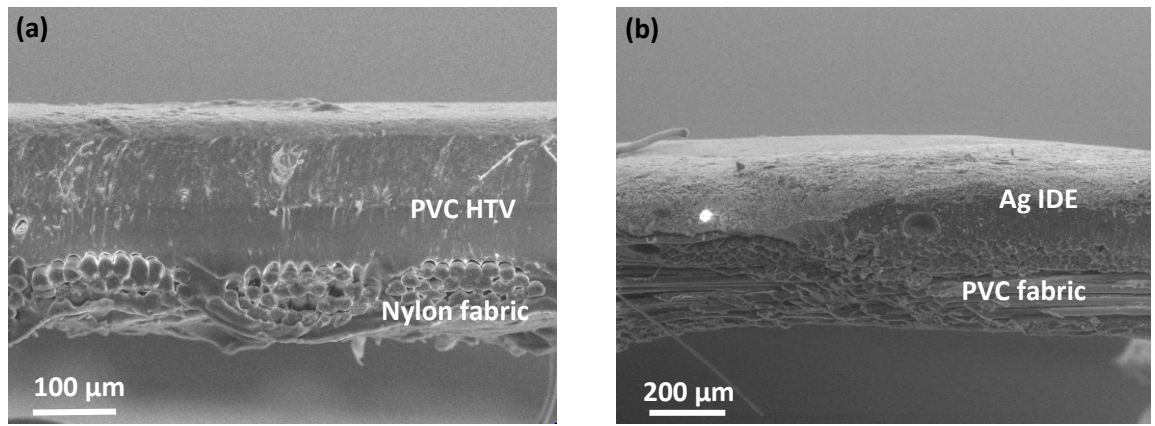


**Figure 4.12** Scanning electron microscope (SEM) images of (a) the upper substrate and (b) the lower substrate.

The flexibility of the pnG-TENG is demonstrated in the photographs of the upper and lower substrates of the pnG-TENG for  $N = 10$  in Figure 4.11a and b, respectively. Note that the number of Ag tines on the lower substrate is  $2N+2$  since the left most and right most tines serve as the connections to the external circuit. The SEM images of the upper and lower substrates are illustrated in Figure 4.12a and b, respectively. They show that the PVC HTC and the Ag IDEs are firmly bonded to the lower fabric substrates.

To compare the performance of the pnG-TENG with the conventional FT-mode TENGs, the TENGs with no grating ( $N = 1$ ) and the G-TENGs with single triboelectric material (pG-TENGs and nG-TENGs) were also fabricated. The schematic illustration of the TENGs with no grating and the G-TENGs with single triboelectric material are represented in Figure 4.13a and b, respectively. The structure of the TENGs with no grating is similar to the pnG-TENGs. The difference is that the triboelectric materials of the upper substrate were made of a single piece of nylon fabric or PVC HTV. The lower Ag IDEs are the same as those of the pnG-TENGs, except the IDEs for  $N = 1$  that have only 2 tines. For the fabrication of the upper substrate of the pG-TENGs and the nG-TENGs, the acrylic upper substrate was laser-cut into grating structures with  $N$  segments. Then, the 1-mm-thick

fabric, the double-sided tapes and the triboelectric material were stuck to the acrylic and cut into the same configuration as the acrylic. As a result, alternating strips of the air gaps and the triboelectric material occur.

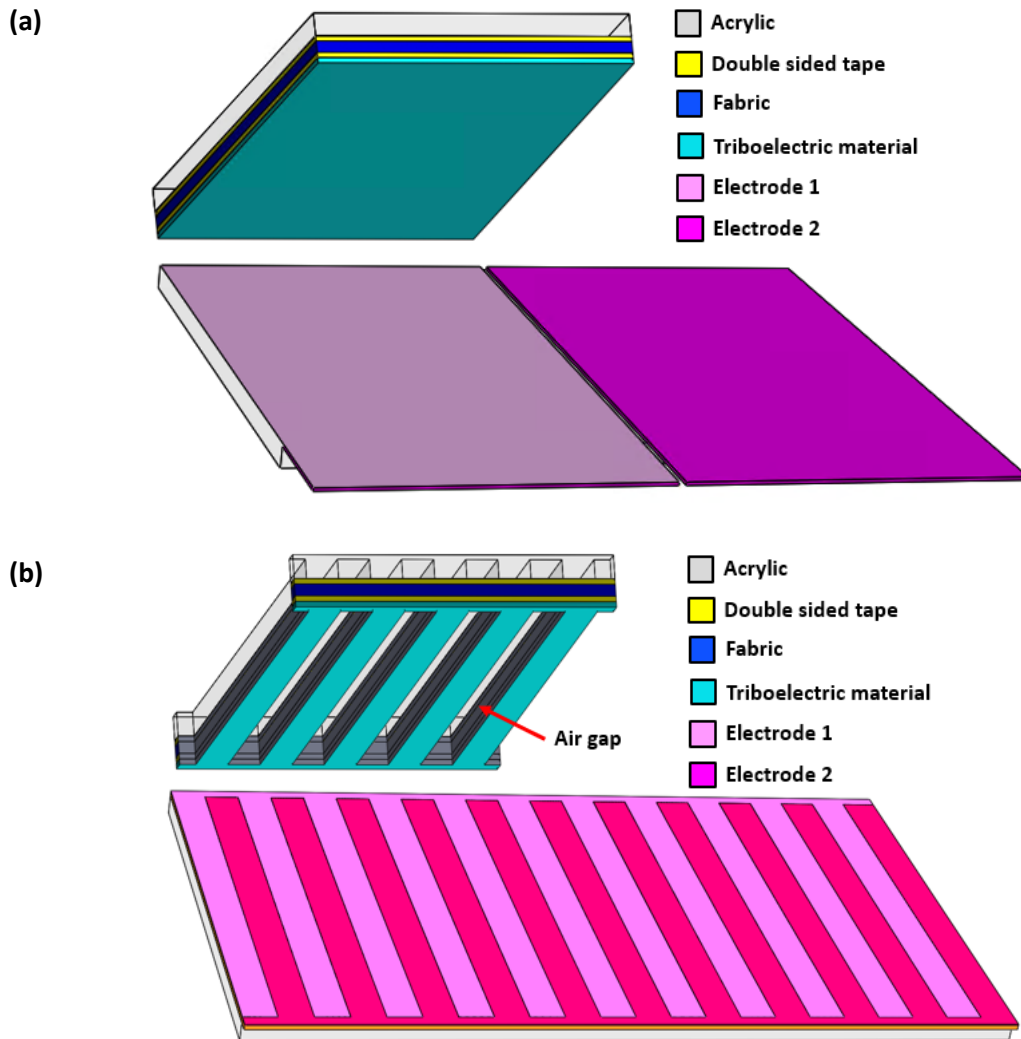


**Figure 4.13** Schematic illustration of (a) TENGs with no grating and (b) G-TENGs with single triboelectric material.

#### 4.2.2 Working principle

The operation mechanism of pnG-TENG for  $N = 2$  is illustrated in Figure 4.14. When the positive triboelectric material (nylon fabric) and negative triboelectric material (PVC HTV) with respect to the Ag electrodes are brought into contact with the Ag electrodes, positive and negative charges build up at their surface respectively and at the same time, the same amount of charge with the opposite polarity is transferred to the electrodes based on the contact electrification effect. Initially (Figure 4.14(i)), the upper substrate fully overlaps with the first two tines (from left) of the electrodes. In this state, no charge transfer occurs due to the electrostatic equilibrium between the electrodes. When the upper substrate moves further to the right-hand side and partly

overlaps with the next electrode tine (Figure 4.14(ii)), the electrons flow from the first and the third tine to the second tine, because the electric potential of the second tine increases due to the presence of the positive surface charge of the above positive material based on the electrostatic induction effect. At the same time, the electric potential of the first and the third tine decreases due to the absence of the positive material and the presence of the negative material, respectively. As a result, current flows from metal electrode 2 to 1 until another electrostatic equilibrium is reached at the next fully overlapping position (Figure 4.14(iii)). When the upper substrate continues to move, the electric potential in the electrodes increase and decrease alternately resulting in an alternating current through the load. As shown in Figure 4.14(ii, iv, vi, viii)), four current cycles are generated in one moving cycle. The number of current cycles per moving cycle is twice the grating number.

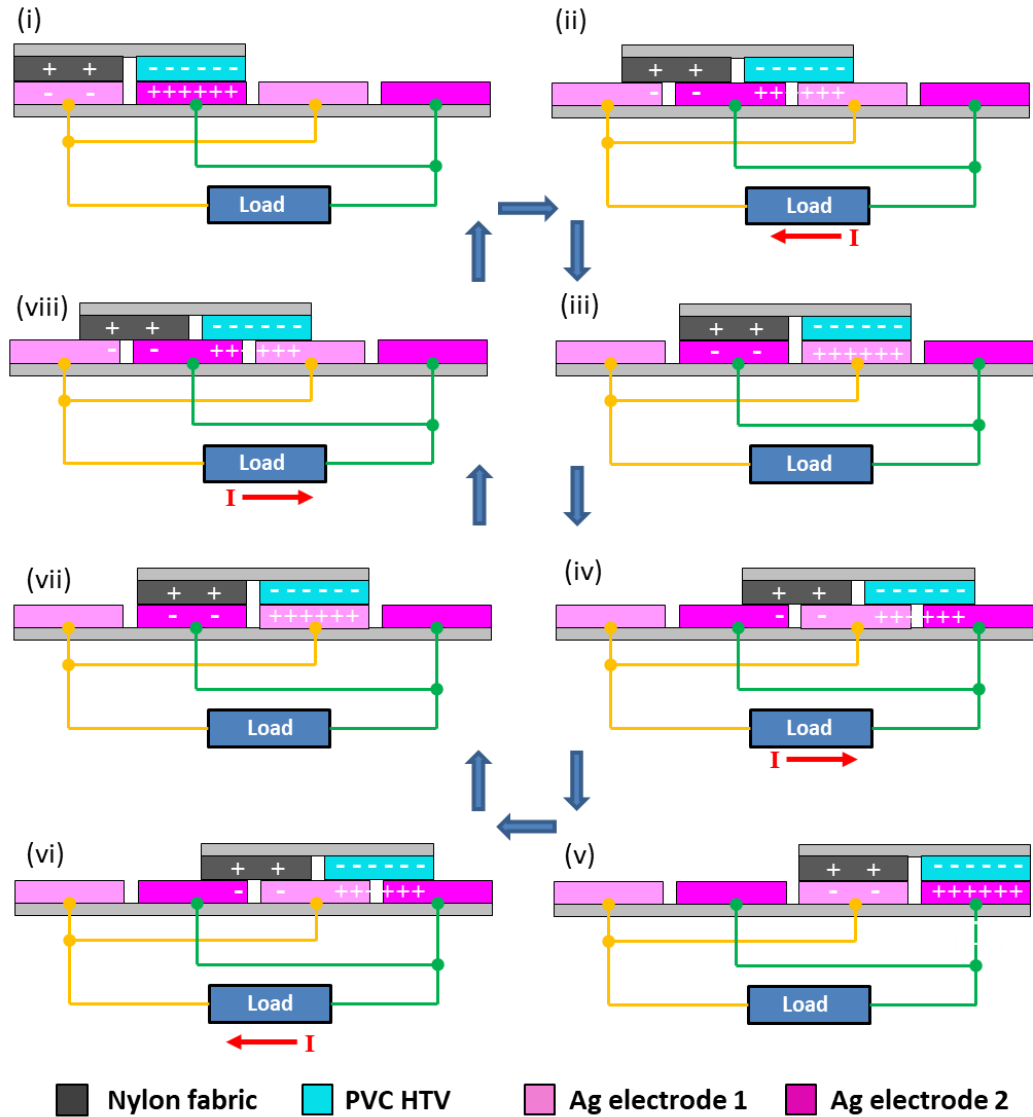


**Figure 4.14** Schematic illustration of the operating mechanism of pnG-TENG for  $N = 2$  with finite load resistance.

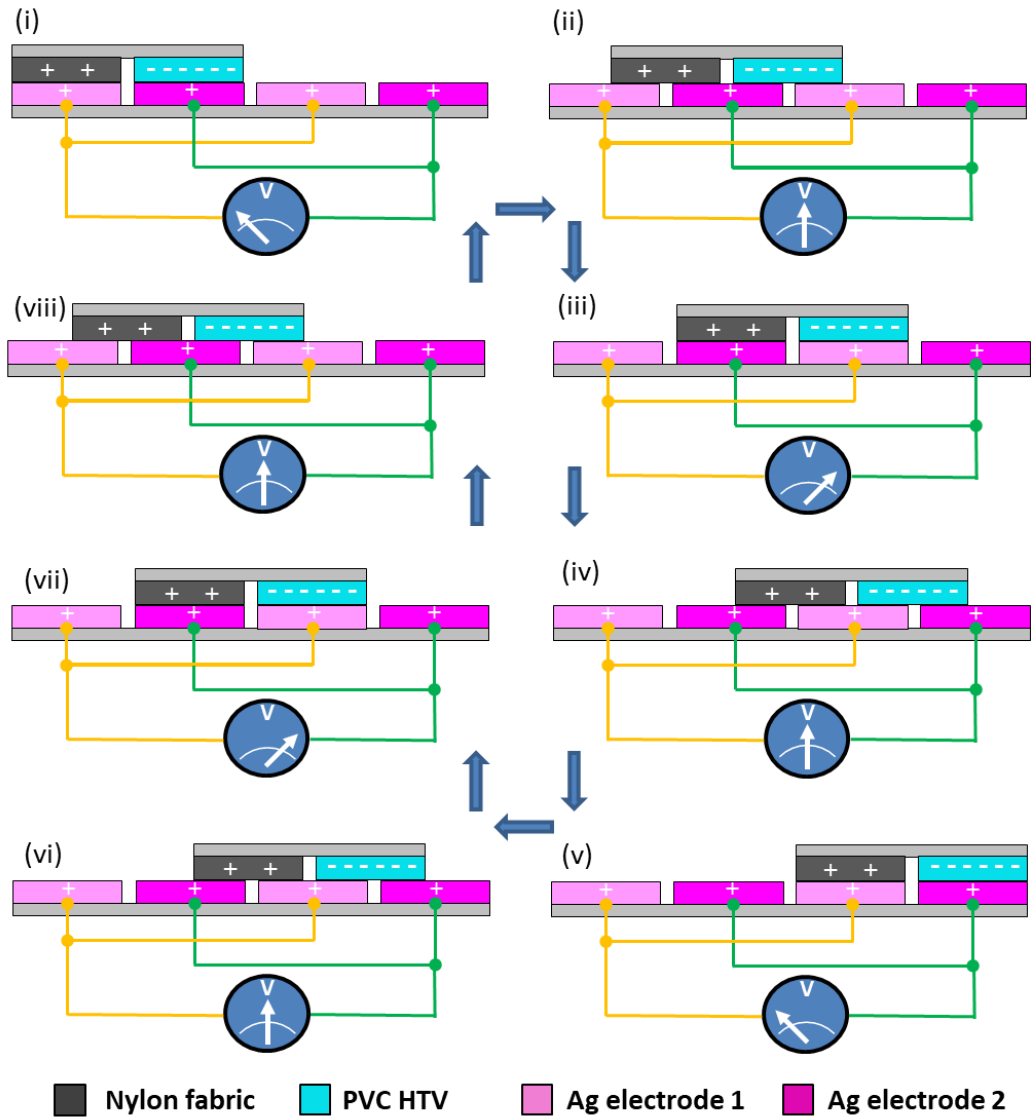


**Figure 4.15** Schematic illustration of the operating mechanism of pnG-TENG for  $N = 2$  in open-circuit condition.

Figure 4.15 shows the Schematic illustration of the operating mechanism of pnG-TENG for  $N = 2$  in open-circuit condition. The initial state shown Figure 4.15(i) is the state when the freestanding triboelectric materials are rubbed against the electrodes for a while, until triboelectric charge transfer is in equilibrium and the surface charges on all materials are saturated. At this state, the sum on the charge on the triboelectric materials are equal to the sum of the charge on the electrodes. Since all electrodes are symmetric and are in open-circuit condition, the number of the charges on both electrodes are always equal and they always offset each other when calculating the electric potential difference between the electrodes. For this reason, the charges on the electrodes can be neglect when calculating the  $V_{oc}$ . The charges which contribute to  $V_{oc}$  are the charges on the triboelectric materials. In state (i), the positive charges are over Ag electrode 1 and the negative charges are over Ag electrode 2, thus the electric potential on Ag electrode 1 is higher than Ag electrode 2 and the  $V_{oc}$  is positive. When the triboelectric materials move further and



locate in the middle of the tines (Figure 4.15(ii)), the number of the positive charges and the negative charges over Ag electrode 1 and 2 are equal, thus  $V_{oc}$  is zero. In state (iii), the triboelectric materials move further, and the positive charges and negative charges present over Ag electrode 2 and 1, respectively, resulting in negative  $V_{oc}$ . When the upper substrate continues to move, the electric potential in the electrodes increase and decrease alternately resulting in an alternating  $V_{oc}$ .

### 4.2.3 Characterisation and measurement

To obtain scientifically rigorous measurement results and to assure the repeatability of the experiments, the belt-driven linear actuator placed in the environmental chamber (Weiss Technik WKL100) was used to generate a lateral sliding motion between the upper and lower substrates, as explained in detail in Section 3.2.1. All measurements were performed at an oscillation frequency of 2 Hz, an amplitude of 48 mm, a contact force of 5 N, a humidity of 25 %RH and a temperature of 25 °C, except during the frequency and force dependence measurements during which the frequency and force were varied. Open-circuit voltage ( $V_{oc}$ ) and short-circuit current ( $I_{sc}$ ) measurements were carried out using an oscilloscope (Agilent DSO3062A) at 1 G $\Omega$  load and a DC power analyzer (Agilent N6705B), respectively. The outputs of the TENGs were rectified using a commercial full-wave bridge rectifier (Diodes Inc DF10M). The rectified outputs were then used to charge a 10- $\mu$ F electrolytic capacitor. During charging, the capacitor voltages ( $V_c$ ) were measured using a digital multimeter (Tenma 72-7780). The average widths of the IDEs gap and the average thickness of the IDEs were calculated from the measurement at 10 different points over the whole lower substrate using an optical microscope (Nikon Eclipse LV100) and an Alphastep profiler (Tencor PZ11), respectively. COMSOL Multiphysics software was employed for the electrical simulations. It is to note that 3 pnG-TENGs were built and tested, and the best output is presented in the following experimental result section.

## 4.3 Results and discussion

### 4.3.1 Grating number dependence

The dependence of the outputs of the pnG-TENG, pG-TENG and nG-TENG on the grating number  $N$  were firstly simulated using COMSOL, then theoretically calculated and finally experimentally investigated as follows.

#### 4.3.1.1 Simulation and theoretical calculation

To theoretically investigate the effect of the different grating numbers on the outputs of TENGs, the peak  $V_{oc}$  of FT-mode TENGs with no grating ( $N = 1$ ) and different types of G-TENGs (pG-

TENG, nG-TENG and pnG-TENG) with  $N = 2, 4, 6, 8, 10$  were simulated using COMSOL and the corresponding average  $I_{sc}$  were theoretically calculated based on electrostatic induction and the charge conservation principle. The positive and negative triboelectric material were nylon and PVC, respectively, whereas the IDEs were made of Ag. The electrostatics physics with normal free triangular mesh was used to simulate the maximum  $V_{oc}$  at a stationary state of the G-TENGs when the triboelectric materials fully overlap with the electrodes tines. The surface charge density of the negative material (PVC) and the positive material (nylon) defined in the simulation were  $-17.07 \mu\text{C}/\text{m}^2$  and  $11.15 \mu\text{C}/\text{m}^2$ , respectively taken from the surface charge density measurement for the PVC HTV and nylon fabric against Ag using the bespoke Faraday's cup, shown in Figure 3.9b. It was assumed that the surface charge density of the TENG with no grating and the G-TENGs stay the same, although the contact pressure for the pG-TENGs and nG-TENGs double under a constant contact force compared to the pnG-TENGs and the TENGs with no grating because the total surface area of the pG-TENGs and nG-TENGs are only the half of the total surface area of the pnG-TENGs and the TENGs with no grating due to the air gaps.

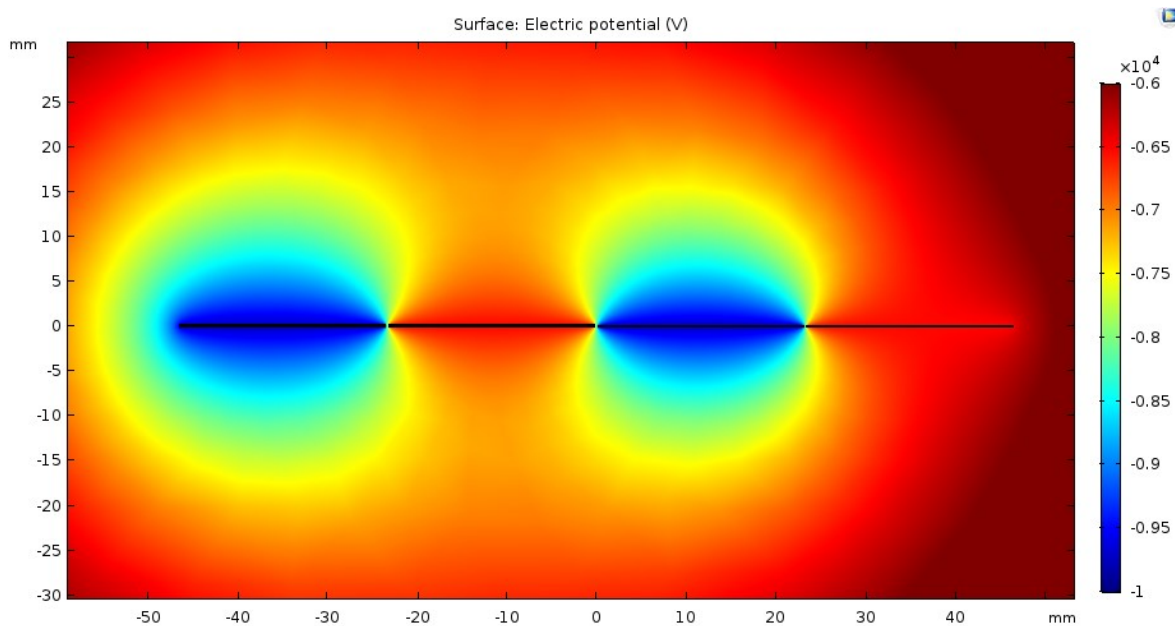


**Figure 4.16** Simulated electric potential distribution of pnG-TENG with nylon and PVC for  $N = 2$  using Comsol.

The simulated electric potential of pnG-TENG for  $N = 2$  in 2D is shown in Figure 4.16. In this cross-section view, the pnG-TENG consists of 4 Ag tines. The first and the third tine, and the second and the fourth tine (from left) are connected together forming the first and the second electrode of the IDEs respectively. As a consequence, the connected tines always exhibit the same electric potential. The PVC and nylon are placed over the first and second Ag tine, respectively. Due to the predefined surface charge density on the PVC and nylon surface ( $-17.07 \mu\text{C}/\text{m}^2$  and  $11.15 \mu\text{C}/\text{m}^2$ ), an electric potential of  $-9724 \text{ V}$  and  $-6524 \text{ V}$  are induced at the first and second electrode,

respectively, resulting in a  $V_{OC}$  of 3200 V. The reason why the potential of the second electrode is negative, although the surface charge density of nylon is positive, is that the surface charge density of the PVC is greater than that of the nylon and it induces a strong negative potential all around its environment, which outweighs the positive potential from the nylon.

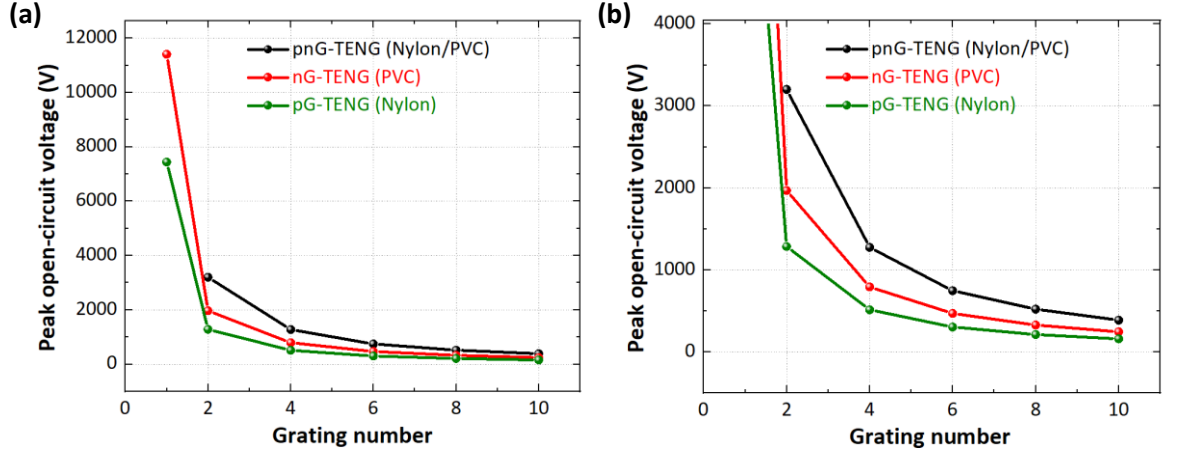


**Figure 4.17** Peak  $V_{OC}$  as a function of grating number for different types of TENGs (a) for  $N = 1 - 10$  and (b) zoom-in illustration for  $N = 2 - 10$ .

The  $V_{OC}$  of the different types of TENGs for the different grating numbers are represented in Figure 4.17a. Figure 4.17b shows the zoom-in illustration of the graph in Figure 4.17a for  $N = 2 - 10$ . With increasing grating number, the  $V_{OC}$  decreases for all types of TENGs. The result can be explained by Equation 4.1 below [150]:

$$V_{OC} = \frac{\Delta\sigma_{sc} \cdot S}{C} \quad (4.1)$$

where  $\Delta\sigma_{sc}$  is the short-circuit transferred charge density,  $S$  is the total area of the first or second electrode and  $C$  is the capacitance between the first and the second electrode. Because  $\Delta\sigma_{sc}$  and  $S$  are constant for  $N = 2 - 10$  and  $C$  increases when the electrodes are divided into small segments,  $V_{OC}$  decreases with increasing grating number. The  $V_{OC}$  of the TENGs with no grating ( $N = 1$ ) is much higher than the others since the area of the triboelectric material for  $N = 1$  is twice as large as the total area of the triboelectric materials of the pG-TENG and nG-TENG for  $N = 2 - 10$ , which is partly replaced by air gaps (see Figure 4.13b). The  $V_{OC}$  of the pnG-TENGs is enhanced for all grating numbers compared to the pG-TENGs and the nG-TENGs since  $\Delta\sigma_{sc}$  is proportional to the difference between the surface charge densities of the materials placed on the electrodes, which will be next demonstrated in Equation 4.7.

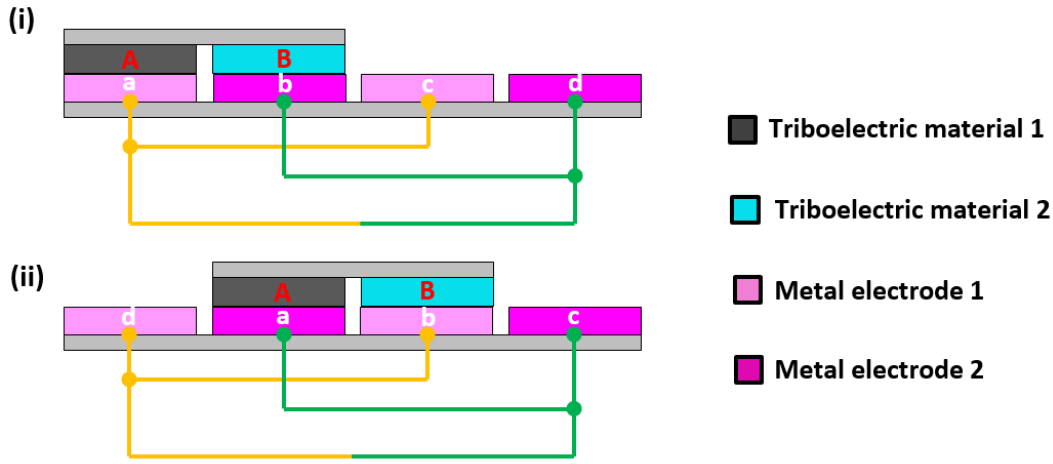


**Figure 4.18** Schematic illustration applied for theoretical calculation of average  $I_{SC}$ .

The model applied for the theoretical calculation of the average  $I_{SC}$  is revealed in Figure 4.18. Two stationary states of a pnG-TENG with  $N = 2$  in a short-circuit condition at equilibrium are depicted. At the first state (i), the triboelectric materials fully overlap with the first two tines (from left) of the electrodes. The amount of charge on the triboelectric materials 1 and 2 are denoted  $A$  and  $B$ . The amount of induced charge at the first, second, third and fourth electrode tine are represented by  $a$ ,  $b$ ,  $c$  and  $d$ , respectively. The amount of charge can be either negative or positive. Due to triboelectric charge separation and charge conservation principle, the sum of the charges on the top substrate is equal to the sum of the charges on the electrodes but with opposite polarity. This relationship can be expressed as the following equation:

$$A + B = -(a + b + c + d) \quad (4.2)$$

At equilibrium, the electric potential at each electrode tine has to be the same, therefore the sum of the charges at each tine are equal. This can be expressed by Equation 4.3 below:

$$A + a = B + b = c = d \quad (4.3)$$

At the second state (ii), the triboelectric materials move to the right and fully overlap with the second and the third tine (from left). Assuming that all tines are identical, the induced charge at the first, second, third and fourth electrode tine are now  $d$ ,  $a$ ,  $b$  and  $c$ , respectively. Similarly, the sum of the charges at each tine are equal at the equilibrium and the same equation is obtained. Equation 4.3 can be rewritten as Equation 4.4 below:

$$a - b = B - A \quad (4.4)$$

The amount of transferred charge between the electrode 1 and 2 ( $\Delta Q_{SC}$ ) is the difference in the charge at electrode 2 in the first and second states. This can be expressed as the following equation:

$$\Delta Q_{SC} = (a + c) - (b + d) = a - b \quad (4.5)$$

because  $c$  is equal to  $d$  (Equation 4.3). By substitution of Equation 4.4 into Eq. Equation 4.5, we obtain

$$\Delta Q_{SC} = a - b = B - A \quad (4.6)$$

According to Equation 4.6, the  $\Delta Q_{SC}$  is equal to the difference in the amount of charge on the triboelectric materials. It is to note that, since Equation 4.2 has not been applied for the derivation of the  $\Delta Q_{SC}$ , Equation 4.6 is still valid, even though the transferred triboelectric charge on the electrodes are initially discharged and the total number of charges on the electrodes is zero. This case can happen quite often, for instance, the electrodes can be discharged through contact with the skin. With a constant area of the triboelectric materials ( $A_M$ ), the surface charge density on triboelectric material 1 ( $\rho_{q,A}$ ) and the surface charge density on triboelectric material 2 ( $\rho_{q,B}$ ). The  $\Delta Q_{SC}$  in Equation 4.6 can be expressed as Equation 4.7 below:

$$\Delta Q_{SC} = B - A = A_M \cdot (\rho_{q,B} - \rho_{q,A}) = A_M \cdot \Delta \rho_q = S \cdot \Delta \sigma_{SC} \quad (4.7)$$

and combined with Equation 4.1, the average  $I_{SC}$  can be calculated using Equation 4.8 below:

$$I_{SC} = \frac{\Delta Q_{SC}}{\Delta t} = \frac{A_M \cdot (\rho_{q,B} - \rho_{q,A})}{\Delta t} = \frac{A_M \cdot \Delta \rho_q}{\Delta t} = \frac{S \cdot \Delta \sigma_{SC}}{\Delta t} \quad (4.8)$$

where  $\Delta t$  is the time taken of the upper substrate to move from one electrode time to the next electrode time.

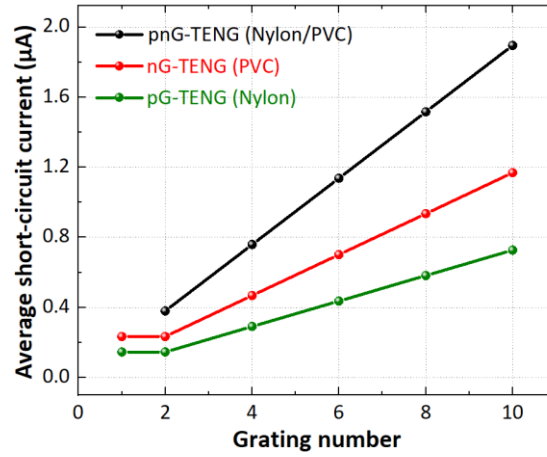


**Figure 4.19** Calculated average  $I_{SC}$  as a function of grating number for different types of TENGs.

The calculated average  $I_{SC}$  of the different types of TENGs for the different grating numbers are represented in Figure 4.19. With increasing grating number, the average  $I_{SC}$  increases linearly for all types of the G-TENGs ( $N \geq 2$ ), because the  $\Delta t$  reduces when the grating number rises. The average  $I_{SC}$  of the TENGs with no grating ( $N = 1$ ) and the G-TENGs ( $N = 2$ ) are equal because both the  $\Delta t$  and the area  $A_M$  of the TENGs with no grating are twice the G-TENGs ( $N = 2$ ). As before, a constant surface charge density of nylon of  $11.15 \mu C/m^2$  and PVC of  $-17.07 \mu C/m^2$  are used in the

calculation for all TENGs. However, from the result of contact force dependence measurement shown in Section 4.3.3., the surface charge densities for the G-TENGs ( $N \geq 2$ ) can be higher than those of the TENGs with no grating since the contact pressure for the G-TENGs doubles under a constant applied force due to the half contact area.

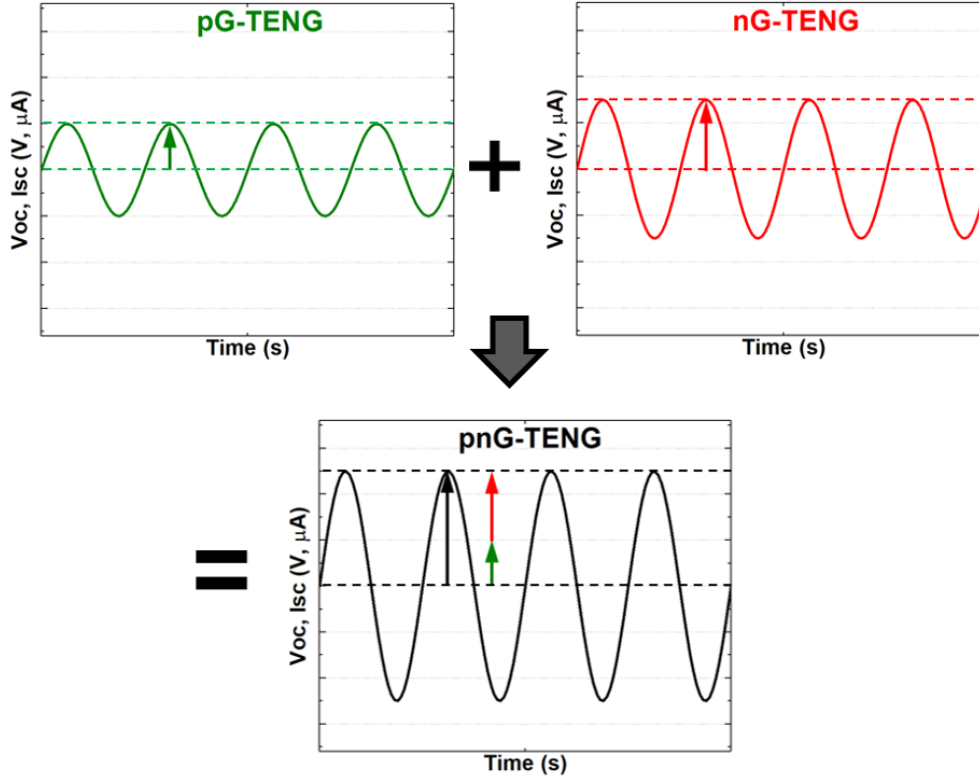


**Figure 4.20** Schematic illustration of the electrical outputs of pnG-TENG compared to pG-TENG and nG-TENG. The outputs of pnG-TENG are equal to the sum of the outputs of pG-TENG and nG-TENG.

According to Equation 4.1 and Equation 4.8, both the  $V_{oc}$  and  $I_{sc}$  of the pnG-TENGs are directly proportional to the difference in the surface charge densities of the triboelectric materials, therefore the  $V_{oc}$  and  $I_{sc}$  of the pnG-TENGs are theoretically equal to the sum of those values of the pG-TENGs and the nG-TENGs as observed in Figure 4.17 and Figure 4.19. To better demonstrate this relationship, the schematic illustration of the transient outputs ( $V_{oc}$  and  $I_{sc}$ ) of pnG-TENG compared to the outputs of pG-TENG and nG-TENG is presented in Figure 4.20.

#### 4.3.1.2 Experiment

The electrical measurements were performed for the TENGs with no grating ( $N = 1$ ) and the different types of G-TENGs with  $N = 2, 4, 6, 8, 10$ . The upper substrates of the TENGs are made of nylon fabric and/or PVC HTV. The electrodes are made of the screen-printed Ag. The time-dependent  $V_{oc}$  and  $I_{sc}$  of non-grated TENG with nylon fabric (nylon ( $N = 1$ )), non-grated TENG with PVC HTV (PVC HTV ( $N = 1$ )), pG-TENG with nylon fabric (nylon ( $N = 10$ )), nG-TENG with PVC HTV

(PVC HTV ( $N = 10$ )) and pnG-TENG with nylon fabric and PVC HTV (Nylon/PVC HTV ( $N = 10$ )) are illustrated in Figure 4.21a and b, respectively.

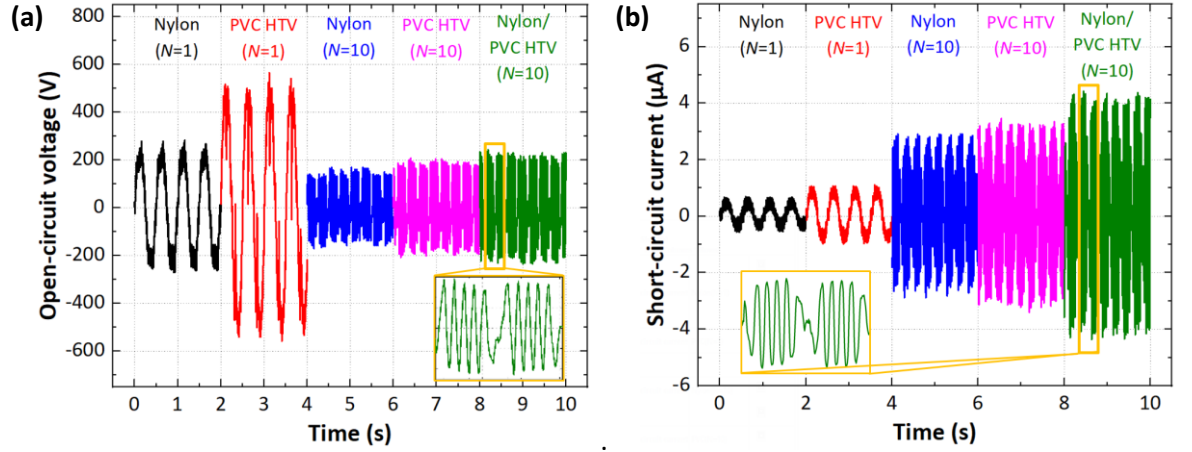


**Figure 4.21** (a) Transient  $V_{OC}$  and (b)  $I_{SC}$  of different types of TENGs. The insets show the magnified illustration of the  $V_{OC}$  and  $I_{SC}$  of the pnG-TENG with  $N = 10$  for one moving cycle ( $\Delta t = 0.5$  s).

In good accordance with the simulation result, the TENGs with no grating generate a greater  $V_{OC}$  than the G-TENGs. The insets show the zoom-in illustration of the  $V_{OC}$  and  $I_{SC}$  of the pnG-TENG for one moving cycle ( $\Delta t = 0.5$  s). Instead of one peak per oscillation as for the TENG with no grating, ten peaks are generated during the forwards movement and another ten peaks during the backwards movement, including both positive and negative peaks. The same result is also observed for the pG-TENGs and the nG-TENGs with the different grating numbers that the frequency of peaks per moving direction is equal to the grating number ( $N$ ). Apart from the number of the peaks, the amplitude of the  $I_{SC}$  also increases according to Equation 4.8 since the  $\Delta t$  for a certain transferred charge  $\Delta Q_{SC}$  is significantly reduced due to the reduction in the width of the Ag electrode tines. From these two main reasons (frequency and amplitudes of peaks), the current outputs of G-TENGs are significantly enhanced.

To investigate the total transferred charges, the rectified output currents were used to charge a 10- $\mu F$  capacitor. In Figure 4.22a, the time-dependent  $V_C$  for the same types of TENGs are revealed. The  $V_C$  for the pnG-TENG reaches a value of 61.9 V in 600 s, which is considerably higher than the nG-TENG, the pG-TENG and more than 4 times higher than the TENGs with no grating. The corresponding transient capacitor charging current and the transient capacitor charging power are shown in Figure 4.22b and c, respectively. The transient capacitor charging current  $I_C$  (Figure 4.19b) is calculated from the  $V_C$  (Figure 4.22a) using Equation 4.9 below:

$$I_C = \frac{\Delta Q}{\Delta t} = \frac{C \cdot \Delta V_C}{\Delta t} \quad (4.9)$$

where  $\Delta Q$  is the transferred charge during a charging time  $\Delta t$  of 30 s,  $\Delta V_C$  is the change in  $V_C$  between a charging time  $\Delta t$  of 30 s and  $C$  is the capacitance e.g. 10  $\mu F$ .

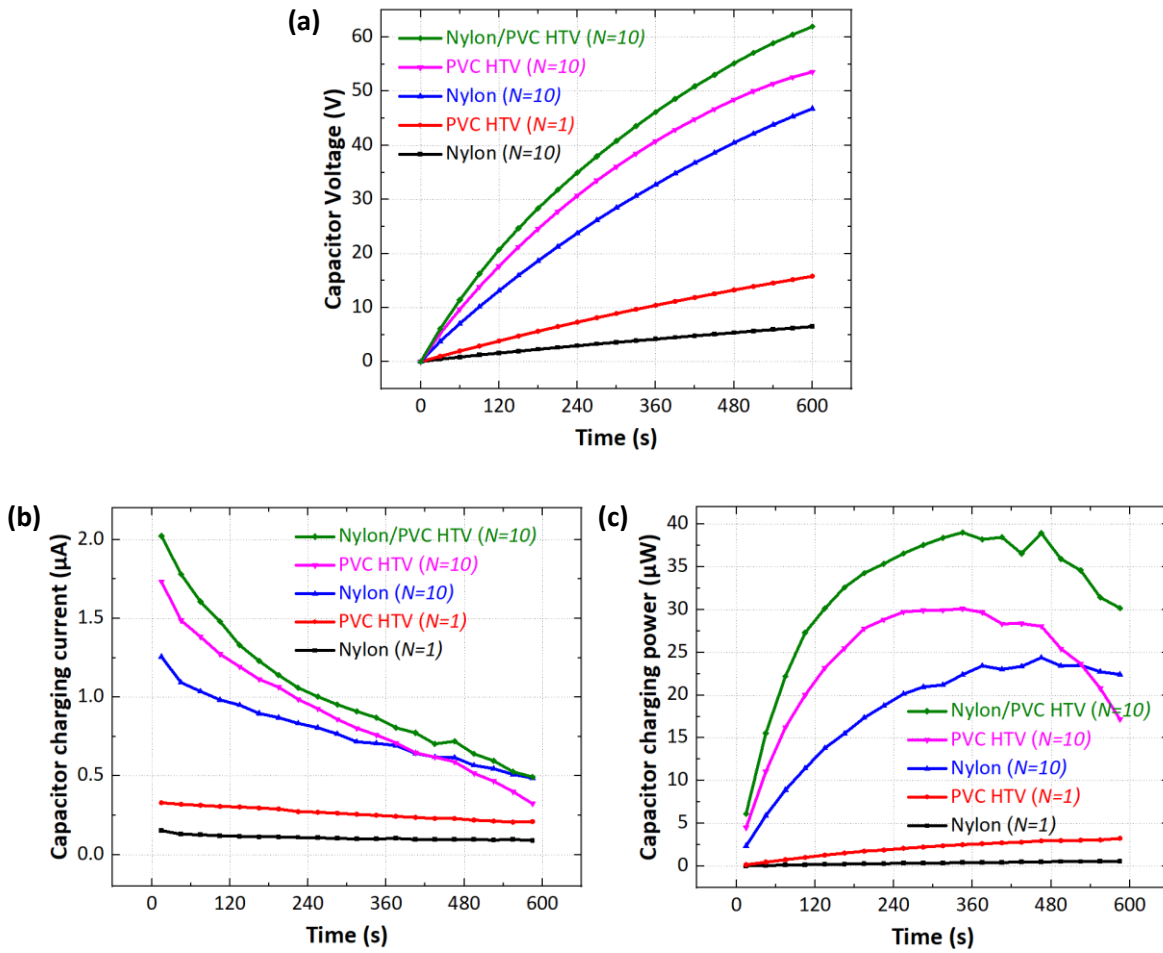


**Figure 4.22** (a) Capacitor voltage, (b) calculated capacitor charging current and (c) calculated capacitor charging power as a function of time for different types of TENGs.

The  $I_c$  decreases over time for all TENGs. The pnG-TENG produces the maximum  $I_c$  of 2.02  $\mu\text{A}$ , followed by the pG-TENG, the nG-TENG and the TENGs with no grating. The reason for the reduction in  $I_c$  over time is due to the growth in  $V_c$  and the increase in the stored charge in the capacitor, reducing the movement of electrons. The transient capacitor charging power  $P_c$  (Figure 4.22c) is also calculated from the  $V_c$  (Figure 4.22a) using Equation 4.10 below:

$$P_c = \frac{\Delta E}{\Delta t} = \frac{\frac{1}{2}C(V_{C,2}^2 - V_{C,1}^2)}{\Delta t} \quad (4.10)$$

where  $\Delta E$  is the change in capacitor energy between a charging time  $\Delta t$  of 30 s. The  $P_c$  of the pnG-TENG reaches the maximum value of 39.0  $\mu\text{W}$ , with the  $P_c$  of the other TENGs in the same peak performance sequence as the two previous graphs.



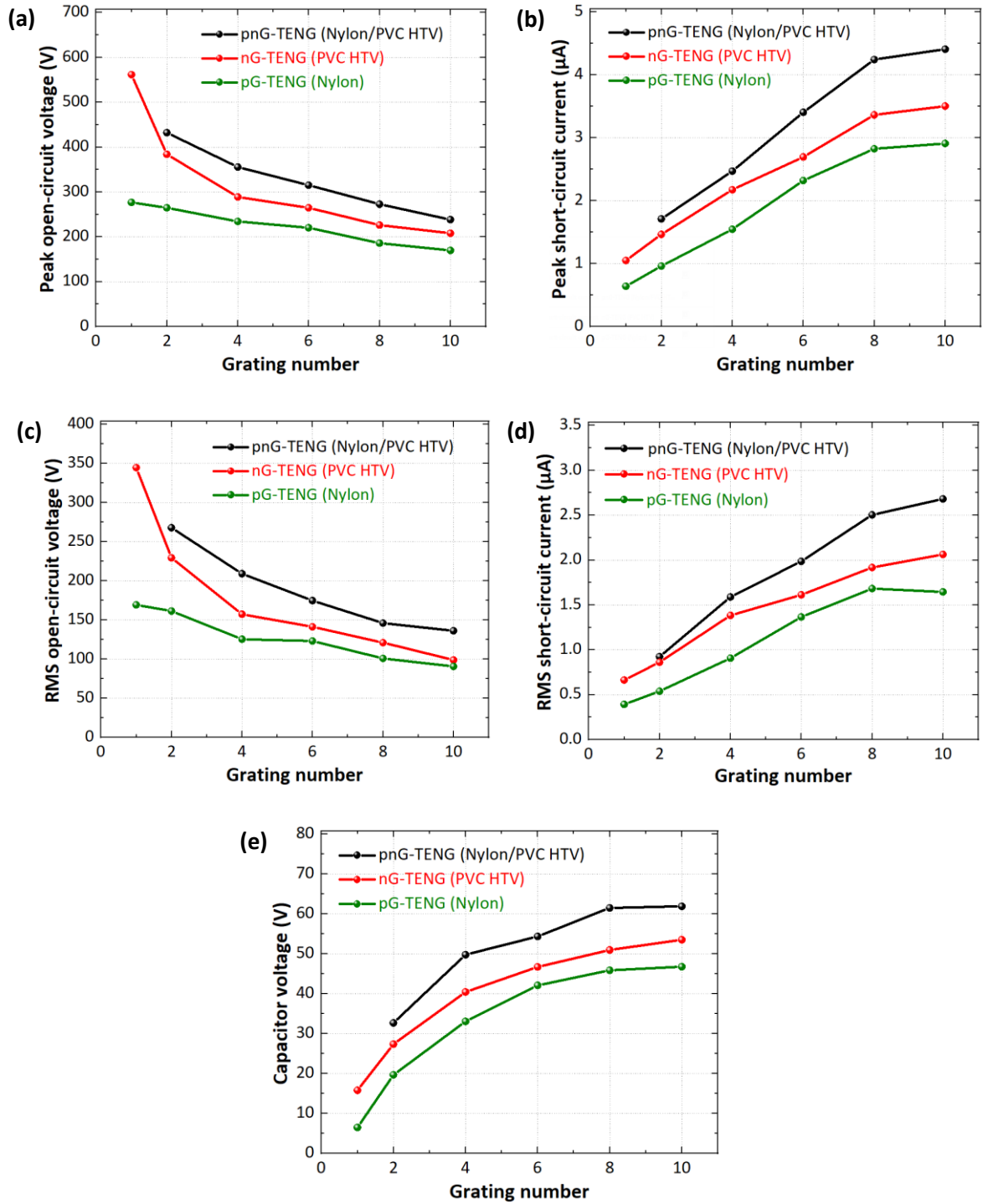


**Figure 4.23** (a) Peak  $V_{OC}$ , (b) Peak  $I_{SC}$ , (c) RMS  $V_{OC}$ , (d) RMS  $I_{SC}$  and (f)  $V_C$  at a charging time of 600 s as a function of grating number for the different types of TENGs.

The zero to peak values of the  $V_{OC}$  and  $I_{SC}$ , the root mean square (RMS) values of the  $V_{OC}$  and  $I_{SC}$  and the maximum  $V_C$  at a charging time of 600 s as a function of grating number for the different types of TENGs are represented in Figure 4.23a - e, respectively. In good agreement with the simulation result,  $V_{OC}$  has a tendency to decrease with increasing grating number for all types of TENGs, whereas the  $I_{SC}$  and  $V_C$  show an increasing trend. As expected, the  $I_{SC}$  of the pG-TENG and nG-TENG for  $N = 2$  are higher than those of the TENGs with no grating due to the higher surface charge densities as discussed in the simulation section. Compared to the nG-TENGs and the pG-

TENGs, the outputs of the pnG-TENG are enhanced for all grating numbers. Nevertheless, the outputs of the pnG-TENG are smaller than the sum between the outputs of the pG-TENGs and the nG-TENGs because the surface charge densities of the nylon fabric and the PVC HTV of the pnG-TENGs are less than those of the individual pG-TENGs and nG-TENGs for the same applied contact force. The contact force is spread across the contact area and the effective contact area of the pnG-TENGs is double that of the single material TENGs and thus have half the contact pressure. To confirm this, double the contact force was applied on the pnG-TENG with 10 gratings so that the contact pressure was equivalent to the single material TENGs and this result is presented in the contact force dependence study in Section 4.3.3. Both the  $V_{OC}$  and  $I_{SC}$  increase from 72% to 92% of the sum between the outputs of the pG-TENG and the nG-TENG, when the contact force is doubled. The small deviation compared to the simulation stem from the reduction in the effective contact area due to the gap between the IDEs and an uneven surface between nylon fabric and PVC HTV.

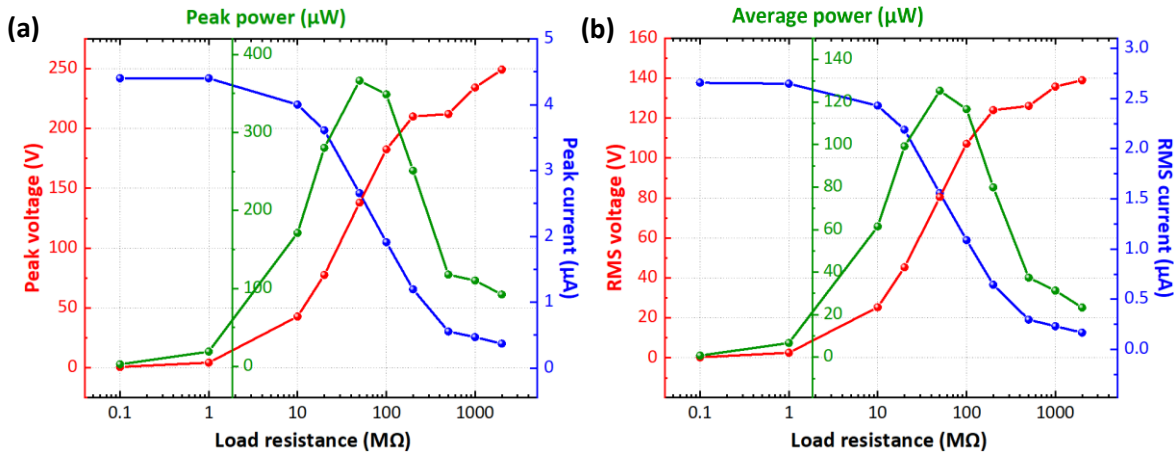


**Figure 4.24** (a) The dependence of the peak voltage  $V_{pk}$ , peak current  $I_{pk}$  and peak power  $P_{pk}$  on the external load resistance for the pnG-TENG (Nylon/PVC,  $N = 10$ ) and (b) the corresponding RMS and average values.

The dependence of the peak voltage  $V_{pk}$ , peak current  $I_{pk}$  and peak power  $P_{pk}$  on the external load for the pnG-TENG (Nylon/PVC,  $N = 10$ ) and the corresponding  $V_{RMS}$ ,  $I_{RMS}$  and  $P_{avg}$  are illustrated in Figure 4.24a and b, respectively. The  $V_{pk}$  rises with increasing load resistance, then remains constant and reaches a  $V_{OC}$  of 238 V, while the  $I_{pk}$  exhibits a reversed tendency. It starts from an  $I_{SC}$  of 4.41 μA, then drops to zero at very large resistance. The  $V_{RMS}$  and  $I_{RMS}$  show the same tendency. The  $V_{OC,RMS}$  and  $I_{SC,RMS}$  are 139 V and 2.66 μA, respectively. The  $P_{pk}$  and  $P_{avg}$  are calculated using Equation 4.11 and 4.12 below:

$$P_{pk} = I_{pk} \cdot V_{pk} \quad (4.11)$$

$$P_{avg} = I_{RMS} \cdot V_{RMS} \quad (4.12)$$

The maximum  $P_{pk}$  and  $P_{RMS}$  reach 366  $\mu\text{W}$  and 125  $\mu\text{W}$  at a load resistance of 50  $\text{M}\Omega$ , corresponding to a power density of 114  $\text{mW}/\text{m}^2$  and 38.8  $\text{mW}/\text{m}^2$ , respectively.

In Figure 4.25a and b, the  $P_{pk}$  and  $P_{RMS}$  for the different types of TENGs are compared. At a load resistance of 50  $\text{M}\Omega$ , the pnG-TENG (Nylon/PVC,  $N = 10$ ) generates the highest  $P_{pk}$  and  $P_{RMS}$ , followed by the nG-TENG (PVC,  $N = 10$ ), the pG-TENG (Nylon,  $N = 10$ ), the TENG with no grating (PVC,  $N = 1$ ) and the TENG with no grating (Nylon,  $N = 1$ ). The result shows that at this load, the  $P_{RMS}$  of the pnG-TENG increases by a factor of 1.94 and 6.43, compared to the nG-TENG and the TENG with no grating, respectively. For the TENGs with no grating, the maximum  $P_{pk}$  and  $P_{avg}$  are at a load of 500  $\text{M}\Omega$ . At this load, the output voltage is very high but the current is very low, which are undesirable for electronic devices.

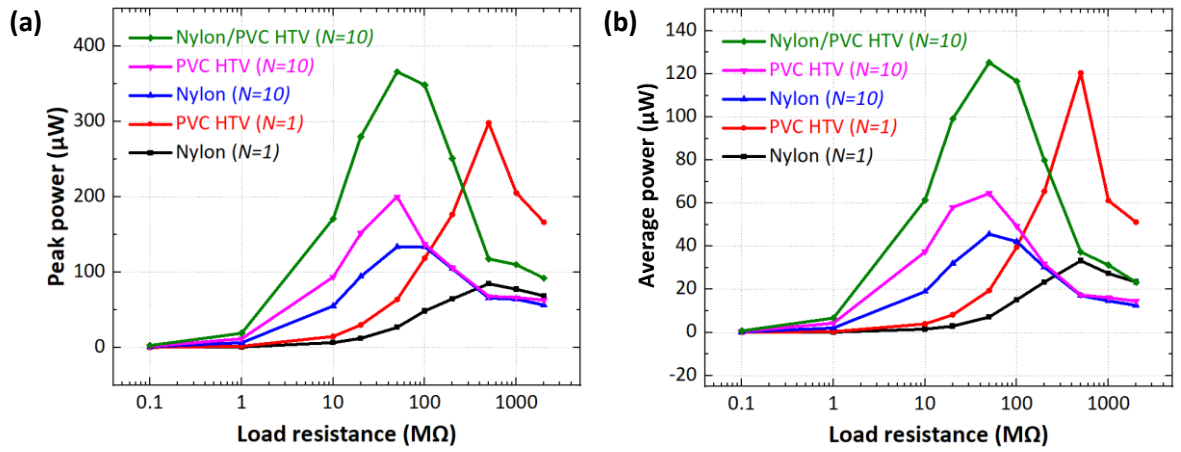


**Figure 4.25** (a) Load-dependent peak power  $P_{pk}$  and (b) load-dependent average power  $P_{avg}$  for different types of TENGs.

**Table 4.1** Summary of the electrical outputs of the different TENGs

TENG	$V_{OC}$ (V)	$V_{OC,RMS}$ (V)	$I_{SC}$ ( $\mu\text{A}$ )	$I_{SC,RMS}$ ( $\mu\text{A}$ )	$I_{C,max}$ ( $\mu\text{A}$ )	$P_{C,max}$ ( $\mu\text{W}$ )	$P_{pk}$ ( $\mu\text{W}$ )	$P_{avg}$ ( $\mu\text{W}$ )
Nylon/PVC ( $N = 10$ )	238	136	4.41	2.68	2.02	39.0	366	125
PVC ( $N = 10$ )	208	99	3.51	2.06	1.73	30.1	200	64.5
Nylon ( $N = 10$ )	170	91	2.91	1.65	1.26	24.4	134	45.7
PVC ( $N = 1$ )	562	345	1.05	0.66	0.33	3.25	64.0	19.5
Nylon ( $N = 1$ )	277	169	0.64	0.39	0.15	0.59	26.9	7.16

The electrical outputs of the different types of TENGs are summarised in Table 4.1. The results in this table confirm that the performance of the pnG-TENG (Nylon/PVC) outweighs the G-TENGs with single triboelectric material and the TENGs with no grating in almost all aspects, except that the  $V_{OC}$  of the TENGs with no grating are higher. The values of the maximum capacitor charging current  $I_{C,max}$  are considerably lower than  $I_{RMS}$ , which could be due to a loss in the rectifier circuit and a difference in the load resistance. The  $P_{avg}$  are much greater than the maximum capacitor

charging power  $P_{C,max}$  because the  $P_{C,max}$  represents the power at a smaller load (rectifier and capacitor), while the  $P_{avg}$  is obtained at a very high load (50 M $\Omega$ ).

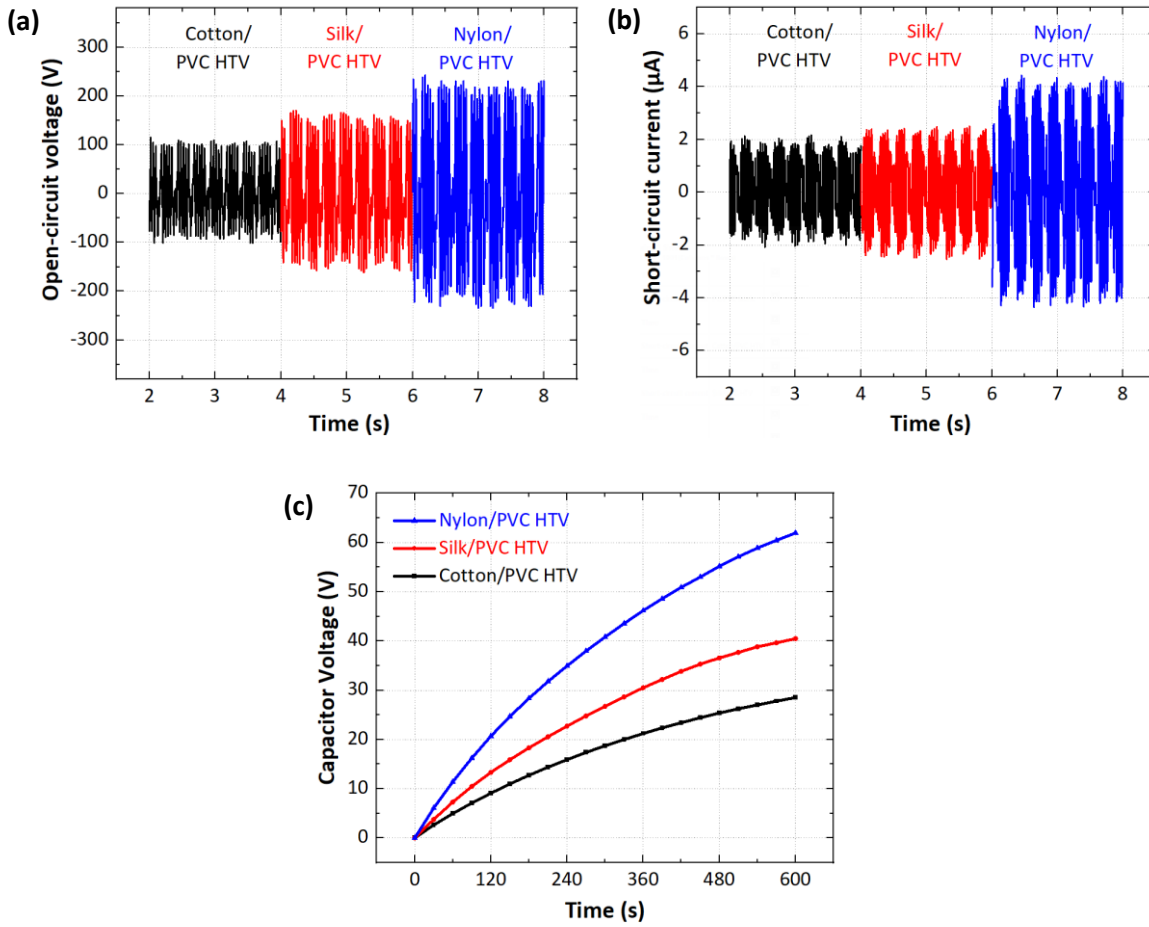


**Figure 4.26** (a)  $V_{OC}$ , (b)  $I_{SC}$  and (c)  $V_C$  of pnG-TENGs ( $N = 10$ ) as a function of time for different triboelectric materials.

To investigate the effect of the different fabric substrates, the pnG-TENG ( $N = 10$ ) with cotton/PVC HTV and silk/PVC HTV were fabricated with the same fabrication method described in Section 4.2.1. Their electrical outputs were then compared with the pnG-TENG with nylon/PVC HTV and plotted in the same graphs. The transient  $V_{OC}$ ,  $I_{SC}$  and  $V_C$  are illustrated Figure 4.26a – c, respectively. The pnG-TENG with nylon/PVC HTV produced by far the highest outputs with a peak  $V_{OC}$  of 238 V, a peak  $I_{SC}$  of 4.41  $\mu A$  and a maximum  $V_C$  of 61.94 V, followed by the outputs for the silk/PVC HTV, the cotton/PVC HTV. The order of the outputs are in good agreement with the positions of the materials in the triboelectric series.

### 4.3.2 Oscillation frequency dependence

The frequency dependence measurements were performed for the pnG-TENG with nylon and PVC HTV upper substrate and Ag IDEs ( $N = 10$ ) by varying the oscillation frequency of the linear actuator from 1 Hz to 3 Hz in increments of 0.5 Hz and maintaining the contact force at 5 N. The

transient  $V_{OC}$  and  $I_{SC}$  of the pnG-TENG for the different frequencies are demonstrated in Figure 4.27a and b, respectively. In Figure 4.28a and b, the corresponding peak values and RMS values of the  $V_{OC}$  and the  $I_{SC}$  are plotted as a function of oscillation frequency, respectively. At the beginning, the  $V_{OC}$  increases with increasing frequency, then it saturates for the frequency over 2.5 Hz. This can be explained by Equation 4.1 and Equation 4.7 that the  $V_{OC}$  is related to the difference in the surface charge densities of the triboelectric materials, which build up and saturate after a certain frequency. The  $I_{SC}$  rises approximately linearly with the frequency. The reason for this is that according to Equation 4.8, the  $I_{SC}$  is inversely proportional to time and thus directly proportional to frequency.

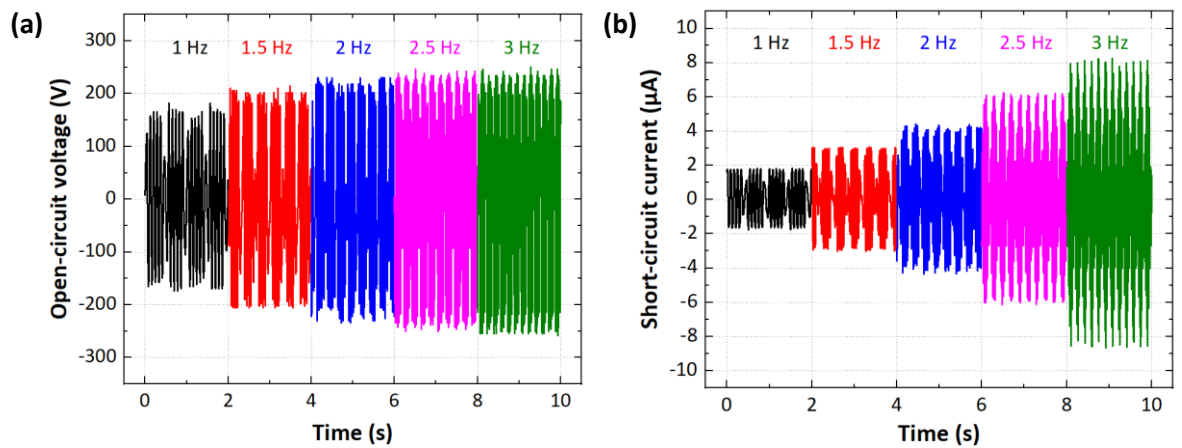


**Figure 4.27** Transient (a)  $V_{OC}$  and (b)  $I_{SC}$  of pnG-TENG (Nylon/PVC HTV,  $N = 10$ ) for the different frequencies.

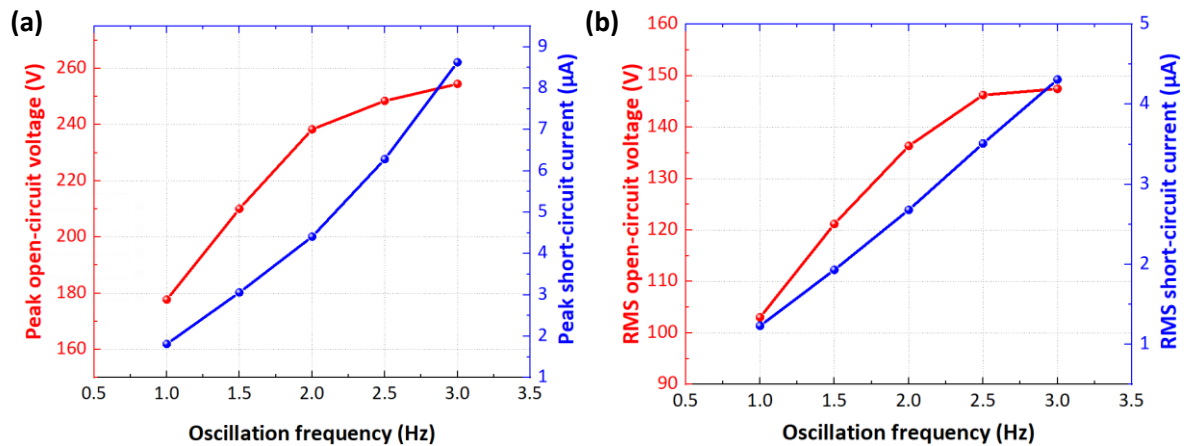


**Figure 4.28** Corresponding (a) peak values and (b) RMS values of  $V_{OC}$  and  $I_{SC}$  as a function of oscillation frequency.

The time-dependent  $V_C$  for the different frequencies is represented in Figure 4.29a. The slopes of the  $V_C$  curves grow up with a larger frequency. At a frequency of 3 Hz, the  $V_C$  reaches 73.6 V at a charging time of 600 s. The corresponding maximum  $V_C$ ,  $I_C$  and  $P_C$  as a function of frequency are calculated from Figure 4.29a and revealed in Figure 4.29b. The maximum  $V_C$ ,  $I_C$  and  $P_C$  show an increased tendency when the frequency increases, since they are related to the charging current,

which is proportional to the RMS  $I_{SC}$  (Figure 4.28b). At a frequency of 3 Hz,  $I_C$  and  $P_C$  reach 3.30  $\mu A$  and 80.84  $\mu W$ , respectively.-

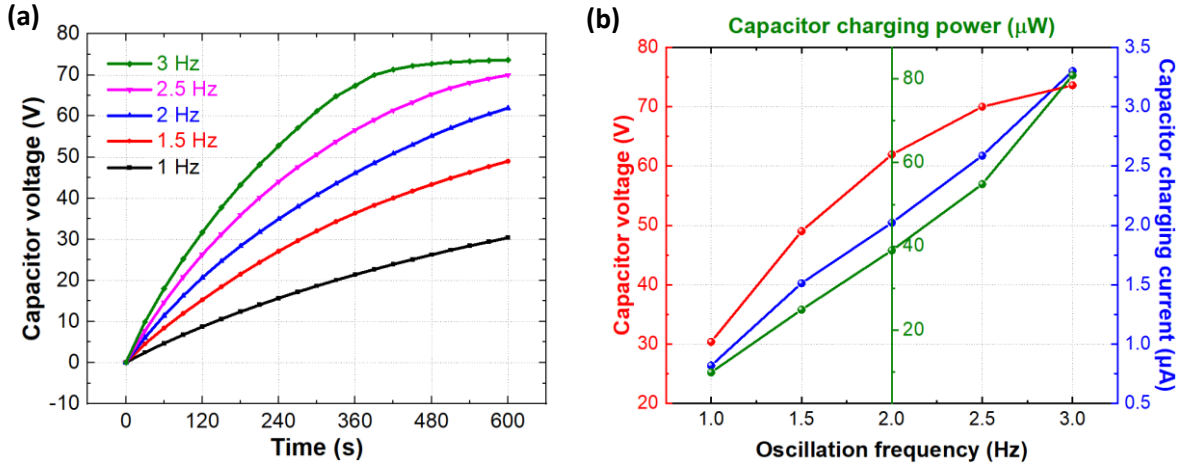


**Figure 4.29** (a) Transient  $V_C$  of pNG-TENG for different oscillation frequencies, (b) corresponding maximum  $V_C$ ,  $I_C$  and  $P_C$  as a function of oscillation frequency.

### 4.3.3 Contact force dependence

The contact force dependence measurements were performed for the pNG-TENG with nylon and PVC HTV upper substrate and Ag IDEs ( $N = 10$ ) by varying the weight on top of the upper substrate from 1 N to 12 N by a step of 1 N and fixing the frequency at 2 Hz. The transient  $V_{OC}$  and  $I_{SC}$  for the different contact forces can be found in Figure 4.30a and b, respectively. The corresponding peak values and RMS values of the  $V_{OC}$  and  $I_{SC}$  are plotted as a function of contact force in Figure 4.31a and b, respectively. At the beginning, both of the outputs rise steeply with increasing contact force until they saturate at a force over 9 N. This can be explained by the fact that the increased contact force leads to a growth in the effective contact area, which will saturate at a certain force. The time-dependent  $V_C$  for the different contact forces is shown in Figure 4.32a. It confirms that the  $V_C$  reaches a saturation point at a contact force of 9 N with a maximum  $V_C$  of 71.8 V at a charging time of 600 s. The corresponding maximum  $V_C$ ,  $I_C$  and  $P_C$  as a function of contact force are calculated and illustrated in Figure 4.32b. All the outputs remain relatively constant for the contact force over 9 N because they depend on the charging current, which is proportional to the RMS  $I_{SC}$  (Figure 4.31b).

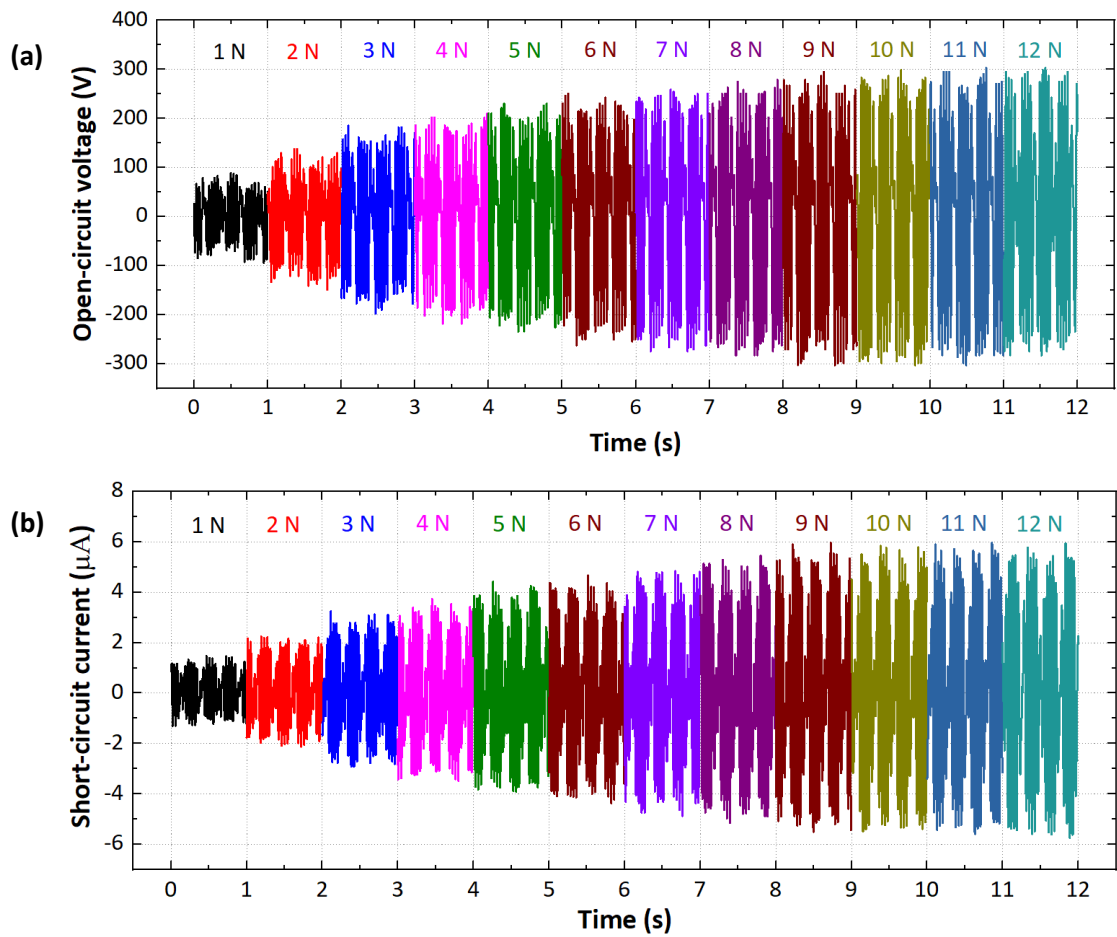


**Figure 4.30** Transient (a)  $V_{OC}$  and (b)  $I_{SC}$  of the pnG-TENG (Nylon/PVC HTV,  $N = 10$ ) for the different contact forces.

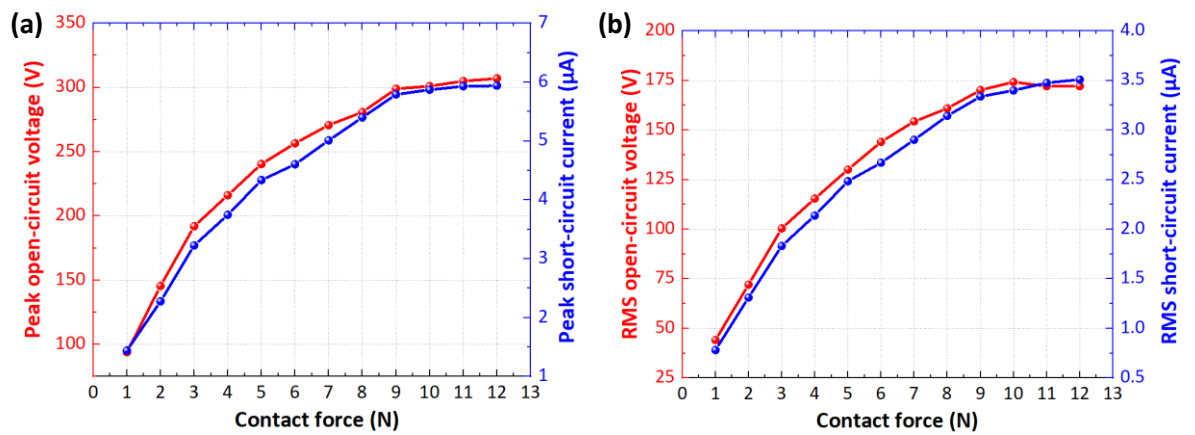


**Figure 4.31** Corresponding (a) peak values and (b) RMS values of  $V_{OC}$  and  $I_{SC}$  as a function of contact force.



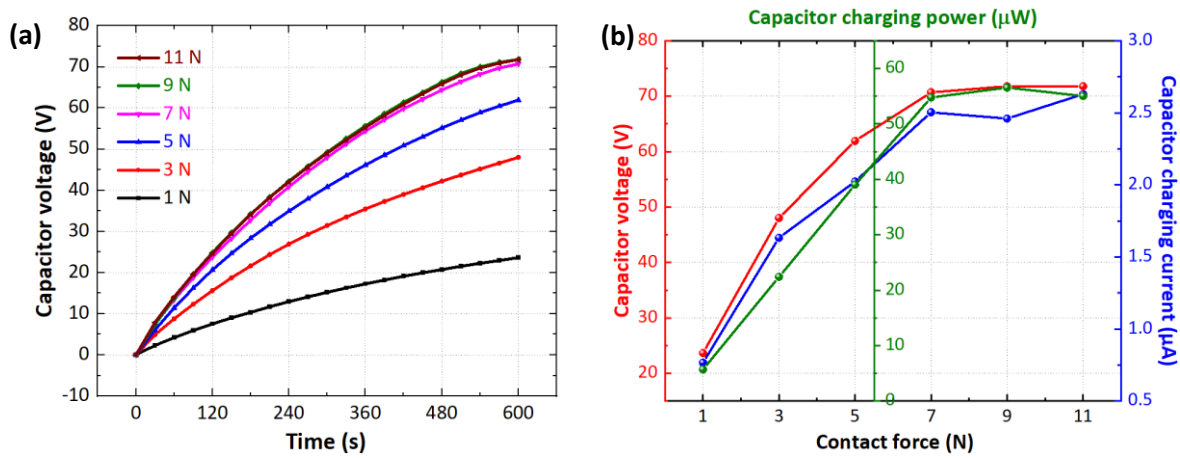


**Figure 4.32** (a) Transient  $V_c$  of pnG-TENG for different contact forces, (b) corresponding maximum  $V_c$ ,  $I_c$  and  $P_c$  as a function of contact force.

#### 4.3.4 Durability and washability

Regarding stability, the pnG-TENG ( $N = 10$ ) was continuously tested for 30000 cycles. The transient  $V_{OC}$  and  $I_{SC}$  of pnG-TENG for the different operating cycles are shown in Figure 4.33a and b, respectively. There is a slight reduction in the RMS  $V_{OC}$  and  $I_{SC}$  of the pnG-TENG of around 17% and 19% after 30000 operating cycles compared to the outputs before the stability test, respectively. However, the  $V_{OC}$  and  $I_{SC}$  return to approximately the original value after cleaning the contact surfaces with isopropyl alcohol. The SEM images in Figure 4.34a and b show the surface of the Ag IDE before and after the stability test. They illustrate that at the beginning, the IDEs are covered with tiny Ag flakes. After certain operating cycles, they are mostly removed and the robust Ag bulk film remains. However, no notable conductivity change has been observed. These are in good agreement with the result shown in Figure 4.33 that the  $V_{OC}$  and  $I_{SC}$  reduce only at the beginning of the stability test (<5000 cycles), then remains almost constant until the 30000<sup>th</sup> cycle. Moreover, adhesive tape tests have been performed. The result shows that the Ag IDEs do not peel off from the substrate and are tightly bonded to the substrate, as shown in Figure 4.35.



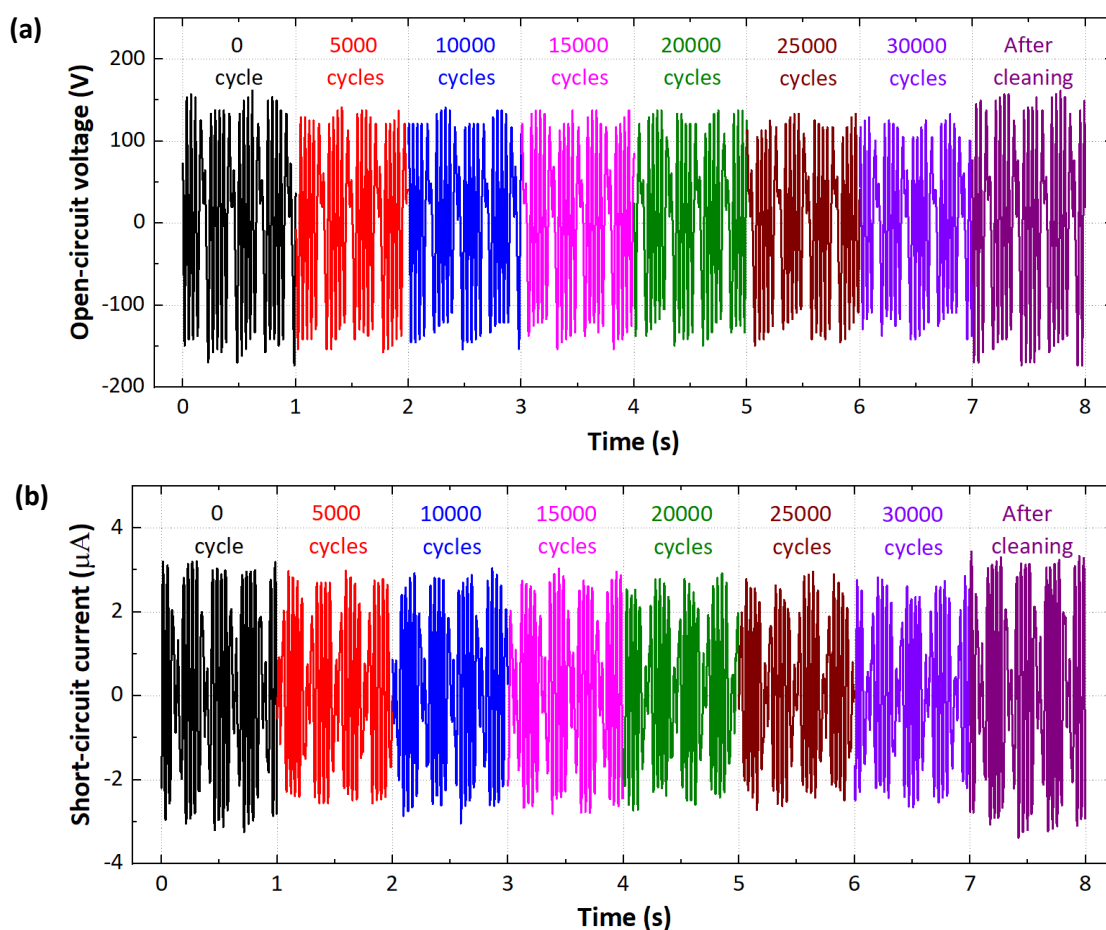


**Figure 4.33** Transient (a)  $V_{OC}$  and (b)  $I_{SC}$  of pnG-TENG for the different operating cycles and after cleaning.

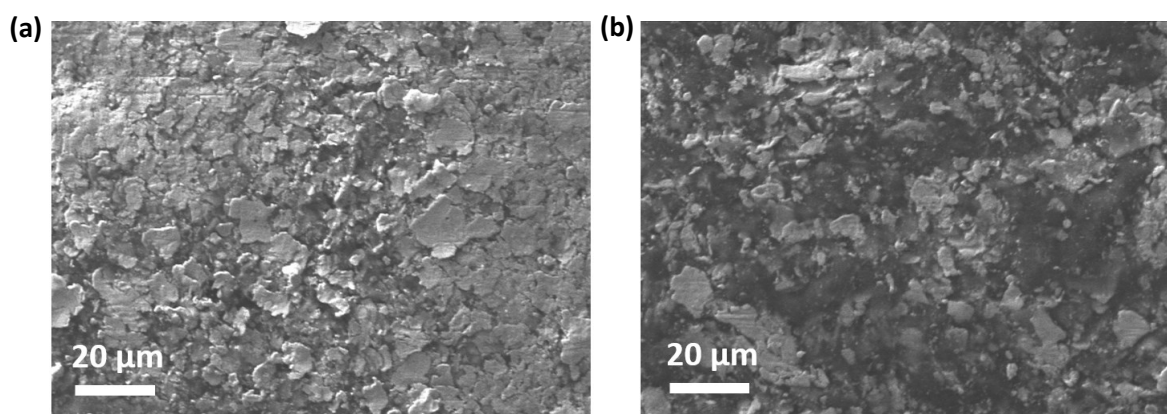


**Figure 4.34** SEM images of Ag IDE (a) before and (b) after stability test (30000 cycles).

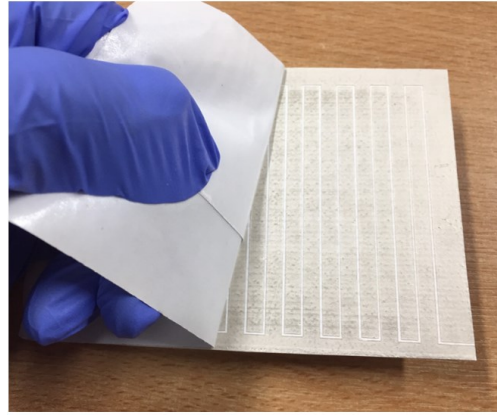


**Figure 4.35** Photograph of an adhesive tape test during which the tape does not pick up any material.

Regarding the washability, the pnG-TENG ( $N=10$ ) with the acrylic sheet was first placed in a laundry bag and then in a commercial wash machine (Beko WME7247) together with normal clothes and detergent. It was washed for 43 min at a water temperature of 30 °C using the hand-wash mode without spinning and then dried at room temperature. Figure 4.36a and b show the transient  $V_{OC}$  and  $I_{SC}$  of pnG-TENG for the different washing cycles, respectively. They demonstrate that there is no notable degradation in the performance of the pnG-TENG after 5 washes and this shows that the pnG-TENG can withstand these wash cycles.

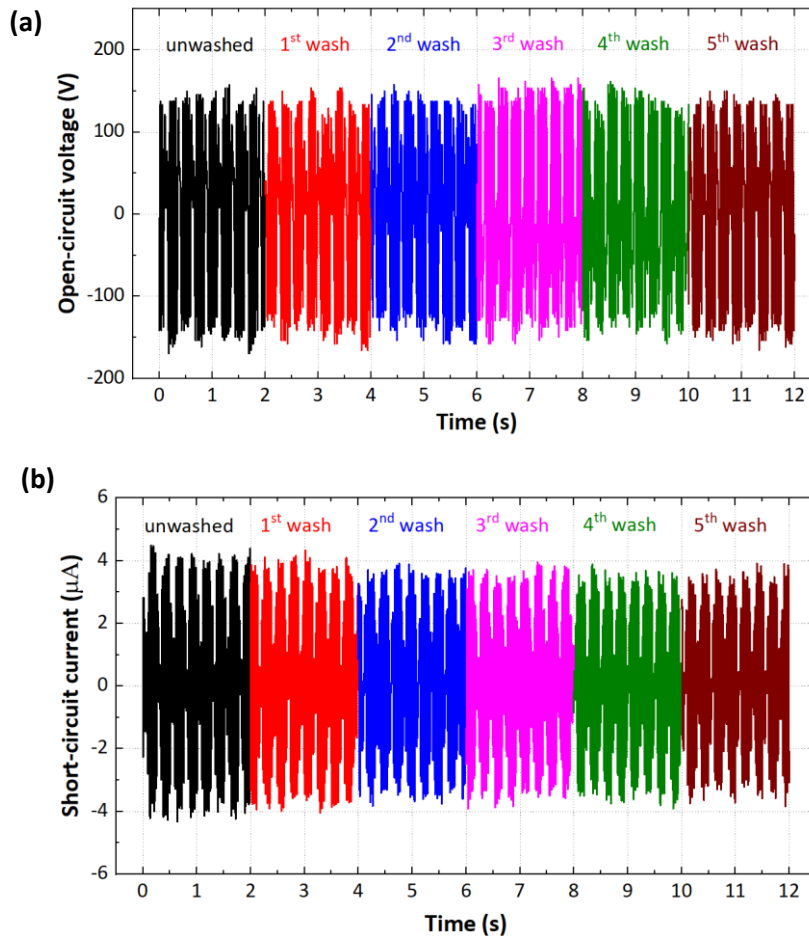


**Figure 4.36** Transient (a)  $V_{OC}$  and (b)  $I_{SC}$  of pnG-TENG for the different washing cycles.

### 4.3.5 Energy harvesting from human motion and applications

To demonstrate a possible use of the pnG-TENG in wearable electronics, the pnG-TENG ( $N = 10$ ) was embedded into a lab coat. As shown in Figure 4.37a and b, the nylon/PVC HTV was attached to a lower sleeve and the IDEs were attached to the waist and hip parts of the coat for harvesting energy from walking and running, respectively. The energy is generated from the relative movement between the arm and torso and the different IDEs location and orientation corresponds to a typical natural position for the arm during walking and running. The transient  $V_{OC}$  of the pnG-TENG for walking and running are demonstrated in Figure 4.38a and b, respectively. With an arm swing frequency of around 1 Hz for walking and 2.5 Hz for running, the pnG-TENG produces an RMS  $V_{OC}$  of 46.65 V and 46.72 V, respectively. The output of the pnG-TENG was used to charge various capacitors (1  $\mu\text{F}$ , 4.7  $\mu\text{F}$ , 10  $\mu\text{F}$  and 22  $\mu\text{F}$ ). The  $V_C$  for walking and running are revealed in Figure 4.39a and b, respectively. The capacitors can be charged to a useful voltage for wearable electronics in a short period of time. For example, it takes only 11 s and 3 s to charge the 1- $\mu\text{F}$  capacitor to 3 V for walking and running, respectively.

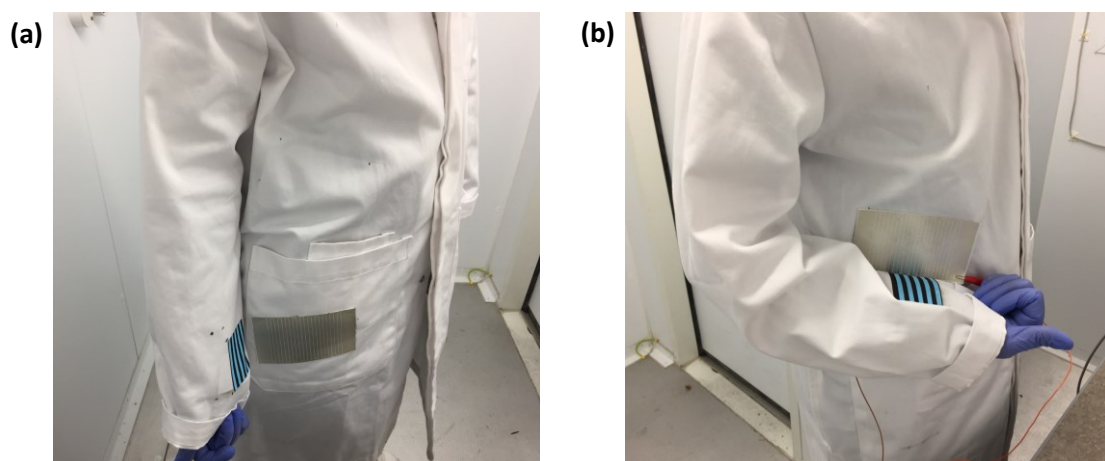


**Figure 4.37** Photographs of pnG-TENG embedded into a lab coat for harvesting energy from (a) walking and (b) running.

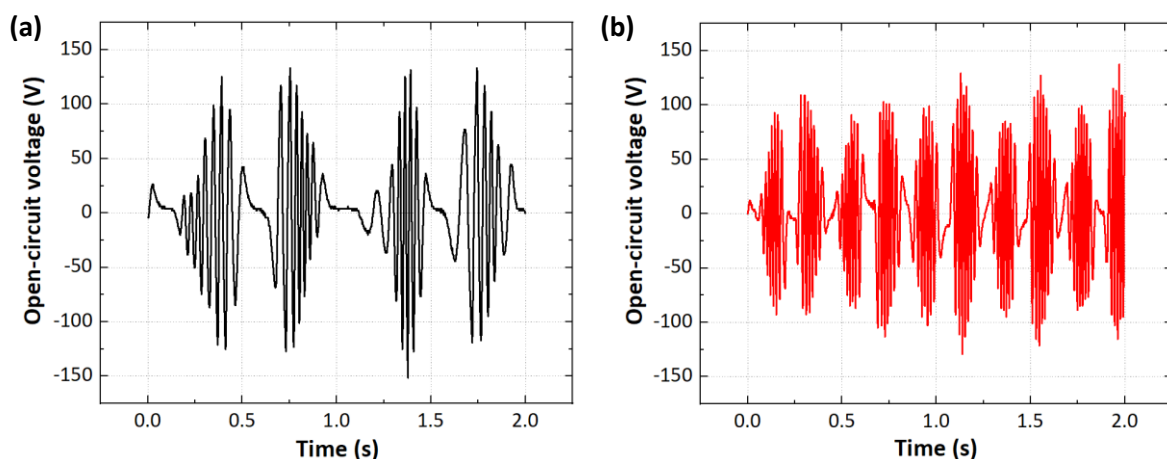


**Figure 4.38** Transient  $V_{OC}$  of the pnG-TENG produced during (a) walking and (b) running.

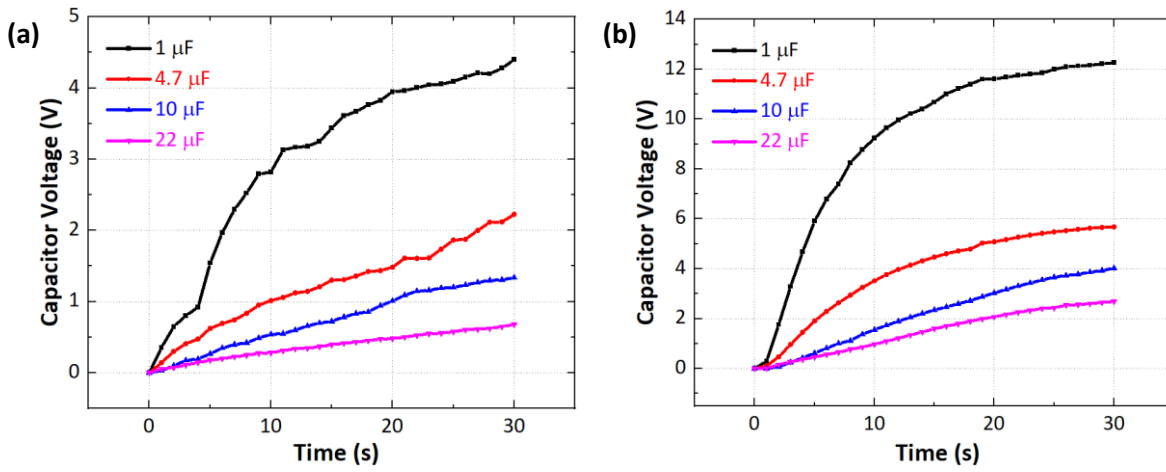


**Figure 4.39**  $V_C$  of the pnG-TENGs as a function of time for different capacitors charged during (a) walking and (b) running.

To demonstrate practical applications of the pnG-TENG as energy harvesters, its output was used to drive a digital watch, a wearable night-time warning indicator for pedestrians and a wireless transmitter. As a demonstration of a sensing device, the voltage peaks of the pnG-TENG was detected and applied for step counting through arm motion (pedometer). The circuit diagrams for all applications are revealed in Figure 4.40a - d. For the digital watch, the output of the pnG-TENG is rectified and stored in a 10- $\mu\text{F}$  electrolytic store capacitor ( $C_{\text{store}}$ ) (Figure 4.40a). When the capacitor voltage reaches 1.2 V, the watch is switched on and then operates continuously, as shown in Figure 4.41a. For the night-time warning indicator, the AC output of the pnG-TENG can directly illuminate 42 forward bias LEDs and 42 reverse bias LEDs, which are connected in series (Figure 4.40b) and forms a sign “STOP” to warn upcoming vehicles of the pedestrians at night, as shown in Figure 4.38b.

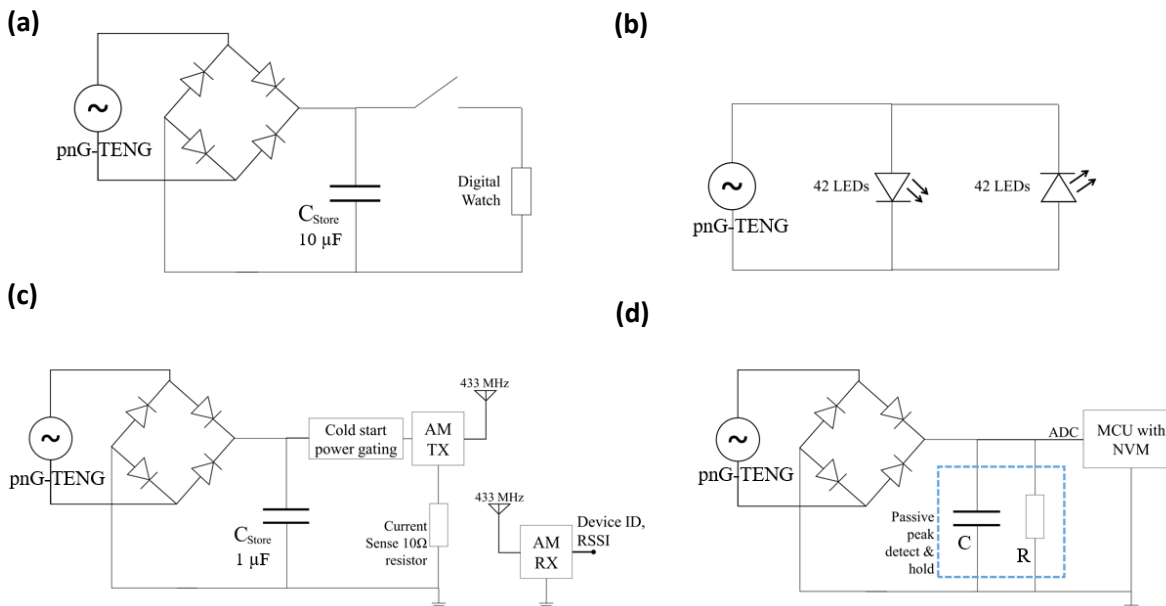


**Figure 4.40** Circuit diagrams of using pnG-TENG for powering (a) a digital watch, (b) night-time warning indicator, (c) wireless transmitter and (d) pedometer.

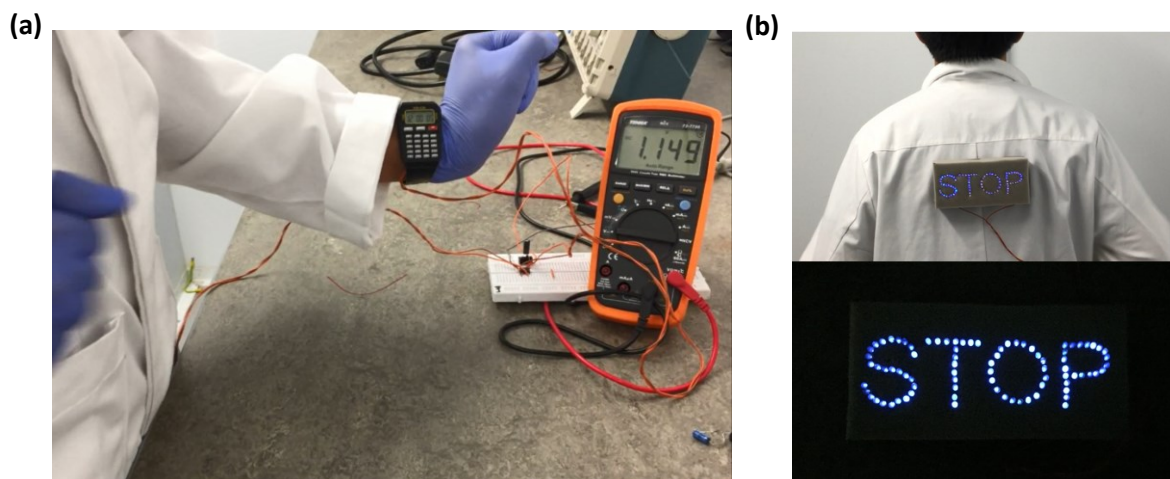


**Figure 4.41** Photographs of (a) digital watch and (b) wearable night-time warning indicator for pedestrians driven by the output of pnG-TENG ( $N = 10$ ) during running.

Regarding the wireless transmitter, a commercial 433 MHz Amplitude Modulation transmitter (AM TX), (AM-RT14-433P), is powered up using the energy stored in a 1- $\mu$ F electrolytic capacitor charged by the pnG-TENG in walking mode (Figure 4.40c). The transmitter is turned on once the voltage reaches a switch-on voltage threshold of 4 V and is allowed to transmit indefinitely until the energy storage is depleted ( $V_c < 2$  V). Figure 4.42a shows the capacitor charging voltage  $V_c$ , the active current consumption of the transmitter  $I_T$ , and the Received Signal Strength Indicator *RSSI* output rising at the receiver that demonstrates a successfully received message. The transmitter operating at 4 V consumes an active current of 16 - 18 mA and requires  $\sim 30$   $\mu$ s for the transmitter to turn on and the receiver to receive the first packet, as shown in the magnified image in Figure 4.42b of the box marked in yellow in Figure 4.42a. Thus, the energy requirement per transmission is approximately 2  $\mu$ J. Such a transiently-powered wireless transmitter can be applied in applications such as indoor positioning [159] or activity monitoring based on the periodicity of the received packet. To illustrate, as the triboelectric generator's output is dependent on the activity, as shown in Figure 4.39a and b, the charging time of the capacitor, and hence the time interval between wireless transmissions can be utilized to monitor the user's activity, such as running, walking or resting. Furthermore, when a transmitter is utilized with multiple receivers, the *RSSI*, which is a function of the distance from the transmitter, could be used for accurate indoor positioning.



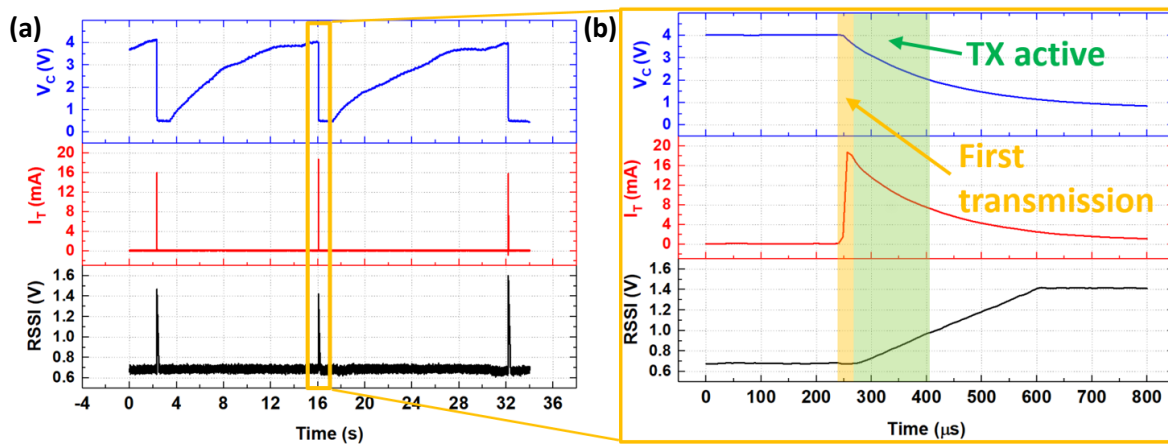


**Figure 4.42** (a) Transient RSSI at the receiver, and transient  $V_c$  and  $I_T$  at the wireless transmitter powered by the pnG-TENG during walking. (b) The zoom-in image showing the first transmission and the transmitter active period.

With respect to the pedometer, a passive peak detect and hold circuit, composed of a shunt capacitor and resistor (Figure 4.40d), is used to filter the high-frequency component of the output of the pnG-TENG and preserves the peak for a duty-cycled analogue to digital converter (ADC) to detect it. The Arduino code for the peak detection is shown in Appendix A. A microcontroller (MCU) samples the ADC at 300 ms intervals (the maximum stride rate while running [160]) and counts a step when the voltage output exceeds the step threshold. The values of the capacitor and the resistor ( $1 < C < 10$  pF,  $100 < R < 500$  k $\Omega$ ) are tuned based on the step-detection threshold of the MCU. To explain, the circuit is tuned to allow the step's peak voltage to be held above the threshold for approximately 300 ms, to ensure it is detected by the ADC and to ensure it decays below the threshold before the next sample. Figure 4.43 shows the operation of the pedometer demonstrated through toggling a digital output pin when a step is detected. The step count can be written to non-volatile memory (NVM) to allow intermittent activity tracking when powered from the pnG-TENG.

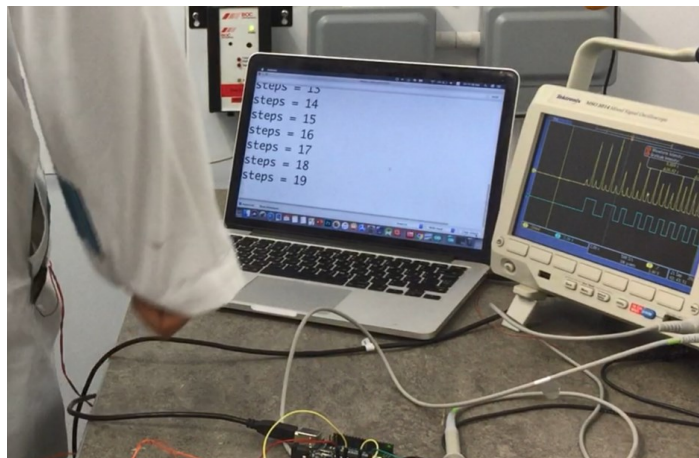


**Figure 4.43** Photograph showing the utilisation of the pnG-TENG as a sensor for step counting via arm motion (pedometer).

## 4.4 Conclusion

A novel textile-based triboelectric generator was successfully fabricated using processes that are compatible with standard textile manufacturing, including screen-printing and heat-transfer printing. The TENG comprises two alternate grated strips of positive triboelectric material (nylon fabric) and negative triboelectric material (PVC heat transfer vinyl), defined as a pnG-TENG. The pnG-TENGs show significant performance improvement compared to single positive material (pG-TENGs), single negative material (nG-TENGs) and TENGs with no gratings. With this novel structure, the  $I_{SC}$  and the  $V_C$  increase with increasing grating number, whereas  $V_{OC}$  shows a reducing trend due to the increasing capacitance of the electrodes. The  $I_{SC}$ ,  $V_{OC}$  and  $V_C$  of the pnG-TENGs are considerably greater than those of the pG-TENGs and the nG-TENGs for all the grating numbers. The average power generated by the pnG-TENG with 10 gratings is 1.94 and 6.43 times greater than the power generated by the TENG with single triboelectric material (nG-TENG) and the TENG with no grating at a load resistance of 50 M $\Omega$ , a mechanical oscillation of 2 Hz, a contact force of 5 N, a humidity of 25%RH and a temperature of 25 °C.





## Chapter 5 Textile-based triboelectric energy harvester with alternating positive and negative freestanding woven structure for harvesting kinetic energy in all sliding directions (woven-TENG)

### 5.1 Introduction

Most TENGs operating in freestanding triboelectric-layer mode (FT-mode) can only harvest energy in one translational direction [150], [158] or rotational direction [79], [80], as shown in Section 4.1. The first TENG, which can generate energy from all sliding directions has been proposed by Guo et al. [161]. They reported a checker-like TENG with interdigitated electrodes and used a sliding contact between a PET thin film covering on checker-like Al electrodes and a PTFE sliding panel with matching structure as a source for the triboelectric charge generation, as shown in Figure 5.1.

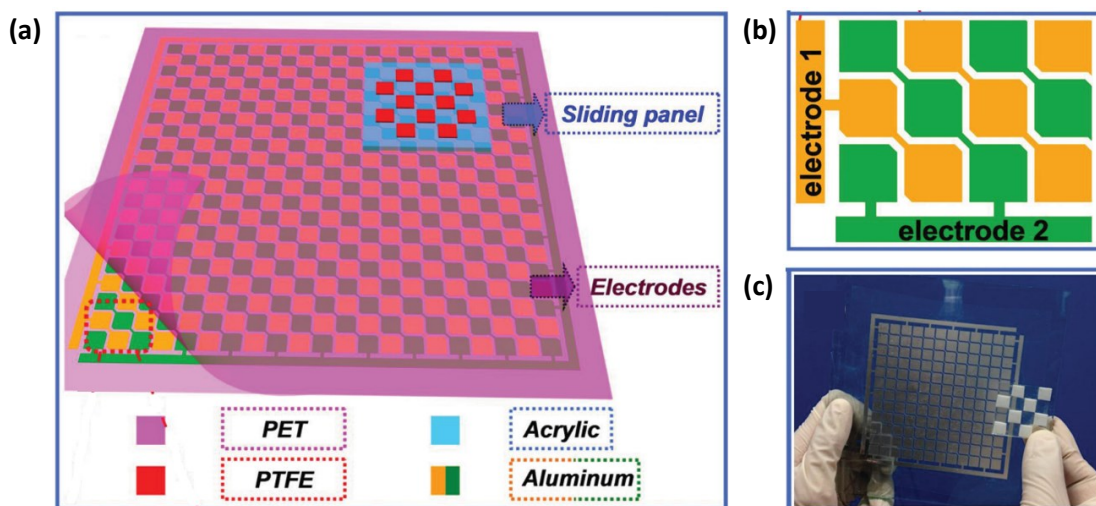


**Figure 5.1** (a) Schematic illustration of the triboelectric nanogenerator based on checker-like electrodes proposed by Guo et al. (b) Enlarged illustration of the red dotted box in (a) showing the electrode alignment. (c) Photograph of the sliding panel and electrodes. Reproduced with permission from Ref. [161]. Copyright 2015, John Wiley & Sons, Inc.

Next, Xia et al. has redesigned the electrodes by introducing a new honeycomb-like three-electrodes structure [162] illustrated in Figure 5.2. Recently, a similar idea to the checker-like TENG has been proposed by Ma et al. They developed a biomimetic fish-scale-like TENG, which was also manufactured based on PET film and PTFE sheet [163]. However, these examples are made of rigid

materials, which are inappropriate for wearable applications and the second example also suffers from a lower effective contact area, since only a small part of the upper substrate can make a contact with the lower substrate. Additionally, Chen et al. have manually knitted a mosaic patterned TENG for all-direction sliding energy harvesting [140]. However, this work did not demonstrate its successful operation as an energy harvester.

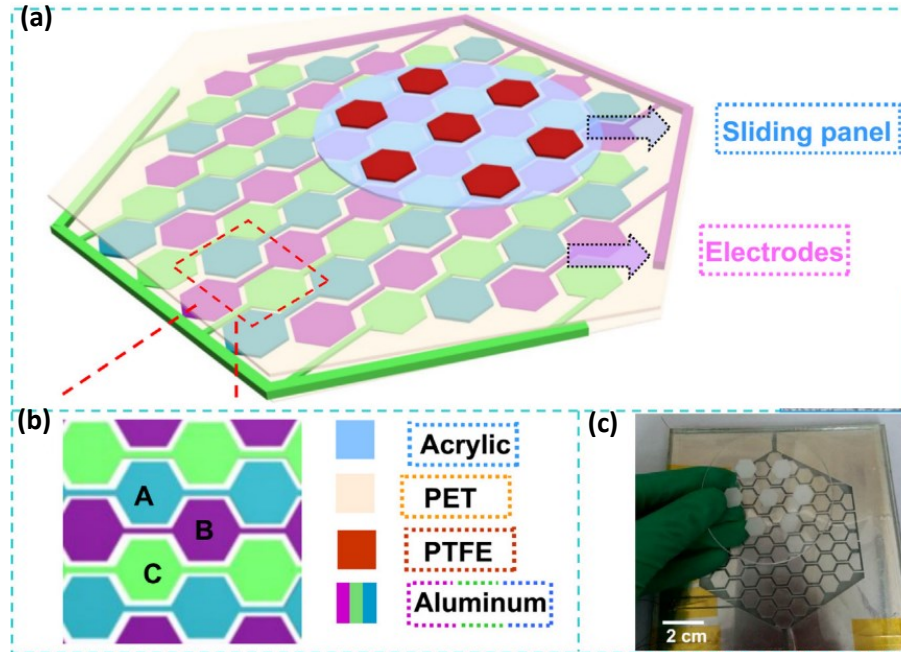


**Figure 5.2** (a) Schematic illustration of the triboelectric nanogenerator based on honeycomb-like electrodes proposed by Xia et al. (b) Enlarged illustration of the red dotted box in (a) showing the electrode alignment. (c) Photograph of sliding panel and electrodes. Reproduced with permission from Ref. [162]. Copyright 2018, Elsevier.

This chapter proposed a novel textile-based TENG with woven structure (woven-TENG). While most woven-structured TENGs operate in the contact-separation FT-mode or the contact-separation mode and consist of one type of triboelectric material as freestanding material [37], [39], [91], [92], [164] (see Chapter 2, Figure 2.6 and Figure 2.17), this woven-TENG comprises woven electrodes and woven strips of positive and negative triboelectric material and operates in the sliding FT-mode. Because of the nature of the woven structure, a symmetric and periodic arrangement of the electrodes and alternating triboelectric materials are self-formed. In contrast to the conventional woven-structured TENGs, the proposed woven electrode structure is unique, for which a different working principle is applied, because the potential difference between the electrodes is induced by the shielding effect and the difference in distance between the top and the bottom underlying electrode. Moreover, the implementation of the alternating positive and negative triboelectric material can considerably enhance the performance of a TENG operating in the sliding FT-mode [44] as demonstrated in Section 4.3.1. In addition, the fabrication processes of

the woven-TENG, including doctor-blading and weaving, are common, low-cost and compatible with standard textile manufacturing.

## 5.2 Design and methodology

### 5.2.1 Fabrication

A schematic illustration of the woven-TENG is shown in Figure 5.3. The woven-TENG is composed of an upper substrate comprising woven strips of positive and negative triboelectric materials and a lower substrate serving as electrodes. Through a sliding movement of the upper substrate in all arbitrary directions relative to the lower substrate, AC power can be generated through the load.

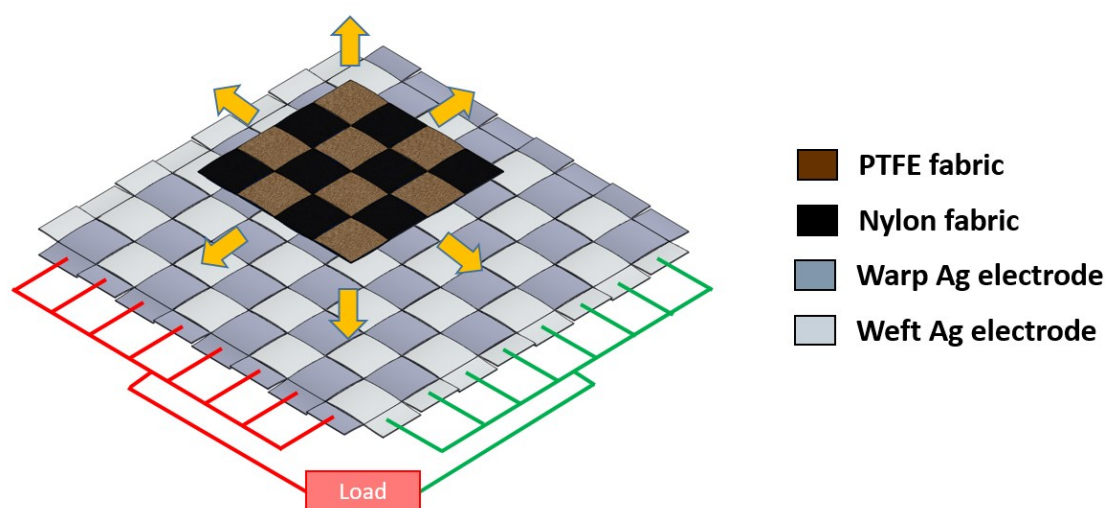


**Figure 5.3** Schematic illustration of woven-TENG for  $N = 4$  with nylon fabric as positive material and PTFE fabric as negative material.

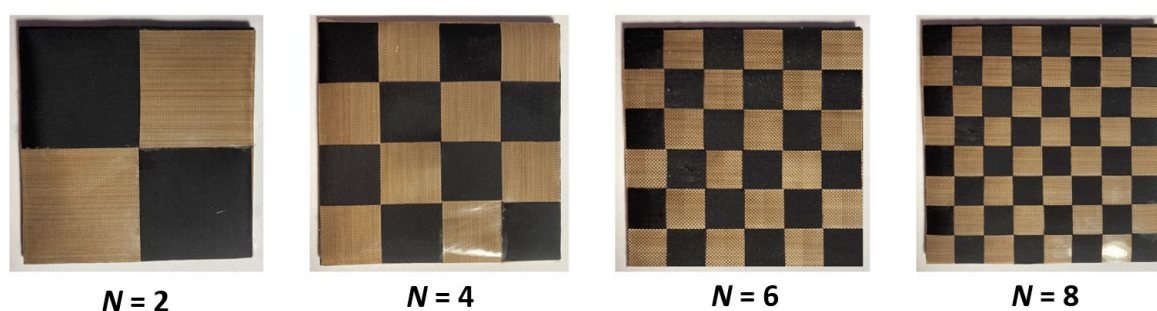


**Figure 5.4** Photograph of the upper substrates woven-TENG with nylon fabric (black) and PTFE fabric (brown) for the different element numbers ( $N = 2, 4, 6$  and  $8$ ).

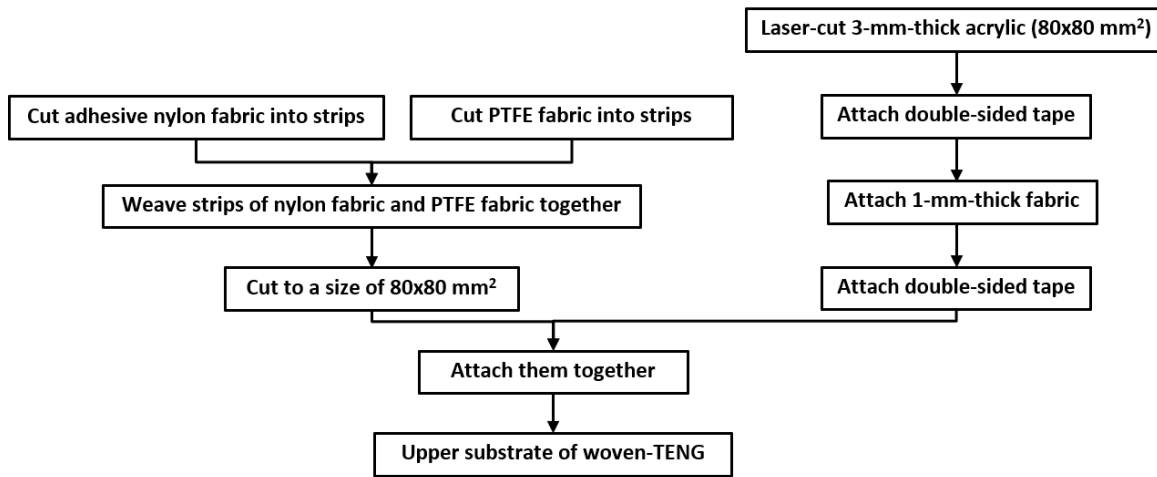


**Figure 5.5** Flowchart showing the fabrication steps of upper substate of woven-TENG.

The photograph of the upper substrates is illustrated in Figure 5.4. The flowchart of the fabrication steps of the upper substrate is shown in Figure 5.5. It was fabricated by cutting adhesive nylon fabric (Hemline) and PTFE coated fibreglass fabric (PTFE fabric, Xinghoo) into strips of the same size and weaving them together forming a checker-like pattern with a total size of 80 mm x 80 mm. They are then attached to the 1-mm-thick fabric carrier and a 3-mm-thick acrylic sheet using double-sided tapes for testing purposes. The upper substrates were produced with various numbers of elements ( $N$ ) on each side with  $N$  equalling 2, 4, 6 and 8 with strip widths of 4 cm, 2 cm, 1.33 cm and 1 cm, respectively, thereby maintaining a constant overall area. The PTFE fabric and the nylon fabric were chosen as the triboelectric materials, because PTFE and nylon are among the most negative and positive material according to the triboelectric series proposed by Zou et al. [28], respectively and exhibit good triboelectric performance as shown in Section 3.2. Moreover, they are available in a commercial fabric form and have good properties for implementation in wearable devices, such as flexibility, lightweight, biocompatibility and washability.

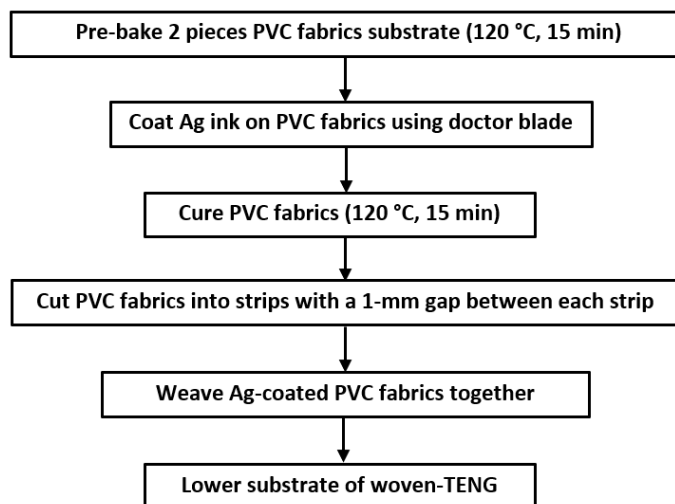


**Figure 5.6** Flowchart showing the fabrication steps of lower substate of woven-TENG.



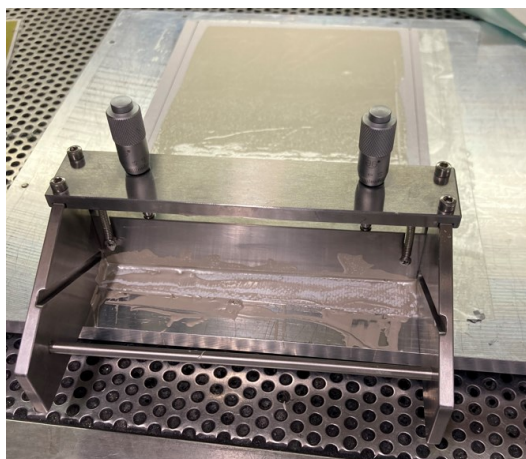


**Figure 5.7** Photograph of doctor blade coating of Ag ink on PVC fabric.

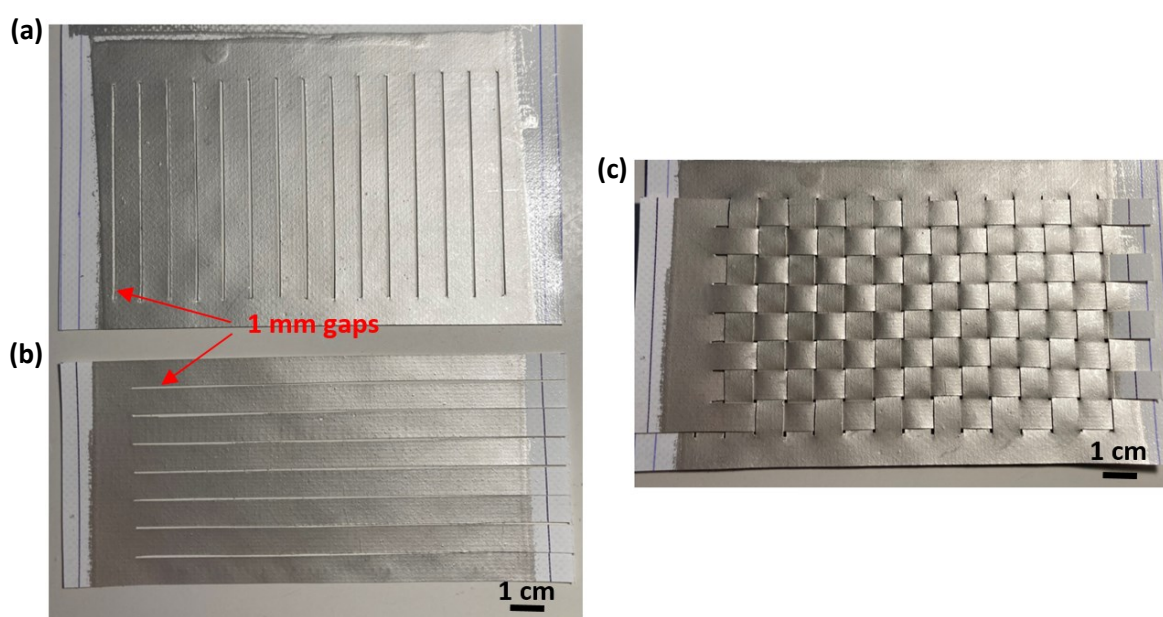


**Figure 5.8** Photograph of (a) warp Ag electrode, (b) weft Ag electrode before weaving and (c) Ag electrodes of woven-TENG for  $N = 8$  after weaving.

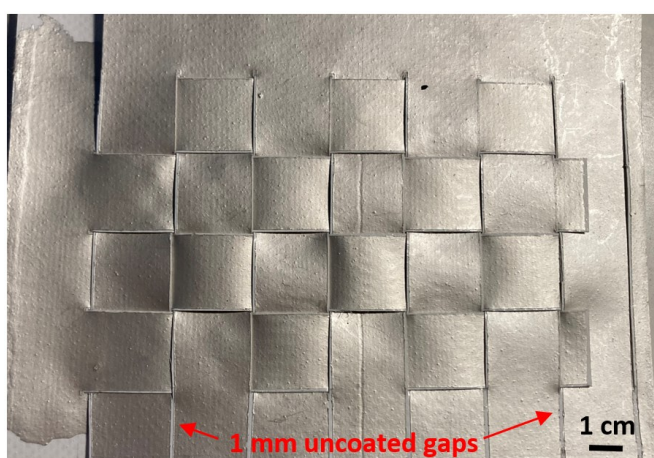


**Figure 5.9** Photograph of lower electrodes of woven TENG for  $N = 4$  fabricated using adhesive vinyl stencil and doctor blading.

The flowchart of the fabrication steps of the lower substrate of the woven-TENG is shown in Figure 5.6. The lower electrodes were fabricated by firstly pre-baking two pieces of 450- $\mu\text{m}$ -thick PVC coated polyester fabric (PVC fabric, VALMEX FR 7546) at 120 °C for 15 minutes in a Carbolite box oven to eliminate outgassing from the PVC layer. Next, doctor blading was used to coat the PVC fabric with a 100- $\mu\text{m}$ -thick Ag ink (Fabinks TC-C4001) as shown in Figure 5.7 and curing at a temperature of 120 °C for 15 minutes. The Ag coated PVC fabrics were then cut into strips of the same size with a 1-mm gap between each strip and leaving one end uncut. The uncut ends enable the warp strips and weft strips to be electrically connected forming separate warp and weft electrodes shown in Figure 5.8a and b. The 1-mm gap ensures the warp and weft electrodes are electrically isolated after weaving. Finally, the two Ag coated PVC fabrics are woven together forming the lower woven electrodes shown in Figure 5.8c. To match with the size of the strips of the upper substrate, the lower electrodes were also produced for  $N = 2, 4, 6$  and 8 with strip widths of 4 cm, 2 cm, 1.33 cm and 1 cm, respectively. Alternatively, the electrodes can be fabricated using a similar process shown in Figure 4.8. In this process, a pre-cut adhesive vinyl stencil with a width of 1 mm was attached to the PVC fabric before doctor-blading it with Ag ink. After removing the vinyl stencil, the 1-mm uncoated gap is formed between the electrode strips as shown in Figure 5.9. The advantage of this method is that it can absolutely prevent the electrodes from electrical short circuits. However, more fabrication steps are required and it is therefore not be chosen. The flexibility of the upper and the lower substrate is demonstrated in Figure 5.10a and b, respectively. They can be later sewing to any garment and can be conformal to the garment and the body. The scanning electron microscope (SEM) images in Figure 5.11a and b review the magnified cross section structure of the upper substrate and lower substrate in detail, respectively.

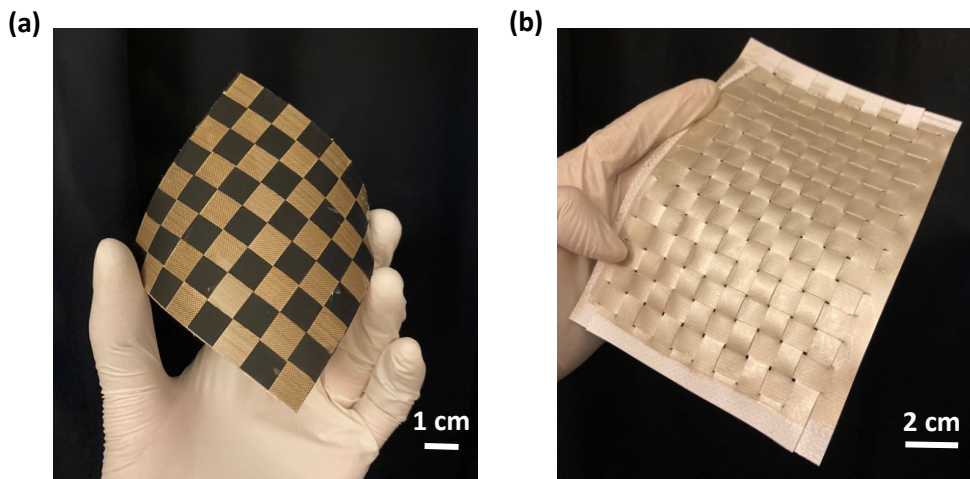


**Figure 5.10** Photograph of (a) the upper substrate and (b) the lower substrate of woven-TENG for  $N = 8$  showing their flexibility.

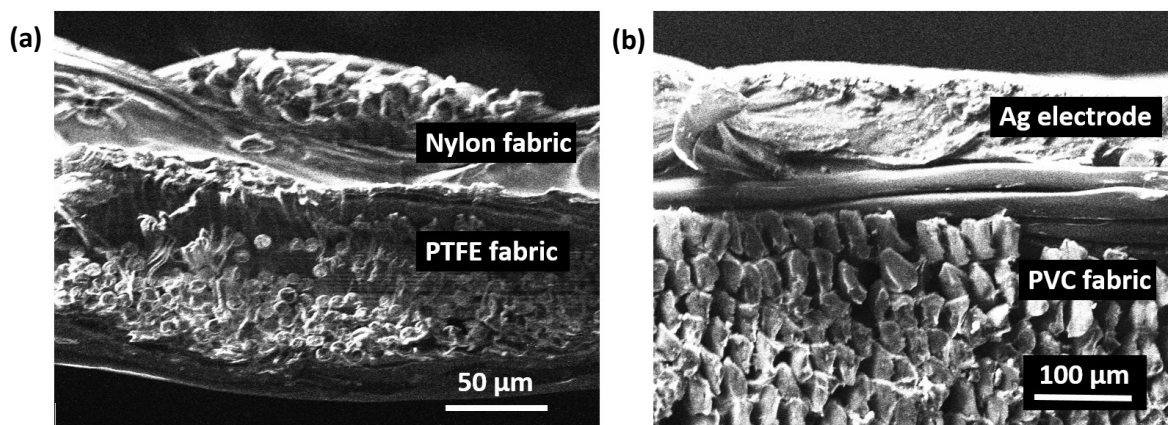


**Figure 5.11** Scanning electron microscope (SEM) images of (a) the upper substrate and (b) the lower substrate of woven-TENG.

### 5.2.2 Working principle

The operating mechanism of the woven-TENG for  $N=2$  is revealed in Figure 5.12. The top insets show the bird's eye view of each location of the upper layer relative to the lower woven electrodes, while the bottom drawings show the corresponding cross-sectional view at the position of the dashed blue line shown in the top inset. When the upper substrate slides on the lower Ag electrodes and make a contact with them. The PTFE fabric and the nylon fabric will be negatively and positively charged, respectively. The same amount of charge with the opposite polarity is transferred to the electrodes due to the contact electrification effect. In the beginning, the PTFE fabric and the nylon fabric fully overlap with the warp and the weft electrode, respectively (Figure 5.12 (i)). In this state, there is no charge transfer between the electrodes. They are in electrostatic equilibrium since the number of positive and negative charges on their surfaces are equal. In Figure 5.12 (ii), the upper substrate is sliding further to the right-hand side along the waft electrode. In this state, the electrons flow from the weft to the warp electrode through the load, because the electric potential of the weft electrode decreases, while that of the warp electrode increases due to the presence of the PTFE fabric (negative) and the nylon fabric (positive) on the weft and the warp electrode, respectively. When the PTFE fabric and the nylon fabric fully overlap with the weft and the warp electrode, respectively (Figure 5.12 (iii)), another electrostatic equilibrium is reached and the charge transfer stops. In the 4<sup>th</sup> state (Figure 5.12 (iv)), the upper substrate is moving back to the left-hand side. The electric potential of the warp electrode decreases, while that of the weft electrode increases, resulting in a current flow through the load from the weft to the warp electrode. The current keeps flowing until the potential gradient terminates when the next full overlap occurs. When the upper substrate continually slides in cycles, an alternating current is generated through the load. The same effect occurs when the upper substrate moves perpendicularly along the warp electrode. The output of the woven-TENG according to the

movement of the upper substrate at different angles with respect to the weft electrode (x-axis) will be further discussed in Section 5.3.3.

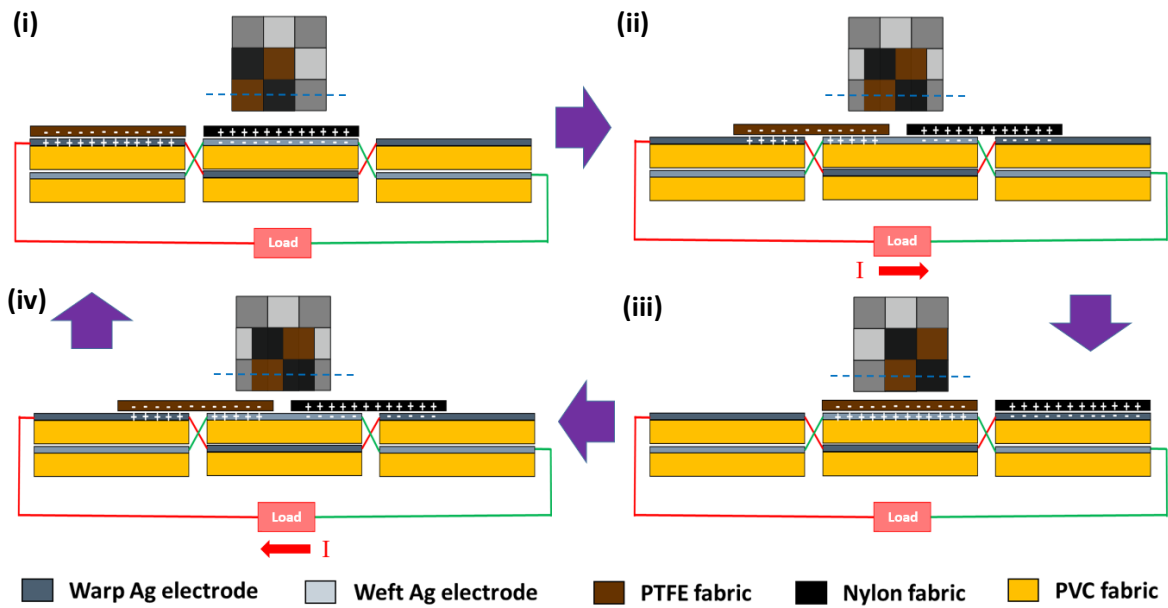


**Figure 5.12** Schematic illustration of the operating mechanism of woven-TENG for  $N = 2$  connected to a finite load resistance.

Figure 5.13 shows the Schematic illustration of the operating mechanism of woven-TENG for  $N = 2$  in open-circuit condition. The initial state shown Figure 5.13(i) is the state when the freestanding triboelectric materials are rubbed against the electrodes for a while, until triboelectric charge transfer is in equilibrium and the surface charges on all materials are saturated. At this state, the sum on the charge on the triboelectric materials are equal to the sum of the charge on the electrodes. Since all electrodes are symmetric and are in open-circuit condition, the number of the charges on both electrodes are always equal and they always offset each other when calculating the electric potential difference between the electrodes. For this reason, the charges on the electrodes can be neglect when calculating the  $V_{OC}$ . The charges which contribute to  $V_{OC}$  are the charges on the triboelectric materials. In state (i), the negative charges are over warp electrode and the positive charges are over the weft electrode, thus the electric potential on the warp electrode is lower than weft electrode and the  $V_{OC}$  is negative. When the triboelectric materials move further and locate in the middle of the tines (Figure 5.13(ii)), the number of the positive charges and the negative charges over the warp electrode and the weft electrode are equal, thus  $V_{OC}$  is zero. In state (iii), the triboelectric materials move further, and the negative charges and positive charges present over the weft and the warp electrode, respectively, resulting in positive  $V_{OC}$ . When the upper substrate continues to move, the electric potential in the electrodes increase and decrease alternately resulting in an alternating  $V_{OC}$ .



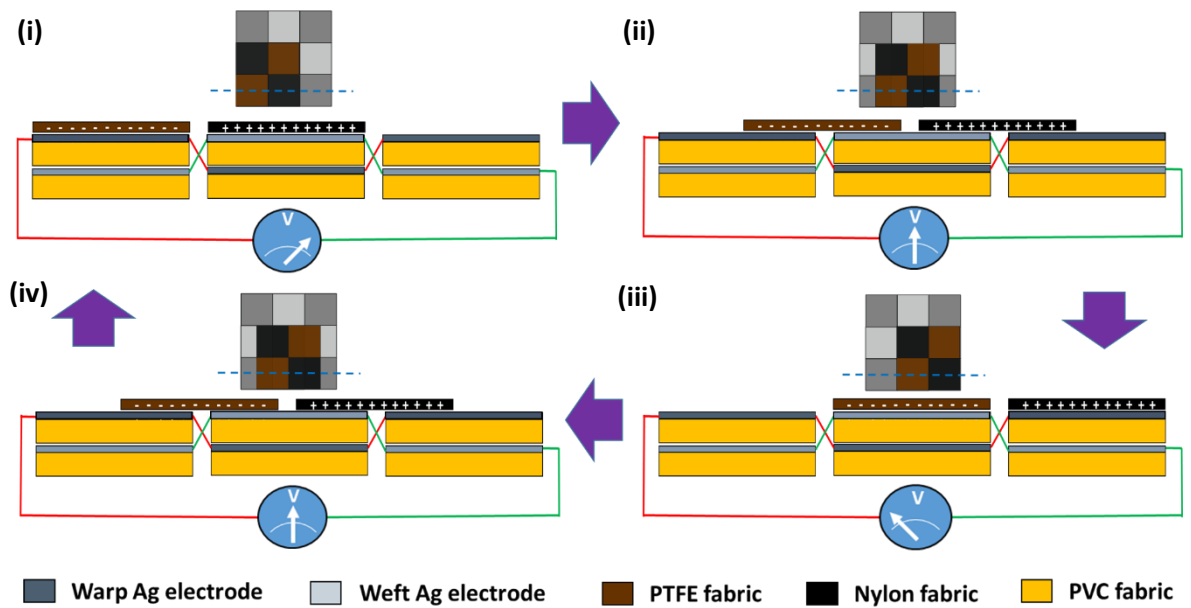


**Figure 5.13** Schematic illustration of the operating mechanism of woven-TENG for  $N = 2$  in open-circuit condition.

### 5.2.3 Characterisation and measurement

The experiments were performed using the belt-driven linear actuator, which can produce periodically sliding motion between the upper and the lower substrates with a constant contact force thereby ensuring a repeatable experimental measurement process as shown in Figure 3.2. For initial testing purposes, the upper and the lower substrates were first attached to a piece of 1 mm-thick fabric, then an acrylic sheet. The fabric allows the triboelectric material to conform to the electrodes and thus maintain the effective contact area of the triboelectric materials, while the acrylic sheet enables consistent and repeatable testing but would not be required in an actual application (see Section 5.3.7). If not specified otherwise, all measurements were carried out in the environmental chamber (Weiss Technik WKL100) at an oscillation frequency of 2 Hz, an amplitude of 40 mm, a contact force of 5 N, a temperature of 25 °C and a humidity of 25 %RH. Open-circuit-voltage ( $V_{oc}$ ) and Short-circuit-current ( $I_{sc}$ ) were measured using an oscilloscope (Agilent DSO3062A) at 1 G $\Omega$  load and a DC power analyzer (Agilent N6705B), respectively. For the capacitor charging measurement, the output of the woven-TENGs was first rectified using a commercial full-wave bridge rectifier (Diodes Inc DF10M) and then used to charge a 10- $\mu$ F electrolytic capacitor. During charging, the capacitor voltages ( $V_c$ ) were measured using a digital multimeter (Tenma 72-7780) and oscilloscope (Agilent DSO3062A). Surface charge densities of the triboelectric materials were measured using the bespoke Faraday cup connected to an electrometer (Keithley 6514), as shown in Figure 3.6. COMSOL Multiphysics software was employed for the  $V_{oc}$  simulation. It is to

note that 3 woven-TENGs were built and tested, and the best output is presented in the following experimental result section.

### 5.3 Result and discussion

#### 5.3.1 Effect of the number of elements per each side of the upper substrate (N)

##### 5.3.1.1 Simulation and theoretical calculation

For the theoretical investigation of the effect of element number per each side of the upper substrate on the outputs of woven-TENG, the peak  $V_{OC}$  of the woven-TENGs for  $N = 2, 4, 6$  and  $8$  were simulated using COMSOL. Electrostatics physics with a normal free triangular mesh was used to simulate the maximum  $V_{OC}$  at a stationary state when the positive and negative triboelectric materials fully overlap with the electrodes.

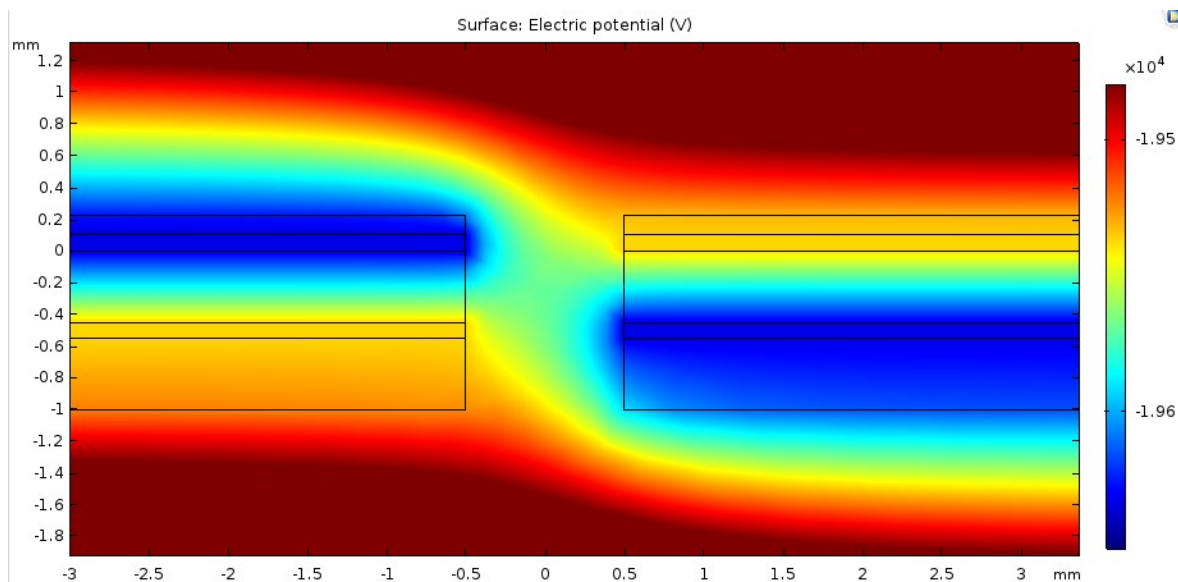


**Figure 5.14** Simulated electric potential distribution of woven-TENG for  $N = 2$  using COMSOL.

Figure 5.14 demonstrates a magnified cross-section simulation result of the electric potential distribution for the woven-TENG with  $N = 2$ . The stack of the materials on the left-hand side from top to bottom is PTFE, Ag warp electrode, PVC, Ag weft electrode and PVC, respectively. The stack of the materials on the right-hand side from top to bottom is nylon, Ag weft electrode, PVC, Ag warp electrode and PVC, respectively. The surface charge density of the PTFE and nylon in the simulation were pre-defined as  $-19.24 \mu\text{C}/\text{m}^2$  and  $11.15 \mu\text{C}/\text{m}^2$ , respectively. These values were obtained from measurements of the PTFE fabric and the nylon fabric using the Faraday's cup shown in Section 3.2.2.2. The top-left and the bottom-right electrode were electrically connected with the same floating potential, similar to the bottom-left and the top-right electrode. Due to the presence of the negative charges on the PTFE surface on the left-hand side, the electric potential on the warp

electrode is -19633 V, while the underlying weft electrode has a higher potential of -19537 V. The reasons for this are firstly, the electric field from the negative charge is shielded by the top electrode [84]. Secondly, the lower electrode is located further from the negatively charged surface and electric potential increases with increasing distance from negative point charges according to Equation 5.1 below:

$$V_E = \frac{1}{4\pi\epsilon_0} \frac{Q}{r} \quad (5.1)$$

where  $V_E$  is the electric potential,  $Q$  is the point charge,  $r$  is the distance from the point charge and  $\epsilon_0$  is the permittivity of vacuum. Thirdly, the positively charged surface on the right-hand side induces a positive electric potential at the top-right electrode, which is electrically connected to the bottom-left electrode. However, the net electric potential of both electrodes is negative because of the dominance of the negative surface charge density of the PTFE over the nylon. The  $V_{oc}$  can be determined from the difference of the electric potentials between the electrodes and plotted in Figure 5.15. It decreases with increasing element number, which can be explained by Equation 5.2 as described in Section 4.3.1.1:

$$V_{oc} = \frac{\Delta\sigma_{sc} \cdot S}{C} \quad (5.2)$$

where  $\Delta\sigma_{sc}$  is the short-circuit transferred charge density,  $S$  is the total area of the warp or weft electrode and  $C$  is the capacitance between the electrodes.  $\Delta\sigma_{sc}$  and  $S$  are consistent for all  $N$  but  $C$  rises when the electrodes are divided into small elements, therefore  $V_{oc}$  reduces with increasing element number [150]. The simulated  $V_{oc}$  of the woven TENG with  $N = 2, 4, 6$  and  $8$  are 95.6 V, 94.7 V, 93.8 and 92.9 respectively.

The theoretical calculation of the corresponding average  $I_{sc}$  for FT-mode TENG with positive and negative triboelectric material was performed based on electrostatic induction and the charge conservation principle. This can be expressed as Equation 5.3 derived in Section 4.3.1.1:

$$I_{sc} = \frac{A_M \cdot \Delta\rho_q}{\Delta t} \quad (5.3)$$

where  $A_M$  is the total area of the triboelectric materials,  $\Delta\rho_q$  is the difference of the surface charge density between the triboelectric materials and  $\Delta t$  is the time taken of the upper substrate to move from one electrode element to the next electrode element. As before, a constant surface charge density of the PTFE fabric of  $-19.24 \mu\text{C}/\text{m}^2$  and the nylon fabric of  $11.15 \mu\text{C}/\text{m}^2$  are used in the calculation. With a constant  $A_M$  of  $64 \text{ cm}^2$ , a constant  $\Delta\sigma_{sc}$  of  $30.40 \mu\text{C}/\text{m}^2$  and a different  $\Delta t$  for  $N = 2, 4, 6$  and  $8$ , the calculated average  $I_{sc}$  are  $0.39 \mu\text{A}$ ,  $0.78 \mu\text{A}$ ,  $1.17 \mu\text{A}$  and  $1.56 \mu\text{A}$ , respectively,

as shown in Figure 5.15. Since  $\Delta t$  reduces linearly with increasing element number, the  $I_{SC}$  grows linearly.

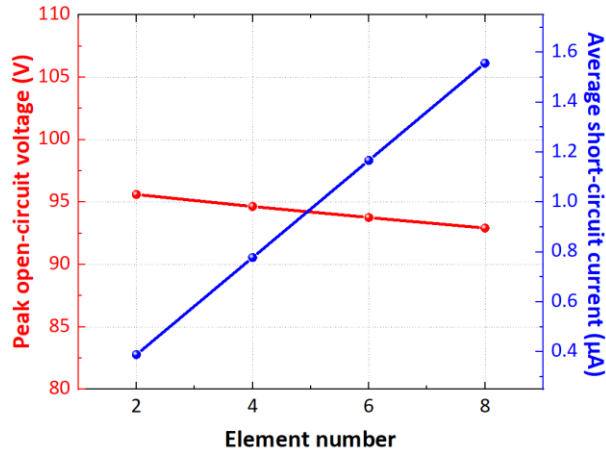


**Figure 5.15** Simulated peak  $V_{OC}$  and calculated average  $I_{SC}$  for different  $N$ .

### 5.3.1.2 Experiment

The electrical experiments for the woven-TENG with  $N = 2, 4, 6$  and  $8$  were carried out using the belt-driven linear actuator under the conditions specified in Section 5.2.3. The transient  $V_{OC}$  and  $I_{SC}$  are represented in Figure 5.16a and b, respectively. Their corresponding peak and RMS values are plotted in Figure 5.17a and b, respectively. Both the peak and RMS  $V_{OC}$  slightly decline with rising element number. The peak  $V_{OC}$  varies between 109 V for  $N = 2$  to 102 V for  $N = 8$ . These are in good agreement with the simulation results. The RMS  $V_{OC}$  also shows a small reduction from 62.9 V for  $N = 2$  to 61.5 V for  $N = 8$ . In contrast, the peak and RMS  $I_{SC}$  show a substantially increasing trend. The peak  $I_{SC}$  rises from 1.29  $\mu A$  for  $N = 2$  to 2.99  $\mu A$  for  $N = 8$  and the RMS  $I_{SC}$  ranges between 0.81  $\mu A$  and 1.77  $\mu A$ , which matches well with the simulated average  $I_{SC}$ .

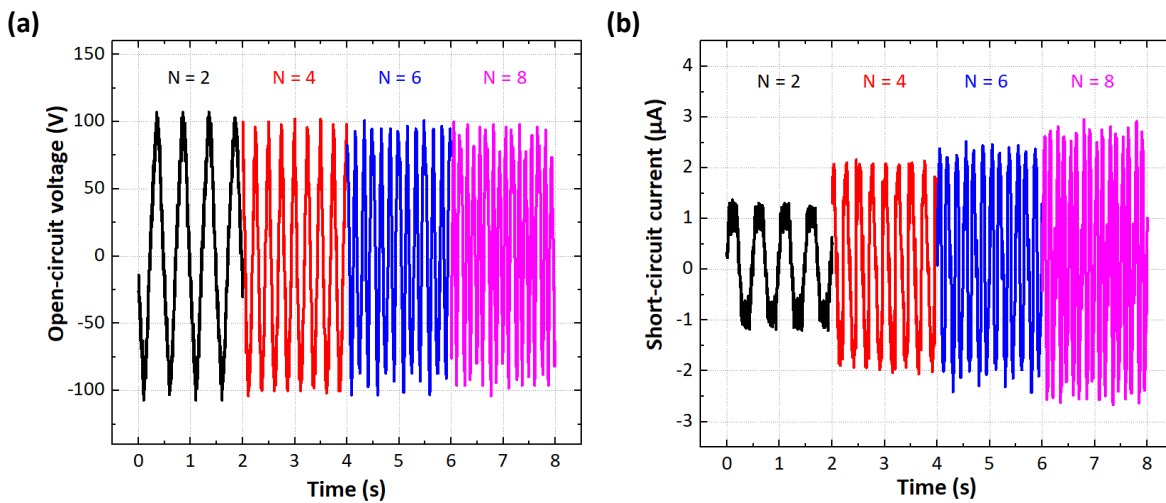


**Figure 5.16** Experimental results of transient (a)  $V_{OC}$  and (b)  $I_{SC}$  of woven-TENGs for different  $N$ .

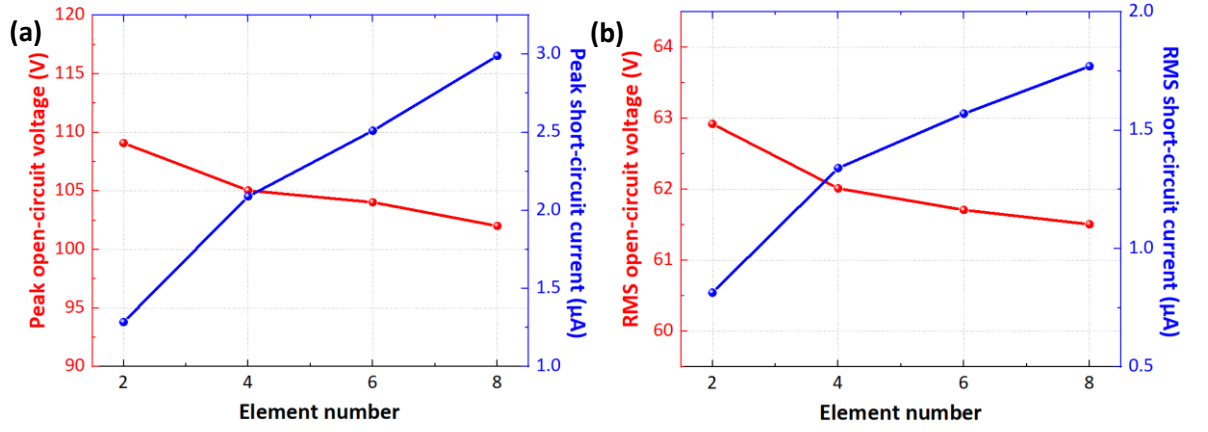


**Figure 5.17** (a) Corresponding experimental peak values of  $V_{OC}$  and  $I_{SC}$  for different  $N$ . (b) Corresponding experimental RMS values of  $V_{OC}$  and  $I_{SC}$  for different  $N$ .

To investigate the total transferred charges, the rectified output currents were used to charge a 10-μF capacitor. The transient capacitor voltage  $V_C$  for the woven-TENGs with the different element numbers are plotted in Figure 5.18a. The  $V_C$  for the woven-TENG with  $N = 8, 6, 4$  and  $2$  reaches a value of 38.6 V, 36.5 V, 31.9 V and 21.2 V in 600 s, respectively. The corresponding maximum  $V_C$ , maximum capacitor charging current  $I_C$  and the maximum capacitor charging power  $P_C$  for the different  $N$  are shown in Figure 5.18b. The  $I_C$  is calculated from the  $V_C$  using Equation 5.4 below:

$$I_C = \frac{\Delta Q}{\Delta t} = \frac{C \cdot \Delta V_C}{\Delta t} \quad (5.4)$$

where  $\Delta Q$  is the transferred charge during a charging time  $\Delta t$  of 30 s,  $\Delta V_C$  is the change in  $V_C$  between a charging time  $\Delta t$  of 30 s and  $C$  is the capacitance e.g. 10 μF. The maximum  $I_C$  rises with increasing  $N$ . The maximum  $I_C$  of 1.25 μA is produced by the woven-TENG with  $N = 8$ . The  $P_C$  is also calculated from the  $V_C$  using Equation 5.5 below:

$$P_C = \frac{\Delta E}{\Delta t} = \frac{\frac{1}{2}C(V_{C,2}^2 - V_{C,1}^2)}{\Delta t} \quad (5.5)$$

where  $\Delta E$  is the change in capacitor energy between a charging time  $\Delta t$  of 30 s. Similarly The  $I_C$  increases with increasing  $N$ . The maximum  $P_C$  of 14.9 μW is generated by the woven-TENG with  $N = 8$ .

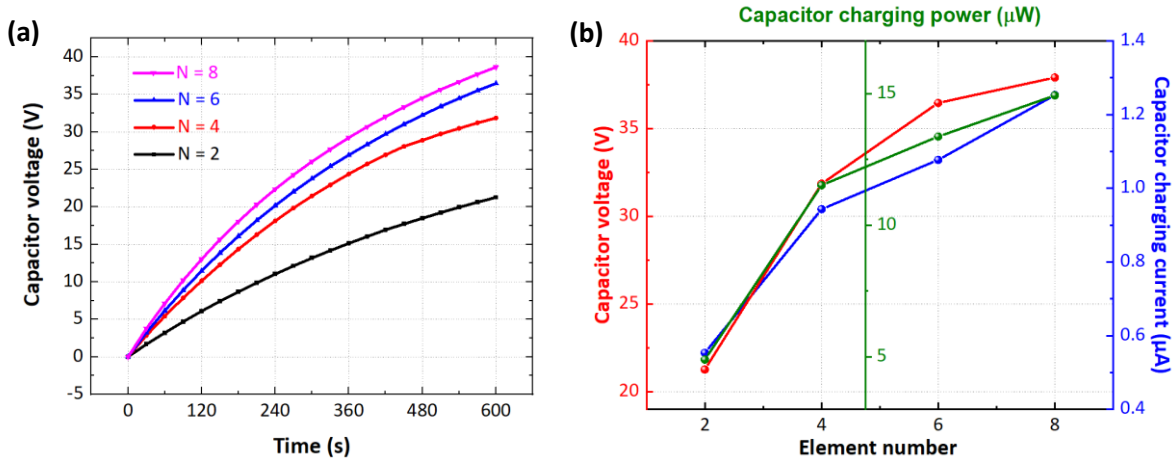


**Figure 5.18** (a) Transient capacitor voltage  $V_c$  and (b) corresponding maximum capacitor voltage at a charging time of 600 s, maximum capacitor charging current  $I_c$  and maximum capacitor charging power  $P_c$  for different  $N$ .

Figure 5.19a and b demonstrate the dependence of the peak values and the RMS values of the voltage, current and power on the external load resistance for the woven-TENG with  $N = 8$ , respectively. The peak and RMS voltage climb with rising load resistance and reaches maximum values of 100 V and 62.9 V at a load resistance of 2 G $\Omega$ , respectively, whereas the peak and RMS current reduce with increasing load resistance. They start from maximum values of 2.90  $\mu A$  and 1.77  $\mu A$  at no load, respectively, and falls to zero at the maximum load. The power is derived from the product of the voltage and the current. The maximum peak and average power of 99.3  $\mu W$  and 34.8  $\mu W$  are obtained at a load resistance of 50 M $\Omega$ , corresponding to a maximum peak and average power density of 15.5 mW/m<sup>2</sup> and 5.43 mW/m<sup>2</sup>, respectively. The peak and average power for the different  $N$  are compared in Figure 5.20a and b, respectively. The peak power for  $N = 2, 4, 6$  and 8 reach a maximum of 47.5  $\mu W$ , 81.5  $\mu W$ , 97.7  $\mu W$  and 99.3  $\mu W$  at the same load resistance of 50 M $\Omega$ , while the average power for  $N = 2, 4, 6$  and 8 reach a peak of 17.0  $\mu W$ , 30.8  $\mu W$ , 34.2  $\mu W$  and 34.8  $\mu W$  at the same load resistance of 50 M $\Omega$ , respectively. Compared to the three previously reported TENGs which can also generate power from all sliding directions (Guo et al. [161] with the maximum power density of 1.9 W/m<sup>2</sup>, Xia et al. [162] with the maximum power density of 2.1 W/m<sup>2</sup> and Ma et al. [163] with the maximum power density of 0.124 W/m<sup>2</sup>), the power generated by the proposed woven-TENG seems to be very low. However, these three TENGs are made of rigid materials and the claimed power is the instantaneous peak power output, which does not reflect the true output of the device. Comparing the peak output current at the same frequency of 2 Hz, these TENGs produces a peak  $I_{SC}$  of around 3  $\mu A$ , 3.5  $\mu A$  and 0.7  $\mu A$ , respectively, which are comparable with the peak  $I_{SC}$  of 2.99  $\mu A$  produced by the woven-TENG ( $N = 8$ ).

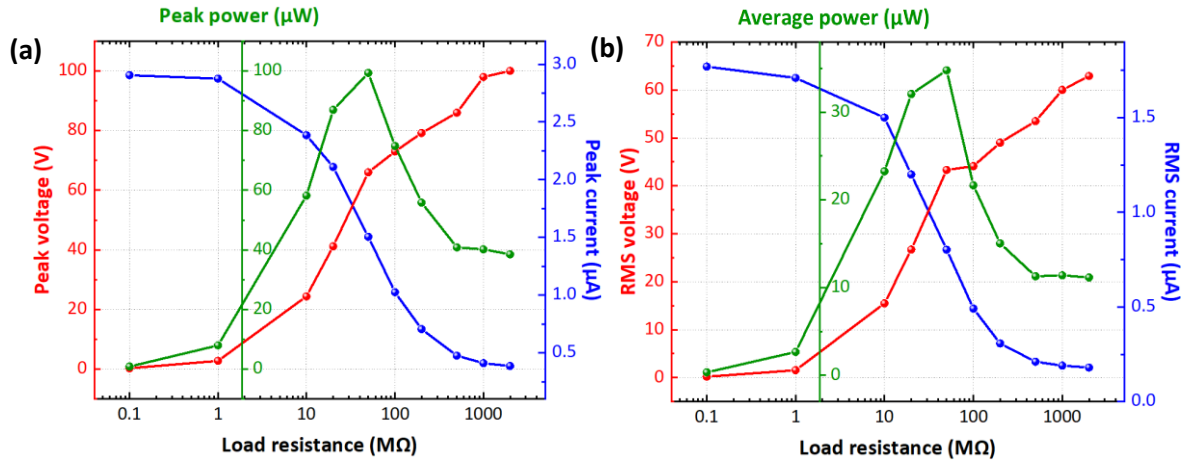


**Figure 5.19** Dependence of (a) peak values and (b) RMS values of voltage, current and average power on the external load resistance for the woven-TENG with  $N = 8$ .

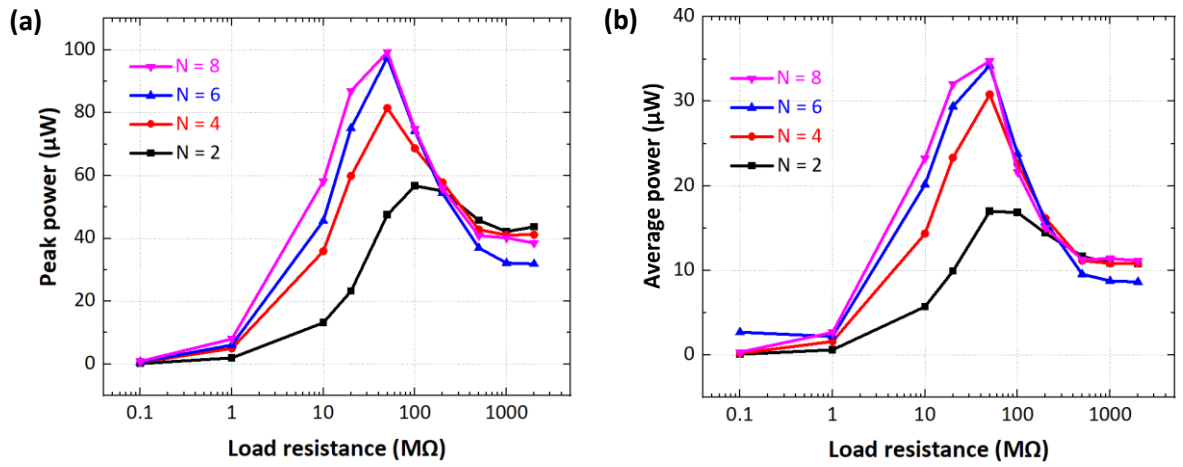


**Figure 5.20** (a) Peak power and (b) average power as a function of load resistance for the woven-TENG with different  $N$ .

### 5.3.2 Effect of the positive and negative triboelectric material

To demonstrate that the implementation of the positive and negative triboelectric material substantially enhances the outputs of woven-TENGs, the woven-TENG with PTFE/nylon ( $N = 4$ ) was compared with checker-like patterned TENGs with only one negative material (PTFE) and with only one positive material (nylon), tested under the same conditions. The photographs of the TENGs with single triboelectric material are illustrated in Figure 5.21. For testing a checker-like patterned TENG with only one positive material and one negative material and comparing the outputs with the woven-TENG, the substrate shown in Figure 5.21a was prepared. A piece of 1-mm-thick fabric was cut to a checker-like pattern, then attached to an acrylic sheet. As illustrated in Figure 5.21b and c, the nylon fabric and PTFE fabric were then attached to the substrate using a double-sided tape forming a checker-like patterned TENG with positive material and negative material, respectively. During testing on the linear actuator due to the surface topology introduced by the 1-mm-thick fabric, only the raised areas of the nylon and PTFE fabrics will contact the electrodes. It

should be noted that the same type of material cannot just be simply woven together without the surface topology introduced by the 1-mm-thick fabric, because the same amount of charge with the same polarity will be generated on the woven weft and the warp triboelectric material and both electrodes will experience the same electric potential due to the presence of the same material and amount of charge on them, which results in no net power generation of the TENG.

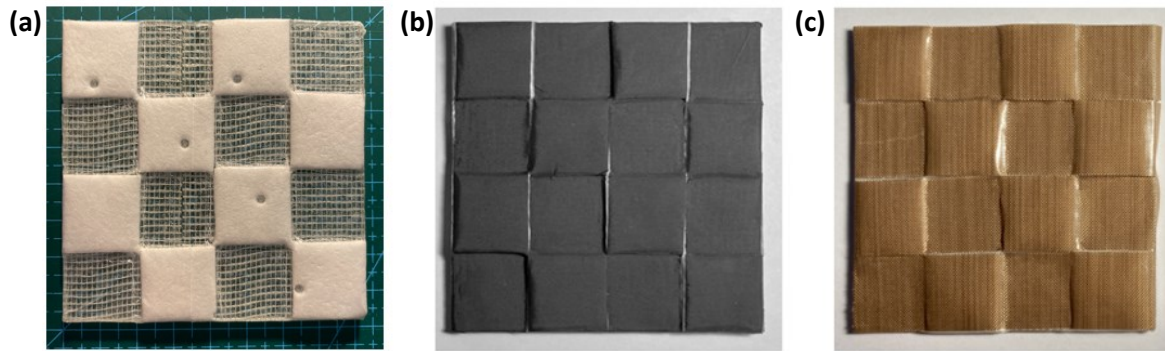


**Figure 5.21** Photograph of (a) bottom substrate before attachment of fabrics, (b) after attached to nylon fabric and (c) after attached to PTFE fabric of checker-like patterned TENG with single triboelectric material.

As shown in Figure 5.22a, the transient  $V_{OC}$  of the woven-TENG with PTFE/nylon are 1.3 times and 2.6 times greater than that of the TENG with PTFE and the TENG with nylon, respectively, while the transient  $I_{SC}$  of the woven-TENG improves by a factor of 1.3 and 3.0 respectively (Figure 5.22b). The transient  $V_C$  for the different TENGs are revealed in Figure 5.23a. The  $V_C$  of a 10- $\mu$ F capacitor charged by the output of the woven-TENG, the TENG with PTFE fabric and the TENG with nylon fabric are plotted in Figure 5.23a. After 600 s of charging, the  $V_C$  reaches 31.9 V, 22.6 V and 9.16 V, respectively. The corresponding transient  $I_C$  and  $P_C$  for the different TENGs, calculated using Equation 5.4 and 5.5, are shown in Figure 5.23b and c, respectively. The  $I_C$  declines over time for all TENGs. The woven-TENG generates the maximum  $I_C$  of 0.94  $\mu$ A, followed by the TENG with PTFE fabric and the TENG with nylon fabric. The reason for the reduction in  $I_C$  over time is due to the growth in  $V_C$  and the increase in the stored charge in the capacitor, reducing the movement of electrons. The  $P_C$  of the woven-TENG, the TENG with PTFE fabric and the TENG with nylon fabric reach the maximum value of 11.5  $\mu$ W, 5.35  $\mu$ W and 0.92  $\mu$ W, respectively. The peak power and the average power as a function of load resistance for different types of TENGs are reviewed in Figure 5.24a and b, respectively. The peak power of the woven-TENG, the TENG with PTFE fabric and the TENG with nylon fabric reach a maximum value of 81.5  $\mu$ W, 42.3  $\mu$ W and 9.44  $\mu$ W, respectively, whereas the average power of the woven-TENG peaks at a maximum value of 30.8  $\mu$ W, which is 2.2 and 12.4 times higher than that of the TENG with PTFE and the TENG with nylon, respectively.



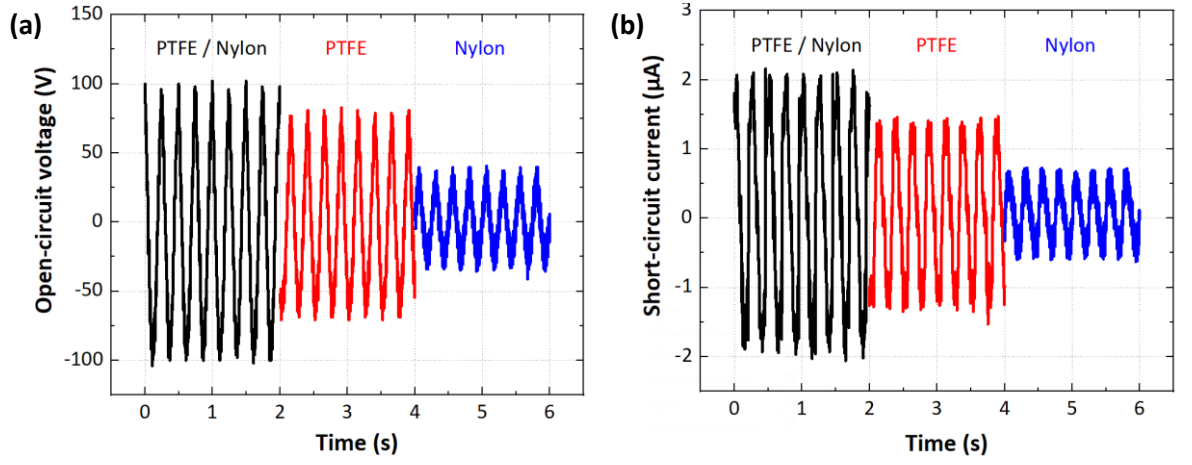


**Figure 5.22** Transient (a)  $V_{OC}$  and (b)  $I_{SC}$  for the woven-TENG with PTFE/nylon ( $N = 4$ ), a checker-like patterned TENG with one negative material (PTFE) and a checker-like patterned TENG with one positive material (nylon).

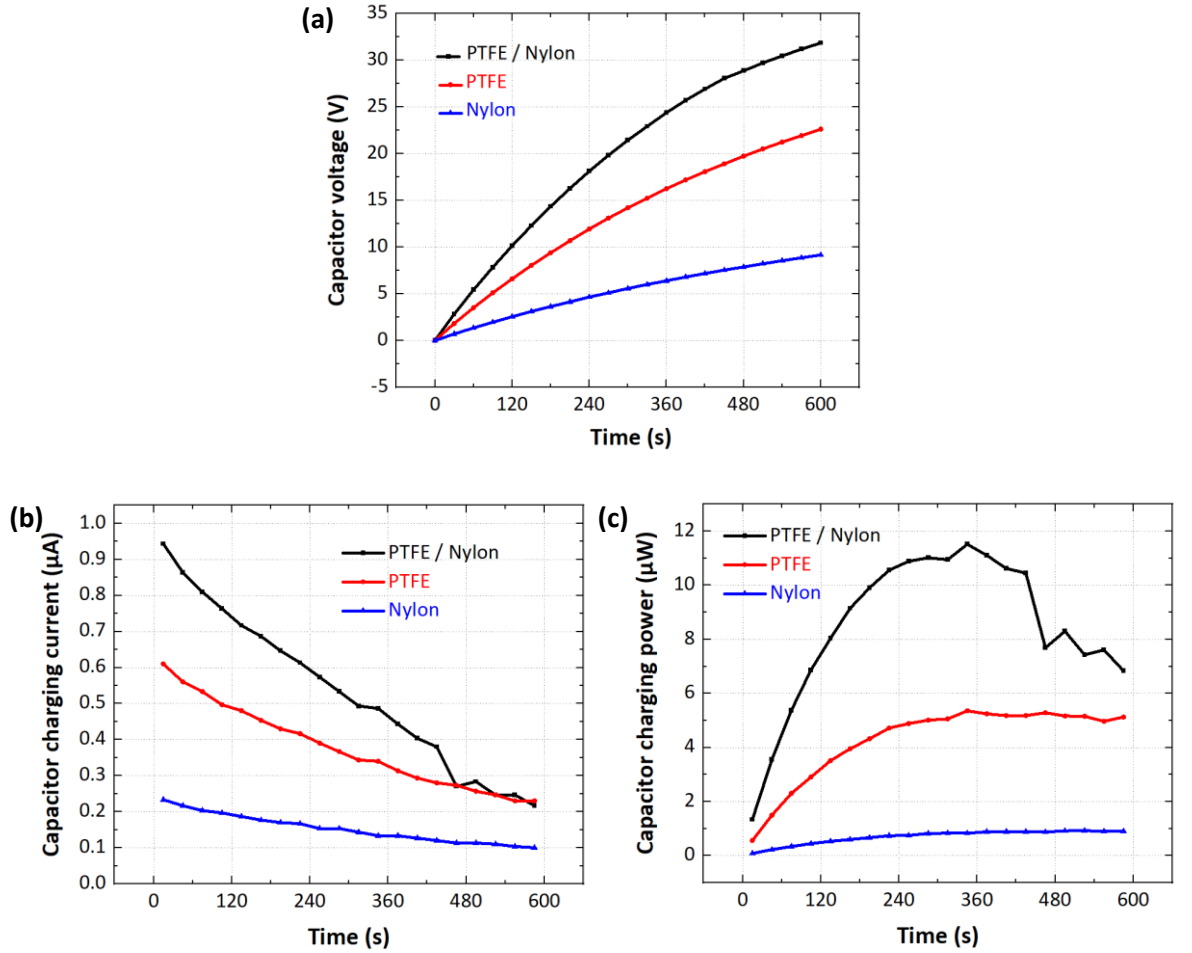


**Figure 5.23** (a) Transient  $V_C$  and (b) corresponding transient  $I_C$  and (c) corresponding transient  $P_C$  for different types of TENGs.

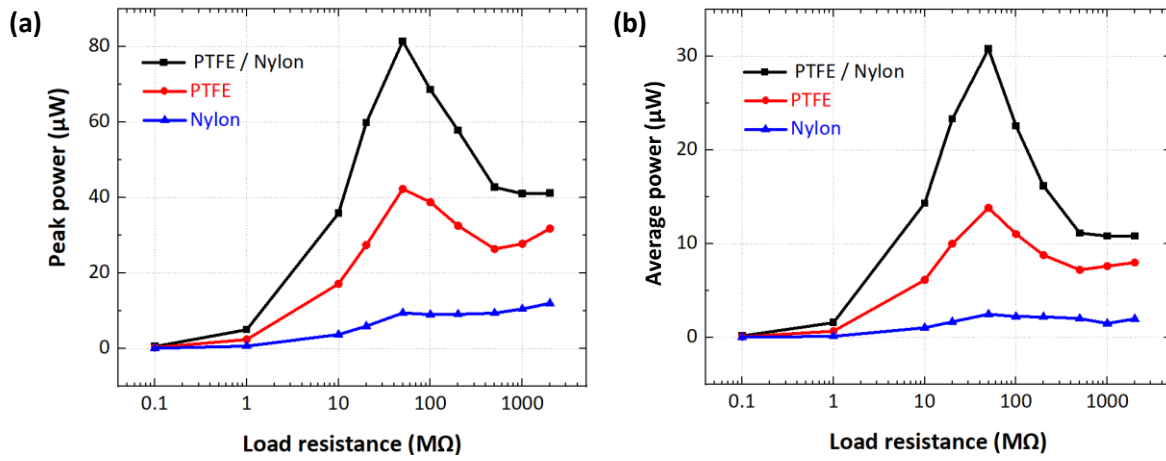


**Figure 5.24** (a) Peak power and (b) average power as a function of load resistance for different types of TENGs

### 5.3.3 Direction dependence

One major advantage of the proposed woven-TENG over the grating structured TENG is the ability to harvest energy from all planar sliding directions. Firstly, a model shown in Figure 5.25 was applied for the theoretical calculation of the electrical outputs of a simple woven-TENG for  $N = 2$ . The upper transparent substrate comprises a nylon fabric marked in blue and a PTFE fabric marked in red. The lower substrate consists of a warp electrode marked in white aligned in y-direction and a weft electrode marked in yellow aligned in x-direction (Figure 5.25 (i)). Figure 5.25 (ii) shows the initial state when the upper substrate fully overlaps with the electrodes. In Figure 5.25 (iii), the upper substrate moves at an angle  $\theta$  relative to the x-axis. The upper substrate is transparent in this illustration and when the nylon fabric overlaps with the weft electrode, the overlapping areas become green (according to colour mixing). Likewise, when the PTFE fabric overlaps with the weft electrode, the areas become orange (according to colour mixing). In the initial state (ii), electrons accumulate at the warp electrode due to the presence of positive charges on the nylon surface. At the same time, electrons are repelled from the weft electrode due to the presence of negative charges on the surface of the PTFE fabric. In state (iii), the nylon fabric partly overlaps with the weft electrode (green areas) and the PTFE fabric partly overlaps with the warp electrode (red areas) resulting in an electron transfer from the warp to the weft electrode. The amount of the transferred electrons is proportional to the sum of the green and the red areas. Due to the symmetry of the elements, the sum of the green and the red areas are always equal. For this reason, the model can be simplified by considering only the green areas.

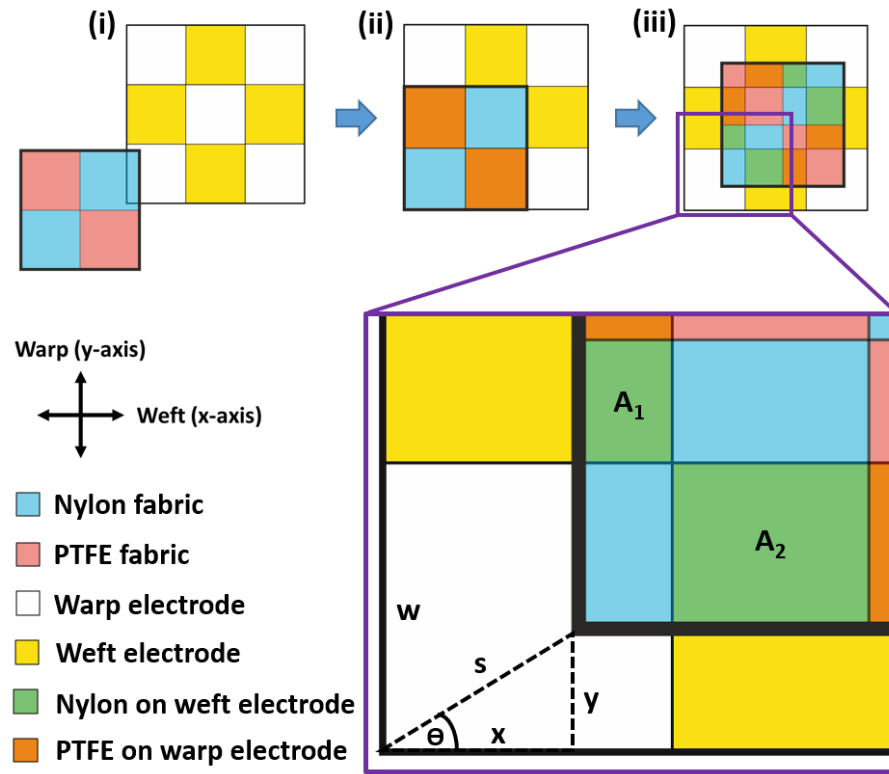


**Figure 5.25** Schematic illustration applied for theoretical calculation of woven-TENG for  $N = 2$ .

The maximum sum of the green areas and thus the maximum transferred charges are obtained, when  $\theta$  equals  $0^\circ$  and  $90^\circ$ , while the minimum transferred charge of 50% of the maximum is obtained for  $\theta$  equals  $45^\circ$ . These are illustrated in Figure 5.26. The maximum charge transfer is obtained from the  $0^\circ$  and  $90^\circ$  directions shown in Figure 5.26a (ii) and c (ii), respectively, where the sum of the green and the red areas reaches the maximum. When the top substrate moves in a  $45^\circ$  direction with respect to the x-axis, the sum of the green and the red areas is the highest in the state shown in Figure 5.26b (i), which is 50% of the sum of the areas shown in Figure 5.26a (ii) and Figure 5.26c (ii). As a result, only half of the charge is transferred for  $45^\circ$  compared to the  $0^\circ$  and  $90^\circ$  directions.

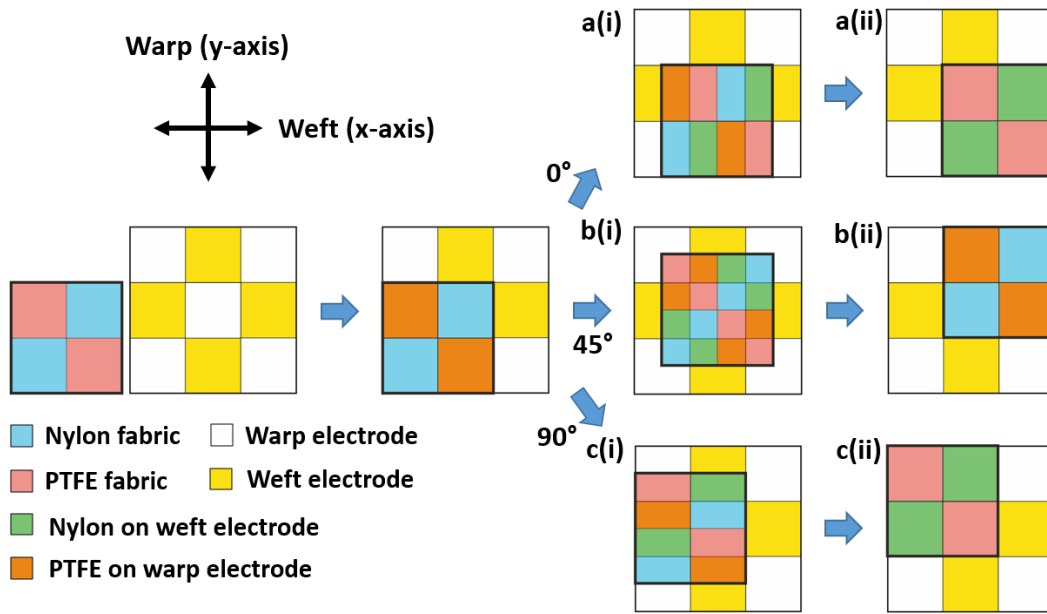


**Figure 5.26** Schematic illustration applied for theoretical calculation of transferred charges in (a) 0°, (b) 45°, and (c) 90° direction with respect to the x-axis.

To determine a percentage of the transferred electrons for a given angle  $\theta$  compared to the maximum output, the sum of the green areas  $A$  in the zoom-in inset in Figure 5.25 (iii) is calculated using the following equations:

$$A = A_1 + A_2 = y(w - x) + x(w - y) \quad (5.6)$$

where  $A_1$  is the first green area,  $A_2$  is the second green area,  $w$  is the width of the element and  $s$  is the travel distance of the upper substrate from the initial state. Assuming that the nylon fabric element does not travel further than the adjacent electrode element,  $x$  and  $y$  can be expressed by Equation 5.7 and 5.8 below:

$$x = s \cos \theta, \quad s \cos \theta \leq w \text{ and } 0^\circ \leq \theta \leq 90^\circ \quad (5.7)$$

$$y = s \sin \theta, \quad s \sin \theta \leq w \text{ and } 0^\circ \leq \theta \leq 90^\circ \quad (5.8)$$

By substitution of Eq. 5.7 and 5.8 into Equation 5.6, Equation 5.6 can be rewritten as a function of  $s$  below (The detailed calculation can be found in Appendix D):

$$A(s) = ws(\sin \theta + \cos \theta) - s^2 \sin 2\theta \quad (5.9)$$

This function is a parabola function opening downward, which has a maximum at a travel distance  $s_{max}$ . To find this, the first derivative of Equation 5.9 is set equal to zero as below:

$$A'(s_{max}) = w(\sin \theta + \cos \theta) - 2s_{max} \sin 2\theta = 0 \quad (5.10)$$

After solving for  $s_{max}$ , we obtain

$$S_{max} = \frac{w(\sin \theta + \cos \theta)}{2 \sin 2\theta} \quad (5.11)$$

By substitution of Equation 5.11 into Equation 5.9, the maximum area  $A_{max}$  can be expressed as Equation 5.12 below:

$$A_{max} = \frac{w^2(\sin \theta + \cos \theta)^2}{4 \sin 2\theta} \quad (5.12)$$

The percentage of the transferred electrons  $p$  in at an angle  $\theta$  compared to the maximum transferred electrons can be calculated by the Equation 5.13 below:

$$p = \frac{A_{max}}{w^2} \times 100 = \frac{25(\sin \theta + \cos \theta)^2}{\sin 2\theta} \quad (5.13)$$

Considering the conditions in Equation 5.7 and Equation 5.8,  $\theta$  must be in the range between  $18.44^\circ$  and  $71.56^\circ$ . For  $0^\circ \leq \theta < 18.44^\circ$ , the maximum area is obtained when  $x = w$ , thus  $S_{max} = \frac{w}{\cos \theta}$ . For  $71.56^\circ < \theta \leq 90^\circ$ , the maximum area is obtained when  $y = w$ , thus  $S_{max} = \frac{w}{\sin \theta}$ . By substitution them into Equation 5.9 and with the same calculation method, we obtain

$$\begin{aligned} p &= (1 - \tan \theta) \times 100, & 0^\circ \leq \theta < 18.44^\circ \\ p &= \frac{25(\sin \theta + \cos \theta)^2}{\sin 2\theta}, & 18.44^\circ \leq \theta \leq 71.56^\circ \\ p &= (1 - \cot \theta) \times 100, & 71.56^\circ < \theta \leq 90^\circ \end{aligned} \quad (5.14)$$

Equation 5.14 are plotted in green for  $0^\circ \leq \theta \leq 90^\circ$  in Figure 5.27a and compared to the experimental RMS  $V_{OC}$  and  $I_{SC}$  of the woven-TENG ( $N = 4$ ) for  $\theta = 0^\circ, 15^\circ, 30^\circ, 45^\circ, 60^\circ, 75^\circ$  and  $90^\circ$  on the same graph. The maximum outputs are produced for  $\theta = 0^\circ$ , when the upper substrate moves parallel to the PTFE fabric, followed by  $\theta = 90^\circ$ , when the upper substrate moves parallel to the nylon fabric and the minimum outputs of around the half of the maximum outputs are generated for  $\theta = 45^\circ$ . These are in very good accordance with the theoretical calculation. Figure 5.27b shows the  $V_C$  of a  $10\text{-}\mu\text{F}$  capacitor charged by the output of the woven-TENG moving in different directions. The maximum  $V_C$  is also obtained, when the  $\theta = 0^\circ$  and  $\theta = 90^\circ$ , while the minimum  $V_C$  is obtained, when the  $\theta = 45^\circ$ , which is also around the half of the maximum  $V_C$  at  $\theta = 0^\circ$  and  $\theta = 90^\circ$ . Since the power of the TENG is calculated from the product of voltage and current or in case of a capacitor,  $P_C = \frac{1}{2} \frac{C V^2}{t}$ , the power of the woven-TENG will reduce to 25% of the maximum power output.

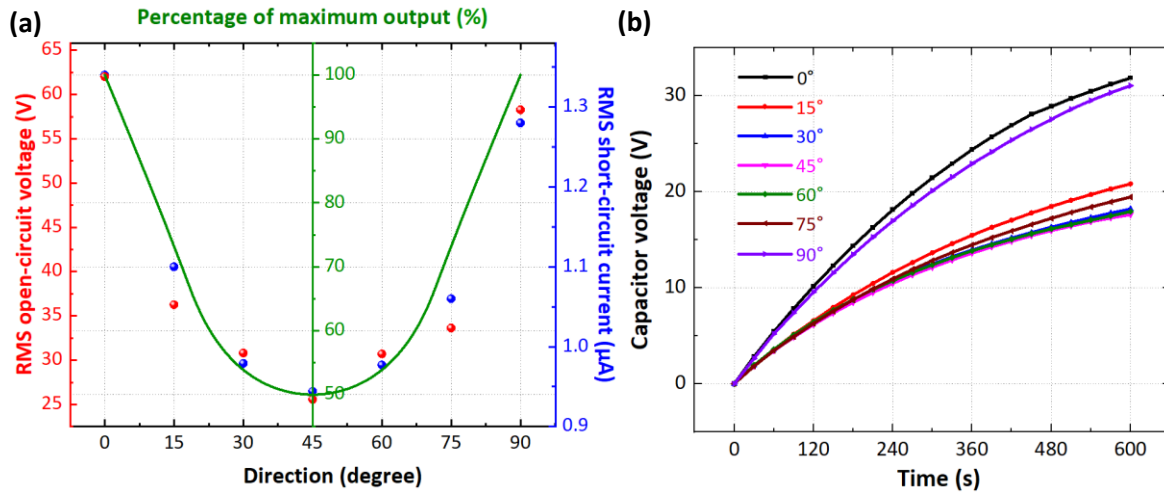


**Figure 5.27** (a) Calculated percentage of maximum output compared with experimental RMS  $V_{oc}$  and RMS  $I_{sc}$  as a function of sliding direction with respect to the x-axis. (b) Transient  $V_c$  for different sliding directions.

### 5.3.4 Oscillation frequency dependence

The frequency dependence measurements were carried out for the woven-TENG with  $N = 4$  by varying the oscillation frequency of the linear actuator from 1 Hz to 3 Hz in steps of 0.5 Hz and keeping the other parameters constant (see Section 5.2.3). The transient  $V_{oc}$  and  $I_{sc}$  of the woven-TENG with  $N = 4$  for the different frequencies are presented in Figure 5.28a and b, respectively. The corresponding peak values and RMS values of  $V_{oc}$  and  $I_{sc}$  of the woven-TENG are plotted as a function of frequency in Figure 5.29a and b, respectively. At first, the peak and the RMS  $V_{oc}$  gradually grow with rising frequency and begin to saturate at a frequency of 2.0 Hz. According to Equation 5.2, the  $V_{oc}$  is explicitly independent on the frequency. However, the reason for this growth stems from a change in the surface charge density that increases with the frequency and saturates at a certain value. At a frequency of 3 Hz, the peak and the RMS  $V_{oc}$  are 101.0 V and 61.4 V, respectively. The peak and the RMS  $I_{sc}$  increase linearly with increasing frequency since they are inversely proportional to the time  $\Delta t$  according to Equation 5.3, which decline with increasing frequency. At a frequency of 3 Hz, the peak and the RMS  $I_{sc}$  reach 3.19  $\mu A$  and 1.79  $\mu A$ , respectively. The rectified output of the woven-TENG was used to charge a 10- $\mu F$  capacitor for 600 s and is shown in Figure 5.30a. The maximum  $V_c$ , capacitor charging current  $I_c$  and capacitor charging power  $P_c$  are calculated from the transient  $V_c$  and illustrated in Figure 5.30b. They all show an increased tendency. At a frequency of 3 Hz, the  $V_c$ ,  $I_c$  and  $P_c$  peak at 35.9 V, 1.3  $\mu A$  and 13.0  $\mu W$ , respectively.

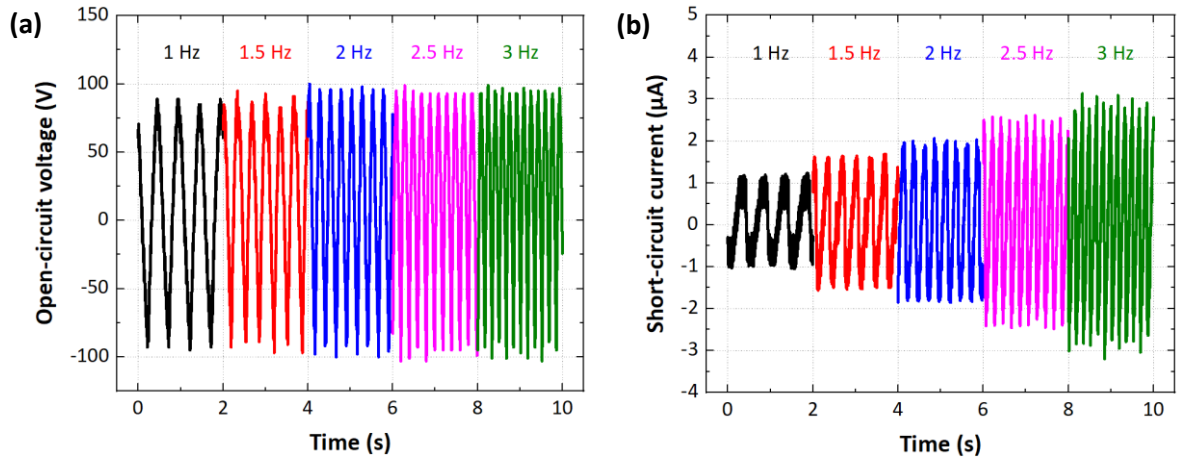


**Figure 5.28** Transient (a)  $V_{OC}$  and (b)  $I_{SC}$  of the woven-TENG with  $N = 4$  for the different frequencies.

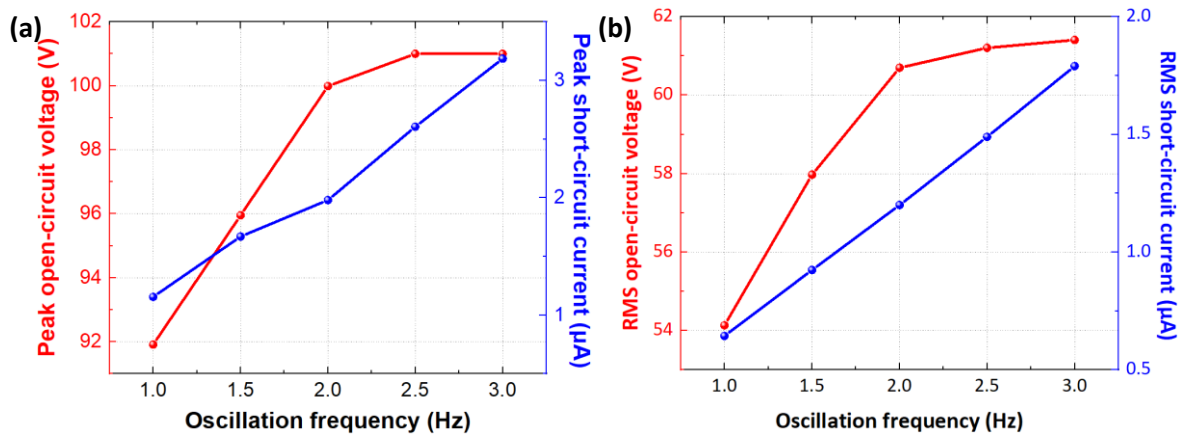


**Figure 5.29** Corresponding (a) peak values and (b) RMS values of  $V_{OC}$  and  $I_{SC}$  as a function of oscillation frequency.

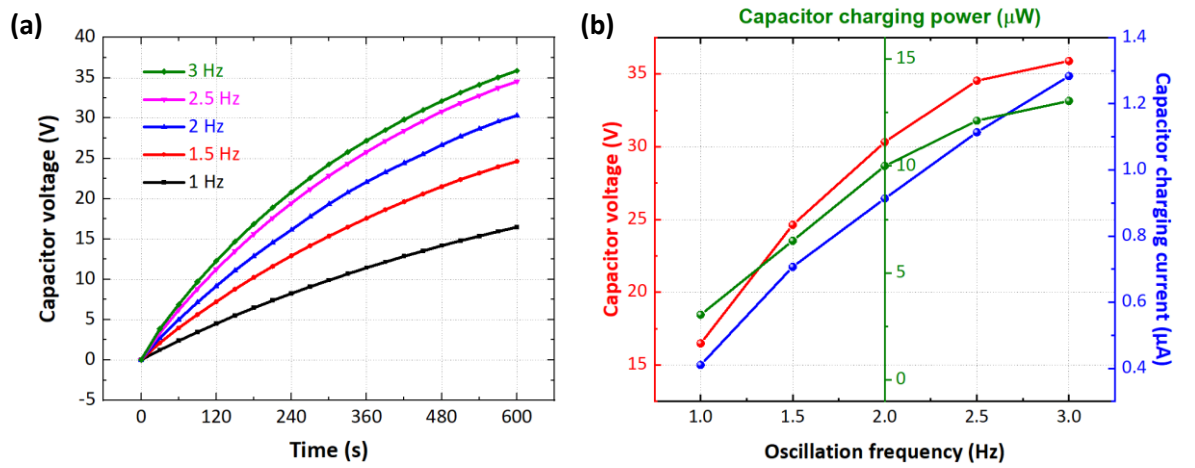


**Figure 5.30** (a) Transient  $V_C$  of the woven-TENG with  $N = 4$  for different oscillation frequencies. (b) Corresponding maximum  $V_C$ ,  $I_C$  and  $P_C$  as a function of oscillation frequency.

### 5.3.5 Contact force dependence

The force dependence measurements were performed for the woven-TENG with  $N = 4$  by changing the weight on top of the upper substrate from 1 N to 12 N in increments of 2 N and keeping the other parameters constant. The transient  $V_{OC}$  and  $I_{SC}$  of the woven-TENG for different contact forces are revealed in Figure 5.31a and b, respectively. The corresponding dependence of the peak values and the RMS values of  $V_{OC}$  and  $I_{SC}$  on the contact force are shown in Figure 5.32a and b, respectively. In the beginning, both of the outputs increase sharply with increasing contact force until they become essentially constant at a contact force over 7 N, since the surface charge density increases with the contact force and saturates a certain value. At a contact force of 3 Hz, the peak and the RMS  $V_{OC}$  reach 106.1 V and 64.8 V, while the peak and the RMS  $I_{SC}$  are 2.07  $\mu$ A and 1.28  $\mu$ A, respectively. The transient  $V_C$  as a function of contact force is shown in Figure 5.33a. The corresponding maximum  $V_C$ ,  $I_C$  and  $P_C$  for the different contact forces are represented in Figure 5.33b. They show the same tendency as the  $V_{OC}$  and  $I_{SC}$ . The  $V_C$ ,  $I_C$  and  $P_C$  saturate at around 30.9 V, 1.1  $\mu$ A and 10.1  $\mu$ W, respectively.

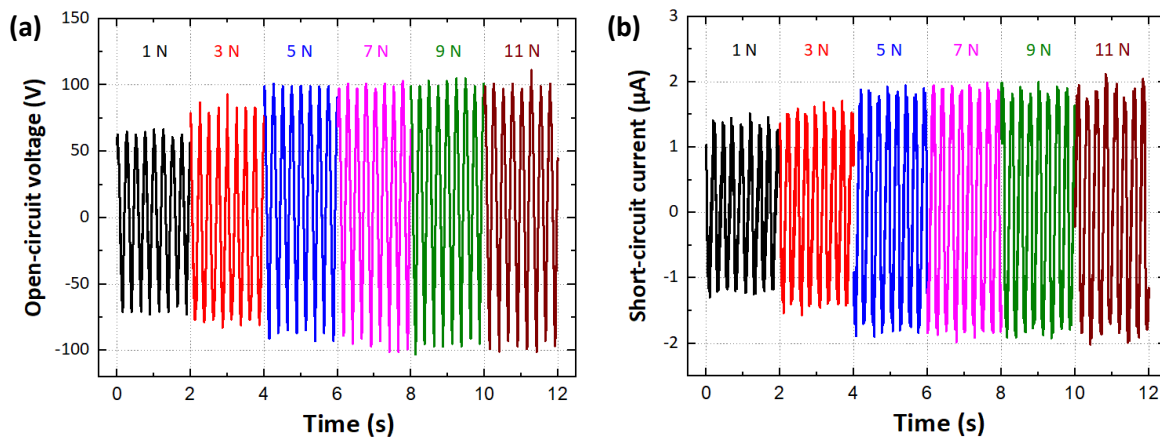


**Figure 5.31** Transient (a)  $V_{OC}$  and (b)  $I_{SC}$  of the woven-TENG with  $N = 4$  for different contact forces.

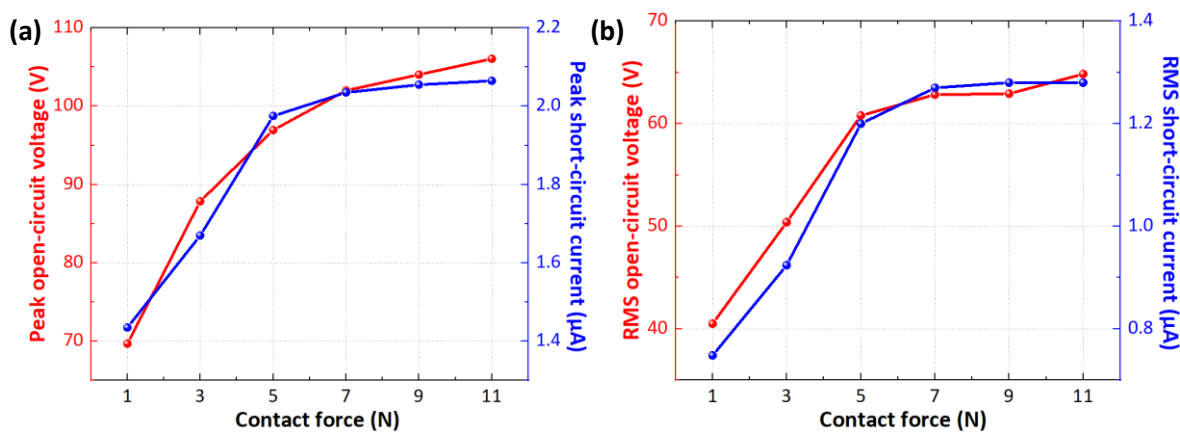


**Figure 5.32** Corresponding (a) peak values and (b) RMS values of  $V_{OC}$  and  $I_{SC}$  as a function of contact force.



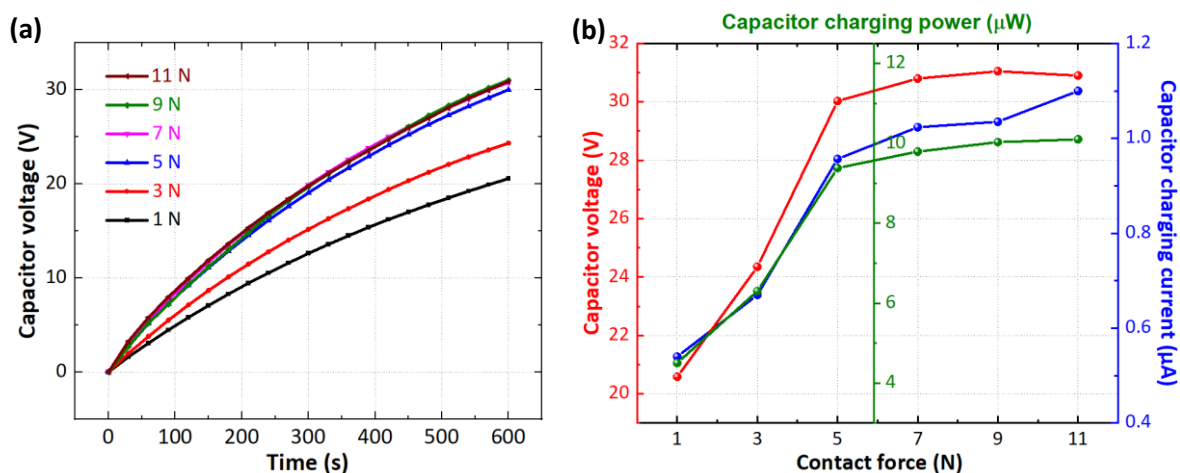


**Figure 5.33** (a) Transient  $V_c$  of the woven-TENG with  $N = 4$  for different contact forces. (b) Corresponding maximum  $V_c$ ,  $I_c$  and  $P_c$  as a function of contact force.

### 5.3.6 Durability and washability

Durability and washability are important properties that need to be tested for the practical utilisation of the woven-TENG in wearable devices. The upper and the lower substrate of the woven-TENG with  $N = 4$  were first rubbed against each other using the linear actuator under the condition specified in Section 5.2.3. The recorded transient  $V_{oc}$  and  $I_{sc}$  are illustrated in Figure 5.34a and b, respectively. The peak  $V_{oc}$  falls slightly from 102 V to 85 V by 16.7% after 40,000 operating cycles, while the peak  $I_{sc}$  drops by 12.5%. After hand-washing, the TENG output is restored to its original value. After 40,000 operating cycles, a minimal material transfer, abrasion of the Ag electrodes and fraying of the nylon fabric were observed. The fraying can be prevented by an adhesive layer on the backside of the nylon fabric. The photographs of the upper and the lower substrate after 40,000 operating cycles and during hand washing are shown in Figure 5.35a-d. A small part of Ag particles and other contamination are transferred between the electrodes and the triboelectric materials (nylon/PTFE fabric) and accumulate on their surfaces. However, this contamination can be easily cleaned away during hand-washing using water, detergent and brush (Figure 5.35c and d) or by using a machine wash cycle. Figure 5.36a-f show the SEM images of the Ag electrode, PTFE fabric and nylon fabric before and after 40000 operating cycles, hand wash and machine washes. After 40000 operating cycles followed by a hand wash and 4 machine washes, small defects (cracks) are observed at some part on the Ag electrode surface. A small part of Ag particles and other contamination are partly transferred between the electrodes and the triboelectric materials, and accumulate on their surfaces, especially on the nylon surface.

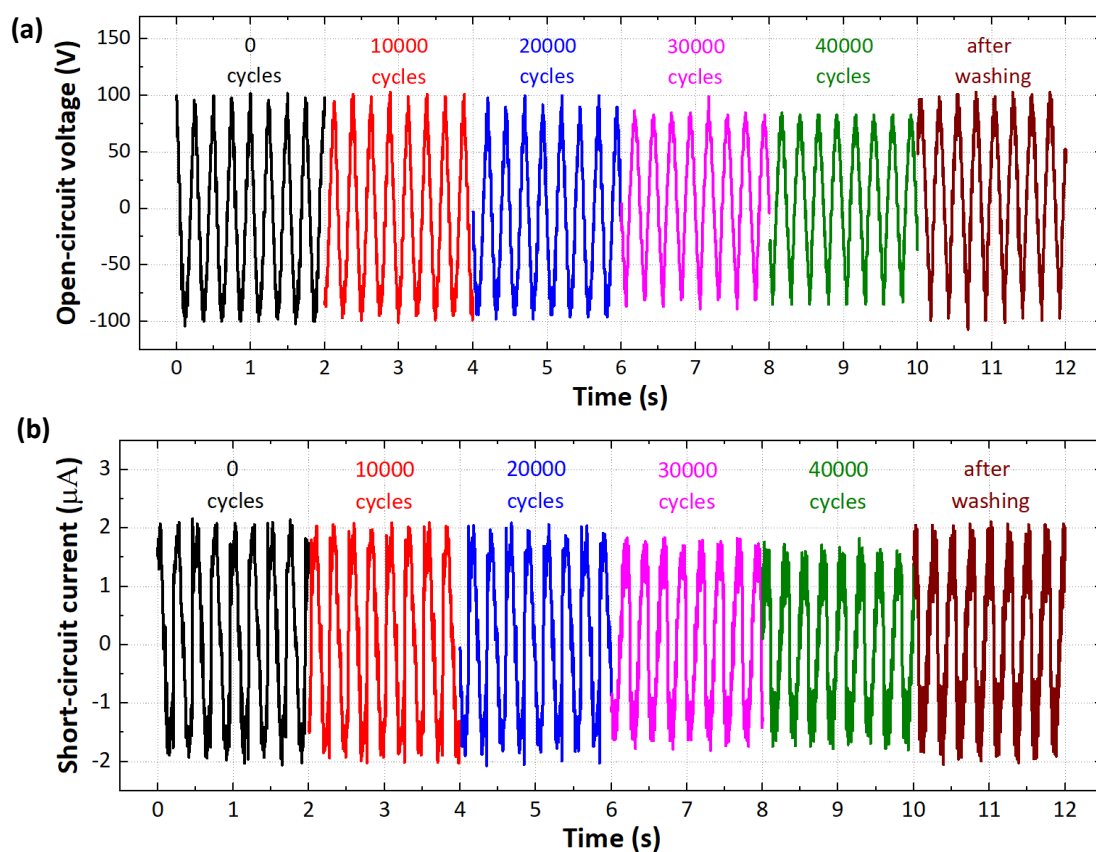


**Figure 5.34** Transient (a)  $V_{oc}$  and (b)  $I_{sc}$  of the woven-TENG with  $N = 4$  for various operating cycles and after hand-washing.

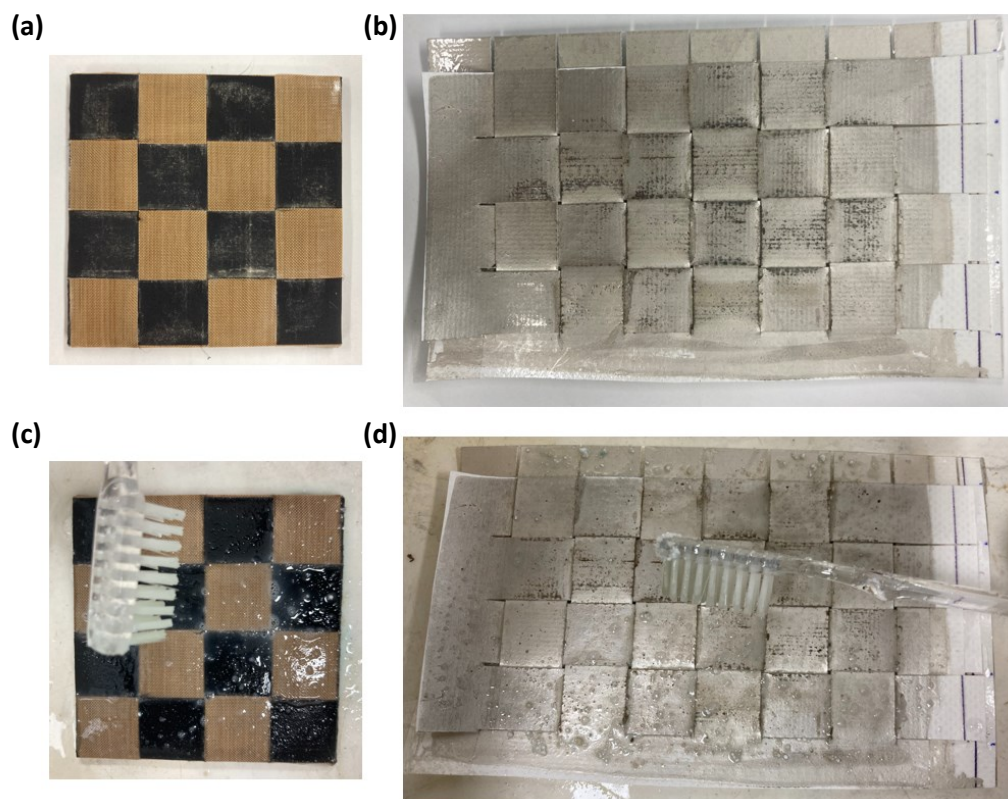


**Figure 5.35** Photograph of (a) top triboelectric materials and (b) bottom electrodes after 40000 operating cycles before washing. Photograph of (c) top triboelectric materials and (d) bottom electrodes during hand-washing using a brush.

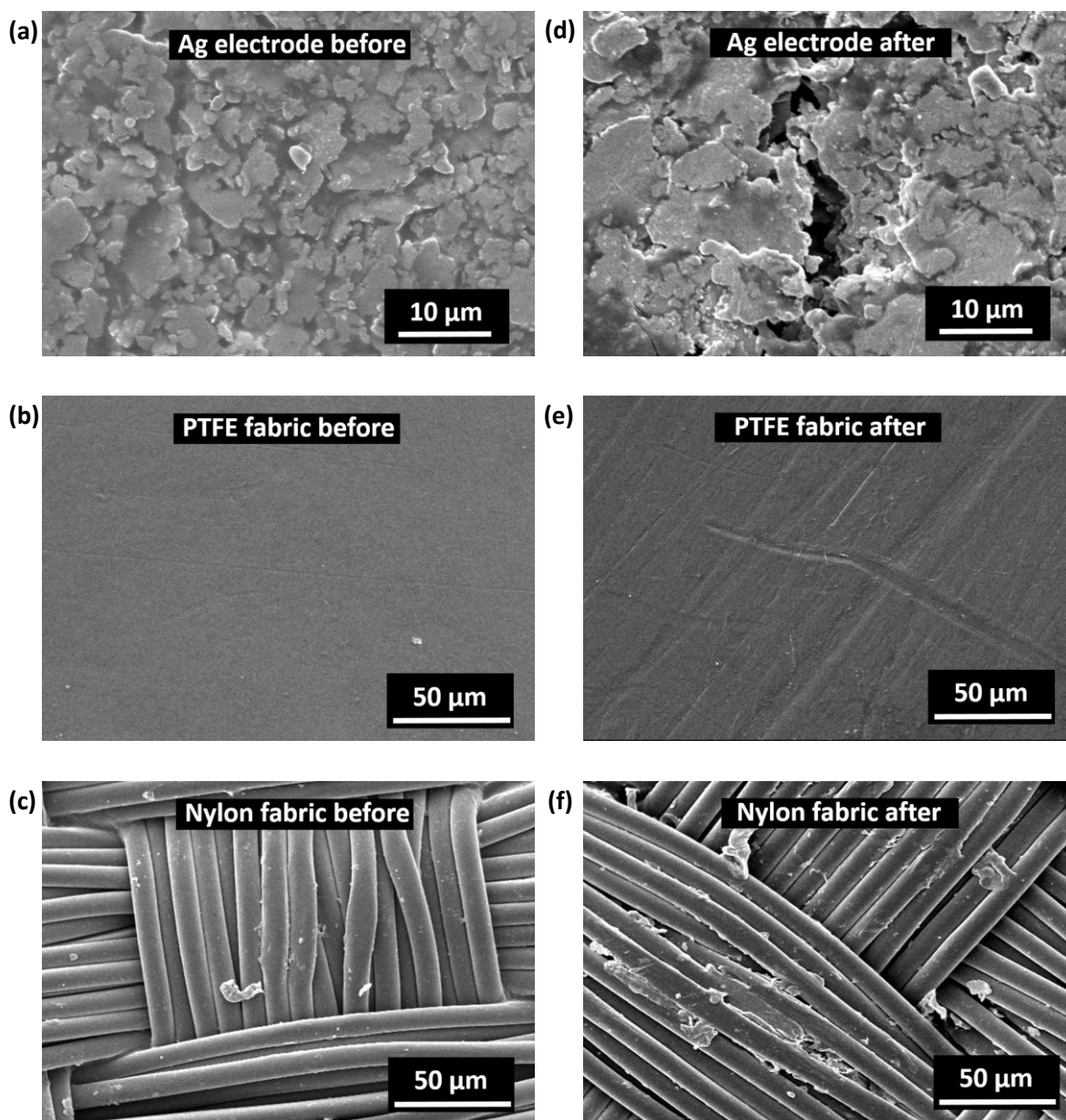


**Figure 5.36** SEM image of (a) Ag electrode (b) PTFE fabric and (c) nylon fabric before operation. SEM image of (d) Ag electrode (e) PTFE fabric and (f) nylon fabric after 40000 operating cycles followed by a hand wash and 4 machine washes.

Figure 5.37a and b reveal the transient  $V_{OC}$  and  $I_{SC}$  after different numbers of washing cycles. The woven-TENG with the acrylic sheet was initially hand-washed using water, detergent and brush, then dried at room temperature. After drying, the outputs of the woven-TENG was recorded. Next, it was placed in a laundry bag and washed using a commercial washing machine (Beko WME7247) for 49 min at a water temperature of 30 °C and a spin speed of 1000 rpm in hand-wash mode together with normal clothes and detergent. The woven-TENG was washed up to 4 times and the outputs were recorded after each wash. Both outputs remain stable indicating that the woven-TENG can survive this wash program.

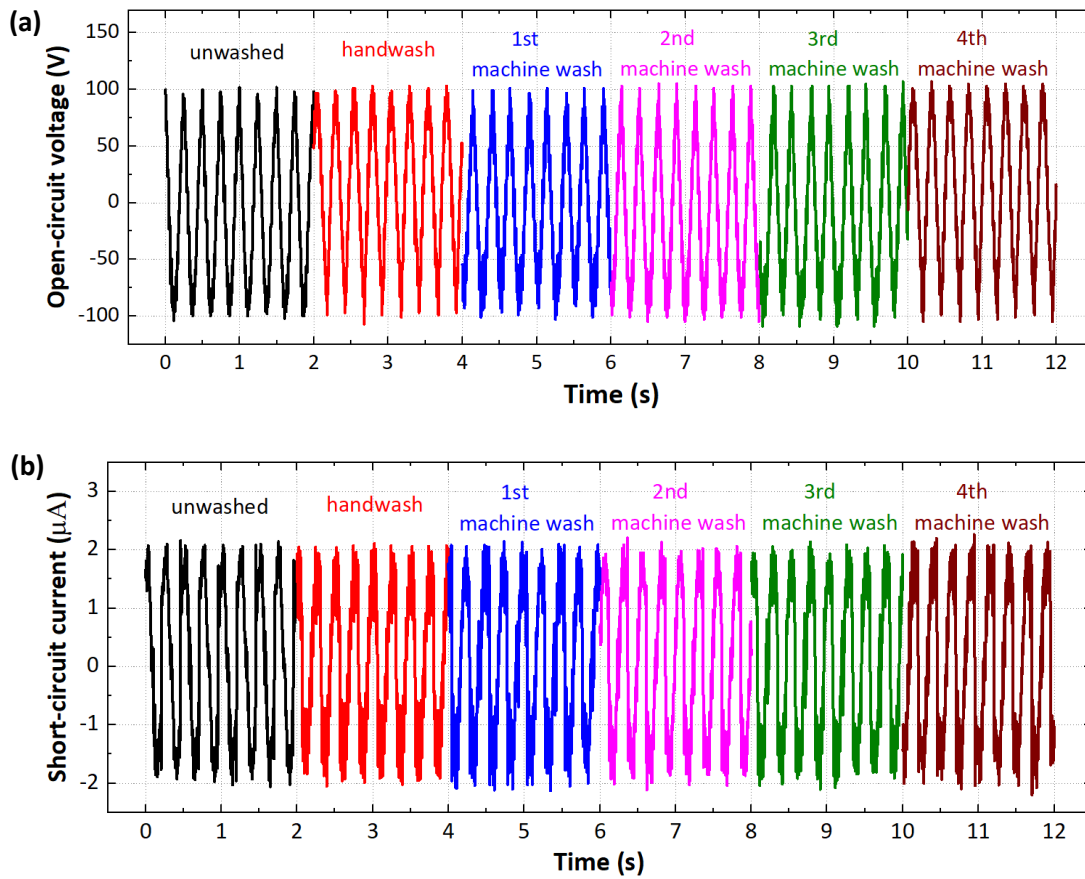


**Figure 5.37** Transient (a)  $V_{OC}$  and (b)  $I_{SC}$  of the woven-TENG with  $N = 4$  after different washing times.

### 5.3.7 Applications in wearable electronics

To illustrate a potential utilisation of the woven-TENG in wearable electronics, the woven-TENG with  $N = 8$  was embedded into a lab coat. The upper substrate was attached to a lower sleeve and the lower electrodes were attached to the hip and waist parts of the coat to harvest energy from walking and running as shown in Figure 5.38a and b, respectively. The energy is generated from the relative movement between the arm and torso, which does normally not occur in an exact straight line. For examples, the position of the arm movement can deviate from the direction of the electrode orientation by dozens of degrees during running depending on the physical characteristics of each person and the running speed and style. In all such cases, the device can still operate effectively and this is the major advantage of the woven-TENG presented here compared with TENGs with linear-grating structure, which require precise movement between the freestanding layer (arm) and the electrodes (torso). Figure 5.39a and b represent the  $V_{OC}$  produced during an arm swing frequency of around 0.75 Hz for walking and 2.30 Hz for running, respectively. A peak  $V_{OC}$  of around 120 V is observed for both activities but the peaks for running are much more frequent. As shown in Figure 5.40a and b, the output is rectified and used to charge different capacitors during walking and running, respectively. A 1- $\mu$ F capacitor can be charged to a  $V_C$  of 3.92 V and 10.8 V after 30 s. This level of energy is sufficient to operate some wearable applications. To

demonstrate this, the output of the woven-TENG was used to drive a wearable night-time warning indicator for pedestrians, a digital watch and a Bluetooth transceiver. The circuit diagrams for all applications are exhibited in Figure 5.41.

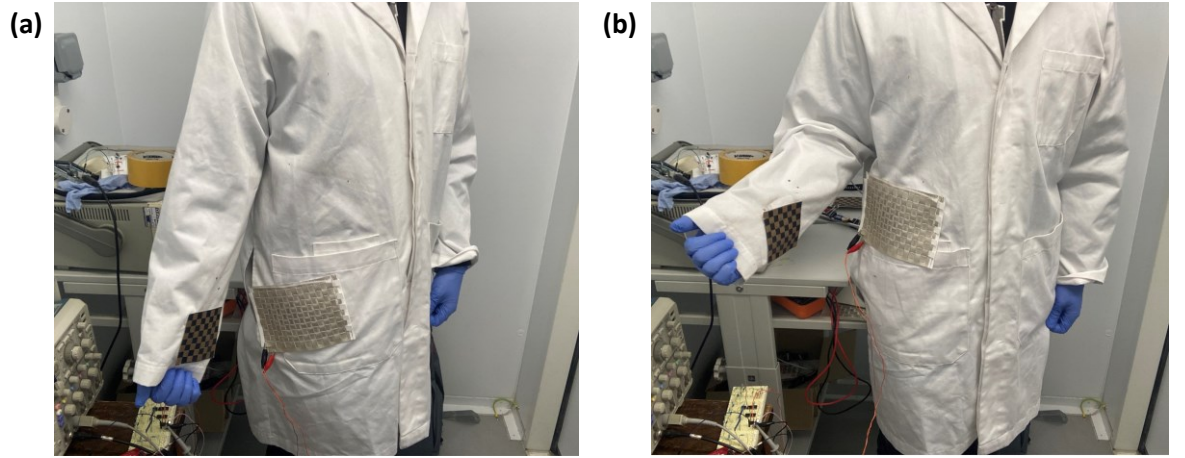


**Figure 5.38** Photographs of the woven-TENG with  $N = 8$  embedded into a lab coat for harvesting energy from (a) walking and (b) running.

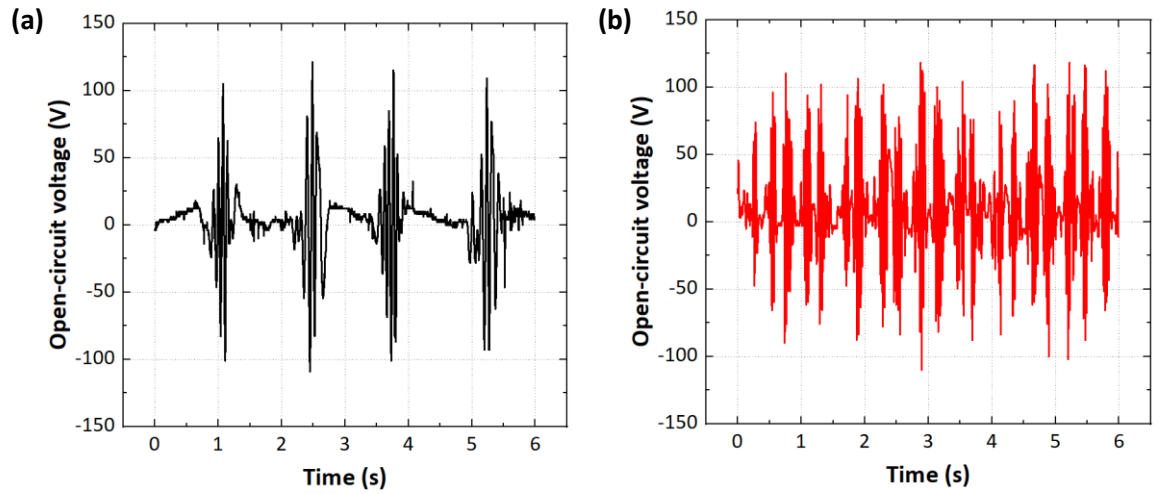


**Figure 5.39** Transient  $V_{oc}$  of the woven-TENG with  $N = 8$  produced during (a) walking and (b) running.

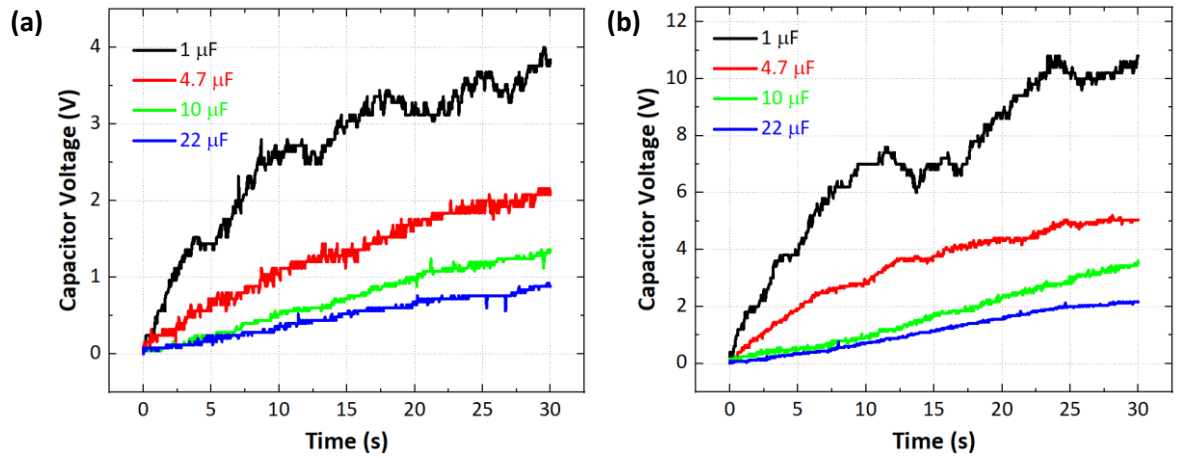


**Figure 5.40**  $V_c$  of the woven-TENG with  $N = 8$  as a function of time for different capacitors charged by (a) walking and (b) running.



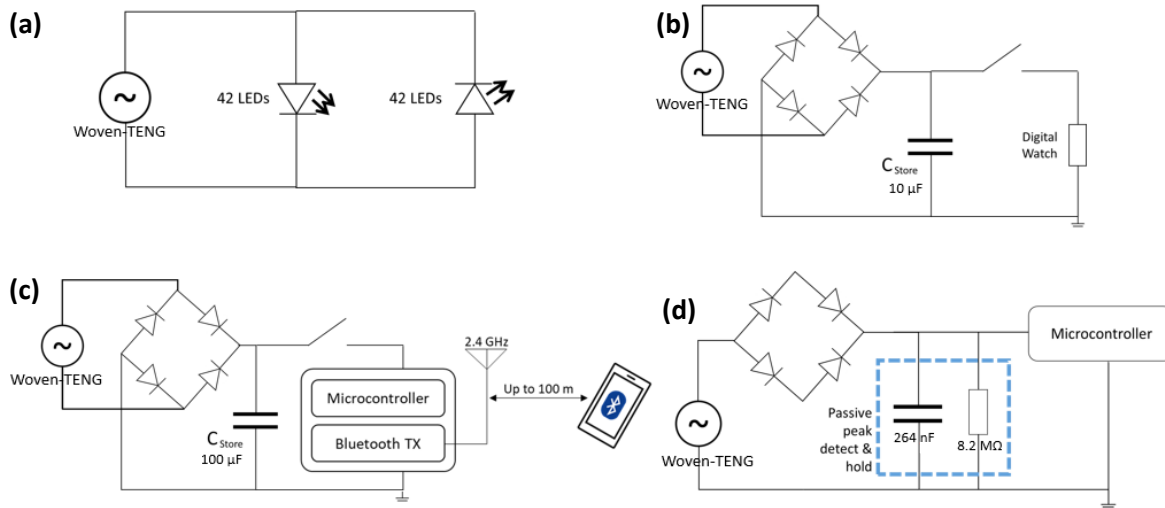


**Figure 5.41** Circuit diagrams of using woven-TENG for powering (a) a night-time warning indicator, (b) digital watch, (c) Bluetooth transceiver and (d) pedometer.

Regarding the night-time warning indicator, the AC output of the woven-TENG can be directly used to flash 42 forward bias LEDs and 42 reverse bias LEDs aligning in a sign “STOP” for warning upcoming vehicles of the pedestrians at night, as shown in Figure 5.42a. Regarding the watch, the output is rectified and used to charge a 10- $\mu\text{F}$  capacitor. When the  $V_C$  reaches 1.3 V, the watch is turned on and can then be continuously powered, as shown in Figure 5.42b.

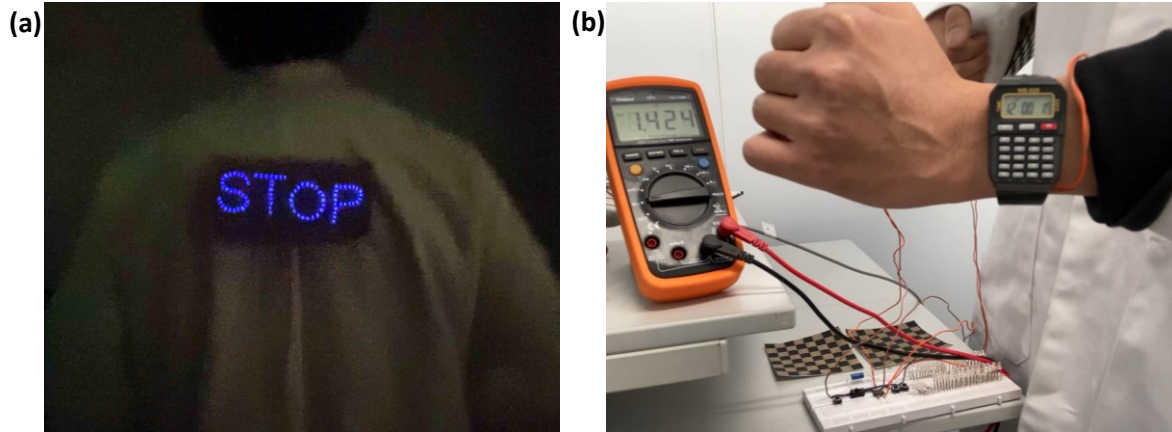


**Figure 5.42** Photograph of (a) wearable night-time warning indicator for pedestrians and (b) digital watch powered by the output of the woven-TENG with  $N = 8$  during running.

Regarding the Bluetooth transceiver, the output is used to power an internet of things sensor node based on a microcontroller unit (Arm Cortex-M3) and a Bluetooth low energy (BLE) transceiver integrated in a system on chip (SoC). The rectified output is used to charge a 100- $\mu\text{F}$  capacitor up to 4.0 V, which takes approximately 5 min when running. Next, the transceiver is turned on. An identification packet is then transmitted to a BLE gateway. The  $V_C$  and the transceiver current  $I_T$  consumed by the node are shown in Figure 5.43a. The lower magnified inset in Figure 5.43b reveals that the harvested energy could sustain the node’s operation for almost 2 s with over 17 successful

transmissions taking place in that period, observed through the 5–12 mA duty-cycled current spikes. The transmitted packet, at 1 mW RF power level, can be received by a standard BLE gateway at a distance of over 100 m away from the user, such as a smartphone shown in Figure 5.43c. In addition, wearable BLE nodes can be used as battery-free indoor localization beacons based on the relative signal strength [165].

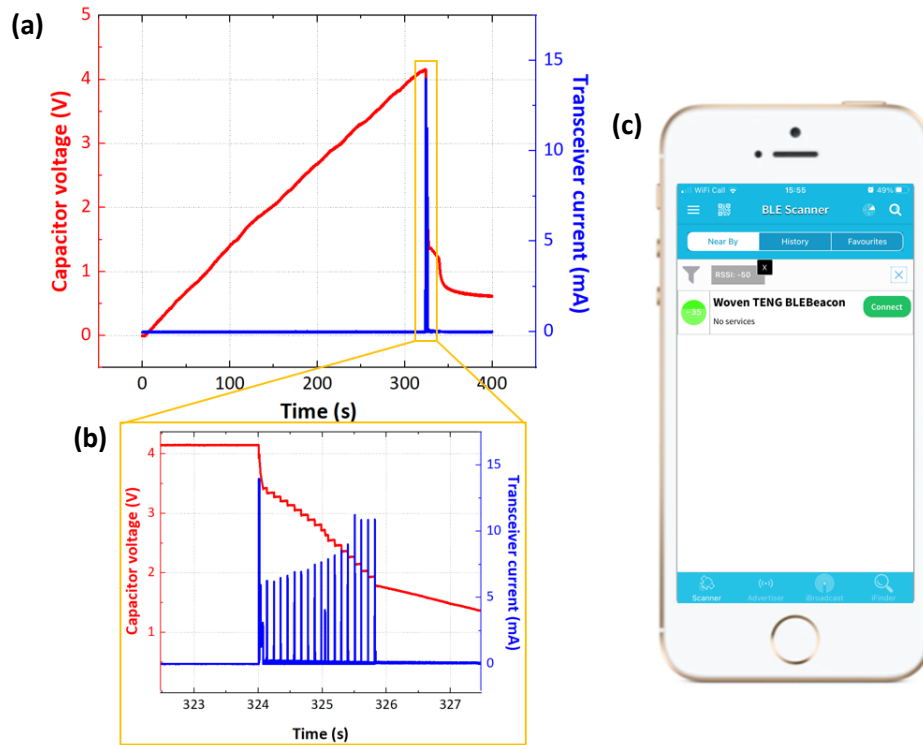


**Figure 5.43** (a) Transient  $V_C$  and  $I_T$  of a Bluetooth transceiver and microcontroller SoC driven by the woven-TENG with  $N = 8$  during running. (b) Zoom-in transient  $V_C$  and  $I_T$  of the area marked in yellow in (a). (c) Photograph of a Bluetooth advertisement received by a smartphone using BLE scanner application.

Moreover, the woven-TENG can also be implemented as a sensing device. To demonstrate this, a pedometer that can be interfaced with a simple low-power microcontroller was built. A passive peak detect and hold circuit was implemented using a shunt RC filter. The Arduino code for the peak detection is shown in Appendix A. The values of the resistor and the capacitor were chosen as 8.2 M $\Omega$  and 264 nF, to control the delay of the signal for correct step detection. The voltage across the capacitor is measured using a microcontroller's analogue to digital converter every 300 ms and compared against a predetermined threshold to detect the walking or running steps, as shown in Figure 5.44.

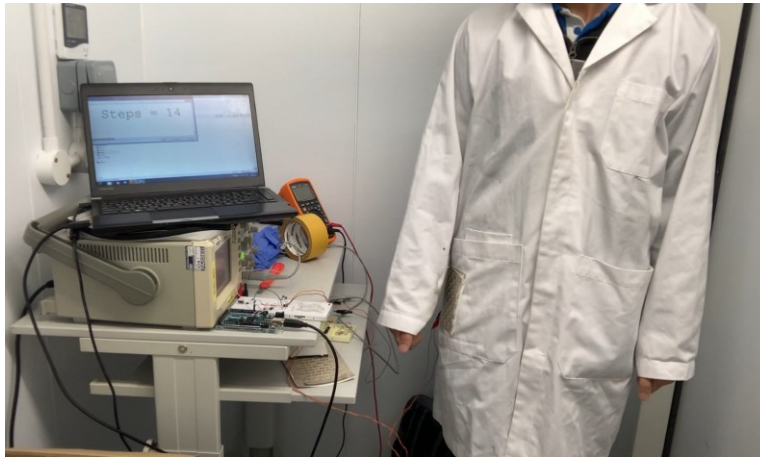


**Figure 5.44** Photograph presenting the use of the woven-TENG as a sensor for step counting via arm motion (pedometer).

## 5.4 Conclusion

A novel textile-based triboelectric energy harvester with woven strips of positive and negative triboelectric material (woven-TENG) designed to operate at all angles of relative sliding displacement has been demonstrated and characterised. The woven electrodes are made of Ag coated PVC fabric. The nylon fabric and PTFE fabric have been shown to be practical positive and negative triboelectric materials respectively for e-textile applications. The checker-like pattern can harvest energy from arbitrary sliding directions when operated as a freestanding triboelectric-layer TENG. The maximum electrical output is produced, when the triboelectric materials slide parallel to the electrodes, whereas the minimum output (50% of the maximum output) is generated when the triboelectric materials move diagonally at an angle of  $45^\circ$  with respect to the alignment of the electrodes, meanwhile the power reduce to 25% of the maximum power output. The use of both positive and negative triboelectric material enhances the power of the woven-TENG by 2.2 times compared to the TENG with single triboelectric material. The woven-TENG with  $N = 8$  can generate an RMS  $V_{OC}$  of 62.9 V and an RMS  $I_{SC}$  of  $1.77 \mu\text{A}$ . The average power transfer reaches a maximum value of  $34.8 \mu\text{W}$  at a load resistance of  $50 \text{ M}\Omega$  from a mechanical oscillation of 2 Hz and a contact force of 5 N. This corresponds to an average power density of  $5.43 \text{ mW/m}^2$ .



## Chapter 6 Conclusions and future work

### 6.1 Conclusions

This thesis has explored the feasibility of textile-based triboelectric energy harvesters (T-TENGs). Two novel designs of T-TENGs have been proposed, namely textile-based triboelectric energy harvesters with alternating positive and negative freestanding grating structure (pnG-TENG), and textile-based triboelectric energy harvester with an alternating positive and negative freestanding woven structure for harvesting kinetic energy in all sliding directions (woven-TENG). It is the first time that positive and negative triboelectric materials have been utilised as the freestanding triboelectric layer in TENGs operating in the sliding freestanding triboelectric-layer mode. This implementation has significantly improved the electrical output performance of the devices compared to the conventional TENGs with single triboelectric material. The devices have been integrated into a lab coat as a demonstrator to harvest energy from the relative sliding movement between arm and torso during normal walking and running. They have demonstrated successful practical applications as both energy harvesters and sensors. The processes involved in the manufacture of the devices are cost-effective, straightforward and compatible with standard textile manufacturing.

In Chapter 2, the background theory of TENGs and a review of T-TENGs has been revealed. The triboelectric effect is also known as triboelectricity. It is a type of contact electrification, in which electrical charges are separated and transferred from one material to the other material after they are brought into physical contact. It is believed that the effect involves electron transfer, ion transfer and/or mass transfer. However, it has been recently proposed by Z. L. Wang's research group that it is an electron-dominated transition process. Concerning the structure, T-TENGs can be classified into two main groups, including fabric-based TENG and fibre-based TENG. Fabrics can be used directly as a triboelectric material but more often they only serve as substrates for other materials that possess better triboelectric properties. The fibre-based TENGs are made of interlacing fibres, which are typically fabricated in a core-shell structure. Concerning the performance of T-TENGs, their power densities are relatively low compared to bulk TENG because of a decrease in their effective contact area relating to their structure. Depending on their designs and structures, the peak power density of the fibre-based and the fabric-based devices vary from  $22.5 \mu\text{W}/\text{m}^2$  to  $953 \text{ mW}/\text{m}^2$  and from  $1.25 \text{ mW}/\text{m}^2$  to  $8,920 \text{ mW}/\text{m}^2$ , respectively.

Chapter 3 focuses on fundamental experiments which enable the fabrication of the pnG-TENG and the woven-TENG. Firstly, 16 different flexible triboelectric materials were investigated to

find the most appropriate materials. Simple FT-mode TENGs with these materials have been fabricated and their open-circuit voltage ( $V_{OC}$ ), short-circuit current ( $I_{SC}$ ) and surface charge density ( $\rho_q$ ) were compared. Considering the textile-based triboelectric materials, the best negative triboelectric material is PTFE fabric ( $\rho_q = -19.24 \mu\text{C}/\text{m}^2$ ) and the best positive triboelectric material is nylon fabric ( $\rho_q = 11.15 \mu\text{C}/\text{m}^2$ ). Considering the fabrication process and the triboelectric performance, the PU HTV and PVC HTV have also great potential to be used as triboelectric materials. The 4 main factors that strongly affect the performance of TENGs were identified in this chapter: the operating frequency, contact force, humidity and temperature. Regarding frequency, both  $V_{OC}$  and  $I_{SC}$  increase with increasing frequency but  $V_{OC}$  will saturate above a certain frequency (around 2.5 Hz). Regarding contact force, both  $V_{OC}$  and  $I_{SC}$  increase with increasing contact force but they will reach a saturation point at a certain contact force (around 9 N) due to a saturation in the surface charge density. Regarding humidity and temperature in the wearable range, TENGs will deliver the best performance at low humidity and low temperature. Since the electrical outputs of TENGs are alternating and variable, a suitable method to evaluate the performance of TENGs is to monitor the transient capacitor voltage by charging a suitable capacitor, which requires a suitable rectifier circuit. The experimental and simulation results in this chapter showed that for FT-mode TENGs, the most suitable rectifier circuit is the full-wave bridge rectifier.

The pnG-TENG was fully investigated in Chapter 4. A novel design for the freestanding triboelectric layer was developed, comprising two alternate grated strips of positive triboelectric material (nylon fabric) and negative triboelectric material (PVC heat transfer vinyl) fabricated by heat-pressing the PVC heat transfer vinyl to the nylon fabric. The interdigitated electrodes with matching structures have been fabricated using screen-printing. The pnG-TENGs show significant performance improvement compared to single positive material (pG-TENGs), single negative material (nG-TENGs) and TENGs with no gratings. With this novel structure, the  $I_{SC}$  increases with increasing grating number, whereas  $V_{OC}$  shows a reducing trend due to the increased capacitance of the electrodes. The  $I_{SC}$ ,  $V_{OC}$  of the pnG-TENGs are considerably greater than those of the pG-TENGs and the nG-TENGs for all the grating numbers.

The pnG-TENG with 10 gratings delivers an RMS  $V_{OC}$  of 136 V and an RMS  $I_{SC}$  of 2.68  $\mu\text{A}$ . The average power transfer reaches a maximum value of 125  $\mu\text{W}$  at a load resistance of 50 M $\Omega$ , a mechanical oscillation of 2 Hz, a contact force of 5 N, a humidity of 25% and a temperature of 25°C. This corresponds to an average power density of 38.8 mW/m<sup>2</sup>, which is 1.94 and 6.43 times greater than the power generated by the TENG with single triboelectric material (nG-TENG) and the TENG with no grating.

A novel woven-TENG design was demonstrated and characterised in Chapter 5. In contrast to the pnG-TENG, this woven design can harvest energy from all angles of relative sliding displacement. The woven electrodes are made of Ag coated PVC fabric fabricated using doctor blading. The nylon fabric and PTFE fabric have been woven to form an alternating chequered positive and negative freestanding triboelectric layer. The maximum electrical output is produced, when the triboelectric materials slide parallel to the electrodes, whereas the minimum output (50% of the maximum output) is generated when the triboelectric materials move diagonally at an angle of  $45^\circ$  with respect to the alignment of the electrodes, meanwhile the power reduces to 25% of the maximum power output. The use of both positive and negative triboelectric material enhances the power of the woven-TENG by 2.2 times compared to the TENG with single triboelectric material. The woven-TENG with 8 elements per each side can generate an RMS  $V_{oc}$  of 62.9 V and an RMS  $I_{sc}$  of  $1.77 \mu\text{A}$ . The average power transfer reaches a maximum value of  $34.8 \mu\text{W}$  ( $5.43 \text{ mW/m}^2$ ) at a load resistance of  $50 \text{ M}\Omega$ , a mechanical oscillation of 2 Hz, a contact force of 5 N, a humidity of 25% and a temperature of  $25^\circ\text{C}$ .

## 6.2 Future work

Future work could be focused on the following topics:

- The effect of humidity and temperature on the performance of T-TENGs could be further studied. The range of the humidity and temperature could be extended to cover the whole wearable range. Unfortunately, we could not perform any experiments at a humidity below 25%RH and a temperature below  $15^\circ\text{C}$  due to the limitation of the available environmental chamber. The effect of sweat, which directly relates to humidity, could be studied. Since the performance of TENGs is significantly degraded at high humidity, an encapsulation or fabrication technique should be developed to protect the device from high humidity. For CT-mode T-TENG, it is quite simple to encapsulate the device but for FT-mode T-TENGs, it is still a big challenge because a contact and a large sliding displacement between the freestanding triboelectric materials and the electrodes are required.
- The effect of different textile structures on the performance of T-TENGs could be investigated since different weaving and knitting techniques can achieve a diverse range of fabric structures, which can considerably influence the effective contact area of TENGs and thus their power outputs. This is the main reason that textile-based TENGs have a lower power density compared to bulk TENGs.
- The surface modification could be performed to improve the performance of T-TENGs by, for example, introducing micro- or nanostructures on their surface, such as nanowires and nanoparticles or performing a chemical surface modification. However, these processes are

typically complex, expensive and inappropriate for large-scale textile manufacturing, which are big challenges for T-TENGs fabrication.

- Alternative fabrication methods and triboelectric materials could be found for the fabrication of the pnG-TENG and the woven-TENG. For example, the pnG-TENG can be fabricated by dispensing liquid PTFE on nylon fabric. It has been demonstrated in Appendix C that dispensing liquid PTFE does not work so well. However, a recent undergraduate student project under the authors tutelage has successfully fabricated a pnG-TENG by dispensing a solution of PTFE powder and liquid PU on nylon fabric but the performance is still relatively low due to a high percentage of the liquid PU in the solution.
- Since T-TENGs are typically attached to a conformal surface and deformed during the practical application, the effect of the deformation on the conductivity of the electrodes and their performances should be investigated, for example, by performing a bending test to measure the conductivity of the electrodes at different bending radii and also to consider their durability after several bending cycles.
- The T-TENGs could be attached to different parts of the body, for example, they can be attached between arm and torso, at armpit or between thighs. The output of the device should be measured by different activities, such as during working, manual labour, walking and running. The design of the T-TENGs might need to be optimised according to the body movement to obtain the maximum performance. The output of the TENG during long term daily activities could be observed, for instance, by measuring the charge in a capacitor charged by the TENG for 5 hours during daily activity.
- In Chapter 5, only the translation of the woven-TENG in the different sliding directions has been studied. A further study on the dependence of the output of the woven-TENG on the rotation of the upper substrate relative to the electrodes, which slides in different directions, would be interesting because it might identify the optimal angle which could then feedback into future designs.
- Because T-TENGs produce very high voltage but low current output and the maximum power is obtained at a very high load, a conditioning circuit is required to maximise the energy transfer between the T-TENGs and electronic devices. Moreover, the claimed maximum power densities were obtained with an external load resistance in the order of M $\Omega$ . However, in real application of TENGs, the load resistance of the circuit is much lower, and the desired operating voltage is in the range of a few volts. This disparity, therefore, requires the use of a power conditioning circuit, which should be further reviewed.

## Appendix A      Arduino codes for the $\mu$ -stepper motor and pedometer

The Arduino command for driving the stepper motor can be found below. This example command was used to drive the motor in full step mode. The driving mode can be selected at the Jumper on the controller board. The travel distance was 48 mm, and the frequency was 2 Hz. The number of cycles can be varied at “const int”. The travel distance can be adjusted at “stepper.moveSteps”. The frequency can be changed at “stepper.setMaxVelocity” and “stepper.setMaxAcceleration”. Table A.1 represents the values of the different parameters used for the frequency dependence measurement of the simple-TENG and the pnG-TENG at a travel distance of 48 mm. Table A.2 shows the values of the different parameters used for the frequency dependence measurement of the woven-TENG at a travel distance of 40 mm. The reason why the  $\frac{1}{4}$  step mode was used at low frequencies is that at these frequencies, it can run much smoother and make less noise.

**Table A.1**      Setting command for the frequency dependence measurement at a travel distance of 48 mm.

Frequency (Hz)	Mode	moveSteps	setMaxVelocity	setMaxAcceleration
1.0	$\frac{1}{4}$ step	640	1450	14000
1.5	$\frac{1}{4}$ step	640	2460	22000
2.0	Full step	160	810	8100
2.5	Full step	160	1110	11100
3.0	Full step	160	1550	15500

**Table A.2**      Setting command for the frequency dependence measurement at a travel distance of 40 mm.

Frequency (Hz)	Mode	moveSteps	setMaxVelocity	setMaxAcceleration
1.0	$\frac{1}{4}$ step	534	1202	11500
1.5	$\frac{1}{4}$ step	640	1960	19600
2.0	Full step	134	610	8049
2.5	Full step	134	925	9156
3.0	Full step	134	1233	12330

## Appendix A

The Arduino code for the  $\mu$ -stepper motor is shown below.

```
#include <uStepper.h>
uStepper stepper;
int x = 0;
const int cycle = 15000;

void setup() {
  // put your setup code here, to run once:
  stepper.setup();
  stepper.setMaxVelocity(810);
  stepper.setMaxAcceleration(8100);
  Serial.begin(115200);
}

void loop() {
  // put your main code here, to run repeatedly:
  if(!stepper.getMotorState() && ++x <= cycle*2)
  {
    stepper.moveSteps(160, !stepper.getCurrentDirection(), SOFT);
  }
  Serial.print("Temperature: ");
  Serial.print(stepper.temp.getTemp());
  Serial.println(" Degrees Celsius");
  Serial.print("Angle: ");
  Serial.print(stepper.encoder.getAngle());
  Serial.println(" Degrees");
  Serial.println(x);
}
```

The Arduino code for the pedometer is shown below. To optimise the peak detection of the pedometer, the float threshold, which is the threshold voltage of the to be detected peak and the delay(300), which is the delay time between each peak detection, could be changed.

```
// These constants won't change. They're used to give names to the pins used:
const int analogInPin = A0; // Analog input pin that the potentiometer is attached to
const int analogOutPin = 9; // Analog output pin that the LED is attached to
int sensorValue = 0; // value read from the pot
int outputValue = 0; // value output to the PWM (analog out)
int steps = -1;
float step_voltage_current = 0;
float step_voltage_prev = 0;
float idleCycles=0;
float DCVolt=0;
float threshold=70;
float n=0;

void setup() {
  // initialize serial communications at 9600 bps:
  Serial.begin(9600);
```

```

pinMode(A2, OUTPUT);
delay(300);
steps=-1;
}
void loop() {
  // read the analog in value:
  //Maps 0-5V to 0-1023, 3.3 V at 676
  sensorValue = analogRead(analogInPin);
  // map it to the range of the analog out:
  //outputValue = map(sensorValue, 0, 1023, 0, 255);
  step_voltage_current = sensorValue/0.204; //DC Voltage in mV
  // change the analog out value:
  analogWrite(analogOutPin, outputValue);
  if(step_voltage_current-step_voltage_prev>threshold)
  {
    steps++;
    idleCycles=0;
    n=1;
  }
  else
  {
    idleCycles++;
    n=0;
  }
  // print the results to the Serial Monitor:
  //Serial.print("Voltage Current= ");
  //Serial.print(step_voltage_current);
  //Serial.print("\t Voltage Prev= ");
  //Serial.print(step_voltage_prev);
  //Serial.print("\t Diff= ");
  //Serial.print(step_voltage_current-step_voltage_prev);
  //Serial.print("\t n= ");
  //Serial.print(n);
  Serial.print("\t Steps = ");
  Serial.println(steps);
  step_voltage_prev=step_voltage_current;
  digitalWrite(A2, n);
  // wait 300 milliseconds before the next loop for the analog-to-digital
  // converter to settle after the last reading:
  delay(500);
}

```





## Appendix B Simple pnG-TENG

PowerMEMS 2018

IOP Publishing

Journal of Physics: Conference Series

1407 (2019) 012124 doi:10.1088/1742-6596/1407/1/012124

### Textile-based freestanding triboelectric-layer nanogenerator with alternate positive and negative grating structure

W Paosangthong, R Torah and S Beeby

Department of Electronics and Computer Science (ECS), University of Southampton, Southampton SO17 1BJ, UK

E-mail: wp1y15@soton.ac.uk

**Abstract.** This paper reports a novel design of textile-based triboelectric nanogenerator (TENG) with alternate grated strips of positive and negative triboelectric material operating in freestanding triboelectric-layer mode (pnG-TENG). Whereas most grating-structured TENGs operating in a freestanding triboelectric-layer mode comprise gratings of one type of triboelectric material separated by air gaps, this design presents a replacement of the air gaps by another triboelectric material with the opposite polarity to the existing triboelectric material. The pnG-TENG with 10 gratings of PTFE and nylon fabric delivers an open-circuit voltage of 250 V, a short-circuit current of 5.94  $\mu\text{A}$  and a maximum peak power of 600  $\mu\text{W}$  at a load resistance of 50  $\text{M}\Omega$  and a mechanical oscillation of 2 Hz. This corresponds to a maximum power density of 186  $\text{mW}/\text{m}^2$ , which is 1.73 and 2.20 times greater than the power generated by the TENG with single triboelectric material and the TENG with no grating, respectively.

#### 1. Introduction

In spite of a substantial growth in the wearable and portable electronics market, most of these types of devices still rely on batteries, which require persistent recharging and replacement. An effective way to solve this problem is to introduce a wearable self-charging power system using an energy harvester to scavenge energy from the surrounding environment. Triboelectric nanogenerators (TENGs) are one of the most promising candidates for powering these systems. They can efficiently convert kinetic energy into electricity based on contact electrification and the electrostatic induction effect [1–3]. Various examples of TENGs have demonstrated flexibility, lightness, biocompatibility and good performance that are essential for wearable devices [4,5]. According to these properties, textile-based TENGs are determined to be highly suitable for this propose, since textiles are often used on the human body, which is one of the most powerful kinetic energy sources for powering the wearable electronics [6–10].

This paper proposes a novel structure of textile-based TENG with alternate grated strips of positive and negative triboelectric material operating in freestanding triboelectric-layer mode; defined as a pnG-TENG. Whilst most grating-structured TENGs (G-TENGs) operating in a freestanding triboelectric-layer mode comprise gratings of one type of triboelectric material separated by air gaps [2,3], this design presents a replacement of the air gaps by a triboelectric material with the opposite polarity to the existing triboelectric material. In this work, the electrical outputs of pnG-TENGs with the different grating number ( $N$ ) were measured and compared with the G-TENGs with single positive triboelectric material (pG-TENGs), the G-TENGs with single negative triboelectric material (nG-TENGs) and the TENG with no grating ( $N=1$ ). The objective of this work is to demonstrate that the pnG-TENGs exhibit an improvement in performance compared to the single material G-TENGs.



Content from this work may be used under the terms of the [Creative Commons Attribution 3.0 licence](https://creativecommons.org/licenses/by/3.0/). Any further distribution of this work must maintain attribution to the author(s) and the title of the work, journal citation and DOI.

Published under licence by IOP Publishing Ltd

1



## 2. Device and working principle

A schematic illustration of the proposed pnG-TENG is shown in figure 1. It is composed of an upper substrate with  $N$  alternate strips of Nylon and PTFE fabric ( $N=10$  for figure 1(a)) and a lower substrate with two interdigitated Aluminium (Al) electrodes (IDEs) with matching periodicity shown in figure 1(b). The upper substrate has a size of 46x70 mm. It was made of stacks of acrylic, a double-sided tape, a 1-mm-thick fabric, a double-sided tape and the triboelectric materials (Nylon and PTFE). The acrylic layer is just for testing to make it a consistent and repeatable test, and would not be required in an actual e-textile device, whereas the 1-mm-thick fabric helps improve the flexibility and thus increases the effective contact area of the triboelectric materials. The rectangular lower substrate with a size of 100x70 mm was made of an acrylic fully covered by strips of Al tape with a width of  $50/N$  mm separated by a 200-micron-wide cut after adhesion to the substrate to prevent a short circuit between the IDEs.

The schematic illustration of the upper substrate of G-TENG for  $N=10$  with one type of triboelectric material is shown in figure 2. Firstly, the acrylic was laser-cut into grating structures with  $N$  segments (including the air gaps). Then, the 1-mm-thick fabric, the double-sided tapes and the triboelectric material were stuck to the acrylic and cut into the same configuration as the acrylic by hand. Thus, alternate strips of air gaps and triboelectric material occur. The triboelectric material used for the pG-TENG and nG-TENG are nylon and PTFE fabric, respectively. The structure of the lower substrate remains the same as the pnG-TENG. For the G-TENGs with different  $N$ , the total effective area of the devices remains the same, thus a larger  $N$  will lead to a smaller width of each grating unit.

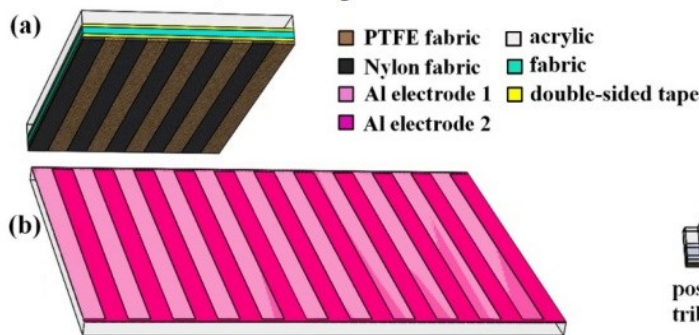


**Figure 1.** Schematic illustration of pnG-TENG ( $N=10$ ) comprising (a) an upper substrate with alternate strips of Nylon and PTFE fabric and (b) a lower substrate with two interdigitated Al electrodes.

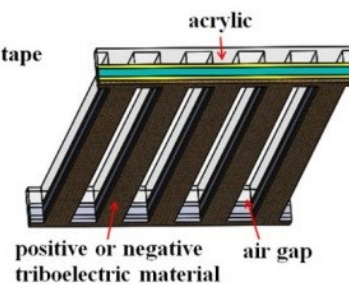


**Figure 2.** Schematic illustration of upper substrate of G-TENG ( $N=10$ ) with single triboelectric material.

The operating mechanism of pnG-TENG with nylon and PTFE fabric for  $N=2$  is illustrated in figure 3. It is operated based on contact electrification and the electrostatic induction effect. When the nylon fabric and PTFE fabric are brought into contact with Al electrodes, they will become positively and negatively charged, respectively, whereas the same amount of charge with the opposite polarity is generated on the Al electrodes. Initially (figure 3(i)), the upper substrate fully overlaps with the first two fingers (from left) of the electrodes. In this state, no charge transfer occurs due to the electrostatic equilibrium between the electrodes. When the upper substrate moves further to the right-hand side and partly overlaps with the next Al finger (figure 3(ii)), the electrons flow from the first and the third Al finger to the second finger, because the electric potential of the second Al finger increases due to the presence of the positive surface charge of the above nylon fabric and the electric potential of the first and the third Al finger decreases due to the absence of nylon and the presence of PTFE fabric, respectively. As a result, a current flows from Al electrode 2 to 1 until another electrostatic equilibrium is reached at the next fully overlapping position (figure 3(iii)). When the upper substrate continues to move, the electric potential in the electrodes increase and decrease alternately resulting in an alternating current through the load. As can be seen in figure 3(ii, iv, vi, viii), four current cycles are generated in one moving cycle. The number of current cycles per moving cycle is twice the grating number.



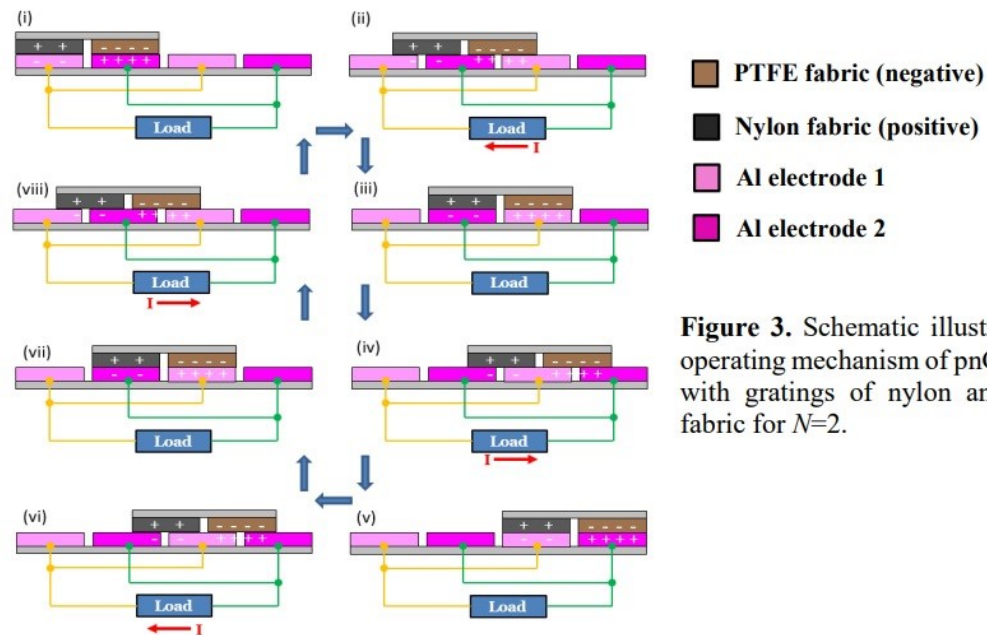


**Figure 3.** Schematic illustration of operating mechanism of pnG-TENG with gratings of nylon and PTFE fabric for  $N=2$ .

### 3. Simulation and Experimental results

#### 3.1. Simulation results

To theoretically investigate the effect of the different grating numbers on the G-TENGs, the open-circuit voltage ( $V_{OC}$ ) of the different types of G-TENGs for  $N = 1, 2, 4, 6, 8, 10$  were simulated using COMSOL finite element modelling software. Based on work by Xie et al. [3], the surface charge density of the negative material (PTFE) and the positive material (Nylon) was estimated to be  $-26 \mu\text{C}/\text{m}^2$  and  $10 \mu\text{C}/\text{m}^2$ .

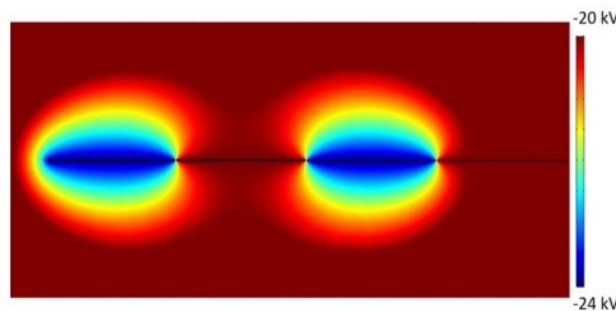


**Figure 4.** Electric potential of pnG-TENG in 2D for  $N=2$  simulated using COMSOL Multiphysics.

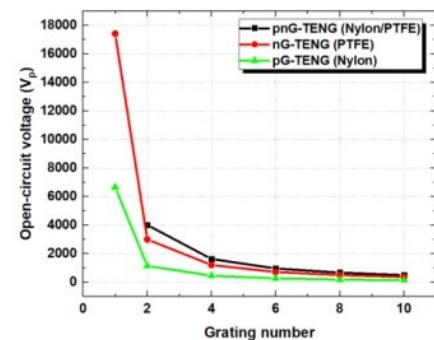


**Figure 5.** Simulation result of  $V_{OC}$  for TENGs with the different grating numbers.

The simulated electric potential of the pnG-TENG for  $N=2$  in 2D is shown in figure 4. In this cross-section view, the G-TENG consists of 4 Al fingers. The first and third finger, and the second and fourth finger (from left) are connected together forming the Al electrode 1 and 2 respectively. A PTFE and a nylon are placed over the first and the second Al finger, respectively. Due to the predefined surface charge densities [3], an electric potential of  $-24 \text{ kV}$  and  $-20 \text{ kV}$  are induced at the first and the second electrode, respectively, resulting in a  $V_{OC}$  of  $4 \text{ kV}$ . The reason why the potential of the second electrode is negative, although the surface charge density of nylon is positive is that the surface charge density of the PTFE is much greater than that of the nylon and this induces a strong negative potential, which outweighs the positive potential from the nylon.

The  $V_{OC}$  of the different types of TENGs for the different grating numbers is represented in figure 5. With increasing grating number, the  $V_{OC}$  decreases for all types of the G-TENGs. The result can be explained by equation (1) below [3]:

$$V_{OC} = \frac{\Delta\sigma_{sc} \cdot S}{C} \quad (1)$$

where  $\Delta\sigma_{sc}$  is the transferred charge density,  $S$  is the total area of the Al electrode 1 or 2 and  $C$  is the capacitance between the electrodes. Because  $\Delta\sigma_{sc}$  and  $S$  are constant for ( $N=2$  to 10) and  $C$  increases when the electrodes are divided into small segments,  $V_{OC}$  decreases with increasing grating number. The  $V_{OC}$  of the TENG with no grating ( $N=1$ ) is much higher than the others, since the area of the triboelectric material for ( $N=1$ ) is twice as large as the area of the triboelectric material for ( $N=2$  to 10), which is partly replaced by air gaps. The  $V_{OC}$  of the pnG-TENGs are enhanced for all grating numbers compared to the pG-TENGs and the nG-TENGs since  $\Delta\sigma_{sc}$  rises due to the assumption that the  $\Delta\sigma_{sc}$  is proportional to the potential difference at the surface of nylon and PTFE, which relates to the different between the surface charge density.

### 3.2. Experimental results

All experiments were performed using a belt drive linear actuator at a mechanical oscillation frequency of 2 Hz and a contact force of 5 N, which cyclically slides the upper substrate over the bottom substrate. The  $V_{OC}$  measurements were carried out using an oscilloscope (Agilent DSO3062A) with a load resistance of 1 G $\Omega$  and the short-circuit current ( $I_{SC}$ ) was measured using a DC power analyzer (Agilent N6705B). In figure 6, the experimental results for  $V_{OC}$  shows the same decreased tendency and is in good agreement with the simulation result. In contrast to  $V_{OC}$ , the  $I_{SC}$  of the pnG-TENGs rises significantly with increasing grating number and is greater than that of the TENG with no grating ( $N=1$ ), the pG-TENGs and the nG-TENGs for almost all the grating numbers as shown in figure 7. The increase in  $I_{SC}$  follows equation (2) below:

$$I_{SC} = \frac{\Delta Q_{SC}}{t} \quad (2)$$

Since the time taken  $t$  for a certain transferred charge  $\Delta Q_{SC}$  is significantly reduced due to the reduction in the width of the Al fingers, when the sliding velocity is fixed, the  $I_{SC}$  rises.

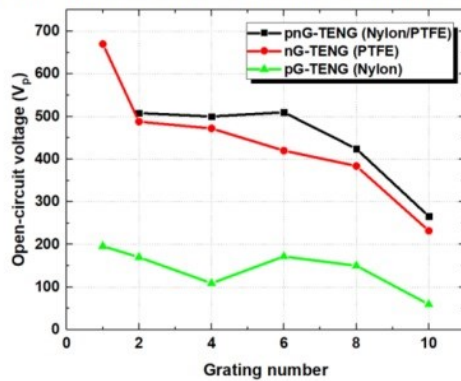


**Figure 6.** Experimental results of  $V_{OC}$  for TENGs with different grating numbers.

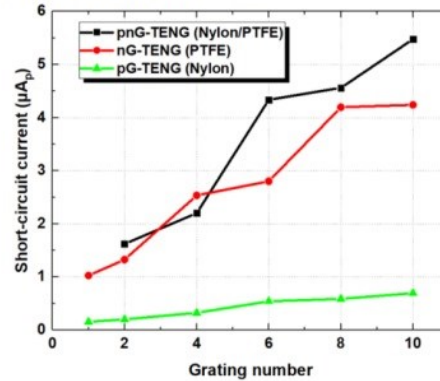


**Figure 7.** Experimental results of  $I_{SC}$  for TENGs with the different grating numbers.

In figure 8, the load dependence measurements were performed to find the maximum power point of the G-TENGs by measuring  $V_{OC}$  and  $I_{SC}$  at different external load resistances varying from 0.1 M $\Omega$  to 10 G $\Omega$ . The powers were calculated from the product of  $V_{OC}$  and  $I_{SC}$ . For the pnG-TENG (Nylon/PTFE,  $N=10$ ), the maximum peak power reaches 600  $\mu W$  at a resistance of 50 M $\Omega$ , corresponding to a power density of 186 mW/m<sup>2</sup>. For the nG-TENG (PTFE,  $N=10$ ), the maximum power is 346  $\mu W$  at the same load. For the TENG with no grating (PTFE,  $N=1$ ), the maximum power of 273  $\mu W$  is generated at a load resistance of 1 G $\Omega$ . The result shows that the peak power of the pnG-TENG increases by a factor of 1.73 and 2.20, compared to the nG-TENG and the TENG with no grating, respectively.



To provide a more complete picture of the energy harvesting potential, the outputs of the TENGs were used to charge up a 10- $\mu$ F capacitor. The capacitor voltages at a charging time of 600 s for the different TENGs and the different grating numbers are shown in figure 9. It shows an increased tendency similar to the  $I_{SC}$ . The average charging power calculated from the capacitor voltage for the pnG-TENG with  $N=10$  is 41.29  $\mu$ W, corresponding to a power density of 12.82 mW/m<sup>2</sup>.

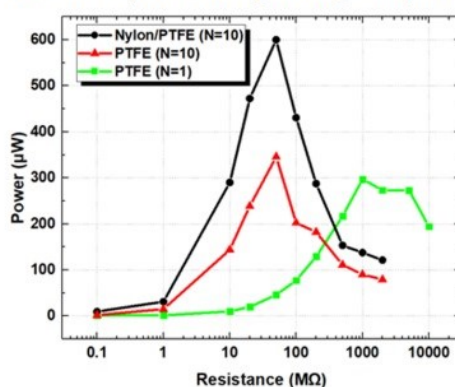


**Figure 8.** Load-dependent peak power of different types of TENGs.

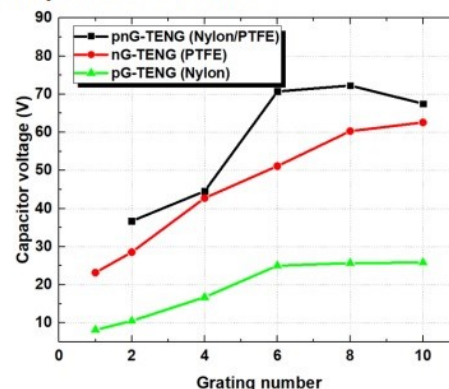


**Figure 9.** Capacitor charging voltages for TENGs with the different grating numbers.

#### 4. Conclusions

This paper has introduced a novel textile-based triboelectric generator design, using two alternate grating strips of positive and negative triboelectric material, defined as a pnG-TENG. The pnG-TENGs show significant improvement in performance compared to single positive material (pG-TENGs), single negative material (nG-TENGs) and TENGs with no grating. With this novel structure, the  $I_{SC}$  increases with increasing grating number, whereas  $V_{OC}$  shows a reducing trend due to the increasing capacitance of the electrodes. Both, the  $I_{SC}$  and the  $V_{OC}$  of the pnG-TENGs are considerably greater than those of the pG-TENGs and the nG-TENGs for almost all the grating numbers. The maximum power generated by the pnG-TENG with 10 grating is 1.73 and 2.20 times greater than the power generated by the TENG with single triboelectric material and the TENG with no grating, respectively.

#### Acknowledgments

The authors gratefully acknowledge the Engineering and Physical Science Research Council (EPSRC) for supporting this research with grant reference EP/P010164/1

#### References

- [1] Zhu G, Zhou Y S, Bai P, Meng X S, Jing Q, Chen J and Wang Z L 2014 *Adv. Mater.* **26** 3788–96
- [2] Bi M, Wang S, Wang X and Ye X 2017 *Nano Energy* **41** 434–42
- [3] Xie Y, Wang S, Niu S, Lin L, Jing Q, Yang J, Wu Z and Wang Z L 2014 *Adv. Mater.* **26** 6599–607
- [4] Hinchet R, Seung W and Kim S W 2015 *ChemSusChem* **8** 2327–44
- [5] Ha M, Park J, Lee Y and Ko H 2015 *ACS Nano* **9** 3421–7
- [6] Chen J, Guo H, Pu X, Wang X, Xi Y and Hu C 2018 *Nano Energy* **50** 536–43
- [7] Chu H, Jang H, Lee Y, Chae Y and Ahn J-H 2016 *Nano Energy* **27** 298–305
- [8] Tian Z *et al.* 2017 *Nano Energy* **39** 562–70
- [9] Cui N, Liu J, Gu L, Bai S, Chen X and Qin Y 2015 *ACS Appl. Mater. Interfaces* **7** 18225–30
- [10] Zhou T, Zhang C, Han C B, Fan F R, Tang W and Wang Z L 2014 *ACS Appl. Mater. Interfaces* **6** 14695–701



## Appendix C      Alternative fabrication methods for the pnG-TENGs

For the reason that the upper substrate of the simple pnG-TENG was fabricated by laterally attaching the alternate strips of nylon and PTFE fabric together using a double-sided tape and the lower substrate was made from the manually cut adhesive Al tapes, their fabrication process is not compatible with the standard textile manufacturing. Therefore, new fabrication methods were developed as follows.

### 1. The upper substrate

- **Method 1**: Using PTFE as one of the triboelectric material

Considering the triboelectric materials investigation in Section 3.2, PTFE fabric exhibits the best triboelectric properties. Thus, it should be used as one of the triboelectric material of the upper substrate. The first idea is to use the PTFE fabric as a substrate and to coat another triboelectric material on it. Unfortunately, the PTFE surface is highly hydrophobic and non-stick to anything. Because of this, we attempted to modify its surface by oxygen ( $O_2$ ) plasma treatment. An RIE, Oxford Instruments PlasmaLab 80 Plus, was used to dry-etch the PTFE surface for 120 s at 3 following conditions:

1.  $O_2$  flow rate of 40 sccm, chamber pressure of 50 mTorr and power of 50 W.
2.  $O_2$  flow rate of 40 sccm, chamber pressure of 100 mTorr and power of 50 W.
3.  $O_2$  flow rate of 40 sccm, chamber pressure of 50 mTorr and power of 300 W.

To evaluate the result of the plasma treatment, a drop test analysis was immediately performed by measuring the contact angles of the water droplets on the PTFE fabric using a drop shape analyzer (Krüss, DSA30). The second idea is to coat the positive triboelectric materials with PTFE. As a quick test, a liquid PTFE (Cura) was disperser-printed and smeared on a PVC fabric by hand and a dry PTFE (Rocol) was spray on a PVC fabric from a distance of 15 cm. They were then cured at room temperature for a few hours.

The contact angle measurement of 5 different substrates, including 3 treated PTFE fabrics, an untreated PTFE fabric and an untreated PVC fabric, are represented in Table C.1. The photographs of the water droplets on the different substrates for the treatment condition no. 1 to 5 are depicted in Figure C.1a to e, respectively. The numbers marked in red are the corresponding contact angles. Compared to the untreated PTFE fabric, the contact angle at the treatment condition 1 and 2 reduce from  $105.7^\circ$  to  $93.6^\circ$  and  $103.2^\circ$ , respectively, which indicates that the

PTFE surfaces are more hydrophilic. In contrast, at condition 3, the wettability of the PTFE fabric significantly deteriorates. However, this small improvement at condition 1 is still not sufficient to make the PTFE fabric become a good substrate for printing with another triboelectric material. As a comparison, the contact angle of PVC fabric, which is a good printing substrate, is  $70.4^\circ$ . It is to note that the treatment condition for PDMS substrate is used as a guideline [38], [87], [116]. Unlike PDMS, the surface treatment of PTFE is not straightforward. The main reason is that PDMS and PTFE are very different. With PDMS the  $O_2$  plasma process breaks a weak Si-C bond and replaces the methyl group with a hydroxyl group. In the case of PTFE, a C-F bond need to be broken. This is one of the strongest bonds and it will take much more power to do this compared to the Si-C bond.

**Table C.1** Contact angle measurement of water droplets on different substrates.

Treatment condition no.	Substrate	Chamber pressure [mTorr]	Power [W]	Contact angle [Degree]	Figure no.
1	PTFE fabric	50	50	93.6	C.1(a)
2	PTFE fabric	100	50	103.2	C.1 (b)
3	PTFE fabric	50	300	144.7	C.1 (c)
4	PTFE fabric	No treatment		105.7	C.1 (d)
5	PVC fabric	No treatment		70.4	C.1 (e)

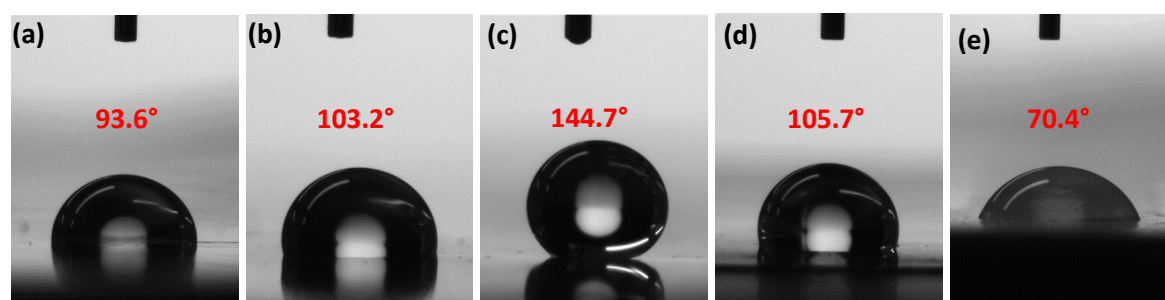


**Figure C.1** Photographs of water droplets on different substrates. (a) Treated PTFE fabric at the condition 1, (b) treated PTFE fabric at the condition 2, (c) treated PTFE fabric at the condition 3, (d) untreated PTFE fabric and (e) untreated PVC fabric. The numbers marked in red are the corresponding contact angles.

The second idea is to coat a positive triboelectric material with negative PTFE. Photograph of a liquid PTFE smeared on a PVC fabric and a dry PTFE sprayed on a PVC fabric are demonstrated in Figure C.2a and b, respectively. The result for the liquid PTFE shows that the liquid PTFE was still sticky even after curing for several days or curing in an oven. Hence, it is inappropriate to act as a sliding material. In the case of the dry PTFE spray, a thin film of PTFE powder was formed on the PVC fabric after spraying but this powder was very easy to remove through rubbing.



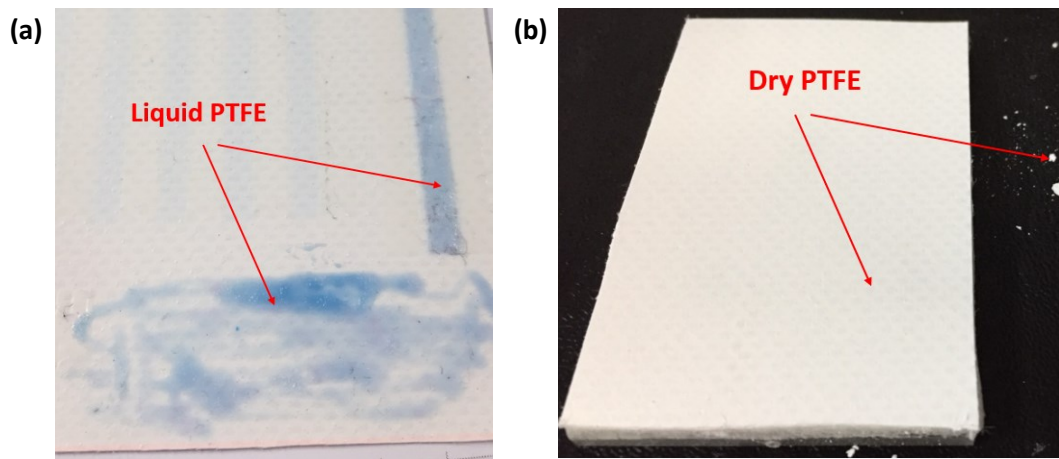


**Figure C.2** Photograph of (a) liquid PTFE smeared on PVC fabric and (b) dry PTFE sprayed on PVC fabric.

- **Method 2:** Dispenser-printing PU interface on a PVC fabric

Although PU and PVC are not the best triboelectric material for TENGs in term of the electrical outputs, in term of the fabrication, PU interface can be easily printed on textile using methods, like screen-printing or dispenser-printing, whereas PVC fabric is widely used as a substrate for printing. In this project, PU was dispenser-printing on a PVC fabric using a self-built dispensing robot controlled by LabVIEW programme. Before printing, the PVC fabric surface was first laser-scanned at a laser profile spacing of 5 mm and a laser profile speed of 10 mm/s to find the height profile of the surface. Afterwards, a liquid PU was dispensed through a 3-cc syringe with a 250- $\mu\text{m}$  tapered dispensing tip on the PVC fabric at a printing speed of 13 mm/s, a separation distance from the substrate of 220  $\mu\text{m}$ , a printing pressure of 55 kPa and a back vacuum of 1 kPa. After printing, the PU-printed substrate was UV-cured for 60 s. Lastly, the height profile of the PU along the width was investigated using an Alphastep profiler (Tencor PZ11). Ten measurements were performed over the whole substrate and an average of the PU thickness was calculated.

The upper substrate of pnG-TENG with 10 gratings of PU interface and PVC fabric was successfully fabricated and shown in Figure C.3a. Since the PU interface is transparent, it is quite hard to see. The scanned height profile along the width of a PU strip is revealed in Figure C.3b. The average PU thickness is  $159 \pm 23 \mu\text{m}$ . The PU surface exhibits a convex profile due to its high surface tension. This can lead to a reduction of the effective contact area, as only the area in the middle of the PU will make contact to the electrodes when they are rubbed together.

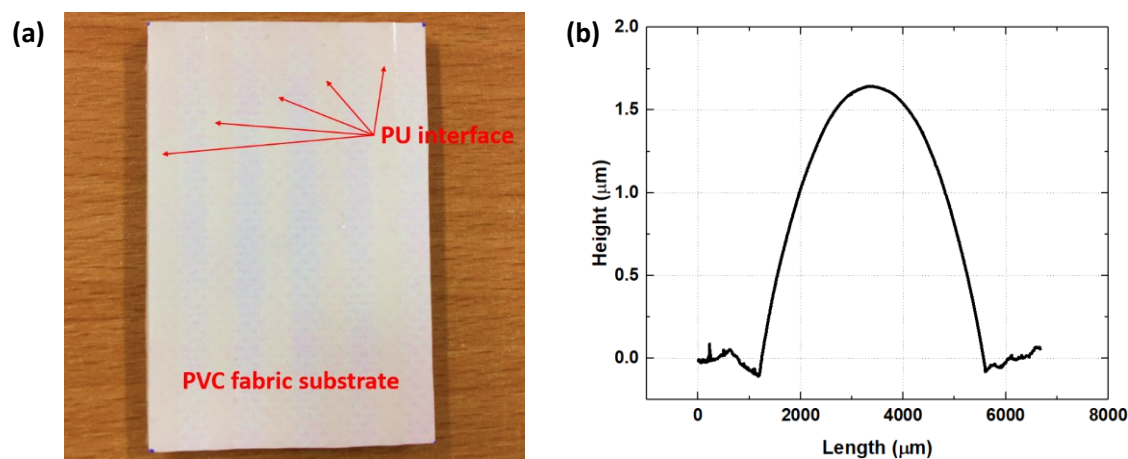


**Figure C.3** Photograph of (a) upper substrate of pNG-TENG with 10 gratings of PU interface and PVC fabric and (b) Height profile of a PU strip scanned along its width.

## 2. The interdigitated electrodes (IDEs)

- **Method 1:** Dispenser-printing Ag ink on PVC fabric

Firstly, a piece of PVC fabric was pre-baked in a box oven (Carbolite) at a temperature of 120 °C for 15 min to avoid the outgassing of the PVC fabric in the later processes. Ag ink was dispenser-printed on the PVC fabric using the self-built dispensing robot controlled by the LabVIEW programme mentioned in method 2 above. The printing steps and parameters are all identical to the PU interface, except that the printing pressure was set to 22 kPa. The total printed area of the IDEs was 70x100 cm<sup>2</sup>, excluding the connectors area. The printing gap between the IDEs was designed at 0.7 mm. After printing the Ag ink was cured in the oven at a temperature of 120 °C for 15 min. The widths of the gap were measured at 10 different points over the whole substrate using an optical microscope (Nikon Eclipse LV100) and the average width was calculated.

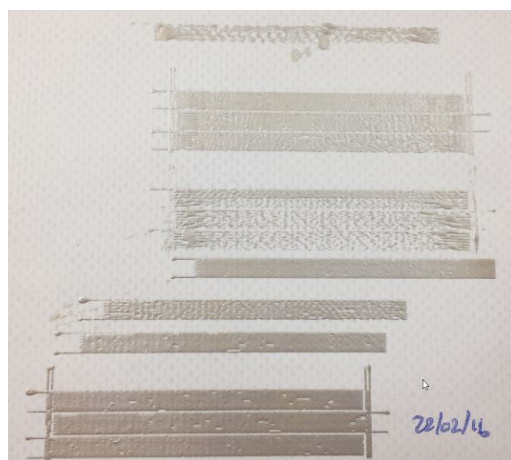


**Figure C.4** Photograph of a PVC fabric dispenser-printed with Ag ink.

Figure C.4 presents a photograph of a PVC fabric dispenser-printed with Ag ink. The result shows that the printing quality is not uniform, especially for a large printing area. In the beginning, the printing is acceptable but after a certain time, the printing tip begins to clog resulting in a broken line or inconsistent line width and line thickness. Moreover, this method takes considerably more printing time compared to screen-printing. The result shows that the width of the gap shrank from the designed width of 700  $\mu\text{m}$  to  $363\pm 26$   $\mu\text{m}$  due to the finite size of the printing tip.

- ***Method 2:*** Screen-printing the IDEs on a heat transfer paper (HTP), then heat pressed on a garment

The pnG-TENG has been successfully demonstrated, however it was fabricated on a piece of PVC fabric, which need to be later sewed to a garment. To enable the direct printing of the Ag IDEs on the garment, a PU-interface layer is normally required. However, it is impractical to put the whole garment in the screen-printer, therefore the HTP (dark transfer paper for t-shirt, Photo paper direct) is introduced to act as an interface. The Ag IDEs was firstly screen-printed on the HTP through a pre-designed screen. After printing, the Ag-IDEs was cured at a temperature of 120 °C for 15 min. The Ag printed HTP was then heat-pressed to a garment at 190 °C for 12 s. Figure C.5 shows the photograph of Ag IDEs heat-pressed on a garment. This method is suitable for large scale manufacturing but not for various prototypes and testing designs since a pre-designed screen is required and expensive.



**Figure C.5** Photograph of Ag IDEs heat-pressed directly on a garment.



## Appendix D Direction dependence calculation for the woven-TENG

$$A = A_1 + A_2 = y(w - x) + x(w - y) \quad (D.1)$$

$$= yw - yx + xw - xy$$

$$= w(x + y) - 2xy \quad (D.2)$$

$$x = s \cos \theta, \quad s \cos \theta \leq w \text{ and } 0^\circ \leq \theta \leq 90^\circ \quad (D.3)$$

$$y = s \sin \theta, \quad s \sin \theta \leq w \text{ and } 0^\circ \leq \theta \leq 90^\circ \quad (D.4)$$

By substitution of Equation D.3 and D.4 into Equation D.2, we obtain

$$\begin{aligned} A(s) &= ws(\sin \theta + \cos \theta) - 2s^2 \sin \theta \cos \theta \\ &= ws(\sin \theta + \cos \theta) - s^2 \sin 2\theta \end{aligned} \quad (D.5)$$

The first derivative of Equation D.5 is,

$$A'(s) = w(\sin \theta + \cos \theta) - 2s \sin 2\theta \quad (D.6)$$

To find the maximum travel distance, the Equation D.6 is set equal to zero as below:

$$A'(s_{max}) = w(\sin \theta + \cos \theta) - 2s_{max} \sin 2\theta = 0 \quad (D.7)$$

$$s_{max} = \frac{w(\sin \theta + \cos \theta)}{2 \sin 2\theta} \quad (D.8)$$

By substitution of Equation D.8 into Equation D.5, the maximum area  $A_{max}$  can be expressed as below:

$$A_{max} = \frac{w^2(\sin \theta + \cos \theta)^2}{2 \sin 2\theta} - \frac{w^2(\sin \theta + \cos \theta)^2}{4 \sin 2\theta} \quad (D.9)$$

$$A_{max} = \frac{w^2(\sin \theta + \cos \theta)^2}{4 \sin 2\theta} \quad (D.10)$$

The percentage of the transferred electrons  $p$  in at an angle  $\theta$  compared to the maximum transferred electrons can be calculated by the Equation D.11 below:

$$p = \frac{A_{max}}{w^2} \times 100 = \frac{25(\sin \theta + \cos \theta)^2}{\sin 2\theta} \quad (D.11)$$

Considering the conditions in Equation D.3,

$$s_{max} \cos \theta \leq w \quad (D.12)$$

$$\frac{w(\sin \theta + \cos \theta)}{2 \sin 2\theta} \cos \theta \leq w$$

$$\frac{(\sin \theta + \cos \theta)}{2 \sin 2\theta} \cos \theta \leq 1$$

$$\frac{(\sin \theta + \cos \theta)}{4 \sin \theta \cos \theta} \cos \theta \leq 1$$

$$\frac{(\sin \theta + \cos \theta)}{4 \sin \theta} \leq 1 \quad (D.13)$$

Considering the conditions in Equation D.4,

$$s_{max} \sin \theta \leq w \quad (D.14)$$

$$\frac{w(\sin \theta + \cos \theta)}{2 \sin 2\theta} \sin \theta \leq w$$

$$\frac{(\sin \theta + \cos \theta)}{2 \sin 2\theta} \sin \theta \leq 1$$

$$\frac{(\sin \theta + \cos \theta)}{4 \sin \theta \cos \theta} \sin \theta \leq 1$$

$$\frac{(\sin \theta + \cos \theta)}{4 \cos \theta} \leq 1 \quad (D.15)$$

Considering the conditions in Equation D.13 and D14, we obtain that  $18.44^\circ \leq \theta \leq 71.56^\circ$ .

For  $0^\circ \leq \theta < 18.44^\circ$ , the maximum area is obtained when  $x = w$ , thus from D.3  $s_{max} = \frac{w}{\cos \theta}$ .

By substitution this into Equation D.5, we obtain

$$A_{max} = w \frac{w}{\cos \theta} (\sin \theta + \cos \theta) - \frac{w^2}{\cos \theta^2} \sin 2\theta \quad (D.16)$$

$$= w \frac{w}{\cos \theta} (\sin \theta + \cos \theta) - \frac{w^2}{\cos \theta^2} 2 \sin \theta \cos \theta$$

$$= \frac{w^2}{\cos \theta} (\sin \theta + \cos \theta) - \frac{w^2}{\cos \theta} 2 \sin \theta$$

$$= \frac{w^2}{\cos \theta} (\cos \theta - \sin \theta)$$

$$= w^2 (1 - \tan \theta) \quad (D.17)$$

By substitution D.17 into Equation D.11, we obtain

$$p = \frac{w^2(1-\tan \theta)}{w^2} \times 100 = (1 - \tan \theta) \times 100 \quad (\text{D.18})$$

For  $71.56^\circ < \theta \leq 90^\circ$ , the maximum area is obtained when  $y = w$ , thus from D.4  $s_{\max} = \frac{w}{\sin \theta}$ .

By substitution this into Equation D.5, we obtain

$$A_{\max} = w \frac{w}{\sin \theta} (\sin \theta + \cos \theta) - \frac{w^2}{(\sin \theta)^2} \sin 2\theta \quad (\text{D.19})$$

$$= w \frac{w}{\sin \theta} (\sin \theta + \cos \theta) - \frac{w^2}{(\sin \theta)^2} 2 \sin \theta \cos \theta$$

$$= \frac{w^2}{\sin \theta} (\sin \theta + \cos \theta) - \frac{w^2}{\sin \theta} 2 \cos \theta$$

$$= \frac{w^2}{\sin \theta} (\sin \theta - \cos \theta)$$

$$= w^2(1 - \cot \theta) \quad (\text{D.20})$$

By substitution D.20 into Equation D.11, we obtain

$$p = \frac{w^2(1-\cot \theta)}{w^2} \times 100 = (1 - \cot \theta) \times 100 \quad (\text{D.21})$$

We therefore obtain,

$$p = (1 - \tan \theta) \times 100, \quad 0^\circ \leq \theta < 18.44^\circ$$

$$p = \frac{25(\sin \theta + \cos \theta)^2}{\sin 2\theta}, \quad 18.44^\circ \leq \theta \leq 71.56^\circ \quad (\text{D.22})$$

$$p = (1 - \cot \theta) \times 100, \quad 71.56^\circ < \theta \leq 90^\circ$$





## List of References

- [1] W. Zeng, L. Shu, Q. Li, S. Chen, F. Wang, and X. M. Tao, "Fiber-based wearable electronics: A review of materials, fabrication, devices, and applications," *Adv. Mater.*, vol. 26, no. 31, pp. 5310–5336, 2014.
- [2] M. Peng, B. Dong, and D. Zou, "Three dimensional photovoltaic fibers for wearable energy harvesting and conversion," *J. Energy Chem.*, vol. 27, no. 3, pp. 611–621, May 2018.
- [3] J. Liu, Y. Li, S. Arumugam, J. Tudor, and S. Beeby, "Screen Printed Dye-Sensitized Solar Cells (DSSCs) on Woven Polyester Cotton Fabric for Wearable Energy Harvesting Applications," *Mater. Today Proc.*, vol. 5, no. 5, pp. 13753–13758, 2018.
- [4] R. Mather and J. Wilson, "Fabrication of Photovoltaic Textiles," *Coatings*, vol. 7, no. 5, p. 63, Apr. 2017.
- [5] Q. Wu and J. Hu, "A novel design of wearable thermoelectric generator based on 3D fabric structure," *Smart Mater. Struct.*, vol. at press, 2017.
- [6] Z. Cao, M. J. Tudor, R. N. Torah, and S. P. Beeby, "Screen Printable Flexible BiTe-SbTe-Based Composite Thermoelectric Materials on Textiles for Wearable Applications," *IEEE Trans. Electron Devices*, vol. 63, no. 10, pp. 4024–4030, 2016.
- [7] J. A. Lee *et al.*, "Woven-Yarn Thermoelectric Textiles," *Adv. Mater.*, pp. 5038–5044, 2016.
- [8] S. Song and K. S. Yun, "Design and characterization of scalable woven piezoelectric energy harvester for wearable applications," *Smart Mater. Struct.*, vol. 24, no. 4, 2015.
- [9] D. Matsouka, S. Vassiliadis, and D. V. Bayramol, "Piezoelectric textile fibres for wearable energy harvesting systems," *Mater. Res. Express*, vol. 5, no. 6, pp. 0–10, 2018.
- [10] A. Almusallam *et al.*, "Flexible piezoelectric nano-composite films for kinetic energy harvesting from textiles," *Nano Energy*, vol. 33, no. January, pp. 146–156, 2017.
- [11] F.-R. Fan, Z.-Q. Tian, and Z. Lin Wang, "Flexible triboelectric generator," *Nano Energy*, vol. 1, no. 2, pp. 328–334, Mar. 2012.
- [12] S. Wang, L. Lin, and Z. L. Wang, "Nanoscale-triboelectric-effect enabled energy conversion for sustainable powering of portable electronics," *Nano Lett.*, vol. 12, no. 12, pp. 6339–46, 2012.

## List of References

- [13] G. Zhu *et al.*, "Toward large-scale energy harvesting by a nanoparticle-enhanced triboelectric nanogenerator," *Nano Lett.*, vol. 13, no. 2, pp. 847–853, 2013.
- [14] S. Lee *et al.*, "Triboelectric energy harvester based on wearable textile platforms employing various surface morphologies," *Nano Energy*, vol. 12, pp. 410–418, Mar. 2015.
- [15] W. Seung *et al.*, "Nanopatterned Textile-Based Wearable Triboelectric Nanogenerator," *ACS Nano*, vol. 9, no. 4, pp. 3501–3509, Apr. 2015.
- [16] X. S. Zhang *et al.*, "High-performance triboelectric nanogenerator with enhanced energy density based on single-step fluorocarbon plasma treatment," *Nano Energy*, vol. 4, pp. 123–131, 2014.
- [17] J. Luo and Z. L. Wang, "Recent advances in triboelectric nanogenerator based self-charging power systems," *Energy Storage Mater.*, no. November 2018, 2019.
- [18] J. Luo and Z. L. Wang, "Recent progress of triboelectric nanogenerators: From fundamental theory to practical applications," *EcoMat*, vol. 2, no. 4, pp. 1–22, 2020.
- [19] Q. Gao, T. Cheng, and Z. L. Wang, "Triboelectric mechanical sensors—Progress and prospects," *Extrem. Mech. Lett.*, vol. 42, p. 101100, Jan. 2021.
- [20] W. Paosangthong, R. Torah, and S. Beeby, "Recent progress on textile-based triboelectric nanogenerators," *Nano Energy*, vol. 55, pp. 401–423, Jan. 2019.
- [21] W. Wang, A. Yu, J. Zhai, and Z. L. Wang, "Recent Progress of Functional Fiber and Textile Triboelectric Nanogenerators: Towards Electricity Power Generation and Intelligent Sensing," *Adv. Fiber Mater.*, no. 0123456789, Jun. 2021.
- [22] Y. Zou, V. Raveendran, and J. Chen, "Wearable triboelectric nanogenerators for biomechanical energy harvesting," *Nano Energy*, vol. 77, no. August, p. 105303, 2020.
- [23] J. Xiong and P. S. Lee, "Progress on wearable triboelectric nanogenerators in shapes of fiber, yarn, and textile," *Sci. Technol. Adv. Mater.*, vol. 20, no. 1, pp. 837–857, 2019.
- [24] W. Wang *et al.*, "Large-scale fabrication of robust textile triboelectric nanogenerators," *Nano Energy*, vol. 71, no. January, p. 104605, 2020.
- [25] Y. Yang *et al.*, "Triboelectric nanogenerator for harvesting wind energy and as self-powered wind vector sensor system," *ACS Nano*, vol. 7, no. 10, pp. 9461–9468, 2013.
- [26] L. Zhang *et al.*, "Lawn Structured Triboelectric Nanogenerators for Scavenging Sweeping

- Wind Energy on Rooftops,” *Adv. Mater.*, vol. 28, no. 8, pp. 1650–1656, 2016.
- [27] B. Dudem, D. H. Kim, and J. S. Yu, “Triboelectric nanogenerators with gold-thin-film-coated conductive textile as floating electrode for scavenging wind energy,” *Nano Res.*, vol. 11, no. 1, pp. 1–13, 2017.
- [28] T. Jiang *et al.*, “Structural Optimization of Triboelectric Nanogenerator for Harvesting Water Wave Energy,” *ACS Nano*, vol. 9, no. 12, pp. 12562–12572, 2015.
- [29] T. Jiang, Y. Yao, L. Xu, L. Zhang, T. Xiao, and Z. L. Wang, “Spring-assisted triboelectric nanogenerator for efficiently harvesting water wave energy,” *Nano Energy*, vol. 31, no. November 2016, pp. 560–567, 2017.
- [30] T. C. Hou, Y. Yang, H. Zhang, J. Chen, L. J. Chen, and Z. Lin Wang, “Triboelectric nanogenerator built inside shoe insole for harvesting walking energy,” *Nano Energy*, vol. 2, no. 5, pp. 856–862, 2013.
- [31] M. Ha, J. Park, Y. Lee, and H. Ko, “Triboelectric generators and sensors for self-powered wearable electronics,” *ACS Nano*, vol. 9, no. 4, pp. 3421–3427, 2015.
- [32] A. Proto, M. Penhaker, S. Conforto, and M. Schmid, “Nanogenerators for Human Body Energy Harvesting,” *Trends Biotechnol.*, vol. 35, no. 7, pp. 610–624, Jul. 2017.
- [33] S. S. Kwak, H. Yoon, and S. Kim, “Textile-Based Triboelectric Nanogenerators for Self-Powered Wearable Electronics,” *Adv. Funct. Mater.*, vol. 29, no. 2, p. 1804533, Jan. 2019.
- [34] W. Paosangthong, R. Torah, and S. Beeby, “Recent progress on textile-based triboelectric nanogenerators,” *Nano Energy*, vol. 55, no. August 2018. Elsevier Ltd, pp. 401–423, Jan-2019.
- [35] Y. Hu and Z. Zheng, “Progress in textile-based triboelectric nanogenerators for smart fabrics,” *Nano Energy*, vol. 56, no. November 2018, pp. 16–24, Feb. 2019.
- [36] T. Huang *et al.*, “Fabric texture design for boosting the performance of a knitted washable textile triboelectric nanogenerator as wearable power,” *Nano Energy*, vol. 58, no. December 2018, pp. 375–383, 2019.
- [37] Z. Tian *et al.*, “Performance-boosted triboelectric textile for harvesting human motion energy,” *Nano Energy*, vol. 39, no. May, pp. 562–570, 2017.
- [38] M. Shi, H. Wu, J. Zhang, M. Han, B. Meng, and H. Zhang, “Self-powered wireless smart patch for healthcare monitoring,” *Nano Energy*, vol. 32, no. November 2016, pp. 479–487,

## List of References

2017.

- [39] K. Dong *et al.*, “3D Orthogonal Woven Triboelectric Nanogenerator for Effective Biomechanical Energy Harvesting and as Self-Powered Active Motion Sensors,” *Adv. Mater.*, vol. 29, no. 38, p. 1702648, Oct. 2017.
- [40] X. Li *et al.*, “3D fiber-based hybrid nanogenerator for energy harvesting and as a self-powered pressure sensor,” *ACS Nano*, vol. 8, no. 10, pp. 10674–10681, 2014.
- [41] Y. Cheng *et al.*, “A stretchable fiber nanogenerator for versatile mechanical energy harvesting and self-powered full-range personal healthcare monitoring,” *Nano Energy*, vol. 41, no. September, pp. 511–518, 2017.
- [42] Z. Lin *et al.*, “Large-Scale and Washable Smart Textiles Based on Triboelectric Nanogenerator Arrays for Self-Powered Sleeping Monitoring,” *Adv. Funct. Mater.*, vol. 28, no. 1, p. 1704112, Jan. 2018.
- [43] Z. Zhao *et al.*, “Freestanding Flag-Type Triboelectric Nanogenerator for Harvesting High-Altitude Wind Energy from Arbitrary Directions,” *ACS Nano*, vol. 10, no. 2, pp. 1780–1787, 2016.
- [44] W. Paosangthong, M. Wagih, R. Torah, and S. Beeby, “Textile-based triboelectric nanogenerator with alternating positive and negative freestanding grating structure,” *Nano Energy*, vol. 66, p. 104148, Dec. 2019.
- [45] W. Paosangthong, M. Wagih, R. Torah, and S. Beeby, “Textile-based triboelectric nanogenerator with alternating positive and negative freestanding woven structure for harvesting sliding energy in all directions,” *Nano Energy*, vol. 92, p. 106739, Feb. 2022.
- [46] W. Paosangthong, R. Torah, and S. Beeby, “Textile-based freestanding triboelectric-layer nanogenerator with alternate positive and negative grating structure,” *J. Phys. Conf. Ser.*, vol. 1407, no. 1, pp. 0–5, 2019.
- [47] W. Paosangthong, M. Wagih, R. Torah, and S. Beeby, “Textile Manufacturing Compatible Triboelectric Nanogenerator with Alternating Positive and Negative Freestanding Grating Structure,” *Proceedings*, vol. 32, no. 1, p. 23, Jan. 2020.
- [48] A. F. Diaz and R. M. Felix-Navarro, “A semi-quantitative tribo-electric series for polymeric materials: The influence of chemical structure and properties,” *J. Electrostat.*, vol. 62, no. 4, pp. 277–290, 2004.

- [49] P. Iversen and D. J. Lacks, "A life of its own: The tenuous connection between Thales of Miletus and the study of electrostatic charging," *J. Electrostat.*, vol. 70, no. 3, pp. 309–311, 2012.
- [50] M. Williams, "What Creates Static Electricity?," *Am. Sci.*, vol. 100, no. 4, p. 316, 2012.
- [51] L. S. McCarty and G. M. Whitesides, "Electrostatic charging due to separation of ions at interfaces: Contact electrification of ionic electrets," *Angew. Chemie - Int. Ed.*, vol. 47, no. 12, pp. 2188–2207, 2008.
- [52] F. Galembeck, T. A. L. Burgo, L. B. S. Balestrin, R. F. Gouveia, C. A. Silva, and A. Galembeck, "Friction, tribochemistry and triboelectricity: Recent progress and perspectives," *RSC Adv.*, vol. 4, no. 109, pp. 64280–64298, 2014.
- [53] C. Xu *et al.*, "On the Electron-Transfer Mechanism in the Contact-Electrification Effect," *Adv. Mater.*, vol. 30, no. 15, pp. 1–9, 2018.
- [54] Z. L. Wang and A. C. Wang, "On the origin of contact-electrification," *Mater. Today*, vol. 30, no. November, pp. 34–51, 2019.
- [55] J. L. Heilbron, *Electricity in the 17th and 18th centuries: A study of early modern physics*. Univ of California Press., 1979.
- [56] E. M. Charlson, E. J. Charlson, S. Burkett, and H. K. Yasuda, "Study of the Contact Electrification of Polymers using Contact and Separation Current," *IEEE Trans. Electr. Insul.*, vol. 27, no. 6, pp. 1144–1151, 1992.
- [57] A. Wåhlin and G. Bäckström, "Sliding electrification of Teflon by metals," *J. Appl. Phys.*, vol. 45, no. 5, pp. 2058–2064, 1974.
- [58] J. Lowell and A. Brown, "Contact electrification of chemically modified surfaces," *J. Electrostat.*, vol. 21, no. 1, pp. 69–79, 1988.
- [59] A. R. Akande, "Charge correlation in metal/polymer contact," *Compos. Struct.*, vol. 54, no. 2–3, pp. 143–147, Nov. 2001.
- [60] J. Lowell and A. R. Akande, "Contact electrification—why is it variable?," *J. Phys. D. Appl. Phys.*, vol. 21, no. 1, pp. 125–137, 1988.
- [61] J. W. Lee, B. U. Ye, and J. M. Baik, "Research Update: Recent progress in the development of effective dielectrics for high-output triboelectric nanogenerator," *APL Mater.*, vol. 5, no. 7, 2017.

## List of References

- [62] H. Zou *et al.*, “Quantifying the triboelectric series,” *Nat. Commun.*, vol. 10, no. 1, pp. 1–9, 2019.
- [63] Z. L. Wang, J. Chen, and L. Lin, “Progress in triboelectric nanogenerators as a new energy technology and self-powered sensors,” *Energy Environ. Sci.*, vol. 8, no. 8, pp. 2250–2282, 2015.
- [64] Q. Zheng, B. Shi, Z. Li, and Z. L. Wang, “Recent Progress on Piezoelectric and Triboelectric Energy Harvesters in Biomedical Systems,” *Adv. Sci.*, vol. 4, no. 7, p. 1700029, Jul. 2017.
- [65] S. Wang, L. Lin, and Z. L. Wang, “Triboelectric nanogenerators as self-powered active sensors,” *Nano Energy*, vol. 11, pp. 436–462, 2015.
- [66] T. Huang, C. Wang, H. Yu, H. Wang, Q. Zhang, and M. Zhu, “Human walking-driven wearable all-fiber triboelectric nanogenerator containing electrospun polyvinylidene fluoride piezoelectric nanofibers,” *Nano Energy*, vol. 14, pp. 226–235, May 2015.
- [67] L. Liu *et al.*, “A triboelectric textile templated by a three-dimensionally penetrated fabric,” *J. Mater. Chem. A*, vol. 4, no. 16, pp. 6077–6083, 2016.
- [68] Y. Guo, K. Li, C. Hou, Y. Li, Q. Zhang, and H. Wang, “Fluoroalkylsilane-Modified Textile-Based Personal Energy Management Device for Multifunctional Wearable Applications,” *ACS Appl. Mater. Interfaces*, vol. 8, no. 7, pp. 4676–4683, Feb. 2016.
- [69] Y. H. Ko, G. Nagaraju, and J. S. Yu, “Multi-stacked PDMS-based triboelectric generators with conductive textile for efficient energy harvesting,” *RSC Adv.*, vol. 5, no. 9, pp. 6437–6442, 2015.
- [70] P. S. Das, J. Y. Park, and D. H. Kim, “Vacuum filtered conductive nylon membrane-based flexible TENG for wearable electronics,” *Micro Nano Lett.*, vol. 12, no. 9, pp. 697–700, Sep. 2017.
- [71] C. Wu, T. W. Kim, F. Li, and T. Guo, “Wearable Electricity Generators Fabricated Utilizing Transparent Electronic Textiles Based on Polyester/Ag Nanowires/Graphene Core-Shell Nanocomposites,” *ACS Nano*, vol. 10, no. 7, pp. 6449–6457, 2016.
- [72] H. J. Sim *et al.*, “Stretchable Triboelectric Fiber for Self-powered Kinematic Sensing Textile,” *Sci. Rep.*, vol. 6, no. 1, p. 35153, Dec. 2016.
- [73] Z. Wen *et al.*, “Self-powered textile for wearable electronics by hybridizing fiber-shaped nanogenerators, solar cells, and supercapacitors,” *Sci. Adv.*, vol. 2, no. 10, pp. e1600097–

- e1600097, 2016.
- [74] Z. Zhao *et al.*, "Machine-Washable Textile Triboelectric Nanogenerators for Effective Human Respiratory Monitoring through Loom Weaving of Metallic Yarns," *Adv. Mater.*, vol. 28, no. 46, pp. 10267–10274, Dec. 2016.
  - [75] K. N. Kim *et al.*, "Highly Stretchable 2D Fabrics for Wearable Triboelectric Nanogenerator under Harsh Environments," *ACS Nano*, vol. 9, no. 6, pp. 6394–6400, Jun. 2015.
  - [76] J. Zhong *et al.*, "Fiber-Based Generator for Wearable Electronics and Mobile Medication," *ACS Nano*, vol. 8, no. 6, pp. 6273–6280, Jun. 2014.
  - [77] W. Gong *et al.*, "A wearable, fibroid, self-powered active kinematic sensor based on stretchable sheath-core structural triboelectric fibers," *Nano Energy*, vol. 39, no. August, pp. 673–683, Sep. 2017.
  - [78] S. Wang, L. Lin, Y. Xie, Q. Jing, S. Niu, and Z. L. Wang, "Sliding-triboelectric nanogenerators based on in-plane charge-separation mechanism," *Nano Lett.*, vol. 13, no. 5, pp. 2226–2233, 2013.
  - [79] L. Lin *et al.*, "Segmentally structured disk triboelectric nanogenerator for harvesting rotational mechanical energy," *Nano Lett.*, vol. 13, no. 6, pp. 2916–2923, 2013.
  - [80] P. Bai *et al.*, "Cylindrical Rotating Triboelectric Nanogenerator," *ACS Nano*, vol. 7, no. 7, pp. 6361–6366, Jul. 2013.
  - [81] G. Zhu *et al.*, "A shape-adaptive thin-film-based approach for 50% high-efficiency energy generation through micro-grating sliding electrification," *Adv. Mater.*, vol. 26, no. 23, pp. 3788–3796, 2014.
  - [82] S. Jung, J. Lee, T. Hyeon, M. Lee, and D. H. Kim, "Fabric-based integrated energy devices for wearable activity monitors," *Adv. Mater.*, vol. 26, no. 36, pp. 6329–6334, 2014.
  - [83] N. Cui, J. Liu, L. Gu, S. Bai, X. Chen, and Y. Qin, "Wearable Triboelectric Generator for Powering the Portable Electronic Devices," *ACS Appl. Mater. Interfaces*, vol. 7, no. 33, pp. 18225–18230, 2015.
  - [84] S. Niu *et al.*, "Theoretical Investigation and Structural Optimization of Single-Electrode Triboelectric Nanogenerators," *Adv. Funct. Mater.*, vol. 24, no. 22, pp. 3332–3340, Jun. 2014.
  - [85] S. Li *et al.*, "Cloth-based power shirt for wearable energy harvesting and clothes

## List of References

- ornamentation,” *ACS Appl. Mater. Interfaces*, vol. 7, no. 27, pp. 14912–14916, 2015.
- [86] M. Shi, J. Zhang, M. Han, Y. Song, Z. Su, and H. Zhang, “A single-electrode wearable triboelectric nanogenerator based on conductive & stretchable fabric,” in *2016 IEEE 29th International Conference on Micro Electro Mechanical Systems (MEMS)*, 2016, vol. 2016-Febru, no. January, pp. 1228–1231.
- [87] G. Song *et al.*, “Molecularly Engineered Surface Triboelectric Nanogenerator by Self-Assembled Monolayers (METS),” *Chem. Mater.*, vol. 27, no. 13, pp. 4749–4755, 2015.
- [88] Q. Zhang *et al.*, “Service Behavior of Multifunctional Triboelectric Nanogenerators,” *Adv. Mater.*, vol. 29, no. 17, p. 1606703, May 2017.
- [89] Y.-C. Lai, J. Deng, S. L. Zhang, S. Niu, H. Guo, and Z. L. Wang, “Single-Thread-Based Wearable and Highly Stretchable Triboelectric Nanogenerators and Their Applications in Cloth-Based Self-Powered Human-Interactive and Biomedical Sensing,” *Adv. Funct. Mater.*, vol. 27, no. 1, p. 1604462, Jan. 2017.
- [90] X. Pu *et al.*, “Wearable Power-Textiles by Integrating Fabric Triboelectric Nanogenerators and Fiber-Shaped Dye-Sensitized Solar Cells,” *Adv. Energy Mater.*, vol. 6, no. 20, p. 1601048, Oct. 2016.
- [91] A. Yu *et al.*, “Core–Shell-Yarn-Based Triboelectric Nanogenerator Textiles as Power Cloths,” *ACS Nano*, vol. 11, no. 12, pp. 12764–12771, Dec. 2017.
- [92] X. Pu *et al.*, “A self-charging power unit by integration of a textile triboelectric nanogenerator and a flexible lithium-ion battery for wearable electronics,” *Adv. Mater.*, vol. 27, no. 15, pp. 2472–2478, 2015.
- [93] T. Zhou, C. Zhang, C. B. Han, F. R. Fan, W. Tang, and Z. L. Wang, “Woven structured triboelectric nanogenerator for wearable devices,” *ACS Appl. Mater. Interfaces*, vol. 6, no. 16, pp. 14695–14701, Aug. 2014.
- [94] X. Pu *et al.*, “Wearable Self-Charging Power Textile Based on Flexible Yarn Supercapacitors and Fabric Nanogenerators,” *Advanced Materials*, vol. 28, no. 1. pp. 98–105, 2016.
- [95] X. Guan, B. Xu, M. Wu, T. Jing, Y. Yang, and Y. Gao, “Breathable, washable and wearable woven-structured triboelectric nanogenerators utilizing electrospun nanofibers for biomechanical energy harvesting and self-powered sensing,” *Nano Energy*, vol. 80, no. October 2020, p. 105549, 2021.



- [96] S. Niu *et al.*, "Theory of freestanding triboelectric-layer-based nanogenerators," *Nano Energy*, vol. 12, pp. 760–774, 2015.
- [97] S. Niu *et al.*, "Theory of sliding-mode triboelectric nanogenerators," *Adv. Mater.*, vol. 25, no. 43, pp. 6184–6193, 2013.
- [98] R. Kamiya, B. A. Cheeseman, P. Popper, and T.-W. Chou, "Some recent advances in the fabrication and design of three-dimensional textile preforms: a review," *Compos. Sci. Technol.*, vol. 60, no. 1, pp. 33–47, Jan. 2000.
- [99] W. E. Morton and J. W. S. Hearle, *Physical properties of textile fibres*, Fourth ed. Cambridge: Woodhead Publishing Limited, 2008.
- [100] B. P. Corbman, *Textiles : Fiber to Fabric*, Sixth ed. New York: Gregg Division/McGraw-Hill Book Company, 1983.
- [101] K. Bilisik, N. S. Karaduman, and N. E. Bilisik, "3D Fabrics for Technical Textile Applications," in *Non-woven Fabrics*, H.-Y. Jeon, Ed. London: InTech, 2016.
- [102] J. Peterson, *Customisation of Fashion Products Using Complete Garment Technology*, no. November. 2012.
- [103] N. Bhardwaj and S. C. Kundu, "Electrospinning: A fascinating fiber fabrication technique," *Biotechnol. Adv.*, vol. 28, no. 3, pp. 325–347, May 2010.
- [104] Y. Guo *et al.*, "All-fiber hybrid piezoelectric-enhanced triboelectric nanogenerator for wearable gesture monitoring," *Nano Energy*, vol. 48, no. February, pp. 152–160, 2018.
- [105] S. S. Kwak, H. Kim, W. Seung, J. Kim, R. Hinchet, and S.-W. Kim, "Fully Stretchable Textile Triboelectric Nanogenerator with Knitted Fabric Structures," *ACS Nano*, vol. 11, no. 11, pp. 10733–10741, Nov. 2017.
- [106] J. Chen *et al.*, "Micro-cable structured textile for simultaneously harvesting solar and mechanical energy," *Nat. Energy*, vol. 1, no. 10, p. 16138, Oct. 2016.
- [107] Z. Tian *et al.*, "Core-shell coaxially structured triboelectric nanogenerator for energy harvesting and motion sensing," *RSC Adv.*, vol. 8, no. 6, pp. 2950–2957, 2018.
- [108] R. I. Haque, P.-A. Farine, and D. Briand, "Soft triboelectric generators by use of cost-effective elastomers and simple casting process," *Sensors Actuators A Phys.*, vol. 271, pp. 88–95, Mar. 2018.

## List of References

- [109] C. Ning *et al.*, "Washable textile-structured single-electrode triboelectric nanogenerator for self-powered wearable electronics," *J. Mater. Chem. A*, vol. 6, no. 39, pp. 19143–19150, 2018.
- [110] S. Niu *et al.*, "Theoretical study of contact-mode triboelectric nanogenerators as an effective power source," *Energy Environ. Sci.*, vol. 6, no. 12, p. 3576, 2013.
- [111] V. Kaushik *et al.*, "Textile-Based Electronic Components for Energy Applications: Principles, Problems, and Perspective," *Nanomaterials*, vol. 5, no. 3, pp. 1493–1531, 2015.
- [112] J. Lee *et al.*, "Conductive fiber-based ultrasensitive textile pressure sensor for wearable electronics," *Adv. Mater.*, vol. 27, no. 15, pp. 2433–2439, 2015.
- [113] R. B. Reed *et al.*, "Potential Environmental Impacts and Antimicrobial Efficacy of Silver- and Nanosilver-Containing Textiles," *Environ. Sci. Technol.*, vol. 50, no. 7, pp. 4018–4026, 2016.
- [114] X. Wang, H. Hu, Y. Shen, X. Zhou, and Z. Zheng, "Stretchable conductors with ultrahigh tensile strain and stable metallic conductance enabled by prestrained polyelectrolyte nanoplateforms," *Adv. Mater.*, vol. 23, no. 27, pp. 3090–3094, 2011.
- [115] F. Xu and Y. Zhu, "Highly conductive and stretchable silver nanowire conductors," *Adv. Mater.*, vol. 24, no. 37, pp. 5117–5122, 2012.
- [116] K. Kim, G. Song, C. Park, and K. S. Yun, "Multifunctional woven structure operating as triboelectric energy harvester, capacitive tactile sensor array, and piezoresistive strain sensor array," *Sensors (Switzerland)*, vol. 17, no. 11, 2017.
- [117] Y. Yang *et al.*, "Liquid-Metal-Based Super-Stretchable and Structure-Designable Triboelectric Nanogenerator for Wearable Electronics," *ACS Nano*, vol. 12, no. 2, pp. 2027–2034, 2018.
- [118] X. He *et al.*, "A Highly Stretchable Fiber-Based Triboelectric Nanogenerator for Self-Powered Wearable Electronics," *Adv. Funct. Mater.*, vol. 27, no. 4, p. 1604378, Jan. 2017.
- [119] H. Chu, H. Jang, Y. Lee, Y. Chae, and J.-H. Ahn, "Conformal, graphene-based triboelectric nanogenerator for self-powered wearable electronics," *Nano Energy*, vol. 27, pp. 298–305, Sep. 2016.
- [120] M. Zhu *et al.*, "3D spacer fabric based multifunctional triboelectric nanogenerator with great feasibility for mechanized large-scale production," *Nano Energy*, vol. 27, pp. 439–446, Sep. 2016.

- [121] H. Shirakawa, E. J. Louis, A. G. MacDiarmid, C. K. Chiang, and A. J. Heeger, "Synthesis of electrically conducting organic polymers: halogen derivatives of polyacetylene,  $(CH)_x$ ," *J. Chem. Soc. Chem. Commun.*, no. 16, p. 578, 1977.
- [122] S. Cui, Y. Zheng, J. Liang, and D. Wang, "Conducting polymer PPy nanowire-based triboelectric nanogenerator and its application for self-powered electrochemical cathodic protection," *Chem. Sci.*, vol. 7, no. 10, pp. 6477–6483, 2016.
- [123] J. Wang *et al.*, "All-Plastic-Materials Based Self-Charging Power System Composed of Triboelectric Nanogenerators and Supercapacitors," *Advanced Functional Materials*, vol. 26, no. 7, pp. 1070–1076, 2016.
- [124] S. Zhao *et al.*, "Recent Advancements in Flexible and Stretchable Electrodes for Electromechanical Sensors: Strategies, Materials, and Features," *ACS Appl. Mater. Interfaces*, vol. 9, no. 14, pp. 12147–12164, 2017.
- [125] Z. Li *et al.*, "Free-standing conducting polymer films for high-performance energy devices," *Angew. Chemie - Int. Ed.*, vol. 55, no. 3, pp. 979–982, 2016.
- [126] A. Šutka, M. Timusk, J. Metsik, J. Ruža, M. Knite, and U. Mäeorg, "PEDOT electrodes for triboelectric generator devices," *Org. Electron. physics, Mater. Appl.*, vol. 51, no. September, pp. 446–451, 2017.
- [127] M. Zhu *et al.*, "Self-Powered and Self-Functional Cotton Sock Using Piezoelectric and Triboelectric Hybrid Mechanism for Healthcare and Sports Monitoring," *ACS Nano*, vol. 13, pp. 1940–1952, 2019.
- [128] T. Jing, B. Xu, and Y. Yang, "Organogel electrode based continuous fiber with large-scale production for stretchable triboelectric nanogenerator textiles," *Nano Energy*, vol. 84, no. December 2020, 2021.
- [129] Z. Zhang, Y. Chen, D. K. Debeli, and J. S. Guo, "Facile Method and Novel Dielectric Material Using a Nanoparticle-Doped Thermoplastic Elastomer Composite Fabric for Triboelectric Nanogenerator Applications," *ACS Appl. Mater. Interfaces*, vol. 10, no. 15, pp. 13082–13091, 2018.
- [130] J. Xiong *et al.*, "Skin-touch-actuated textile-based triboelectric nanogenerator with black phosphorus for durable biomechanical energy harvesting," *Nat. Commun.*, vol. 9, no. 1, pp. 1–9, 2018.
- [131] F. R. Fan, L. Lin, G. Zhu, W. Wu, R. Zhang, and Z. L. Wang, "Transparent triboelectric

## List of References

- nanogenerators and self-powered pressure sensors based on micropatterned plastic films," *Nano Lett.*, vol. 12, no. 6, pp. 3109–3114, 2012.
- [132] C. K. Jeong *et al.*, "Topographically-designed triboelectric nanogenerator via block copolymer self-assembly," *Nano Lett.*, vol. 14, no. 12, pp. 7031–7038, 2014.
- [133] X. S. Zhang *et al.*, "Frequency-multiplication high-output triboelectric nanogenerator for sustainably powering biomedical microsystems," *Nano Lett.*, vol. 13, no. 3, pp. 1168–1172, 2013.
- [134] W. B. Ko, D. S. Choi, C. H. Lee, J. Y. Yang, G. S. Yoon, and J. P. Hong, "Hierarchically Nanostructured 1D Conductive Bundle Yarn-Based Triboelectric Nanogenerators," *Adv. Mater.*, vol. 29, no. 47, p. 1704434, Dec. 2017.
- [135] C. Lee, S. Yang, D. Choi, W. Kim, J. Kim, and J. Hong, "Chemically surface-engineered polydimethylsiloxane layer via plasma treatment for advancing textile-based triboelectric nanogenerators," *Nano Energy*, vol. 57, no. October 2018, pp. 353–362, 2019.
- [136] H. Y. Li, L. Su, S. Y. Kuang, C. F. Pan, G. Zhu, and Z. L. Wang, "Significant Enhancement of Triboelectric Charge Density by Fluorinated Surface Modification in Nanoscale for Converting Mechanical Energy," *Adv. Funct. Mater.*, vol. 25, no. 35, pp. 5691–5697, 2015.
- [137] A. Y. Choi, C. J. Lee, J. Park, D. Kim, and Y. T. Kim, "Corrugated Textile based Triboelectric Generator for Wearable Energy Harvesting," *Sci. Rep.*, vol. 7, no. 1, p. 45583, Dec. 2017.
- [138] K. Dong *et al.*, "A Highly Stretchable and Washable All-Yarn-Based Self-Charging Knitting Power Textile Composed of Fiber Triboelectric Nanogenerators and Supercapacitors," *ACS Nano*, vol. 11, no. 9, pp. 9490–9499, 2017.
- [139] Y. Chen *et al.*, "3D printed stretchable smart fibers and textiles for self-powered e-skin," *Nano Energy*, vol. 84, no. January, p. 105866, 2021.
- [140] J. Chen, H. Guo, X. Pu, X. Wang, Y. Xi, and C. Hu, "Traditional weaving craft for one-piece self-charging power textile for wearable electronics," *Nano Energy*, vol. 50, no. April, pp. 536–543, Aug. 2018.
- [141] Y. Zi, S. Niu, J. Wang, Z. Wen, W. Tang, and Z. L. Wang, "Standards and figure-of-merits for quantifying the performance of triboelectric nanogenerators," *Nat. Commun.*, vol. 6, no. 1, p. 8376, Dec. 2015.
- [142] V. Nguyen and R. Yang, "Effect of humidity and pressure on the triboelectric

- nanogenerator,” *Nano Energy*, vol. 2, no. 5, pp. 604–608, 2013.
- [143] V. Nguyen, R. Zhu, and R. Yang, “Environmental effects on nanogenerators,” *Nano Energy*, vol. 14, pp. 49–61, 2014.
- [144] F. Xi *et al.*, “Universal power management strategy for triboelectric nanogenerator,” *Nano Energy*, vol. 37, no. May, pp. 168–176, 2017.
- [145] A. Ghaffarinejad *et al.*, “A conditioning circuit with exponential enhancement of output energy for triboelectric nanogenerator,” *Nano Energy*, vol. 51, no. June, pp. 173–184, Sep. 2018.
- [146] Y. Song *et al.*, “All-fabric-based wearable self-charging power cloth,” *Appl. Phys. Lett.*, vol. 111, no. 7, p. 073901, Aug. 2017.
- [147] X. Pu, W. Hu, and Z. L. Wang, “Toward Wearable Self-Charging Power Systems: The Integration of Energy-Harvesting and Storage Devices,” *Small*, vol. 14, no. 1, p. 1702817, Jan. 2018.
- [148] H. Wu, Y. A. Huang, F. Xu, Y. Duan, and Z. Yin, “Energy Harvesters for Wearable and Stretchable Electronics: From Flexibility to Stretchability,” *Adv. Mater.*, vol. 28, no. 45, pp. 9881–9919, 2016.
- [149] S. Liu, W. Zheng, B. Yang, and X. Tao, “Triboelectric charge density of porous and deformable fabrics made from polymer fibers,” *Nano Energy*, vol. 53, no. August, pp. 383–390, Nov. 2018.
- [150] Y. Xie *et al.*, “Grating-Structured Freestanding Triboelectric-Layer Nanogenerator for Harvesting Mechanical Energy at 85% Total Conversion Efficiency,” *Adv. Mater.*, vol. 26, no. 38, pp. 6599–6607, Oct. 2014.
- [151] C. X. Lu *et al.*, “Temperature Effect on Performance of Triboelectric Nanogenerator,” *Adv. Eng. Mater.*, vol. 19, no. 12, pp. 1–8, 2017.
- [152] H. Zhang, Y. Lu, A. Ghaffarinejad, and P. Basset, “Progressive contact-separate triboelectric nanogenerator based on conductive polyurethane foam regulated with a Bennet doubler conditioning circuit,” *Nano Energy*, vol. 51, no. June, pp. 10–18, 2018.
- [153] W. Seung *et al.*, “Nanopatterned textile-based wearable triboelectric nanogenerator,” *ACS Nano*, vol. 9, no. 4, pp. 3501–3509, 2015.
- [154] G. Zhu *et al.*, “Linear-grating triboelectric generator based on sliding electrification,” *Nano*

## List of References

- Lett.*, vol. 13, no. 5, pp. 2282–2289, 2013.
- [155] W. Shang *et al.*, “A Sliding-Mode Triboelectric Nanogenerator with Chemical Group Grated Structure by Shadow Mask Reactive Ion Etching,” *ACS Nano*, vol. 11, no. 9, pp. 8796–8803, 2017.
- [156] M. Bi, S. Wang, X. Wang, and X. Ye, “Freestanding-electret rotary generator at an average conversion efficiency of 56%: Theoretical and experimental studies,” *Nano Energy*, vol. 41, no. August, pp. 434–442, 2017.
- [157] H. Guo *et al.*, “An ultrarobust high-performance triboelectric nanogenerator based on charge replenishment,” *ACS Nano*, vol. 9, no. 5, pp. 5577–5584, 2015.
- [158] S. Wang, Y. Xie, S. Niu, L. Lin, and Z. L. Wang, “Freestanding triboelectric-layer-based nanogenerators for harvesting energy from a moving object or human motion in contact and non-contact modes,” *Adv. Mater.*, vol. 26, no. 18, pp. 2818–2824, 2014.
- [159] A. Canedo-Rodriguez, J. Rodriguez, V. Alvarez-Santos, R. Iglesias, and C. Regueiro, “Mobile Robot Positioning with 433-MHz Wireless Motes with Varying Transmission Powers and a Particle Filter,” *Sensors*, vol. 15, no. 5, pp. 10194–10220, Apr. 2015.
- [160] J. P. HUNTER, R. N. MARSHALL, and P. J. MCNAIR, “Interaction of Step Length and Step Rate during Sprint Running,” *Med. Sci. Sport. Exerc.*, vol. 36, no. 2, pp. 261–271, Feb. 2004.
- [161] H. Guo *et al.*, “A Triboelectric Generator Based on Checker-Like Interdigital Electrodes with a Sandwiched PET Thin Film for Harvesting Sliding Energy in All Directions,” *Adv. Energy Mater.*, vol. 5, no. 1, p. 1400790, Jan. 2015.
- [162] X. Xia, G. Liu, H. Guo, Q. Leng, C. Hu, and Y. Xi, “Honeycomb-like three electrodes based triboelectric generator for harvesting energy in full space and as a self-powered vibration alertor,” *Nano Energy*, vol. 15, pp. 766–775, 2015.
- [163] G. Ma *et al.*, “A bioinspired triboelectric nanogenerator for all state energy harvester and self-powered rotating monitor,” *Nano Energy*, vol. 91, no. October 2021, p. 106637, 2022.
- [164] X. Hou *et al.*, “Stretchable Triboelectric Textile Composed of Wavy Conductive-Cloth-PET and Patterned Stretchable Electrode for Harvesting Multi-variant Human Motion Energy,” *ACS Appl. Mater. Interfaces*, vol. 10, p. acsami.8b16267, 2018.
- [165] Sheng Zhou and J. K. Pollard, “Position Measurement using Bluetooth,” *IEEE Trans. Consum. Electron.*, vol. 52, no. 2, pp. 555–558, May 2006.